# INFORMATION TO USERS

This manuscript has been reproduced from the microfilm master. UMI films the text directly from the original or copy submitted. Thus, some thesis and dissertation copies are in typewriter face, while others may be from any type of computer printer.

**The quality of this reproduction is dependent upon the quality of the copy submitted.** Broken or indistinct print, colored or poor quality illustrations and photographs, print bleedthrough, substandard margins, and improper alignment can adversely affect reproduction.

In the unlikely event that the author did not send UMI a complete manuscript and there are missing pages, these will be noted. Also, if unauthorized copyright material had to be removed, a note will indicate the deletion.

Oversize materials (e.g., maps, drawings, charts) are reproduced by sectioning the original, beginning at the upper left-hand corner and continuing from left to right in equal sections with small overlaps.

Photographs included in the original manuscript have been reproduced xerographically in this copy. Higher quality 6" x 9" black and white photographic prints are available for any photographs or illustrations appearing in this copy for an additional charge. Contact UMI directly to order.

Bell & Howell Information and Learning
300 North Zeeb Road, Ann Arbor, MI 48106-1346 USA

UMI®
800-521-0600

UNIVERSITY OF ALBERTA

# SIMULTANEOUS AIR, HEAT AND MOISTURE TRANSFER IN FIBROUS BUILDING INSULATION

BY

SAULO OCHIENG ODUOR



A thesis submitted to the Faculty of Graduate Studies and Research in partial fulfillment of the requirements for the degree of Doctor of Philosophy.

DEPARTMENT OF MECHANICAL ENGINEERING

Edmonton, Alberta

Fall 1999

University of Alberta

Library Release Form

Name of Author: Saulo Ochieng Oduor

Title of Thesis: Simultaneous Air, Heat and Moisture Transfer in Fibrous Building Insulation.

Degree: Doctor of Philosophy

Year this Degree Granted: 1999



P. O. Box 1039,

Kakamega, Kenya.

Date: May 31, 1999

Proverbs 2:6 "For the LORD gives wisdom, ... knowledge and understanding." (NIV)

UNIVERSITY OF ALBERTA

FACULTY OF GRADUATE STUDIES AND RESEARCH

The undersigned certify that they have read, and recommend to the Faculty of Graduate Studies and Research for acceptance, a thesis entitled **Simultaneous Air, Heat and Moisture Transfer in Fibrous Building Insulation** submitted by **Saulo Ochieng Oduor** in partial fulfillment of the requirements for the degree of Doctor of Philosophy.

Dr. T. W. Forest (Supervisor)

Dr. E. P. Lozowski

Dr. J. D. Dale

Dr. K. Nandakumar

Dr. D. Li

Dr. R. Besant (External)

Date: May 28, 1999

To my parents, Peter Oduor Chila (deceased) and Grace Awiti Oduor, for the sacrifices they made to give me an education.

## Abstract

A new explicit model for the rate of condensation of moisture in fibrous insulation, named the "Saturation Method for the Approximation of the Rate of Condensation" or SMARC, is introduced. A new numerical technique, named the "Quasi-transient Procedure" is advanced as an alternative to the fully transient solution method for use in predicting long-term moisture and temperature profiles after the quasi-steady stage. The model and the numerical technique are verified for one and two-dimensional applications using three examples by others: a one-dimensional quasi-steady moisture condensation problem with constant physical properties whose solution had been found by a complex semi-analytical method; a one-dimensional experimental investigation of transient moisture deposition and temperature profiles in cellulose insulation; and, a two-dimensional experimental investigation of moisture deposition in fiberglass insulation adjacent to a cold plate and the average heat conduction rate through the plate. SMARC and the quasi-transient procedure are then used to solve the problem of moisture condensation in slits and holes in open attic insulation. It is found that the pressure difference, the slit width or hole diameter, the room relative humidity, and the attic temperature (for a fixed room temperature) affect the heat and mass transfer rates significantly, but the exit relative humidity has a negligible effect on the transfer rates. For a dry system, the bulk air flowrates are related to

the boundary conditions by flow coefficients and pressure indices in a power law pressure-flow relationship. The total heat transfer rate through the insulation is found to have a linear relationship with the temperature difference. This relationship is written as the sum of two components; one accounting for the contribution from conduction heat transfer, and the other representing the contribution due to advection.

## Acknowledgements

The author wishes to thank the thesis supervisor, Dr. T.W. Forest, for conceiving the thesis topic and for his guidance and motivation in the course of the research work. The important roles played by Dr. J.D. Dale and Dr. E. Lozowski as members of the thesis supervisory committee are acknowledged with gratitude. The author is also grateful to Dr. K. Nandakumar, Dr. D. Li, and Dr. R. Besant for their time and the recommendations they made in the course of examining the thesis.

The study program was funded by the Canadian Commonwealth Scholarship and Fellowship Plan, to which organization the author is immensely grateful. Further financial support was kindly provided by Dr. T.W. Forest.

Speedy generation of simulation data was made possible by the involvement of Mark Ackerman, Ron Senda, Diego Novillo, Ivan Ourdev, and Eva Wong. Ali Atai shared his knowledge of programming in FORTRAN, while Bill Peck shared his text books and software.

The Department of Mechanical Engineering General Office was a pleasant place to visit, do business, and even make friends, thanks to Helen Wozniuk, Gail Anderson, Doris Amero, Shelley Josey, Betty Saelhof, Liping Wang, and Betty-Ann Bloedorn.

Finally, the author wishes to thank his wife Jane N. Ochieng, son Paulo, and daughter Josephine for their perseverance, patience, prayers, and moral support. He remains eternally indebted to Jane for the long hours of hard work she had to endure to provide for the family while he focussed on his studies.

# Table of Contents


Page

Abstract .....

Acknowledgements .....

Table of Contents .....

List of Tables .....

List of Figures .....

Nomenclature .....

Chapter 1. Introduction ..... 1

1.1 Heat and Mass: Sources and Transfer Mechanisms .. 1

1.2 Leakages and Leakage Paths ..... 2

1.3 Effect of Moisture on the Building Envelope .... 3

1.4 Preventive Design Strategies ..... 5

1.5 Scope of Research Project ..... 6

Chapter 2. Literature Review and Research Objectives .... 8

2.1 General Research Findings up to 1998 ..... 8

2.2 Conclusions from the Literature Review ..... 21

2.3 Critical Review ..... 22

2.4 Research Objectives ..... 24

Chapter 3. Problem Statement and Model Development ..... 26

3.1 Introduction ..... 26

3.2 Conceptual Mathematical Model ..... 29

3.3 Macroscopic Analysis and the Volume-averaging of Transport Phenomena in a Porous Medium ..... 32

3.3.1 Terminology ..... 32

3.3.2 Volume-averaging ..... 33

3.4 Simplifying Assumptions and Restrictions ..... 34

3.5 Two-dimensional Quasi-steady Conservation Equations and other Relations in Cartesian Coordinates ..... 35

3.5.1 Mass Conservation Equation ..... 35

3.5.2 Vapour Conservation Equation ..... 35

3.5.3 Darcy's Law and the Momentum Equation .. 36

3.5.4 Energy Conservation Equation ..... 40

3.5.5 Soret and Dufour Effects ..... 46

3.5.6 Thermodynamic Relations ..... 46

3.5.7 Model for the Rate of Condensation .... 48

3.5.8 Porosity, Volumetric Constraint, and the Liquid Volume Fraction ..... 50

3.5.9 Boundary Conditions and Heat and Mass Transfer Coefficients ..... 51

3.6 Summary of Model Equations and Other Relations ..... 53

Chapter 4. Two-dimensional Numerical Model for a Slit ... 58

4.1 The Computational Grid System ..... 58

4.2 Non-dimensional Equations ..... 60

4.3 The QUICK Scheme and the Finite Difference Approximations ..... 63

4.4 The Quasi-steady Numerical Solution Procedure .. 69

4.5 The "Quasi-transient" Numerical Solution Procedure ..... 78

Chapter 5. Model Validation ..... 81

5.1 Introduction ..... 81

5.2 Example 1 [Ogniewicz and Tien (1981)]: 1-D Quasi-steady Solution Using SMARC ..... 81

5.2.1 Problem Description ..... 81

5.2.2 Governing Equations and Other Relations . 83

5.2.3 Physical Data ..... 89

5.2.4 Numerical Solution Procedure ..... 90

5.2.5 Comparison of Results ..... 91

5.2.6 Summary of Results ..... 100

5.3 Example 2 [Yu, R.C.H. (1986)]: 1-D Validation of SMARC and the Quasi-transient Procedure ..... 101

5.3.1 Introduction ..... 101

5.3.2 Problem Description and Experimental Procedure ..... 102

5.3.3 Numerical Simulation Procedure ..... 105

5.3.4 Physical Data ..... 112

5.3.5 Parameter Sensitivity Test Results .... 115

5.3.6 Temperature Profiles ..... 118

5.3.7 Moisture Distribution Profiles ..... 126

5.3.8 Latent Heat and Total Heat Transfer Rate at Exit ..... 131

5.3.9 General Observations ..... 134

5.3.10 Physical Interpretation of Results ... 136

5.3.11 Summary and Conclusions ..... 138

5.4 Example 3 [Chen, H., Besant, R.W., and Tao, Y. (1997a, 1997b)]: 2-D Validation of SMARC and the Quasi-transient Procedure ..... 139

5.4.1 Introduction ..... 139

5.4.2 Problem Description and Experimental Procedure ..... 139

5.4.3 Numerical Simulation: Equations, Assumptions, Physical Data, and Implementation ..... 142

5.4.4 Results and Discussion ..... 145

5.4.5 Sources of Error ..... 159

5.4.6 Conclusion ..... 159

5.5 Summary ..... 160

Chapter 6. Moisture Deposition in Attic Fibrous Insulation ..... 161

6.1 Introduction ..... 161

6.2 Quasi-steady Results for Slits ..... 163

6.2.1 Typical Profiles of Field Variables ... 163

6.2.2 Effect of Increasing the Pressure Difference ..... 164

6.2.3 Effect of Increasing the Inlet Relative Humidity..... 170

6.2.4 Effect of Increasing the Slit Width .. 174

6.2.5 Effect of Lowering the Exit Temperature .178

6.3 Effect of Moisture Accumulation ..... 182

6.4 Summary of Results ..... 185

Chapter 7. Estimation of Bulk Air Flowrates and Heat Transfer Rates in Slits and Round Holes in Attic Fibrous Insulation ..... 192

7.1 Introduction ..... 192

7.2 Flow Domain and Governing Equations ..... 193

7.3 Results and Discussion ..... 194

7.3.1 Results for Slits ..... 195

7.3.2 Results for Round Holes (Axisymmetric Flow) ..... 203

7.4 Summary ..... 205

Chapter 8. Summary, Conclusions, and Recommendations ... 212

8.1 Summary and Conclusions ..... 212

8.2 Recommendations ..... 215

Bibliography ..... 217

Appendix A. Variable Thermophysical Properties of Moist Air and Other Material Properties ..... 223

A.1 Variable Thermophysical Properties of Moist Air ..... 223

A.2 Other Material Properties ..... 236

A.3 Natural and Forced Convective Heat Transfer Coefficients ..... 239

A.4 Convective Mass Transfer Coefficient ..... 241

Appendix B. Reference Values and Boundary Conditions .. 243

B.1 Reference Values ..... 243

B.2 Boundary Conditions ..... 246

B.3 Controlling Parameters ..... 249

B.4 Non-dimensional Variables ..... 251

Appendix C. Finite Difference Approximations (FDAs) for Boundaries ..... 255

C.1 Forced Convective Inlet (Vertical Flow) ..... 256

C.2 Dirichlet Inlet for Vertical Flow ..... 258

C.3 Conductive Entry of Heat ..... 259

C.4 The Far-field ..... 260

C.5 Forced Convective Exit ..... 261

C.6 Symmetric Vertical "Boundary" ..... 262

Appendix D. Heat and Mass Transfer for Axisymmetric Flow ..... 265

D.1 Introduction ..... 265

D.2 Model Equations and Other Relations ..... 265

D.3 Quasi-steady Results for Holes ..... 275

D.4 Effect of Moisture Accumulation ..... 284

Appendix E. Natural Convection ..... 295

E.1 Darcy-modified Rayleigh Number ..... 295

E.2 Conclusion ..... 299

Appendix F. Tables of Simulation Data ..... 300

## List of Tables


| | | Page |
|---|---|---|
| 5.1 | Computation Results Obtained with Ogniewicz and Tien's Dimensionless Parameters (Pe=1.0, Le=2.0, Bi=$10^6$) | 94 |
| 5.2 | Computation Results Obtained with "Appropriate" Dimensionless Parameters (Pe=1.8, Le=1.7, Bi=30.0) | 96 |
| 5.3 | Inlet and Exit Forced-convective Heat Transfer Coefficients for Different Nominal Velocities | 114 |
| 5.4 | Parameter Sensitivity Study Results for a Nominal Velocity of 0.66 mm/s | 119 |
| 5.5 | Comparison Between Experimental Results [Yu, 1986] and Numerical Predictions by SMARC of Long-term Moisture Contents | 131 |
| 5.6 | Moisture Accumulation Results for the Insulation Layer Adjacent to the Cold Plate (x=110 mm to 135 mm) | 152 |
| 5.7 | Experimental and Simulation Average Heat Conduction Rates Through the Cold Plate | 157 |
| 5.8 | Simulation Heat Transfer Rates Into and Out of the Test Cell | 158 |
| 6.1 | Effect of Pressure Difference on Quasi-steady Heat and Mass Transfer Rates | 167 |
| 6.2 | Effect of Inlet Relative Humidity on Quasi-steady Heat and Mass Transfer Rates | 173 |
| 6.3 | Effect of Slit Width on Quasi-steady Heat and Mass Transfer Rates | 178 |

| | | |
|---|---|---|
| 6.4 | Effect of Exit Temperature on Quasi-steady Heat and Mass Transfer Rates | 182 |
| 6.5 | Effect of Moisture Accumulation with Time on Heat and Mass Transfer Rates | 184 |
| D.1 | Effect of Pressure Difference on Quasi-steady Heat and Mass Transfer Rates | 281 |
| D.2 | Effect of Inlet Relative Humidity on Quasi-steady Heat and Mass Transfer Rates | 282 |
| D.3 | Effect of Hole Diameter on Quasi-steady Heat and Mass Transfer Rates | 283 |
| D.4 | Effect of Exit Temperature on Quasi-steady Heat and Mass Transfer Rates | 284 |
| D.5 | Effect of Moisture Accumulation with Time on Heat and Mass Transfer Rates | 285 |
| F.1 | Effect of Pressure Difference and Inlet Relative Humidity on Quasi-steady Heat and Mass Transfer Rates in a Slit | 301 |
| F.2 | Effect of Pressure Difference and Inlet Relative Humidity on Quasi-steady Heat and Mass Transfer Rates in a Hole | 302 |
| F.3 | Dry-air Flowrates for Slits | 303 |
| F.4 | Dry-air Heat Transfer Rates for Slits | 304 |
| F.5 | Dry-air Flowrates for Holes | 305 |
| F.6 | Dry-air Heat Transfer Rates for Holes | 306 |

# List of Figures


| | | Page |
|---|---|---|
| 1.1 | Sketch of Building Envelope Showing Some Potential Leakage Sites | 4 |
| 3.1 | Schematic of the Ceiling Assembly and the Leakage Site | 27 |
| 3.2 | A Representative Elementary Volume Showing the Constituent Elements | 44 |
| 3.3 | Flow Domain and Boundary Conditions | 52 |
| 4.1 | Two-dimensional Staggered Grid System | 59 |
| 4.2 | Solution Sequence for Two-dimensional Simultaneous Heat and Mass Transfer Equations | 70 |
| 4.3 | Time-stepping Procedure for the Quasi-transient Method | 80 |
| 5.1 | Flow-field and Boundary Conditions for Example 1 [Ogniewicz and Tien, 1981] | 82 |
| 5.2 | Solution Sequence for the Simultaneous Heat and Mass Transfer Equations in Example 1 [Ogniewicz and Tien, 1981] | 92 |
| 5.3 | Vapour Density Profiles for Pe=1.0, Le=2.0, $Bi=10^6$ | 97 |
| 5.4 | Condensation Rate Profiles for Pe=1.0, Le=2.0, $Bi=10^6$ | 97 |

| | | |
|---|---|---|
| 5.5 | Temperature Profiles for Pe=1.0, Le=2.0, $Bi=10^6$ | 98 |
| 5.6 | Density Profiles for Two Sets of Dimensionless Numbers | 98 |
| 5.7 | Condensation Rate Profiles for Two Sets of Dimensionless Numbers | 99 |
| 5.8 | Temperature Profiles for Two Sets of Dimensionless Numbers | 99 |
| 5.9 | Flow-field and Boundary Conditions for Example 2 [Yu, 1986] | 103 |
| 5.10 | Location of Temperature Probes in Example 2 [Yu, 1986] | 104 |
| 5.11 | Temperature Profiles for 90%, 100%, and 110% of the Effective Thermal Conductivity (v=0.66 mm/s) | 120 |
| 5.12 | Condensation Rate Profiles for 90%, 100%, and 110% of the Effective Thermal Conductivity (v=0.66 mm/s) | 120 |
| 5.13 | Temperature Profiles for 90%, 100%, and 110% of the Diffusion Coefficient of Water Vapour in Air (v=0.66 mm/s) | 121 |
| 5.14 | Condensation Rate Profiles for 90%, 100%, and 110% of the Diffusion Coefficient of Water Vapour in Air (v=0.66 mm/s) | 121 |
| 5.15 | Temperature Profiles for 90%, 100%, and 110% of the Ratio of Permeability to Dynamic Viscosity of Air (v=0.66 mm/s) | 122 |
| 5.16 | Condensation Rate Profiles for 90%, 100%, and 110% of the Ratio of Permeability to Dynamic Viscosity of Air (v=0.66 mm/s) | 122 |

| | | |
|---|---|---|
| 5.17 | Temperature Profiles for 90%, 100%, and 110% of the Specific Heat Capacity of Air (v=0.66 mm/s) | 123 |
| 5.18 | Condensation Rate Profiles for 90%, 100%, and 110% of the Specific Heat Capacity of Air (v=0.66 mm/s) | 123 |
| 5.19 | Temperature Profiles for 90%, 100%, and 110% of the Latent Heat of Vaporization of Water (v=0.66 mm/s) | 124 |
| 5.20 | Condensation Rate Profiles for 90%, 100%, and 110% of the Latent Heat of Vaporization of Water (v=0.66 mm/s) | 124 |
| 5.21 | Temperature Profiles for 90%, 100%, and 110% of the Latent Heat of Sublimation of Ice (v=0.66 mm/s) | 125 |
| 5.22 | Condensation Rate Profiles for 90%, 100%, and 110% of the Latent Heat of Sublimation of Ice (v=0.66 mm/s) | 125 |
| 5.23 | Temperature Profiles for v=0.30 mm/s | 127 |
| 5.24 | Temperature Profiles for v=0.43 mm/s | 127 |
| 5.25 | Temperature Profiles for v=0.66 mm/s | 128 |
| 5.26 | Temperature Profiles for v=0.87 mm/s | 128 |
| 5.27 | Expansion of Wet Region (v=0.66 mm/s) | 132 |
| 5.28 | Wet-dry Interfaces for 24 hours | 132 |
| 5.29 | Variation of Total Condensation Rate with Time | 133 |

| | | |
|---|---|---|
| 5.30 | Variation of Total Liquid/Frost Content with Time | 133 |
| 5.31 | Schematic of Experimental Test Cell [Chen et al., 1997a] | 140 |
| 5.32 | Typical Velocity Vectors at Inlet | 146 |
| 5.33 | Typical Velocity Vectors at Exit | 146 |
| 5.34 | Typical Pressure Contours | 147 |
| 5.35 | Typical Temperature Contours | 147 |
| 5.36 | Experimental and Simulation (SMARC) Temperature Profiles for a 36.4 L/min. Flowrate, a 60% Inlet RH, and a Time of 3 Hours | 153 |
| 5.37 | Experimental and Simulation (SMARC) Temperature Profiles for a 36.4 L/min. Flowrate, a 70% Inlet RH, and a Time of 3 Hours | 153 |
| 5.38 | Experimental and Simulation (SMARC) Temperature Profiles for a 36.4 L/min. Flowrate, an 84% Inlet RH, and a Time of 3 Hours | 154 |
| 5.39 | Experimental and Simulation (SMARC) Temperature Profiles for a 54.5 L/min. Flowrate, a 60% Inlet RH, and a Time of 3 Hours | 154 |
| 5.40 | Experimental and Simulation (SMARC) Temperature Profiles for an 18.2 L/min. Flowrate, a 60% Inlet RH, and a Time of 3 Hours | 155 |
| 5.41 | Moisture Accumulation Profiles for x-distance from 110 mm to 135 mm | 155 |

| | | |
|---|---|---|
| 6.1 | Typical Inlet Velocity Vectors | 165 |
| 6.2 | Typical Temperature Contours | 165 |
| 6.3 | Typical Vapour Density Contours | 166 |
| 6.4 | Typical Condensate Volume Fraction Contours | 166 |
| 6.5 | Condensation Rate Profiles (x and y direction) for 8 Pa | 168 |
| 6.6 | Condensation Rate Profiles (x and y direction) for 30 Pa | 169 |
| 6.7 | Condensation Rate Profiles (x and y direction) for 40% Inlet RH | 171 |
| 6.8 | Condensation Rate Profiles (x and y direction) for 70% Inlet RH | 172 |
| 6.9 | Condensation Rate Profiles (x and y direction) for 6 mm Slit Width | 176 |
| 6.10 | Condensation Rate Profiles (x and y direction) for 22 mm Slit Width | 177 |
| 6.11 | Condensation Rate Profiles (x and y direction) for 263 K Exit Temperature | 180 |
| 6.12 | Condensation Rate Profiles (x and y direction) for 233 K Exit Temperature | 181 |
| 6.13 | Condensation Rate Profiles (x and y direction) after 6 Hours | 186 |
| 6.14 | Condensation Rate Profiles (x and y direction) after 18 Hours | 187 |

| | | |
|---|---|---|
| 6.15 | Effective Thermal Conductivity Profiles (x and y direction) after 6 Hours | 188 |
| 6.16 | Effective Thermal Conductivity Profiles (x and y direction) after 18 Hours | 189 |
| 6.17 | Condensate/Ablimate Volume Fraction Contours for 6 and 18 Hours | 190 |
| 6.18 | Variation of Total Weight of Moisture in the Insulation with Time | 191 |
| 7.1 | Typical Pressure Contours (Non-dim.) for Isothermal Flow | 198 |
| 7.2 | Isothermal (293 K) Air Flowrates for Slits | 199 |
| 7.3 | Air Flowrates for Different Exit Temperatures | 199 |
| 7.4 | Flow Coefficients ($C_F$) for Slits | 200 |
| 7.5 | Pressure-Difference Indices, n, for Slits | 200 |
| 7.6 | Effective Areas for Slits at 293 K | 201 |
| 7.7 | Effective Areas for Slits at Other Temperatures | 201 |
| 7.8 | Conduction Heat Transfer Coefficients for Slits | 202 |
| 7.9 | Advective Heat Transfer Components for Slits | 202 |
| 7.10 | Isothermal (293 K) Air Flowrates for Holes | 206 |
| 7.11 | Air Flowrates for Different Exit Temperatures (Holes) | 206 |

| | | |
|---|---|---|
| 7.12 | Flow Coefficients ($C_F$) for Holes | 207 |
| 7.13 | Pressure-Difference Indices, n, for Holes | 207 |
| 7.14 | Effective Areas for Holes at 293 K | 208 |
| 7.15 | Effective Areas for Holes at Other Temperatures | 208 |
| 7.16 | Conduction Heat Transfer Coefficients for Holes | 209 |
| 7.17 | Advective Heat Transfer Components for Holes | 209 |
| A.1 | Diffusion Coefficients of Water Vapour in Air | 232 |
| A.2 | Dynamic Viscosities of Dry Air | 233 |
| A.3 | Dynamic Viscosities of Pure Water Vapour | 233 |
| A.4 | Thermal Conductivities of Dry Air | 234 |
| A.5 | Thermal Conductivities of Pure Water Vapour | 234 |
| A.6 | Soret Coefficients of "Dry Air" | 235 |
| A.7 | Soret Coefficients of "Pure Water Vapour" | 235 |
| C.1 | Boundary Grid Cells: (a) Forced-convective Inlet, (b) Dirichlet Inlet, (c) Conductive Inlet, (d) Far-field, (e) Forced-convective Exit, (f) Symmetric Boundary | 263 |
| D.1 | Control Volume for Axisymmetric Flow | 268 |
| D.2 | Typical Inlet Velocity Vectors | 277 |

| | | |
|---|---|---|
| D.3 | Typical Temperature Contours | 277 |
| D.4 | Typical Vapour Density Contours | 278 |
| D.5 | Typical Condensate Volume Fraction Contours | 278 |
| D.6 | Condensation Rate Profiles (r and z direction) for 8 Pa | 279 |
| D.7 | Condensation Rate Profiles (r and z direction) for 30 Pa | 280 |
| D.8 | Condensation Rate Profiles (r and z direction) for 40% Inlet RH | 286 |
| D.9 | Condensation Rate Profiles (r and z direction) for 70% Inlet RH | 287 |
| D.10 | Condensation Rate Profiles (r and z direction) for 6 mm Hole Diameter | 288 |
| D.11 | Condensation Rate Profiles (r and z direction) for 22 mm Hole Diameter | 289 |
| D.12 | Condensation Rate Profiles (r and z direction) for 233 K Exit Temperature | 290 |
| D.13 | Condensation Rate Profiles (r and z direction) after 6 Hours | 291 |
| D.14 | Condensation Rate Profiles (r and z direction) after 18 Hours | 292 |
| D.15 | Condensate/Ablimate Volume Fraction Contours for 6 and 18 Hours | 293 |
| D.16 | Variation of Total Weight of Moisture in the Insulation with Time for a Round Hole | 294 |

## Nomenclature

| | |
|---|---|
| A | Area, $m^2$ |
| Bi | Biot number |
| C | Concentration |
| $C_{adv}$ | Advective heat transfer rate per unit area, $W/m^2$ |
| $C_{cond}$ | Conduction heat transfer coefficient, W/K |
| $C_d$ | Coefficient of discharge |
| $C_F$ | Flow Coefficient |
| $C_p$ | Specific heat capacity at constant pressure, J/kg-K |
| D | Insulation thickness, m |
| d | Vertical length (general), m |
| $D_d$ | Dufour coefficient, $m^2K/s$ |
| $D_s$ | Soret (thermal diffusion) coefficient, $m^2/s$-K |
| $D_v$ | Vapour diffusivity in porous medium, $m^2/s$ |
| $D_{va}$ | Vapour diffusivity in open air, $m^2/s$ |
| dl | half-width of a slit or radius of a hole, m |
| $G_{va}$ | Wilke's constant for the gas pair water vapour-air |
| $H_{adv}$ | Advective heat transfer component, W |

$H_d$ Dufour heat flux, $W/m^2$

$H_L$ Latent heat rate, W

$H_s$ Total heat transfer rate, W

h Specific enthalpy, J/kg-K

$h_f$ Forced convective heat transfer coefficient, $W/m^2$-K

$h_m$ Convective mass transfer coefficient, m/s

$h_n$ Natural convective heat transfer coefficient, $W/m^2$-K

$h_{vap}$ Heat of vaporization, J/kg

$h_{sub}$ Heat of sublimation, J/kg

K Permeability, $m^2$

$k_3$ Number of grid cells within a slit/hole

L Half the width of the flow domain, m

l Horizontal length (general), m

Le Lewis number

MC Moisture content , % by dry mass

$M_i$ Molecular weight of a component/substance i

$\dot{m}$ Condensation rate, kg/s

n Pressure index or exponent

$P$ Pressure, Pa

$P_{si}$ Saturated vapour pressure above ice, Pa

$P_{sw}$ Saturated vapour pressure above water, Pa

Pe Peclet number

$Q_a$ Bulk flowrate of dry air, kg/s

$Q_c$ Total condensation rate, kg/s

$Q_g$ Bulk flowrate of humid air, kg/s

$Q_s$ Soret mass flux, kg/s-$m^2$

$Q_v$ Water vapour flowrate, kg/s

QUICK Quadratic Upstream Interpolation for Convective Kinematics

$q''$ Conductive heat flux, $W/m^2$

$\bar{R}$ Universal gas constant, J/kmol-K

$R_a$ Specific gas constant of air, J/kg-K

$Ra_K$ Darcy-modified Rayleigh number

$Re_K$ Reynolds number, based on permeability K

$R_g$ Residual for bulk air global balance

$R_h$ Residual for heat rate global balance

$R_m$ Residual for water vapour global balance

$R_v$ Specific gas constant of water vapour, J/kg-K

RH Relative humidity

SMARC Saturation Method for the Approximation of the Rate of Condensation

T Absolute temperature, K

t Time, s

u Horizontal velocity component, m/s

V Volume, $m^3$

$V_o$ Reference velocity, m/s

v Vertical velocity component or general velocity, m/s

Greek Symbols

$\alpha$ Thermal diffusivity, $m^2/s$

$\beta$ Volumetric thermal expansion coefficient, $K^{-1}$

$\epsilon$ Porosity

$\lambda$ Thermal conductivity, W/m-K

$\mu$ Dynamic viscosity, kg/m-s

$\nu$ Kinematic viscosity, $m^2/s$

$\rho$ density, $kg/m^3$

$\omega 2$ Quasi-transient time, s

Other Symbols

$\tilde{x}$ Deviation of a variable x

$\bar{x}$ Non-dimensional x

$\vec{x}$ Vector x

$\langle x \rangle$ Volume-average of x (with respect to porous medium)

$\langle x \rangle^g$ Intrinsic volume-average of x (i.e., with respect to a phase g)

Subscripts

a Dry air

av. Average

c Condensate

eff Effective

g Moist/humid air

H Heat

h Heat

i ice

in Interior or room

K Permeability-based or Darcy-modified value

l liquid

| | |
|---|---|
| m | Mass or moisture (as appropriate) |
| Ni | Nitrogen |
| o | Reference |
| out | Exterior or attic |
| Ox | Oxygen |
| P | Plasterboard |
| r | radial direction |
| ref | Reference |
| s | Solid |
| si | Saturation value of a property over ice |
| sv | Saturated vapour |
| sw | Saturation value of a property over water |
| v | Vapour |
| x | Horizontal direction |
| y | Vertical direction |
| z | Vertical direction |

# CHAPTER 1

# INTRODUCTION

Buildings are designed for different purposes and each must, to an acceptable degree, meet the environmental criteria which define its purpose(s). Habitats must be safe, healthy and pleasant to the inhabitants. Annoyance and distraction from whatever source must be minimised so that work and pleasure activities may proceed unhindered physically or mentally. The environment contributes directly towards a person's health, well-being and productivity. [CIBSE Guide A, 1988].

The desired environment is achieved by supplying quality air into the occupied space, and meeting other health and comfort requirements which are recommended in design guide books such as those published by the Chartered Institution of Building Services Engineers (CIBSE) and the American Society of Heating, Refrigerating and Air-Conditioning Engineers (ASHRAE).

Providing and maintaining suitable environmental conditions is the Building Services Engineer's greatest challenge. This is because of the numerous opposing forces which come in the form of heat and mass exchanges within a space, and between any two adjacent spaces separated by some kind of barrier. The adjacent space is quite often the minimally-protected attic or the open exterior where the elements of weather reign supreme.

## 1.1 Heat and Mass: Sources and Transfer Mechanisms

Within an occupied space, internal heat gains (both sensible and latent) take place. Common sources of these gains are human bodies, animal bodies, plants, electric lamps, computers and other powered office equipment, just to name a few. Activities essential to living, such as cooking, are known to be major contributors to both sensible and latent heat gains.

Exchanges of heat and mass between two adjacent spaces are restricted by the structural integrity of the separating barrier. Heat and mass transfer occur in the gas, liquid and solid phases.

In the gas phase, the heat and mass transfer mechanisms are:

(1) vapour diffusion due to vapour concentration gradients;

(2) buoyancy effects due to the density variations induced by temperature or concentration gradients;

(3) air exfiltration or infiltration through holes or cracks due to the small pressure differences across the barrier and the insulation within it;

(4) heat conduction; and

(5) adsorption and desorption.

In the liquid (water) phase:

(1) advection may occur due to gravity, air pressure differences across the barrier, and capillary suction of liquid water in the porous building materials; and

(2) conduction may take place due to temperature gradients.

In the solid phase heat is transferred only by conduction.

Phase changes generate or absorb heat energy at the gas-water or gas-frost interfaces. Condensation or ablimation (i.e. frost formation) occurs when the local vapour concentration at a point exceeds the saturation concentration corresponding to the local temperature.

## 1.2 Leakages and Leakage Paths

Exfiltration and infiltration occur at cracks and holes (i.e., leakage sites) which may exist in the separating barrier between two spaces which are maintained at different

pressures. Figure 1.1 shows the most likely locations of leakage sites in a building. These leakage sites play an important role in determining the overall heat transfer rates as well as the quantity and distribution of any condensate. Tenwolde and Rose (1996) report that airflow through an electric outlet can carry ten to five hundred times as much moisture into the wall as vapour diffusion. The openings occur either due to poor workmanship, physical damage, or aging. They are usually located around doors, windows, chimneys, vent stacks, cables, pipes, and other fixtures. Any place where a joint is required is a potential leakage site. Even with good workmanship, a joint is likely to weaken with time in an inevitable aging process. Aging may also cause the development of openings in the vapour retarders and airflow retarders.

Besides contributing to energy and air losses or gains, leaks lead to the loss of structural integrity of the barrier with its insulation, and may affect the air quality in the space and, hence, the health and comfort of the occupants.

## 1.3 Effect of Moisture on the Building Envelope

High moisture levels may cause wood decay, metal corrosion, discoloration and the peeling of paint. Wood decay leads to structural damage, especially of the external sheathing. Mold and mildew growth, unlike decay, will occur even below moisture saturation levels. These bacterial growths affect the air quality in the building. Freezing damage occurs at sub-zero temperatures when ice forces the external cladding materials off the wall.

Air leakage and the resulting moisture accumulation are very localized, leading to localized damage. However, if exterior sheathing has localized damage then the entire sheathing needs to be replaced - usually at a prohibitive cost to the owner(s) and at great inconvenience to the user(s) of the building.

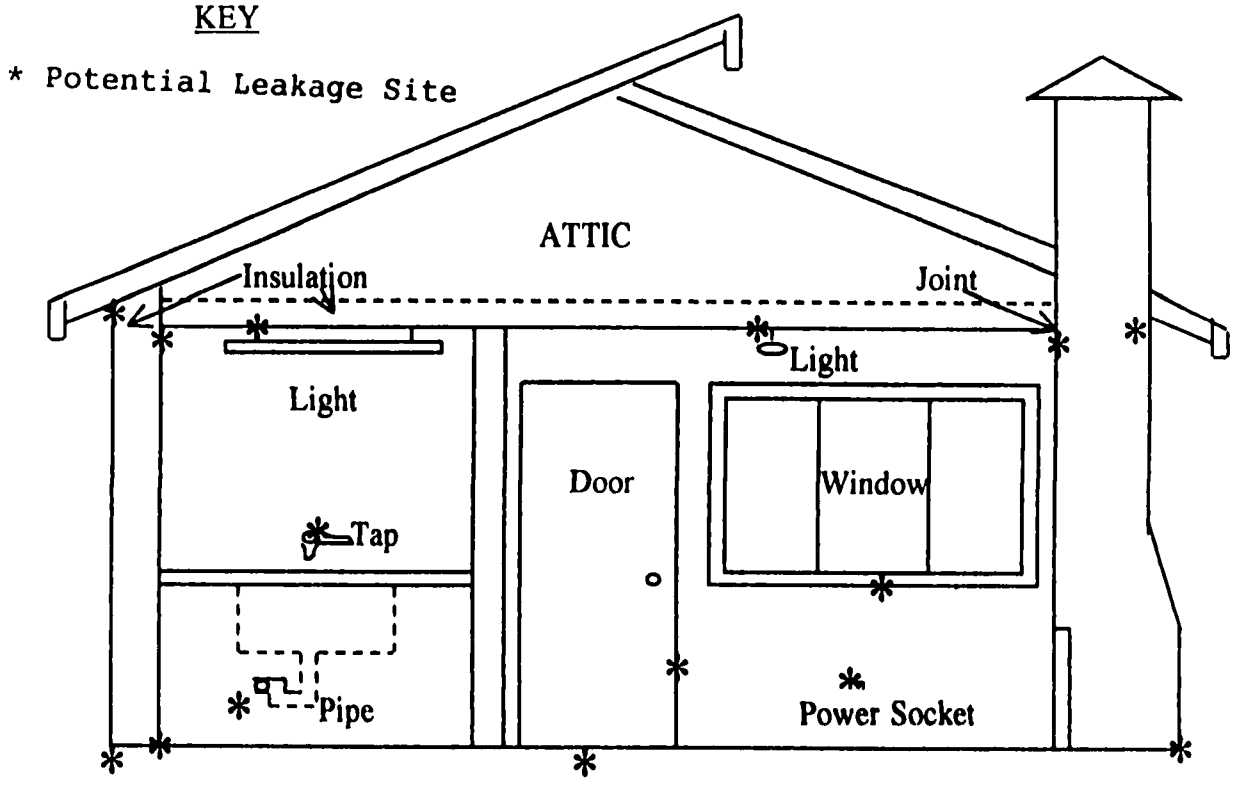


Figure 1.1 : Sketch of Building Envelope Showing Some Potential Leakage Sites.

Designers specify insulation material types and quantities based on their "dry" heat transfer properties. "Dry" insulation contains only air in its pores. The presence of water and/or frost in the insulation dramatically alters its properties. At 293 K, the conductivity of water (0.603 W/m-K) is about twenty-four times that of air (0.0254 W/m-K), while the conductivity of ice (1.955 W/m-K) is about seventy-seven times that of air. Hence even minute quantities of water and frost may have considerable effect on the heat transfer characteristics of the insulation. Natural (organic) insulation materials may also suffer irreversible degradation in the presence of moisture.

## 1.4 Preventive Design Strategies

It is apparent from the preceding discussion that the cost of maintaining a suitable internal environment can be substantial. Even bigger may be the cost of repairing damaged building envelope. The frequency of refurbishment, to give an old building a new lease on life, may be cut down by incorporating preventive measures at the building's design stage.

The International Agency Annex XIV (1991) recommends the limiting of internal relative humidities to less than 70% to prevent the growth of mold. Tenwolde (1996) advances other control strategies such as:

(1) limiting the moisture load (i.e., relative humidities) on the building by limiting the sources of moisture, and limiting the pressure across the building envelope - which is not perfectly airtight - to reduce the risk of wetting by leakage of humid air into the envelope; and

(2) constructing the building for high moisture tolerance by preventing water entry into the envelope, making airtight construction, placing vapour retarders appropriately,

providing a way for the envelope to dry in accidental wetting, and avoiding thermal bridges through the insulation.

Ojanen and Kumaran (1996) state that adding thermal resistance by adding an exterior sheathing significantly reduces the amount of moisture retained by the wall cavity. More thermal energy is retained within the wall, raising the temperatures and the corresponding saturation vapour pressures. The heat flux is also reduced. This is one way of containing a high interior relative humidity.

Buildings must also be constructed to prevent water from external sources from leaking into the wall cavity. A common external source, especially in warm climates, is flood water which may get into the cavity through the foundation and lower portions of walls.

## 1.5 Scope of Research Project

This research project is yet another "chapter" towards the better understanding of the dynamics of heat, air, and moisture transfer through individual leakage paths. It is a numerical simulation, and it must be pointed out at the very beginning that such an exercise requires experimentally-determined physical coefficients for the complex numerical models. Coefficients like conductivity, viscosity and diffusivity of humid air are still estimated from theory. Good field data are required for model verification; but, good field data are hard to find due to the large number of physical and geometric variables. There is still a lack of sensors for accurate measurement of humidity and moisture contents. Real roofs and walls are subjected to boundary conditions which vary continually (with weather), whereas in this investigation each test will consider steady boundary conditions.

A building's leakage characteristics are determined by:

(1) the internal design conditions in temperature, relative humidity and pressure;

(2) the air movements;

(3) the envelope design;

(4) the quality of construction; and

(5) the external conditions (weather), which are mostly beyond the designer's control.

The bulk of experimental research conducted so far on building leakages has considered the leakage characteristics of entire buildings. However, this big picture is the sum of what happens at the individual leakage sites. Leakages will be better contained or managed if what happens at these sites is understood.

# CHAPTER 2

# LITERATURE REVIEW AND RESEARCH OBJECTIVES

## 2.1 General Research Findings up to 1998

Research on the simultaneous transfer of heat and mass in porous insulation intensified in the early 1980s apparently as a result of the wide acceptance of Whitaker's (1977) model and the introduction of more powerful computers and advances in programming techniques. Currently, there are as many numerical simulation cases as there are experimental investigations, and interest in the science of porous media is growing. This subsection chronicles some important and relevant experimental and numerical-simulation findings published in North American journals, International journals, and theses up to 1998.

Bankvall (1972) conducted detailed experimental and theoretical research on the effective thermal conductivities of dry fibrous insulation. This provided vital information on the contributions made by conduction and radiation transfer modes in the gaseous and solid components of the porous medium. The experiments were conducted at different temperatures and insulation densities. It was established that the most important factor was conduction in the gas phase. Radiation heat transfer was considerable at high porosities, but decreased as the insulation density increased. The influence of conduction in the solid phase was negligible at very low densities, but increased significantly as the density increased. Increasing the mean temperature of the material increased its effective thermal conductivity, especially at low density due to increased radiation.

Bankvall (1972) illustrates the relative contributions made by conduction in solids, radiation in the gas, and conduction in the gas to the overall thermal conductivity in a fibrous

material. It is noted that for porosities above 0.98, conduction in the solid elements makes a negligible contribution relative to the contributions of radiation and conduction in the gas. For porosities below 0.975, radiation and conduction in solids make comparable contributions, but the two together account for less than 20% of the total or effective conductivity, the rest being accounted for by conduction in the gas. Radiation becomes significant when the porosity is larger than 0.97. In this range radiation dominates conduction in the solid elements, but not conduction in the gas. Radiation starts to dominate conduction in the gas at porosities above 0.995. The results discussed above were obtained for a temperature of 20°C by Bankvall.

The effective thermal conductivity decreases with temperature, the absolute value of each contributing mode decreasing, but not proportionally. It is observed in Bankvall's (1972) work that, for a porosity of 0.97, the radiation component decreases rapidly with temperature and becomes less than the component due to conduction in the solid elements when the temperature falls below 13°C. The low temperatures make radiation even less significant relative to conduction in the gas.

Ogniewicz and Tien (1981) introduced the semi-analytical solution method by solving a quasi-steady one-dimensional forced convective problem with convective boundary conditions. The inlet temperature was above zero while the exit was below freezing temperature. Both the inlet and exit were unsaturated with moisture. It was found that there existed three regions - a dry region next to the inlet, followed by a wet region, and another dry region before the exit. In the solution of the problem, the wet-dry interfaces were located by searching for locations in the system where there was continuity in the gradients of both temperature and vapour concentration. Although the rate of condensation was relatively small, a

significant effect was observed on the thermal performance of the insulation slab due to the release of latent heat. The rate of condensation increased with external humidities, temperature levels and overall temperature differences. Both the rate of condensation and the heat flux increased with the Peclet number, the Lewis number and the Biot number.

Yu (1986) did an experimental investigation of the effect of exfiltration on the transient moisture accumulation in a one-dimensional cellulose assembly. This investigation and the results are given in detail in Section 5.3.

The investigation revealed that, as the moisture accumulated in the system, the temperature readings decreased continually. Most significantly, the temperature profile became distorted, an inflection appearing on the profile at approximately the triple point of water in all the four test runs considered. The "wet" zone also commenced at the triple point. The results showed that there was one dry zone and one wet zone in the flow domain. Other significant observations and conclusions made were that:

(1) the temperatures within the cellulose increased with the exfiltration rate;

(2) the wet-dry interface shifted towards the exit as the exfiltration rate increased;

(3) the total moisture content increased linearly with time; and,

(4) at higher exfiltration rates, more vapour was convected through the system without condensing, implying that, beyond a certain point, the overall moisture accumulation decreased as the rate of exfiltration increased.

Modi and Benner (1985, Part I) used spray-applied fiberglass and cellulose to demonstrate that the rate of moisture gain

and the total moisture gain increased with the relative humidity and the temperature difference. The arrangement allowed for the advection of liquid water but not water vapour. The main heat transfer modes in this case were vapour diffusion, liquid advection and heat conduction.

After an initial increase, the lumped thermal conductivity would attain a quasi-steady value directly proportional to the moisture gain. That is, the greater the rate of moisture gain and the total moisture gain were, the greater was the lumped thermal conductivity. The cellulose gained slightly more moisture than the fiberglass under the same conditions. Later in the experiment, the cellulose, unlike the fiberglass, experienced free water loss or drippage. After about 100 hours, the temperature reached a quasi-equilibrium state followed by very gradual change. They predicted that it would take much longer for the moisture distribution to attain a quasi-equilibrium state. They thought that the existence of a quasi-steady state indicated that the moisture gained after this time would not increase the rate of heat transfer.

In a numerical simulation of the experimental results, published as Part II, Benner and Modi (1986) concluded that the main transport parameters were the vapour diffusivity and an evaporation coefficient. These parameters were varied in an attempt to reproduce the experimental findings. It was concluded from the numerical simulations that:

(1) the evaporation coefficient was not as dependent on insulation properties as the vapour diffusivity;

(2) the liquid diffusivity did not affect the moisture gain appreciably;

(3) the latent heat contribution was very large initially, but decreased later in the run; and

(4) the contribution of the conductivity increased with

increasing liquid content.

The "effective" thermal conductivity increased rapidly initially and then decreased, eventually levelling off to a pseudo-steady-state value.

Motakef and El-Masri (1986) demonstrated the existence of a wet region sandwiched between two dry zones. They used an unsteady one-dimensional diffusion-conduction model with mobile condensate. The solution was by an analytical method.

Vafai and Whitaker (1986) considered a two-dimensional transient, multi-phase model with constant total gas pressure. There was no forced convection (i.e., the dry component of air was assumed to be immobile, while the vapour migrated by diffusion only). To solve the problem, they introduced the now-famous "two-phase numerical scheme". They showed that condensation occurred at any point in the insulation where the water vapour concentration became greater than the saturation concentration corresponding to the temperature at the point. For the setup the most significant terms in the energy equation were the rate of condensation and the conduction terms.

Vafai and Sarkar (1986) had the first case in which the interface between the wet and dry regions was found directly from the solution of the governing equations. They considered a one-dimensional transient forced convective multi-phase model with variable porous medium coefficients, and found that:

(1) using constant total air density led to significant errors in the magnitude of the mass rate of condensation and in the prediction of the location of the wet-dry interface;

(2) the condensation process was significantly affected by the thermophysical properties of the insulation, the infiltration velocity, and the humidity levels;

(3) condensation and the resulting augmentation of heat transfer is a serious problem for large Peclet numbers; and

(4) a quasi-steady state is attained after about one hour in real time.

Shapiro and Motakef (1990) attributed the discrepancy between their experimental and numerical simulation results mainly to their not varying the thermophysical coefficients with moisture content in the numerical model. The model underpredicted the amount of energy released in the wet region. They used an analytical method to solve the one-dimensional unsteady diffusion-conduction case in which the condensate was considered to be mobile.

Vafai and Tien (1989) investigated a transient, forced convective, intercoupled, two-dimensional, and multi-phase problem. They concluded that a one-dimensional model is not valid, especially when the porosity is high, the temperature difference across the porous matrix is large, and the pressure gradients are small or zero. Higher pressure gradients significantly reduce the two-dimensional distortions of field variables. It was also found that the liquid accumulated heavily in the region adjacent to the hot and humid environment, and that increasing the humidity level enhanced the vapour transport rate, condensation rate, total liquid content, and energy transfer rate.

Wijeysundera et al. (1989) set up an experiment to investigate one-dimensional transient vapour diffusion and heat conduction in an insulation slab. In the first set of experiments, water was sprayed on the hot face of the slab. In the second set of tests, one face was exposed to a warm and humid environment while the other face was maintained at a low temperature. The modes of transport were vapour diffusion, heat conduction, and moisture condensation. After a short initial transient period, the energy and vapour transfer processes reached a quasi-

steady-state. It was found that the lumped thermal conductivity of the experimental insulation slab had a linear relationship with the moisture content, and its magnitude increased with increasing mean slab temperature and temperature difference.

Tien and Vafai (1990) modelled transient convective leakages through walls. The model was two-dimensional, multi-component with phase change. The boundary temperatures were 20 and 35°C. They found that:

(1) liquid accumulated heavily in the region which was exposed to the hot and humid environment;

(2) infiltration played a very important role in determining the overall heat transfer rates as well as the generated condensate;

(3) increasing the pressure difference across the insulation caused increases in the Nusselt number and enhanced the thermal penetration, the vapour transport, the condensation rate, and the liquid content; and

(4) infiltration was the dominant mode of overall heat transfer even for small pressure differences.

Tao, Besant and Rezkallah (1991a) studied the motion of the frozen boundary which started at a cold plate (sink) at subzero temperature. In this one-dimensional transient numerical simulation, the vapour reached the cold plate by diffusion. There was no convection of the gas phase. Initially there was no condensate or frost and the heat and mass transfer were not coupled. The vapour diffused towards the cold plate and, in the process, underwent cooling. As the vapour density rose above the saturation level, a frozen front formed and gradually moved towards the dry boundary. Initially there was no wet region. The frozen front moved until saturation occurred in a region which was above the freezing

point, whereupon condensation occurred adjacent to the frozen front. Three distinct regions evolved: the frozen region; the wet region; and the dry region. Coupling of heat and mass occurred in the former two regions. The quasi-steady period was defined as the period when the temperature, the vapour density and the boundary position seemed unchanged relative to the significant change in the previous periods. Quasi-steady conditions were attained after about one hour. Gradients of temperature and vapour density were used to locate the interfaces. The authors assumed that liquid mobility commenced when the liquid occupied 10% of the void space, but no justification or reference was provided for this assumption.

In a setup that was very identical to the just-described reference, Tao, Besant and Rezkallah (1991b) used "limited experimental data" for comparison with their numerical model. They found that a thin layer of frost existed in the gap between the insulation slab and the cold plate positioned adjacent to it. The growth of a frost layer could result in an increase as high as 20% in the heat flux through the cold plate during the quasi-steady stage.

Wijeysundera and Hawlader (1992) used experimental measurements and a semi-empirical one-dimensional model of vapour and thermal diffusion processes (i.e., no convection) to show that:

(1) initially, the total moisture gain increases linearly with time, later decreasing gradually; and

(2) the heat flux shows a very gradual increase with time.

It was assumed that a moisture content above 50 $kg/m^3$ was caused by liquid movement, while values below this were due to local condensation.

It was also assumed that the experimental setup emulated a one-dimensional transport system.

Wijeysundera (1992) conducted both experimental and numerical investigations of a one-dimensional thermal and vapour diffusion case (i.e., no convection), and found that the rate of total moisture gain was initially nearly constant, but later decreased gradually with time. In this case liquid volume fractions of up to 30% were considered and all temperatures were above the freezing point.

Hokoi and Kumaran (1993) stated that, for a medium density glass fiber insulation (about 50 $kg/m^3$), the value of the local moisture content at the fully saturated moisture state may reach 20 kg/kg or 0.97 $m^3/m^3$ of dry insulation material. Their work involved both experiments and numerical modelling. The numerical model was a transient one-dimensional system which considered:

(1) the vapour transfer caused by vapour pressure gradient;

(2) "the liquid moisture transfer caused by the moisture content gradient";

(3) "the liquid moisture transfer caused by the temperature gradient"; and

(4) "the liquid moisture transfer caused by gravity".

Wijeysundera et al. (1993/94) showed that, for their one-dimensional quasi-steady conduction-diffusion moist system, the lumped effective thermal conductivity varied from about 1.5 to 15 times the dry state value. It also increased with increasing relative humidity and was highest when condensation had just commenced in the slab.

For an experimental one-dimensional forced convective airflow and heat transfer system, Mitchel, Tao and Besant (1995a) found that:

(1) the bulk of the moisture and frost accumulation was within the insulation adjacent to the cold surface located at the

bottom of the assembly;

(2) increasing the air inlet relative humidity from 60% to 90% increased the moisture accumulation in the bottom layer by 85%; and

(3) increasing the airflow rate from 5 to 10 L/min. increased the moisture accumulation in the bottom cold layer by 150%.

A follow-up numerical simulation of the experimental measurements [Mitchel et al., 1995b], revealed that:

(1) the numerical model underpredicted the amount of moisture accumulation within the bottom layer of the insulation (adjacent to the cold plate) by approximately 50%;

(2) compared to a dry insulation sample with no flow, convection-conduction increased the heat flux by a factor of more than thirteen for exfiltration and more than six for infiltration;

(3) increasing the inlet relative humidity from 60% to 90% increased the predicted conductive heat flux by 23%; and

(4) the conductive heat flux increased by 70% (for an inlet relative humidity of 75%) when the air flow speed was increased from 0.5 to 1.5 mm/s.

Murata (1995) conducted experimental and analytical investigations on a two-dimensional insulation slab. One side of the slab was exposed to high temperatures (up to 100°C) and high humidities, while the other side was bounded by a cold surface. Condensation occurred on the cold surface and in the interior of the fibrous insulation. The condensate was allowed to fall away under gravity. The analytical solution used a quasi-steady formulation with forced convection, gas diffusion, heat conduction and moisture condensation terms.

It was noted that:

(1) the vapour concentration was slightly upwardly convex in the dry zone and downwardly convex in the wet zone;

(2) due to condensation, the heat fluxes at the cooling surface were about twelve times the values predicted from an equivalent purely conductive model; and,

(3) in one of the runs, the heat flux due to condensation on the cooling surface accounted for 60% of the total.

Ojanen and Kumaran (1996) analysed an insulated timber frame wall using a steady-state calculation method, and a two-dimensional heat, air and moisture transport numerical model which included a forced convection term to account for infiltration and exfiltration. They found that, as the air flowrate increased, so did the moisture accumulation rate up to a point beyond which it decreased before abruptly dropping to zero or "drying out". The explanation for this occurrence is that, as the flowrate increases, the indoor boundary conditions encroach more and more into the cavity. At some stage the cavity becomes so warm that conditions for condensation cease to exist. It was also observed that the moisture accumulation was greater for higher indoor relative humidities.

Wijeysundera et al. (1996) conducted a numerical simulation of a conductive-diffusive case in which the cold plate was at the top and the warm open ambient was at the bottom of the insulation slab. The model was a one-dimensional, transient, multi-phase flow system with variable physical coefficients. Starting with a dry slab, it was observed that the wet region first developed at the top cold plate and then slowly advanced towards the warm ambient until the entire slab was wet. The intermediate stages consisted of two distinct zones; the wet and the dry regions.

For a one-dimensional coupled problem of heat and vapour

diffusion within fiberglass insulation, considered under transient conditions of heat conduction and water vapour adsorption/desorption, condensation and frosting, Simonson, Tao and Besant (1996) noted that, when the local relative humidity reached 100%, the numerical simulation presented a sudden change in the condensation rate, whereas in the "real situation" the transition from adsorption to bulk condensation is expected to be a continuous process with no sudden change in the rate of phase change or heat flux. They attributed this sudden change to a weakness in the numerical model. It was found that:

(1) in the bottom insulation board (next to the cold plate) the predicted moisture accumulation was 39% less than the measured value; and

(2) the difference between the total predicted mass accumulation in all the insulation boards and the measured mass accumulation was 23%.

They suggested that (in order to improve the numerical model), when the liquid volume fraction becomes large, additional terms to account for surface energy exchanges between the water and other species present (e.g. fiberglass and air) must be included in the calculation of the effective thermal conductivity. It was predicted that the difference between the measured and the predicted heat flux and moisture accumulation levels may be largely due to the model for the effective thermal conductivity.

Chen, Besant and Tao (1997a, 1997b) conducted both experimental and numerical investigations on a transient two-dimensional forced convective case with a warm plate at the top and a cold plate at the bottom of the insulation slab. The flow field was assumed to be steady, i.e. the velocity field was not affected by changes in density or by condensation. This assumption meant that Darcy's model for velocity was

independent of other equations and the viscosity of air was constant. However, it was mentioned that errors in the velocity field resulting from changes in density (due to both pressure gradients and condensation/ablimation) could be 1%. Measurements on apartment buildings show that a total exfiltration rate of 1.0 L/($m^2$-s) is induced by a pressure difference of 10 Pa. The latent heat alters the temperature profiles and heat fluxes. Besides, experimental results gave density changes due to cooling up to 10 to 15%.

A comparison of predicted and measured results indicated that:

(1) the quasi-steady state was reached after about two hours;

(2) the moisture and frost content of some parts of the bottom layer reached 10% by mass or about $5x10^{-3}$ liquid or frost volume fraction for the supply air at 85% RH;

(3) the total mass of moisture and frost accumulation on the insulation slab and cold surface was 0.0156 kg for one case, this being 50% of the total vapour that flowed through the system in a 3.5 hour test;

(4) increasing the inlet flowrate and relative humidity each increased the moisture accumulation within the insulation layer adjacent to the cold boundary;

(5) a 20% decrease in the effective thermal conductivity was predicted to cause temperature, moisture and heat flux variations (over 3.5 hours) of up to 1.5 K, 0.5% and 11%, respectively;

(6) exfiltration heat losses were up to 7.5 times the purely conductive losses; and

(7) increasing the inlet air flowrate and relative humidity increased the conductive heat flux at the cold plate, the temperature throughout the insulation, and the moisture accumulation throughout the insulation, especially within the

layer next to the cold plate.

## 2.2 Conclusions from the Literature Review

The following is a summary of the important points which have been revealed in the literature review.

(1) Condensation or ablimation will occur at any location in the flow domain where the vapour pressure exceeds the saturation vapour pressure, the latter pressure being a function of temperature only.

(2) Condensation/ablimation can occur within an insulation slab even if all its boundaries are unsaturated with vapour.

(3) A quasi-steady stage occurs at some point in time during the evolution of a transient system. This means that the quasi-steady solution is also a solution in a transient analysis of the system and can be used as an "initial" state.

(4) The temperature profile changes gradually after the quasi-steady stage. Condensation may cause a drop in the temperature profile while increasing the heat flux.

(5) The thermophysical properties of the medium, the temperature, the external humidities, the exfiltration rates, and infiltration rates all affect the heat flux and the condensation rates significantly.

(6) Infiltration and exfiltration are usually the dominant modes of overall heat and mass transfer even for small pressure differences. However, cases of forced convection in the literature are relatively few.

(7) The effective thermal conductivity is influenced by the moisture content.

(8) Using a constant total air density may lead to significant errors in the condensation rates and in the location of the wet-dry interface.

## 2.3 Critical Review

Results from both experimental and numerical investigations, revealed in the literature review, show that condensation or ablimation occurs only in regions of the flow domain where the moisture content of the air exceeds saturation levels, the system set-up and modes of transfer under investigation notwithstanding. This means that the thermophysical and other properties of moist air should be given more attention than has been the case to date. The properties of moist air are governed by temperature, pressure and moisture content. However, in most of the research investigations to date, the thermophysical properties of air have been assumed to be constant, the term "variable properties" being used to refer to the variation of the effective and weighted properties of the porous medium with liquid content.

Undue emphasis has been placed on the effects of the temperature differences, instead of the field temperature values, and on the Peclet numbers arising from the flow velocities or pressure differences across the domain, instead of the field pressure values which determine the properties of the air. In a porous medium, the solid matrix is responsible for resistance to fluid flow, while the air condition at a given location determines whether or not condensation or ablimation occurs. The air condition can only be determined accurately if both the temperature and the partial pressure of water vapour at a location are known. Given that air leakages in buildings are caused by pressure differences, there is no compelling reason for the prevalent and sometimes enthusiastic use of velocities instead of the field pressures. It appears that in the eagerness to find solutions to seemingly complex sets of simultaneous equations, researchers resort to "simplifying assumptions" even if these may distort the physics of the problem and lead to errors which could easily be avoided.

Existing heat and mass transfer models tend to either underpredict or overpredict the condensation rates. This is not surprising given that to date no explicit model has been assigned to the condensation or source term in the transport equations. This is unlike the conduction, diffusion and advection terms which are all represented by explicit models. The source term has often been treated as some kind of residual to be linearised so that "Patankar's Method" [Patankar, 1980] can be used in the solution of the equations. The best way to bridge the gap between experimental and simulation condensation rates is to develop definite physical models for the source term.

The determination of bulk air flowrates through leakage paths has not been given much consideration. The flow-field velocities and the bulk air flowrate depend on the geometry and size of the opening and on the shape and size of the flow domain, besides the pressure gradients. To date, bulk flowrates, whenever needed, have been assigned values based on "acceptable" orders of magnitude. Experimental measurements for leakages have related to whole rooms or entire buildings. The results are extremely important in the design of building services systems, especially in the estimation of air and heat losses or gains due to infiltration and exfiltration. However, condensation and ablimation and the damage they cause to the building envelope are localized at the leakage sites. Understanding the localized damage requires the investigation of exfiltration and infiltration through individual cracks and holes.

The contributions of the Soret and Dufour effects to heat and mass transfer are often assumed to be negligible relative to the diffusion and convection terms. This assumption may not always be correct. There is very little data on Soret and Dufour coefficients of gaseous mixtures, but the order-of-magnitude data provided by de Groot and Mazur (1962) should

suffice for a rough comparison between the main transport modes and the Soret and Dufour effects. Estimates of the Soret and Dufour coefficients for mixtures of water vapour and air are listed by Mason and Monchick (1965).

## 2.4 Research Objectives

The first objective of this research project is to develop an explicit model for the condensation/ablimation rate term in the heat and mass transfer equations which, when used in the quasi-steady formulation of the equations, will yield the quasi-steady state solution directly; i.e., without going through the traditional fully-transient evolution from an initial artificial dry state.

The second objective is to develop a simple numerical procedure which can be used to predict moisture accumulation in insulation materials for the long term, like an entire heating season lasting about 6 months. Designers usually do not use complicated solution methods which take long to give results. The procedure is to use the quasi-steady state values as the initial state and then proceed with large time-steps, say one hour at a time, to investigate the evolution of the field variables. Numerical solutions of transient equations usually require very small time steps, of the order of 5 seconds [Chen et al. (1997)], for stability. This requirement leads to long computation times, making it difficult to carry out simulations for long periods.

The third objective is to use the new model for the condensation rate term and the new numerical procedure to investigate the problem of forced-convective heat and mass transfer through slits and round holes in attic fiberglass insulation.

The fourth, and final, objective is to develop approximate mathematical relations which can be used by designers to

estimate the bulk air flowrates and heat transfer rates through slits and round holes in the attic insulation without having to write and run simulation programs. No general relations are developed for the estimation of the condensation rates but the quasi-steady model is reasonably good and involves less computation than the fully transient solutions.

In Chapter 3, the model equations and other relations are developed.

# CHAPTER 3

# PROBLEM STATEMENT AND MODEL DEVELOPMENT

## 3.1 Introduction

The third objective of this research project is to investigate the transfer of air, heat and moisture from a warm and humid interior to the attic which is subjected to the ever-changing weather. The air leaks through openings in ceiling boards and crosses the open fibrous insulation before reaching the attic space. The interior is assumed to be air conditioned and pressurized so that only exfiltration occurs. The changing weather conditions subject the exterior to different temperatures, humidity levels, and wind pressures against the external surfaces. Weather data are recorded as hourly averages and, therefore, changes in the external boundary conditions can only be included as step or discrete inputs in a simulation algorithm. Constant boundary conditions are therefore assumed. Figure 3.1 is a schematic of the flow domain showing the location of the leakage site.

The insulation, which is open at the top (attic), rests on a half-inch plasterboard, all other structural elements which support the assembly being ignored. The geometries considered for the openings are slits and holes. The primary driving force for air leakage is the pressure difference across the insulation. Heat energy is driven mainly by the temperature difference, while humidity levels create concentration gradients which cause vapour diffusion. The effect of temperature and humidity on bulk air flowrates and the effect of condensation on heat flux come out in the all-inclusive analysis that is adopted.

Some researchers [Vafai and Sarkar (1986), Mitchel et al. (1995), and Chen et al. (1997)] have used the fully-transient

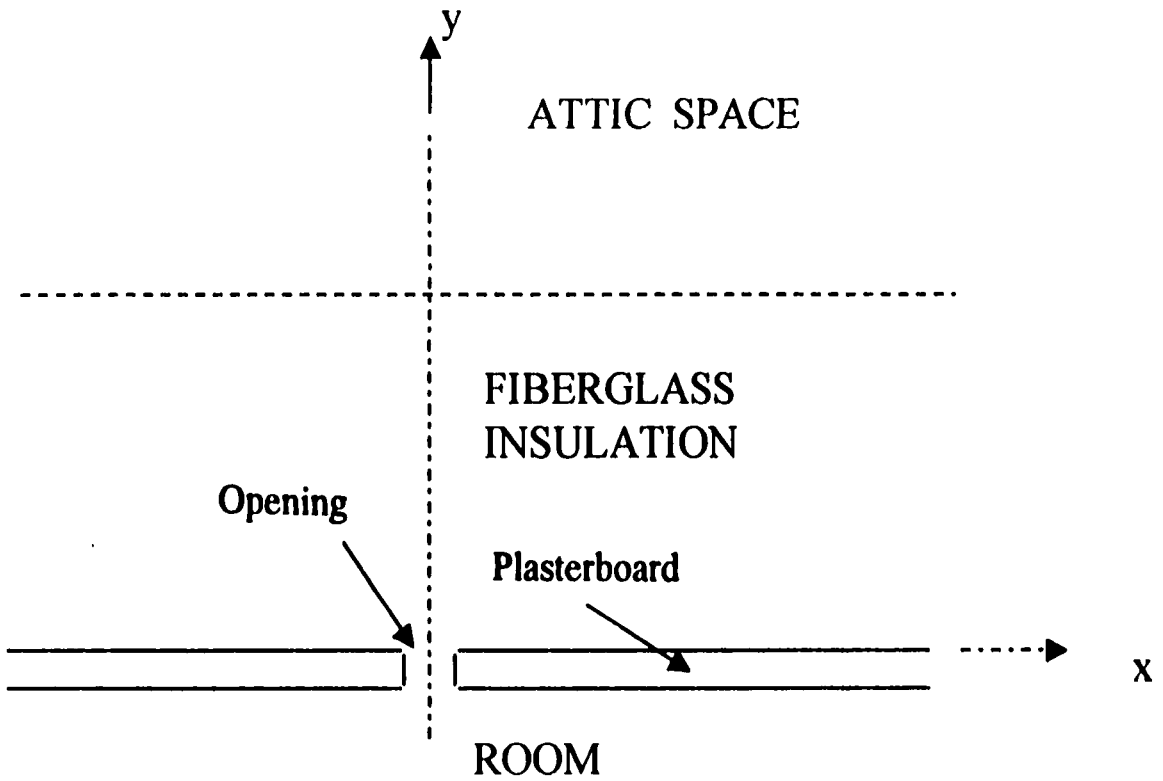


Figure 3.1 : Schematic of the Ceiling Assembly and the Leakage Site.

formulation, with an artificial dry state as an initial state, to carry out the simulation of heat and mass transfer processes in fibrous insulation. However, these investigations have usually terminated at a stage that would still be regarded as the quasi-steady stage. The quasi-steady state transfer rates are a function of the boundary conditions, and it should be possible to arrive directly at this state once the boundary conditions are known. The fully-transient formulation has been preferred over the quasi-steady formulation mainly because in the latter the number of unknowns often exceeds the number of simultaneous equations, unless an explicit model is found for the condensation or ablimation rate term. Ogniewicz and Tien (1981) used a semi-analytical solution method for their simplified model equations. However, the analytical solution method which they applied to the dry region would be impossible to use in the presence of non-linear equations. The equations would be non-linear in a variable velocity field, like in a two-dimensional flow field, and also if the thermophysical properties and density of air were temperature-dependent. In this investigation it will be shown that the quasi-steady state solution can be obtained by using the quasi-steady form of the governing equations, and solving them by an iterative procedure, if an explicit expression is found for the condensation/ablimation rate term in the equations.

The quasi-steady solution sets the transfer rates which can be used to predict the long-term moisture quantities. It also gives the steady-state profiles of the field variables. The steady-state profiles are functions of the boundary conditions. It is known that after the quasi-steady stage, the field variables change gradually [Modi and Benner (1985, Part I), Wijeysundera (1992), and Hokoi and Kumaran (1993)]. The gradual changes are due to the accumulating moisture which causes the properties of the insulation, especially the

effective thermal conductivity, to change. Modi and Benner (1985, Part I) reported that the effective thermal conductivity increased rapidly initially then later decreased, eventually leveling off to a "pseudo-steady state value". It will be shown in Section 5.3 that the quasi-steady moisture accumulation rates and the total moisture contents at each stage in the numerical solution process can be used to track the gradual evolution of the field variables.

Investigations by Vafai and Sarkar (1986) and Tao et al. (1991a) revealed that it takes about 1 hour for the quasi-steady state to be attained if the boundary conditions are fixed and the initial state of the insulation is "dry". Chen et al. (1997) reported that for their transient cold boundary it took about 2 hours for the quasi-steady state to be reached. The current research project is mainly concerned with the prediction of long-term moisture contents and the effects thereof on the field variables. The gradual evolution of the field variables from an initial dry state to the quasi-steady state during the first hour becomes insignificant if long periods are considered. Moreover, in its natural form, insulation always contains at least some adsorbed moisture - whether it is on the shelf, at the construction site, or in the building fabric. The "dry state" is artificial and convenient for initiating solution processes in transient model equations, otherwise it does not feature at all in the performance of insulation in a real situation.

## 3.2 Conceptual Mathematical Model

The objectives of this study are investigated through the development of a numerical model which is used for the simulation of the effects of selected variables and boundary conditions on air, heat and mass transfer.

The mathematical models currently used in the simulation of the processes involved in the simultaneous transfer of heat

and mass in building insulation were developed as recently as the 1970s. Luikov (1975) summarises the developments made in this area over the years by his team of Russian scientists. It was Whitaker (1977) who came up with the models that are currently widely accepted. These have been used by different researchers, with some adjustments to suit different situations.

For investigative purposes, the problem is conceived as:

(1) a two-dimensional fiberglass matrix;

(2) consisting of a non-reacting, multi-component and multi-phase fluid (i.e. dry air, water vapour, liquid water and ice) with interphase heat and mass transfer;

(3) being double-diffusive, i.e. allowing for both the conduction of heat and the diffusion of vapour; and

(4) having pressure-driven forced convection of heat and mass as the dominant transfer phenomenon (- it is shown in Appendix E that natural convection does not occur for the conditions which are investigated in this work).

In general, the thermophysical properties of fiberglass are not scalars, but are assumed to be invariant in this investigation. Properties of water, ice and gas (i.e., dry air and water vapour) are varied with temperature and composition, except when the variations are justifiably negligible within a specified range of state variables.

The contribution made by each transport phenomenon to heat and mass transfer is included as a distinct term in the governing equations. The phenomena include:

(1) heat conduction (due to temperature gradients) in all the phases;

(2) mass diffusion in the gas phase due to gradients of vapour

concentration;

(3) forced convection of heat and mass in the gas phase; and

(4) heat and mass transfer due to phase changes at the gas-liquid and gas-ice interfaces.

In Section 5.3, the Soret and Dufour effects, or coupled phenomena, in the gas phase are found to be negligible for the conditions considered in this project. Effects of adsorption and desorption on heat and mass transfer are neglected since these have been shown to be negligible in most practical situations, i.e., in situations involving sustained condensation. Experimental work by Langlais et al. (1982) showed that liquid volume fractions due to adsorption only are less than $10^{-6}$ $m^3/m^3$; Vafai and Whitaker (1986), Vafai and Sarkar (1986), Vafai and Tien (1989), Tien and Vafai (1990), Tao et al. (1991a, 1991b), and Chen et al. (1997) have shown in their investigations that regions where significant condensation occurs have liquid or frost volume fractions of order $10^{-3}$ to $10^{-5}$. Chen et al. (1997) and Mitchel et al. (1995) also demonstrated that the effects of adsorption were significant in the first 15 or so minutes of the experiments, which commenced with the insulation slab in an artificial "oven-dry" state. However, adsorbed moisture already forms an integral part of fibrous insulation in its natural state.

The heat, mass and momentum model equations used in this investigation have their origin in Whitaker's (1977) work on drying processes. In the model the dispersion of heat is accounted for in the heat conduction term through the "effective" thermal conductivity. Similarly, the dispersion of mass due to concentration gradients in the gas phase is accounted for within the moisture diffusivity. Thermal and mass dispersion may be neglected simply on account of the low airflow velocities in the insulation.

## 3.3 Macroscopic Analysis and the Volume-averaging of Transport Phenomena in a Porous Medium

### 3.3.1 Terminology

In this subsection, terms which are used frequently to describe heat and mass transfer processes in porous media are defined.

(a) Porous Medium

A porous medium is a material consisting of a solid matrix with an interconnected void called pore space.

(b) Porosity

The fraction of the total volume of a porous medium occupied by the void space is called the porosity of the material. Porosity is a determinant of the total fluid-carrying capacity of the medium.

(c) Homogeneous Medium

When, in a porous medium, the solid and the fluid are distributed uniformly throughout, the medium is said to be homogeneous. A medium that does not satisfy this requirement is said to be inhomogeneous or heterogeneous.

(d) Isotropic Medium

When all medium properties are invariant with the direction of measurement, the medium is said to be isotropic. When some or all properties vary with the direction of measurement, the medium is said to be anisotropic.

(e) Macroscopic Approach

The macroscopic approach to transport phenomena in porous media is a continuum approach whereby all quantities are measurable. A quantity is averaged over a defined space (area or volume) called a representative elementary area (REA) or a

representative elementary volume (REV) for convenience. It is then assumed that over a given REA or REV, the value of the quantity does not vary significantly and may, therefore, be allocated a constant or uniform value.

(f) Superficial Velocity or Darcy Velocity

The superficial or Darcy velocity of a fluid in a porous medium is the volume rate of flow per unit cross-sectional area of the flow region. The units are:

$$\frac{m^3}{s} \times \frac{1}{m^2} \text{ or } \frac{m}{s}$$

The Darcy velocity is usually referred to simply as the velocity of flow.

3.3.2 Volume-averaging

As is customary, the macroscopic analysis of the transfer processes in the insulation assembly is done by using volume-averaged equations. When a fluid traverses a porous medium, all the general laws governing the transport of matter and the transfer of heat (e.g., the Navier-Stokes equations) apply at a microscopic level. However, the macroscopic values of extensive quantities are of more interest and practical use to an engineer.

The flow domain of a porous medium usually contains a solid phase, a gaseous phase and one or more liquid phases. The objective is to describe each phase and its behaviour as a continuum that occupies the entire domain. Averaging is used to transform each of the microscopic balance equations of extensive quantities into equations that describe the behaviour of each considered extensive quantity as a continuum occupying the entire domain. This new level is the macroscopic level.

The averaging rules for different mathematical expressions are derived in great detail by Bear and Bachmat (1991, pg 115).

Nield and Bejan (1992, pp 37-43) also present a fairly detailed summary of the averaged transport equations. Whitaker (1977) used averaging extensively when deriving model equations for the simultaneous heat, mass and momentum transfer in porous media.

### 3.4 Simplifying Assumptions and Restrictions

The following are general assumptions made (and restrictions imposed) in order to arrive at the mathematical models.

(1) The fiberglass is assumed to be both homogeneous and isotropic, giving constant permeability: $K_x = K_y = K$. This assumption is valid for loose-fill fiberglass but not fiberglass batts or slabs.

(2) The solid matrix is rigid (i.e., the solid phase velocity, $v_s=0$).

(3) There is no chemical reaction within and between the phases. Also, vapour and dry air are assumed to be insoluble in the insulation material, water and ice. Each phase is distinct.

(4) The densities of the liquid and frozen phases are constant.

(5) The gas phase is ideal in the thermodynamic sense, enabling the application of the equation of state (i.e., perfect gas equation) to the components which are water vapour and dry air.

(6) The liquid and frost exist in small discontinuous quantities (i.e., in a pendular state), and therefore mass convection in the liquid and frozen phases is neglected, giving $v_l = 0$.

(7) In all phases the deviations of state and other variables are considered to be negligible in comparison to the volume-

averaged intrinsic phase averages.

e.g., for gas temperature, $T_g = \langle T_g \rangle^g + \tilde{T}_g \approx \langle T_g \rangle^g$.

Similarly, the products of deviations are negligible in comparison to the products of the averages.

e.g. $v_g T_g = \langle v_g \rangle \langle T_g \rangle^g + \langle \tilde{v}_g \tilde{T}_g \rangle \approx \langle v_g \rangle \langle T_g \rangle^g$.

## 3.5 Two-dimensional Quasi-steady Conservation Equations and other Relations in Cartesian Coordinates

The boundary conditions considered in this project are steady, and a system dealing with dry air only comprises steady equations since the response is steady. Systems dealing with moist air are formulated as quasi-steady systems, and their response to moisture accumulation is investigated by a new technique which has been named the quasi-transient method, discussed in Section 4.5.

All terms, except the source terms, are modelled on Whitaker's (1977) volume-averaged equations.

### 3.5.1 Mass Conservation Equation

The mass conservation equation for moist air is:

$$\nabla \cdot (\rho_g \vec{v}) + \dot{m} = 0 \qquad (3.1)$$

where $\rho_g$ is the bulk air density, $\vec{v}$ is the velocity, $\dot{m}$ is the moisture condensation rate per unit volume of medium, modelled in Section 3.5.7, and $\nabla \cdot (\rho_g \vec{v})$ is the net rate of bulk air convection into unit volume of medium.

### 3.5.2 Vapour Conservation Equation

It is assumed that the liquid and frozen phases each contain only a single component, i.e. there is no diffusion of mass within them. There is also no advection in these two phases. The conservation equation for the vapour is given as:

$$\nabla \cdot (\rho_g \bar{v} C) + \dot{m} = \nabla \cdot (D_v \rho_g \nabla C) \qquad (3.2)$$

where,

C is concentration,

$D_v$ is vapour diffusivity in the porous medium,

$\nabla \cdot (\rho_g \bar{v} C)$ is the net rate of vapour convection into unit volume of medium,

$-D_v \rho_g \nabla C$ is the diffusive vapour flux (Fick's law), and

$\nabla \cdot (D_v \rho_g \nabla C)$ is the net rate of vapour diffusion into unit volume of medium.

The vapour diffusion coefficient, $D_v$, discussed in Section A.1, is given by Equation 3.38.

### 3.5.3 Darcy's Law and the Momentum Equation

The Darcy flow model is adopted for the momentum equations. Darcy's law is used for modelling creeping flow in porous media.

In modern (differential) notation, Darcy's law is expressed as

$$v = -\frac{K}{\mu} \nabla P \qquad (3.3)$$

where,

K is the specific or intrinsic permeability,

$\mu$ is the dynamic viscosity of humid air, and

$\nabla P$ is the pressure gradient, the negative sign taking care of the fact that flow is from the point of high pressure to the point of lower pressure.

Darcy's law is of the nature of a statistical result, giving the empirical equivalent to the Navier-Stokes equations as averaged over a large number of pores [Muskat, 1946]. The Darcy equation does not contain density, $\rho$ , since the inertia

forces are negligible compared to the viscous forces.

Darcy's law has been verified by the results of many experiments, while theoretical backing has been obtained in various ways with the aid of either deterministic or statistical models [Nield and Bejan, 1992, pp 6-7].

For both liquids and gases, Darcy's law is valid only in a certain "seepage" velocity domain, outside of which more general flow equations must be used to describe the flow correctly. The range of validity of Darcy's law is difficult to determine precisely because of the ambiguity in the definition of the length parameter in the Reynolds number. Muskat (1946, pg 67) states:

> "..., it will suffice to accept as a safe lower limit where deviations from Darcy's law will become appreciable as given by a Reynolds number of 1, with d (the length scale) chosen as any reasonable average diameter of the sand grains .... In most practical situations of interest, Reynolds number is less than 1 ...".

Since permeability, K, has units $m^2$, the "length" scale used in defining the upper limit for the validity of Darcy's law for fibrous insulation is $K^{1/2}$ [Nield and Bejan, 1992, pg 10], giving the Reynolds number, $Re_K$, as

$$Re_K = \frac{\rho v K^{\frac{1}{2}}}{\mu} \qquad (3.4)$$

The Reynolds number, for the upper limit of the validity of Darcy's law, lies between 1 and 10 [Nield and Bejan, 1992, pp 10,11]. Beyond this limit, other models for the momentum equation must be found.

From Darcy's law, permeability, or specific/intrinsic

permeability, may be defined as the volume of a fluid of unit viscosity passing through a unit cross-section of the medium in unit time under the action of a unit pressure gradient.

Permeability is determined entirely by the structure of the medium and is independent of the nature of the fluid. It singly characterises the porous medium completely and uniquely with respect to the flow of fluids through it, and completely defines dynamically the porous medium as the carrier of a homogeneous fluid in viscous motion.

The structural properties which constitute permeability are:

(1) porosity;

(2) fiber size distribution;

(3) shapes of the fibers; and

(4) degree of cementation - a difficult factor to take into account.

However, there is no general mathematical relationship between permeability and porosity although various attempts, using simple models, have been made to relate the two properties mathematically. A medium may have a high porosity but have a low permeability due to lack of interconnection of the pores. Permeability may also vary with fiber size even though the porosity is kept constant.

The fiber theory of permeability, as presented by Scheidegger (1974), is summarised below:

(1) The drag on individual elements accounts for permeability in such a way that the solid-fluid interface resistance is given by

$$\text{Resistance} \propto \frac{1}{permeability}$$ [Bear, 1991];

(2) The separation between the fibers and the length of the individual fibers are both large compared to the fiber diameter, resulting in high porosities;

(3) The disturbance due to adjacent fibers on flow around any particular fiber is negligible;

(4) The inertial forces are negligible, i.e. the Reynolds numbers are low;

(5) "Resistance" is due to viscous drag; and

(6) Permeability is not constant, but varies with the flow velocity. (The slow variation of permeability with flow is characteristic of many instances in which the flow is nominally viscous.)

Jackson and James (1986) did a literature survey of experimental and theoretical work related to low-Reynolds-number flow through highly porous fibrous media. A variety of fibrous materials were involved in their analysis, and the findings are very useful in the understanding of the mechanics of fluid flow through fibrous materials. The literature survey revealed that experimental work agreed remarkably well with theoretical findings.

For flow perpendicular to an array of rods (i.e., cross flow), the permeability is found to be almost exactly half of that when arrays are parallel to flow. This ratio of one half is the same as the ratio for parallel and perpendicular drag on a long rod in uniform flow [Cox, 1970].

For flow parallel to an array of rods, theories overpredict experimental permeability since fibers in a real medium are not aligned with the flow but are randomly oriented or across flow and, therefore, offer more resistance.

The more uniform the distribution of fibers (i.e., homogeneous), the lower the permeability. Non-uniformities can

increase the permeability by as much as 50%.

The fiber cross-section also affects permeability. Theoretical work by Epstein and Masliyah (1972) on elliptical fibers revealed that, for flow perpendicular to the fibers, the permeability was 1.8 times that for circular fibers when the major axes were aligned with the flow, and 0.25 times that of circular fibers when the minor axes were aligned with the flow.

The expression for the viscosity of moist air as a function of temperature and moisture content, discussed in Section A.1, is given by Equation 3.41.

### 3.5.4 Energy Conservation Equation

Bird et al. (1960) gave the full energy equation for a multi-component gas mix. The following assumptions are made to simplify the equation for porous media.

(1) The enthalpy of all phases is independent of pressure and is a function of temperature only. That is,

$$h = C_p(T)T,$$

where h is the enthalpy and $C_p$ is the specific heat capacity at constant pressure.

(2) The thermal conductivities of fiberglass, water and ice are assumed to be constant, while those of the gaseous components, i.e., dry air and water vapour, vary with temperature only.

(3) Compressional work and viscous dissipation are negligible in both the liquid and gas phases.

(4) Within a grid cell, the three-phase system is in thermal equilibrium, i.e., $T_s = T_l = T_g = T$. (The subscripts s, l and g respectively stand for "solid", "liquid" and "gas".)

In the absence of thermal equilibrium between the different phases in an elemental volume (i.e., $T_s \neq T_g$ ), there would be a net heat transfer between the phases within a representative elementary volume, REV.

The simplified quasi-steady energy equation, based on Whitaker (1977) and the assumptions stated above, is

$$\rho_g C_{pg} \vec{v} \cdot \nabla T = \nabla \cdot (\lambda_{eff} \nabla T) + h_{vap} \dot{m} \qquad (3.5)$$

where,

$\lambda_{eff}$ is the effective thermal conductivity,

$h_{vap}$ is the latent heat of vaporisation (or sublimation, $h_{sub}$, as appropriate),

$\rho_g C_{pg} \vec{v} \cdot \nabla T$ is the thermal energy (per second) into unit volume of medium, due to advection of the fluid,

$-\lambda_{eff} \nabla T$ is the heat flux (Fourier's law),

$\nabla \cdot (\lambda_{eff} \nabla T)$ is the net rate of heat conducted into unit volume of medium, and

$h_{vap} \dot{m}$ is the latent heat generated in unit volume of the medium.

The specific heat capacity of humid air is discussed in Section A.1 and given as Equation 3.37.

As mentioned in the literature review, some researchers have used "lumped" effective thermal conductivities ($\lambda_{eff}$) [Modi and Benner (1985), Wijeysundera et al. (1989), Wijeysundera et al. (1993/94)]. In their approach, an "overall conductivity" is calculated from the measured total heat flux, temperature difference and length dimension across an entire experimental

assembly. (Most of these works have modelled combined vapour diffusion and heat conduction processes. Very few have touched on convection processes.) There is no denying that the results obtained from these experiments have contributed greatly towards our understanding of the role played by moisture in heat transfer. However, such an approach only provides an apparent or equivalent effective thermal conductivity since heat transfer by all modes (i.e., conduction, convection, and condensation/evaporation) are lumped together. This masks the contributions of the different modes and does not help in the establishment of a macroscopic mathematical model for the effective thermal conductivity. In this investigation the effective thermal conductivity is computed for each grid cell based on its fiber, water/ice, and gas contents.

In a porous medium the fluid flows in the voids only, making the advection term of convection heat transfer fairly straightforward. Thermal conduction processes are extremely complex. On a microscopic scale there is conduction within the fluid in a void, between the fluid and solid elements, between the fluid and any condensate or sublimate, between the condensate or sublimate and the solid to which it is attached, between solid elements at some point of contact (bond), and within a solid element. The actual scenario can be simplified by considering two extreme models; the series model and the parallel model [Bankvall, 1972]. The real situation is a combination of both, and modelling it requires knowledge of both the fraction of the heat transfer that occurs in parallel and the fraction that occurs in series. In series flow, it is assumed that the heat flows successively from a fluid to a solid element, then to the next fluid element, followed by the next solid element, until the end of the slab is reached. In parallel flow, a portion of the heat is transferred exclusively through the solid elements while the remaining portion is conveyed entirely through the fluid sub-system.

To simplify the analysis, it is usually assumed that all the heat transfer occurs on the basis of the parallel model. This assumption is justified by Bankvall's findings. In this project, the values of porosity encountered are 0.91 (cellulose [Yu, 1986]), 0.97 (fiberglass [Tien and Vafai, 1990]) and 0.98 (fiberglass [Ogniewicz and Tien, 1981]). The highest field temperature considered is 25°C, most of the flow domain falling below the freezing point. In all cases, therefore, conduction in the gas dominates. The factors mentioned above combine to justify the simplification of the model by excluding radiation effects and, further, adopting the parallel flow model for the effective thermal conductivity since most of the heat is conducted within the gas. The loss of accuracy due to these assumptions should not be sufficient to distort the trends in heat and mass transfer due to the transport phenomena to be considered in this project. The main transport phenomena are advection of heat and mass, diffusion of vapour, and the conduction of heat.

The properties of a porous medium must be averaged or weighted from the properties of the solid matrix and the percolating fluid. Now consider unit volume of a fibrous insulation which has a volume fraction of solid material $\epsilon_s$, a volume fraction of liquid $\epsilon_l$ or frost $\epsilon_i$, and a volume fraction of moist or dry air $\epsilon_g$. The constituent elements of the porous medium are shown in Figure 3.2. $\epsilon_l$ and $\epsilon_g$ are functions of time in the event of a phase change. The volume fractions are related by the volumetric constraint:

$$\epsilon_s + \epsilon_l(t) + \epsilon_g(t) = 1 \quad . \tag{3.6}$$

where,

$$\epsilon_s = \frac{V_s}{V}, \quad \epsilon_l = \frac{V_l}{V}, \quad \epsilon_g = \frac{V_g}{V},$$

and

$$V_s + V_l + V_g = V. \quad \text{(V in this case is volume)}$$

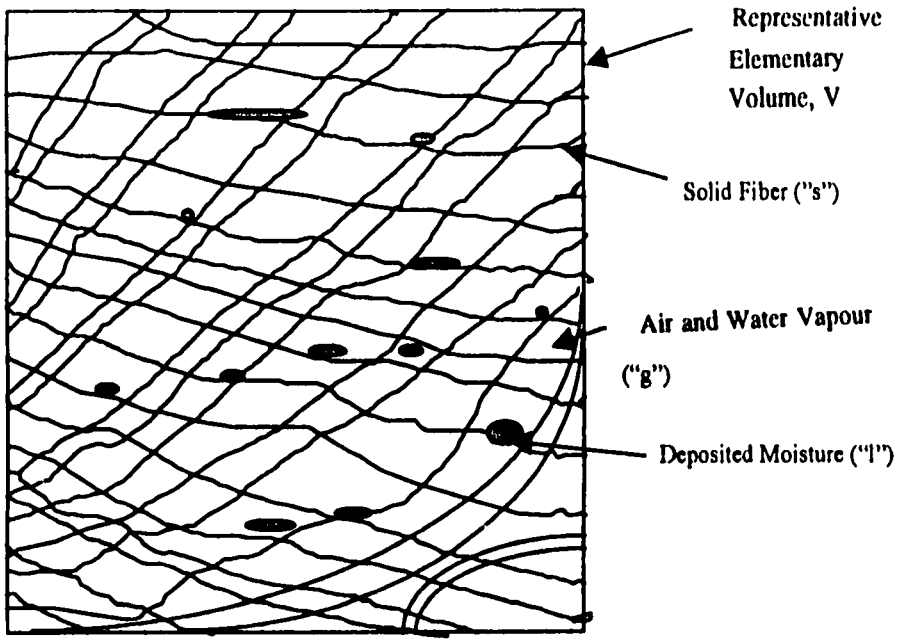


Figure 3.2. A Representative Elementary Volume Showing the Constituent Elements.

In the relations above, "i" (ice) is substituted for "l" (liquid) wherever the temperature is below the freezing point of water.

In this project, the thermophysical properties of the porous medium are obtained by doing mass and volume weighting of the properties of the solid and fluid elements. A parallel flow model is adopted for the effective thermal conductivity and the effect of radiation is neglected. Hence the model simplifies to:

$$\lambda_{eff} = \epsilon_s \lambda_s + \epsilon_l(t)\lambda_l + \epsilon_g(t)\lambda_g . \qquad (3.7)$$

The expressions for the thermal conductivities of dry air and water vapour, and hence humid air, are developed in Section A.1 and given in Section 3.6. The conductivities of the solid elements, liquid and ice are constant and are given in Section A.2.

In this investigation, the parallel model for the effective thermal conductivity has been extended to include situations with phase change. Bankvall's (1972) investigation did not include such cases. The conductivity of ice is about 3 times that of water, while that of water is about 24 times that of moist air. Water and frost usually exist in the medium in minute quantities, such that the product $\epsilon\lambda$ is still much larger for the air than for the liquid (or frost) and the solid. However, should this product for the liquid (or frost) become significant relative to the same product for the moist air, then the validity of the parallel model for the effective thermal conductivity diminishes or becomes questionable. This could occur in the presence of massive condensation or frosting. It then becomes necessary to look for new models for the effective thermal conductivity. In this project, the model given as Equation 3.7 is applied throughout. (It is observed that Equation 3.7 has the appearance of a volume-weighted thermal conductivity.)

### 3.5.5 Soret and Dufour Effects

Luikov (1975) included cross diffusion terms (i.e. Soret and Dufour effects) in his model. These two phenomena were first included in the formulation by Philip and de Vries (1957). They observed that, in the presence of temperature gradients, the vapour transfer had a larger value than that predicted by simple theory (Fick's law). This was due to the Soret effect. Similarly, in the presence of strong concentration gradients, the heat transfer had a larger value than that predicted by Fourier's law. This occurrence was due to the Dufour effect. Philip and de Vries included the two effects in their formulation for heat and mass transfer in soils. de Vries (1958) provided a generalization of the equations for the simultaneous transfer of heat and moisture in porous media under the combined influence of gravity and gradients of temperature and moisture content.

Soret and Dufour terms have rarely been included in subsequent research work. The terms are often important for liquid flows in porous media, but for gases this is only rarely possible. Besides, there is an almost total lack of experimentally-determined coefficients for the phenomena for most common gas mixtures. Most of the few coefficients that are available have been deduced from semi-theoretical considerations. Mason and Monchick (1965) have provided estimates for non-dimensional thermal diffusion coefficients for moist air. de Groot and Mazur (1962) provided experimentally-deduced general orders of magnitude of the coefficients for gaseous and liquid mixtures.

In this project, the Soret and Dufour terms are dropped after being shown in Example 2, Section 5.3, to be negligible relative to other terms in the governing equations.

### 3.5.6 Thermodynamic Relations

In most engineering appplications involving moist air at

ambient temperatures and pressures, it suffices to treat the air as an ideal binary gas mixture of dry air and water vapour. This facilitates the application of ideal gas relations to the mixture without incurring unacceptable loss of accuracy. The relations between the volume, the pressure, and the temperature for the two components are thus written as

$$P_g = P_a + P_v \tag{3.8}$$

$$P_a = \rho_a R_a T \tag{3.9}$$

$$P_v = \rho_v R_v T \tag{3.10}$$

$$\rho_g = \rho_a + \rho_v \tag{3.11}$$

(In Equations 3.8 to 3.11, P is pressure in Pa, R is specific gas constant in J/kg-K, and the subscripts a, v and g stand for dry air, water vapour and gas, respectively.)

When vapour is saturated, the vapour pressure and density may be estimated from empirical relations. CIBSE Guide, Volume C (1988, pg C1-2) provides the following relations for saturated moist air.

Over water, the saturation vapour pressure is given by

$$P_{sw} = 10^{c1}\ Pa \tag{3.12}$$

where,

$$c1 = 33.59051 - 8.2\log_{10}T + 2.4804\times10^{-3}T - \frac{3142.31}{T}$$

and the saturation vapour density is obtained from

$$\rho_{sw} = \frac{P_{sw}}{R_v T} \tag{3.13}$$

where T (K) is the temperature of the water.

Similarly, the vapour pressure over ice at a temperature T is

given by

$$P_{si} = 10^{c2}\ Pa \qquad (3.14)$$

where, $c2 = 12.5380997 - \frac{2663.91}{T}$.

and the saturation vapour density is obtained from

$$\rho_{si} = \frac{P_{si}}{R_v T}. \qquad (3.15)$$

The universally accepted values of the specific gas constants for dry air, $R_a$, and water vapour, $R_v$, are 287 and 462 J/kg-K, respectively.

3.5.7 Model for the Rate of Condensation.

A condensation or an ablimation process commences when the vapour pressure in a given volume of air exceeds the saturation vapour pressure for the temperature of the space or volume. Two ways in which the saturation vapour pressure can be exceeded are:

(1) when a space temperature drops and the corresponding saturation vapour pressure drops below the actual vapour pressure already existent in the space; and

(2) when vapour is convected into a space until its partial pressure rises above the saturation level for the space temperature.

In either case, the system (or space) reacts to restore its equilibrium by "expelling" the excess water vapour from the mixture of water vapour and dry air.

An example of the first case is the formation of dew on the ground at night in warm, humid weather. The second case is represented by the blowing of moist air over a cold surface which is maintained at a constant temperature as, in the operation of air cooler coils.

When moist air is convected through a space at a creeping

velocity, it is assumed, as an approximation, that, if the vapour pressure in the space rises above the saturation level, all the excess vapour condenses or ablimates, and the air condition at the exit of the space is saturated.

The vapour conservation equation can be used to determine the density of the vapour introduced into the space. This is done by first calculating the vapour concentration, C, from the conservation equation, then calculating the vapour density, $\rho_v$, from the total density, $\rho_g$, and the vapour concentration, C, since $\rho_v = C\rho_g$. The energy equation is used to determine the temperature of the space. For the determined temperature, the saturation vapour pressure can be obtained from Equation 3.12 or 3.14, and the saturation vapour density, $\rho_{sv}$, can be obtained using Equation 3.13 or 3.15. If $\rho_v$ is less than or equal to $\rho_{sv}$ then there is no condensation/ablimation. However, if $\rho_v$ is greater than $\rho_{sv}$, then the system contains excess vapour and must get rid of it to restore equilibrium.

As an approximation, it is then assumed that, at the creeping velocity of flow, 100% of the excess vapour is condensed or ablimated . The exit condition of the grid space is set equal to $\rho_{sv}$ while the difference between $\rho_v$ and $\rho_{sv}$ is allocated to the condensation rate. This moisture "balance" may be expressed as

$$\dot{m} \approx -\nabla \cdot (\rho_v \vec{v}) \quad \text{kg/s-m}^3 \qquad (3.16)$$

Equation 3.16 is the proposed model for the condensation rate, $\dot{m}$, in the governing equations for the simultaneous air, heat and moisture transfer. In the numerical solution of a condensation problem, the balance equations are applied to each control volume or grid cell. Hence this model is also applied to each control volume.

Equation 3.16 neglects adsorbed moisture and looks like a vapour conservation equation without the diffusion terms,

but it is not. It simply is a reference equation which applies only when and where the computed $\rho_v$ is greater than $\rho_{sv}$, the reference vapour density. If $\rho_v$ is less than or equal to $\rho_{sv}$ then $\dot{m}$ is set equal to zero. The use of the saturation vapour density as the reference point in the model (Equation 3.16) means that any pockets of condensation due to capillary effects are neglected.

This new method for estimating $\dot{m}$ is hereby named the Saturation Method for the Approximation of the Rate of Condensation, and abbreviated to SMARC.

By simplifying the models used for the governing equations, it is possible to avoid the need for an explicit model for the condensation rate term. This can be achieved, as many researchers in this field have done previously, by assuming just enough constant thermophysical properties to make the number of variables equal to the number of equations. The more the variables, however, the higher the likelihood that the number of variables will exceed the number of equations, making it necessary to have a separate model for the source term, $\dot{m}$. Ogniewicz and Tien (1981) were able to eliminate the source term between the energy and vapour concentration equations because their simplified formulation operated on a constant velocity and constant thermophysical properties. The worst cases are those where authors have laid out the equations then stated that they were solved "by an appropriate scheme" or by "Patankar's method" without giving any further details.

### 3.5.8 Porosity, Volumetric Constraint, and the Liquid Volume Fraction

If it is assumed that the generated liquid (condensate) or ice (frost) exists in a pendular state and is all retained in the space, then its volume fraction, $\epsilon_l$, is given by

$$\epsilon_l(t) = \frac{\dot{m}}{\rho_l}\omega 2 \quad (m^3/m^3), \tag{3.17}$$

where $\omega 2$ is the time (in seconds) during which $\dot{m}$ prevails.

The solution of the quasi-steady equations sets the heat and mass transfer rates at that stage as a function of the boundary conditions. When $\omega 2$ is 1 (second), the value of $\epsilon_l$ represents the rate at which the liquid/frost volume fraction changes.

In Equation 3.17 the density of water is used for temperatures above freezing point and the density of ice below freezing point.

Since the volumetric constraint is given by

$$\epsilon_s + \epsilon_l(t) + \epsilon_g(t) = 1, \tag{3.18}$$

the corresponding volume fraction of the gaseous phase becomes

$$\epsilon_g(t) = 1 - \epsilon_s - \epsilon_l(t) \tag{3.19}$$

In Equations 3.17 to 3.19, $\epsilon_i$ replaces $\epsilon_l$ where the space temperature is less or equal to 273.15 K.

Three examples will be used in Chapter 5 ("Model Validation") to assess the performance of SMARC.

### 3.5.9 Boundary Conditions and Heat and Mass Transfer Coefficients

Figure 3.3 shows the flow domain and its boundaries. The leakage path may be a slit or a round opening on the half-inch plasterboard which separates the pressurized and conditioned warm and humid interior from the unconditioned attic which is at atmospheric pressure (101325 Pa). The attic fiberglass insulation has a thickness D and is open at the top.

The higher interior pressure forces room air through the

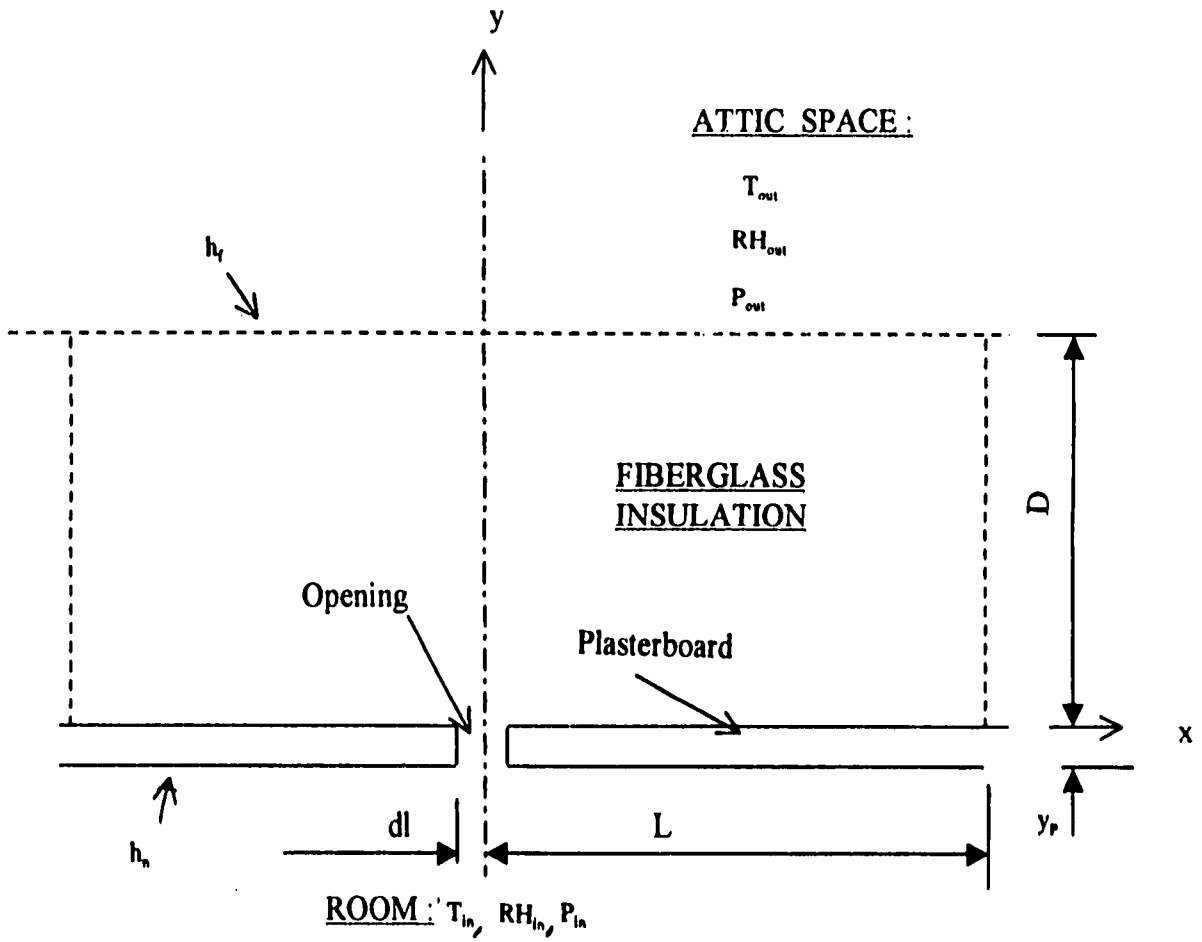


Figure 3.3. Flow Domain and Boundary Conditions.

hole or crack, then through the insulation, and into the attic. Because of the immense size of the room (relative to the opening size), it may be regarded as a reservoir. This allows the assumption of Dirichlet boundary conditions for the inlet. The conditions at the exit (i.e., the open boundary between the insulation and the attic air) are obviously influenced by the local velocities at the exit, giving forced convective boundary conditions for both heat and mass transfer. Away from the opening, heat only is transferred through the natural convective film from the room air to the plasterboard surface, and by conduction through the plasterboard to the insulation.

The convective heat and mass transfer coefficients for the boundaries are discused in Sections A.3 and A.4.

## 3.6 Summary of Model Equations and Other Relations

The equations and relations used for modelling in this project are summarised below.

(1) Mass Conservation Equation:

$$\nabla \cdot (\rho_g \vec{v}) + \dot{m} = 0 \tag{3.20}$$

(2) Vapour Conservation Equation:

$$\nabla \cdot (\rho_g \vec{v} C) + \dot{m} = \nabla \cdot (D_v \rho_g \nabla C) \tag{3.21}$$

(3) Momentum Equation (Darcy's law);

$$v = -\frac{K}{\mu} \nabla P \tag{3.22}$$

(4) Energy Conservation Equation:

$$\rho_g C_{pg} \vec{v} \cdot \nabla T = \nabla \cdot (\lambda_{eff} \nabla T) + h_{vap} \dot{m} \tag{3.23}$$

(5) Thermodynamic Relations:

$$P_g = P_a + P_v \tag{3.24}$$

$$P_a = \rho_a R_a T \tag{3.25}$$

$$P_v = \rho_v R_v T \tag{3.26}$$

$$\rho_g = \rho_a + \rho_v \tag{3.27}$$

(6) Saturation Vapour Pressure:

$$P_{sw} = 10^{c1}\ Pa \tag{3.28}$$

where,

$$c1 = 33.59051 - 8.2\log_{10}T + 2.4804\times10^{-3}T - \frac{3142.31}{T}$$

and,

$$P_{si} = 10^{c2}\ Pa \tag{3.29}$$

where, $c2 = 12.5380997 - \frac{2663.91}{T}$.

(7) Condensation Rate (SMARC):

$$\dot{m} \approx -\nabla.(\rho_v \vec{v}) \tag{3.30}$$

(8) Liquid Volume Fraction:

$$\epsilon_l(t) = \frac{\dot{m}}{\rho_l}\omega 2 \tag{3.31}$$

(9) Volumetric Constraint:

$$\epsilon_s + \epsilon_l(t) + \epsilon_g(t) = 1 \tag{3.32}$$

The variable thermophysical properties of air, water vapour, water (liquid) and frost (ice), developed in Appendix A, are summarised below.

The specific heat capacities (at constant pressure) of water vapour, Nitrogen and Oxygen are:

$$C_{pv} = 1727.3576 + 0.52204T + 6.85660\times10^{-5}T^2 - 3.35606\times10^{-8}T^3 \tag{3.33}$$

$$C_{pNi} = 992.519 + 0.174658T + 1.7388\times10^{-6}T^2 - 7.8048\times10^{-9}T^3 \quad (3.34)$$

$$C_{pOx} = 845.2426 + 0.3390T - 1.16553\times10^{-4}T^2 + 1.59950\times10^{-8}T^3 \quad (3.35)$$

(where T is the temperature in K and $C_p$ is the specific heat capacity in J/kg-K)

There is no chemical reaction involving dry air. Therefore, its properties will be dominated by the properties of Oxygen and Nitrogen. Hence, as an approximation, it is assumed that dry air consists of 23.29% Oxygen and 76.71% Nitrogen by weight, giving its specific heat capacity, in J/kg-K, as

$$C_{pa} = 0.2329C_{pOx} + 0.7671C_{pNi}. \quad (3.36)$$

Mass-weighting gives the specific heat capacity of moist air as

$$C_{pg} = \frac{\rho_v}{\rho_g}C_{pv} + \frac{\rho_a}{\rho_g}C_{pa} \quad (3.37)$$

For the temperature range 203 K to 523 K, the mass diffusion coefficient of water vapour in the porous medium is given by

$$D_v = \epsilon(1.643\times10^{-9}\ T^{1.695}) \quad (3.38)$$

(where $\epsilon$ is the porosity of the medium and the units of $D_v$ are $m^2/s$).

The dynamic viscosities in kg/m-s, for the temperature range 193 K to 573 K, are given by

$$\mu_a = 2.543\times10^{-7}T^{0.750} \quad (3.39)$$

and

$$\mu_v = 1.916\times10^{-8}T^{1.093} \quad (3.40)$$

The combination formula, after Sutherland [Wright, P.G. and Gray, P., 1962], gives

$$\mu_g = \frac{\mu_a}{1 + G_{av}\left(\frac{x_v}{x_a}\right)} + \frac{\mu_v}{1 + G_{va}\left(\frac{x_a}{x_v}\right)}. \qquad (3.41)$$

The G factors, $G_{av}$ and $G_{va}$, are given by Wilke's (1950) combination scheme:

$$G_{av} = \frac{\sqrt{2}}{4}\left(\frac{M_v}{M_a + M_v}\right)^{\frac{1}{2}}\left[1 + \left(\frac{\mu_a}{\mu_v}\right)^{\frac{1}{2}}\left(\frac{M_v}{M_a}\right)^{\frac{1}{4}}\right]^2 \qquad (3.42)$$

and

$$G_{va} = \frac{\sqrt{2}}{4}\left(\frac{M_a}{M_a + M_v}\right)^{\frac{1}{2}}\left[1 + \left(\frac{\mu_v}{\mu_a}\right)^{\frac{1}{2}}\left(\frac{M_a}{M_v}\right)^{\frac{1}{4}}\right]^2 \qquad (3.43)$$

(where $M_i$ is the molecular weight and $X_i$ is the mole fraction of a substance/component i).

The thermal conductivities of dry air and pure water vapour in W/m-K, for the temperature range 193 K to 573 K, are:

$$\lambda_a = 1.814 \times 10^{-4} T^{0.870} \qquad (3.44)$$

and

$$\lambda_v = 1.177 \times 10^{-5} T^{1.281} \qquad (3.45)$$

The combination formula, after Sutherland [Wright, P.G. and Gray, P., 1962], gives

$$\lambda_g = \frac{\lambda_a}{1 + G_{av}\left(\frac{x_v}{x_a}\right)} + \frac{\lambda_v}{1 + G_{va}\left(\frac{x_a}{x_v}\right)} \qquad (3.46)$$

$G_{av}$ and $G_{va}$ in Equation 3.46 take on the same values as those computed for viscosity above, in accordance with Mason and Monchick's (1965) recommendation.

The effective thermal conductivity of the insulation can now be computed from

$$\lambda_{eff} = \epsilon_s \lambda_s + \epsilon_l(t)\lambda_l + \epsilon_g(t)\lambda_g . \qquad (3.47)$$

The latent heat of vaporisation of water, for values of T between 273 K and 303 K, is obtained from

$$h_{vap} \approx (1.175 \times 10^7) T^{-0.276} \; J/kg \qquad (3.48)$$

and the latent heat of sublimation of ice is obtained from

$$h_{sub} \approx (3.129 \times 10^6) T^{-0.0176} \; J/kg \qquad (3.49)$$

for values of T between 253 K and 273 K. Between 233 K and 253 K, the value of $h_{sub}$ is approximately constant at $2.839 \times 10^6$ J/kg.

The convective mass transfer coefficient is related to the convective heat transfer coefficient by the equation

$$h_m = \frac{h_f}{C_{pg} \rho_g Le^{\frac{2}{3}}} \qquad (3.50)$$

The simultaneous model equations and relations, summarised in Equations 3.20 to 3.50, are discretized and solved by the approximate numerical methods described in Chapter 4.

# CHAPTER 4

# TWO-DIMENSIONAL NUMERICAL MODEL FOR A SLIT

Section 1.2 discussed the most likely locations of leakage paths in the building envelope. The most common flow geometry for the leakage path is the slit. Round holes do occur but are less common. The third objective of this research project (Section 2.4) is to investigate the problem of forced-convection through slits and round holes in attic fiberglass insulation. This chapter looks at the numerical model for a slit. The model for a round hole is discussed in Appendix D.

Modelling for a slit is done in Cartesian coordinates. The flow domain, shown in Figure 3.3, is symmetrical, and computations are simplified by considering only one half of the domain.

## 4.1 The Computational Grid System

The control volume approach, with a staggered grid system, is used in the discretization of the governing equations and other relations. The main flow variables (i.e., temperature, pressure, concentration, and condensation rate) are computed at the grid cell centers while all fluxes are computed at the grid cell boundaries. Figure 4.1 shows a two-dimensional staggered grid system.

In the figure "jv" and "iv" denote the cell centers while "j" and "i" are used at the cell boundaries. The result is a two-grid system, with one grid displaced relative to the other.

A Taylor series expansion about the cell center indicates that a two-dimensional mass conservation equation has a truncation error of $O(\Delta x^2, \Delta y^2)$ even when only four grid points are involved. The use of a staggered grid allows the coupling of the fluxes and the fluid properties at adjacent grid points.

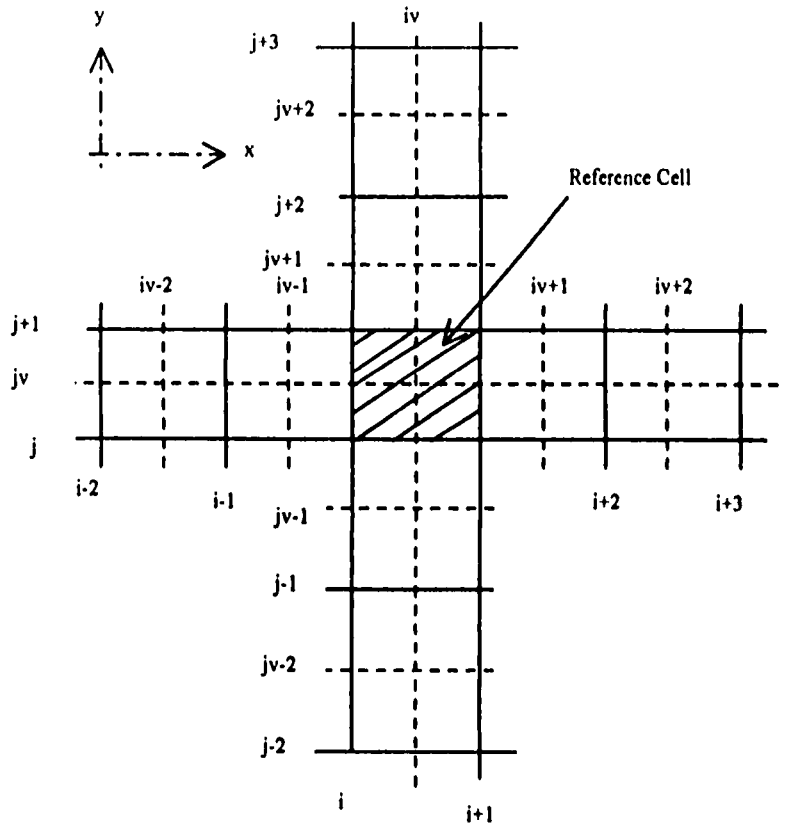


Figure 4.1 : Two-dimensional Staggered Grid System.

This prevents the appearance of oscillatory solutions that may occur if centered differences are used to discretize all derivatives on a non-staggered grid [Fletcher, Vol. 2, 1988, pp 335-336].

The grid cells are arranged in such a way that the edge of the opening coincides with a cell boundary. This is to avoid difficulties that may arise when computing fluid properties or fluxes at this point.

## 4.2 Non-dimensional Equations

The governing equations and other relations which are developed in Chapter 3 are solved for different boundary conditions. They are used in their non-dimensional forms with the cross-transport terms excluded. Justification for this exclusion will be provided during the validation of the models in Chapter 5.

The reference values, shown with subscript "o" in the non-dimensional formulae below, and the non-dimensional parameters ( or groups) are defined and derived in detail in Appendix B.

The relationships between the dimensional and non-dimensional variables are given below.

Length: $\bar{x} = \frac{x}{D}$ ; $\bar{y} = \frac{y}{D}$ .

Temperature: $\bar{T} = \frac{T - T_{out}}{\Delta T}$ ; $\Delta T = T_{in} - T_{out}$ .

Vapour Concentration: $\bar{C} = \frac{C - C_{out}}{\Delta C}$ ; $\Delta C = C_{in} - C_{out}$ .

Total Pressure: $\bar{P} = \frac{P - P_{out}}{\Delta P}$ ; $\Delta P = P_{in} - P_{out}$ .

Partial Pressure (component i): $\bar{P}_i = \frac{P_i - P_{i,out}}{\Delta P}$ .

Density (component i): $\bar{\rho}_i = \frac{\rho_i}{\rho_{io}}$ .

Velocity: $\bar{u} = \frac{u}{v_o}$ ; $\bar{v} = \frac{v}{v_o}$ .

Condensation Rate [Ogniewicz and Tien, 1981]: $\bar{\dot{m}} = \frac{D^2}{D_{vo}\rho_{go}\Delta C}\dot{m}$.

Volume Fraction (component i): $\bar{\epsilon}_i = \frac{\epsilon_i}{\epsilon_o}$ .

Diffusion Coefficients: $\bar{D}_v = \frac{D_v}{D_{vo}}$ ; $\bar{D}_s = \frac{D_s}{D_{so}}$ ; $\bar{D}_d = \frac{D_d}{D_{do}}$ .

Specific Heat Capacity (component i): $\bar{C}_{pi} = \frac{C_{pi}}{C_{pio}}$ .

Viscosity (component i): $\bar{\mu}_i = \frac{\mu_i}{\mu_{io}}$ .

Effective Conductivity: $\bar{\lambda}_{eff} = \frac{\lambda_{eff}}{\lambda_{effo}}$ .

Effective Thermal Diffusivity: $\bar{\alpha}_{eff} = \frac{\bar{\lambda}_{eff}}{\bar{C}_{pg}\bar{\rho}_g}$ .

In a control volume, the mass conservation equation (3.20) for bulk air (i.e., air and water vapour) and condensate becomes

$$\frac{\partial}{\partial \bar{x}}(\bar{\rho}_g \bar{u}) + \frac{\partial}{\partial \bar{y}}(\bar{\rho}_g \bar{v}) + \frac{D_{vo}\Delta C}{V_o D}\bar{m} = 0 \qquad (4.1)$$

The $H_2O$ species in the control volume is conserved by the following equation (- obtained from Equations 3.20 and 3.21):

$$\begin{aligned} &\frac{V_o D}{D_{vo}}\bar{\rho}_g \bar{u}\frac{\partial \bar{C}}{\partial \bar{x}} + \frac{V_o D}{D_{vo}}\bar{\rho}_g \bar{v}\frac{\partial \bar{C}}{\partial \bar{y}} \\ &- \frac{\partial}{\partial \bar{x}}\left(\bar{D}_v \bar{\rho}_g \frac{\partial \bar{C}}{\partial \bar{x}}\right) - \frac{\partial}{\partial \bar{y}}\left(\bar{D}_v \bar{\rho}_g \frac{\partial \bar{C}}{\partial \bar{y}}\right) \\ &- \Delta C \bar{C}\bar{m} + (1 - C_{out})\bar{m} = 0 \end{aligned} \qquad (4.2)$$

The sensible and latent heat energies in a control volume are conserved by the following equation, obtained from Equation 3.23:

$$\frac{V_o D}{\alpha_{effo}} \bar{\rho}_g \bar{C}_{pg} \bar{u} \frac{\partial \bar{T}}{\partial \bar{x}} + \frac{V_o D}{\alpha_{effo}} \bar{\rho}_g \bar{C}_{pg} \bar{v} \frac{\partial \bar{T}}{\partial \bar{y}}$$

$$- \frac{\partial}{\partial \bar{x}} \left( \bar{\lambda}_{eff} \frac{\partial \bar{T}}{\partial \bar{x}} \right) - \frac{\partial}{\partial \bar{y}} \left( \bar{\lambda}_{eff} \frac{\partial \bar{T}}{\partial \bar{y}} \right) \qquad (4.3)$$

$$- h_{vap} \frac{D_{vo}}{\alpha_{effo} C_{pgo}} \frac{\Delta C}{\Delta T} \bar{m} = 0$$

The flow is "creeping" and the velocities can be obtained using Darcy's law (Equation 3.22). The velocity components are

$$\bar{u} = - \frac{K \Delta P}{\mu_o V_o D} \frac{1}{\bar{\mu}_g} \frac{\partial \bar{p}}{\partial \bar{x}} \qquad (4.4)$$

and

$$\bar{v} = - \frac{K \Delta P}{\mu_o V_o D} \frac{1}{\bar{\mu}_g} \frac{\partial \bar{p}}{\partial \bar{y}} . \qquad (4.5)$$

The volumetric constraint (Equation 3.32) is re-written as:

$$\bar{\epsilon}_l(t) + \bar{\epsilon}_g(t) = \frac{(1 - \epsilon_s)}{\epsilon_o} \qquad (4.6)$$

For moist air, assumed to be an ideal gas mixture of dry air and water vapour, the equations of state (Equations 3.24 to 3.27), are written as:

$$\bar{P} = \bar{P}_a + \bar{P}_v \qquad (4.7)$$

$$\bar{\rho}_a = \frac{1}{\rho_{ao} R_a} \frac{(\Delta P \bar{P}_a + P_{a,out})}{(\Delta T \bar{T} + T_{out})} \qquad (4.8)$$

$$\bar{\rho}_v = \frac{1}{\rho_{vo} R_v} \frac{(\Delta P \bar{P}_v + P_{v,out})}{(\Delta T \bar{T} + T_{out})} \qquad (4.9)$$

$$\bar{\rho}_g = \frac{\rho_{ao}}{\rho_{go}} \bar{\rho}_a + \frac{\rho_{vo}}{\rho_{go}} \bar{\rho}_v \qquad (4.10)$$

The specific heat capacity (at constant pressure) of moist

air is obtained by the mass-weighting of the heat capacities of dry air and water vapour (Equation 3.37), and the resulting equation is

$$\overline{C}_{pg} = \frac{\rho_{vo}}{\rho_{go}} \frac{C_{pvo}}{C_{pgo}} \frac{\overline{\rho}_v}{\overline{\rho}_g} \overline{C}_{pv} + \frac{\rho_{ao}}{\rho_{go}} \frac{C_{pao}}{C_{pgo}} \frac{\overline{\rho_a}}{\overline{\rho}_g} \overline{C}_{pa} \qquad (4.11)$$

The effective thermal conductivity is estimated using the parallel model (Equation 3.47):

$$\overline{\lambda}_{eff} = \frac{\epsilon_s \lambda_s}{\lambda_{effo}} + \frac{\epsilon_o \lambda_l}{\lambda_{effo}} \overline{\epsilon}_l(t) + \frac{\epsilon_o \lambda_{go}}{\lambda_{effo}} \overline{\epsilon}_g(t) \overline{\lambda}_\varsigma \qquad (4.12)$$

## 4.3 The QUICK Scheme and the Finite-Difference Approximations

The Quadratic Upstream Interpolation for Convective Kinematics (QUICK) scheme, due to Leonard (1979), is used for the discretization of the advective terms and also for the values of variables at the cell boundaries. This scheme

> "... avoids the stability problems of central differencing while remaining free of the inaccuracies of numerical diffusion associated with upstream differencing .... The algorithm is based on a conservative control-volume formulation with cell wall values of each field variable written in terms of a quadratic interpolation using, in any one coordinate direction, the two adjacent nodal values together with the value at the next upstream node. This results in a convective differencing scheme with greater formal accuracy than central differencing while retaining the basic stable convective sensitivity property of upstream-weighted schemes ...." [Leonard, 1979]

For a uniform grid system, the QUICK scheme estimates the

values of a general variable f at j and j+1 in Figure 4.1 as

$$f_{j-1} = \frac{1}{2}(f_{jv}+f_{jv-1}) - \frac{1}{8}(f_{jv-1}-2f_{jv}+f_{jv-1})$$

and

$$f_j = \frac{1}{2}(f_{jv-1}+f_{jv}) - \frac{1}{8}(f_{jv-2}-2f_{jv-1}+f_{jv}) \quad .$$

The gradients at the two locations are given by

$$\left.\frac{\partial f}{\partial y}\right|_{j-1} = \frac{(f_{jv-1}-f_{jv})}{\Delta y}$$

and

$$\left.\frac{\partial f}{\partial y}\right|_{j} = \frac{(f_{jv}-f_{jv-1})}{\Delta y} \quad ,$$

respectively.

To improve accuracy, more grid refinement (clustering) is done at boundaries and in regions where the gradients of the field variables are large. Less refinement is required in the regions remote from the opening, and in the center of the domain where gradients are not large. At the boundaries there are not enough upstream grid points to enable the application of the more accurate QUICK scheme. Less accurate differencing methods, given in Appendix C, are used, and the only way to improve accuracy is by grid refinement. The grid is clustered at the inlet (including the edge of the opening) and around the line of symmetry because the pressure, the concentration, and the temperature gradients are expected to be high in these regions.

To accommodate a variable (non-uniform or clustered) grid system, the following modifications have been made (See Figure 4.1):

$$f_{j-1} = \frac{1}{2}(f_{jv}+f_{jv-1}) - \frac{q}{3}\left[\left(\frac{d_3}{d_2}\right)f_{jv-1} - \left(\frac{d_3}{d_2}+\frac{d_3^2}{d_1 d_2}\right)f_{jv} + \left(\frac{d_3^2}{d_1 d_2}\right)f_{jv-1}\right]$$

and

$$f_j = \frac{1}{2}(f_{jv-1} + f_{jv}) - \frac{q}{3}\left[\left(\frac{d_1}{d_4}\right) f_{jv} - \left(\frac{d_1}{d_4} + \frac{d_1^2}{d_4 d_5}\right) f_{jv-1} + \left(\frac{d_1^2}{d_4 d_5}\right) f_{jv-2}\right]$$

where $d_1 = \bar{y}_{jv} - \bar{y}_{jv-1}$ ;

$d_2 = \bar{y}_{j-1} - \bar{y}_j$ ;

$d_3 = \bar{y}_{jv-1} - \bar{y}_{jv}$ ;

$d_4 = \bar{y}_j - \bar{y}_{j-1}$ ;

$d_5 = \bar{y}_{jv-1} - \bar{y}_{jv-2}$ ;

$d_6 = \bar{y}_{j-2} - \bar{y}_{j-1}$

From the geometric property of the parabola, that the slope half-way between two points is equal to the slope of the chord joining the two points,

$$\left.\frac{\partial f}{\partial y}\right|_{jv} \approx \frac{(f_{j-1} - f_j)}{d_2}$$

The approximations

$$\left.\frac{\partial f}{\partial y}\right|_{j-1} \approx \frac{(f_{jv-1} - f_{jv})}{d_3}$$

and

$$\left.\frac{\partial f}{\partial y}\right|_{j} \approx \frac{(f_{jv} - f_{jv-1})}{d_1}$$

are accurate when j+1 is midway between jv+1 and jv, and j is midway between jv and jv-1. These conditions are not fulfilled in a non-uniform (or clustered) grid system. To minimise errors that would arise from such a situation, grid refinement is done in blocks. That is, the grid sizes are kept uniform within a region (or block), but the sizes may be different for different regions (or blocks). In this way, any errors due to grid non-uniformity are limited to the boundaries of the refinement blocks, which maintains high accuracy within each

block.

The constant q is selected to improve the accuracy or to alter the numerical dissipation/dispersion characteristics of the scheme. The value of q used in Leonard's uniform grid system is 0.375, so that

$$\frac{q}{3} = \frac{1}{8}$$

This value for q is said to be effective for steady or quasi-steady flows [Fletcher, Volume 2, 1988, pg 346].

The finite difference approximations (FDAs) for a grid cell whose center is located at (iv,jv) in Figure 4.1 are then written as shown below.

Mass Conservation:

$$\begin{aligned} &\frac{1}{(\bar{x}_{i-1}-\bar{x}_i)}\left[\bar{\rho}_{g,i-1}\bar{u}_{i-1} - \bar{\rho}_{g,i}\bar{u}_i\right] \\ &+ \frac{1}{(\bar{y}_{j-1}-\bar{y}_j)}\left[\bar{\rho}_{g,j-1}\bar{v}_{j-1} - \bar{\rho}_{g,j}\bar{v}_j\right] \\ &+ \frac{D_{vo}\Delta C}{V_o D}\bar{m}_{(iv,jv)} = 0 \end{aligned} \tag{4.13}$$

Momentum equations (Darcy's law):

$$\bar{u}_i = -\frac{K\Delta P}{\mu_o V_o D}\frac{1}{\bar{\mu}_{g,i}}\left.\frac{\partial \bar{p}}{\partial \bar{x}}\right|_i \tag{4.14}$$

$$\bar{u}_{i-1} = -\frac{K\Delta P}{\mu_o V_o D}\frac{1}{\bar{\mu}_{g,i-1}}\left.\frac{\partial \bar{p}}{\partial \bar{x}}\right|_{i-1} \tag{4.15}$$

$$\bar{v}_j = -\frac{K\Delta P}{\mu_o V_o D}\frac{1}{\bar{\mu}_{g,j}}\left.\frac{\partial \bar{p}}{\partial \bar{y}}\right|_j \tag{4.16}$$

$$\bar{v}_{j-1} = -\frac{K\Delta P}{\mu_o V_o D}\frac{1}{\bar{\mu}_{g,j-1}}\left.\frac{\partial \bar{p}}{\partial \bar{y}}\right|_{j-1} \tag{4.17}$$

The FDA for the pressure distribution in the flow field is obtained by substituting for velocities in the mass conservation equation (4.13) using the momentum equations (Equations 4.14 to 4.17). This gives

$$\begin{aligned}
&\frac{\bar{\rho}_{g,i-1}}{(\bar{x}_{i-1}-\bar{x}_i)}\left(-\frac{K\Delta P}{\mu_o V_o D}\right)\frac{1}{\bar{\mu}_{g,i-1}}\left.\frac{\partial \bar{p}}{\partial \bar{x}}\right|_{i-1} \\
&- \frac{\bar{\rho}_{g,i}}{(\bar{x}_{i-1}-\bar{x}_i)}\left(-\frac{K\Delta P}{\mu_o V_o D}\right)\frac{1}{\bar{\mu}_{g,i}}\left.\frac{\partial \bar{p}}{\partial \bar{x}}\right|_{i} \\
&+ \frac{\bar{\rho}_{g,j-1}}{(\bar{y}_{j-1}-\bar{y}_j)}\left(-\frac{K\Delta P}{\mu_o V_o D}\right)\frac{1}{\bar{\mu}_{g,j-1}}\left.\frac{\partial \bar{p}}{\partial \bar{y}}\right|_{j-1} \\
&- \frac{\bar{\rho}_{g,j}}{(\bar{y}_{j-1}-\bar{y}_j)}\left(-\frac{K\Delta P}{\mu_o V_o D}\right)\frac{1}{\bar{\mu}_{g,j}}\left.\frac{\partial \bar{p}}{\partial \bar{y}}\right|_{j} \\
&+ \frac{D_{vo}\Delta C}{V_o D}\bar{\dot{m}}_{(iv,jv)} = 0
\end{aligned} \tag{4.18}$$

The FDA for the vapour conservation equation is

$$\begin{aligned}
&\frac{V_o D}{D_{vo}}\bar{\rho}_{g,i}\bar{u}_i\left.\frac{\partial \bar{C}}{\partial \bar{x}}\right|_{iv} + \frac{V_o D}{D_{vo}}\bar{\rho}_{g,j}\bar{v}_j\left.\frac{\partial \bar{C}}{\partial \bar{y}}\right|_{jv} \\
&- \frac{1}{(\bar{x}_{i-1}-\bar{x}_i)}\left[\bar{D}_{v,i-1}\bar{\rho}_{g,i-1}\left.\frac{\partial \bar{C}}{\partial \bar{x}}\right|_{i-1} - \bar{D}_{v,i}\bar{\rho}_{g,i}\left.\frac{\partial \bar{C}}{\partial \bar{x}}\right|_{i}\right] \\
&- \frac{1}{(\bar{y}_{j-1}-\bar{y}_j)}\left[\bar{D}_{v,j-1}\bar{\rho}_{g,j-1}\left.\frac{\partial \bar{C}}{\partial \bar{y}}\right|_{j-1} - \bar{D}_{v,j}\bar{\rho}_{g,j}\left.\frac{\partial \bar{C}}{\partial \bar{y}}\right|_{j}\right] \\
&- \Delta C\bar{C}_{(iv,jv)}\bar{\dot{m}}_{(iv,jv)} + (1-C_{out})\bar{\dot{m}}_{(iv,jv)} = 0
\end{aligned} \tag{4.19}$$

For thermal energy, the FDA for the conservation equation is

$$\frac{V_o D}{\alpha_{effo}} \bar{\rho}_{g,i} \bar{C}_{pg,i} \bar{u}_i \left.\frac{\partial \bar{T}}{\partial \bar{x}}\right|_{iv} + \frac{V_o D}{\alpha_{effo}} \bar{\rho}_{g,j} \bar{C}_{pg,j} \bar{v}_j \left.\frac{\partial \bar{T}}{\partial \bar{y}}\right|_{jv}$$
$$- \frac{1}{(\bar{x}_{i-1} - \bar{x}_i)} \left[ \bar{\lambda}_{eff,i-1} \left.\frac{\partial \bar{T}}{\partial \bar{x}}\right|_{i-1} - \bar{\lambda}_{eff,i} \left.\frac{\partial \bar{T}}{\partial \bar{x}}\right|_{i} \right]$$
$$- \frac{1}{(\bar{y}_{j-1} - \bar{y}_j)} \left[ \bar{\lambda}_{eff,j-1} \left.\frac{\partial \bar{T}}{\partial \bar{y}}\right|_{j-1} - \bar{\lambda}_{eff,j} \left.\frac{\partial \bar{T}}{\partial \bar{y}}\right|_{j} \right] \qquad (4.20)$$
$$- h_{vap} \frac{D_{vo}}{\alpha_{effo} C_{pgo}} \frac{\Delta C}{\Delta T} \bar{m}_{(iv,jv)} = 0$$

The pressure, concentration, and temperature gradients in Equations 4.18, 4.19, and 4.20, respectively, are expanded either by the QUICK scheme or the appropriate boundary approximations (Appendix C), then P, C, or T is made the subject and solved for accordingly.

The two-dimensional FDA for the condensation rate, based on SMARC, is

$$\bar{m}_{(iv,jv)} = \frac{D^2}{D_{vo} \rho_{go} \Delta C} \frac{V_o \rho_{vo}}{D} \times$$
$$\left[ \frac{(\bar{\rho}_{v,i} \bar{u}_i - \bar{\rho}_{sv}|_{(iv,jv)} \bar{u}_{i-1})}{(\bar{x}_{i-1} - \bar{x}_i)} \right. \qquad (4.21)$$
$$\left. + \frac{(\bar{\rho}_{v,j} \bar{v}_j - \bar{\rho}_{sv}|_{(iv,jv)} \bar{v}_{j-1})}{(\bar{y}_{j-1} - \bar{y}_j)} \right]$$

where $\bar{\rho}_{v,i} = \frac{\rho_{go}}{\rho_{vo}} \bar{\rho}_{g,i}(\Delta C \bar{C}_i + C_{out})$ ,

$$\bar{\rho}_{v,j} = \frac{\rho_{go}}{\rho_{vo}} \bar{\rho}_{g,j}(\Delta C \bar{C}_j + C_{out})$$

(since $\rho_v = C\rho_g$),

and, $\bar{\rho}_{sv}|_{(iv,jv)} = \frac{P_{sv}|_{(iv,jv)}}{\rho_{vo} R_v T_{(iv,jv)}}$

(where $T_{(iv,jv)} = \Delta T \bar{T}_{(iv,jv)} + T_{out}$).

The details of the finite difference approximations for all the boundary types encountered in this project are presented in Appendix C.

## 4.4 The Quasi-steady Numerical Solution Procedure

There are eleven unknown main variables. These are $\rho_g$, $\rho_v$, u, v, T, P, $P_a$, $P_v$, $\dot{m}$, $\epsilon_l$ and $\epsilon_g$.

The eleven equations used to solve for these unknowns are:

(1) the vapour concentration equation (4.2);

(2) the energy equation (4.3);

(3) two Darcy equations (4.4 and 4.5);

(4) four thermodynamic relations (Equations 4.7 to 4.10);

(5) the condensation rate equation (SMARC) (Equation 4.21);

(6) the liquid volume fraction equation (3.31); and

(7) the volumetric constraint (4.6).

The flow chart (Figure 4.2) summarises the sequence in which these simultaneous equations and relations are executed. The equations and other relations in non-dimensional forms are

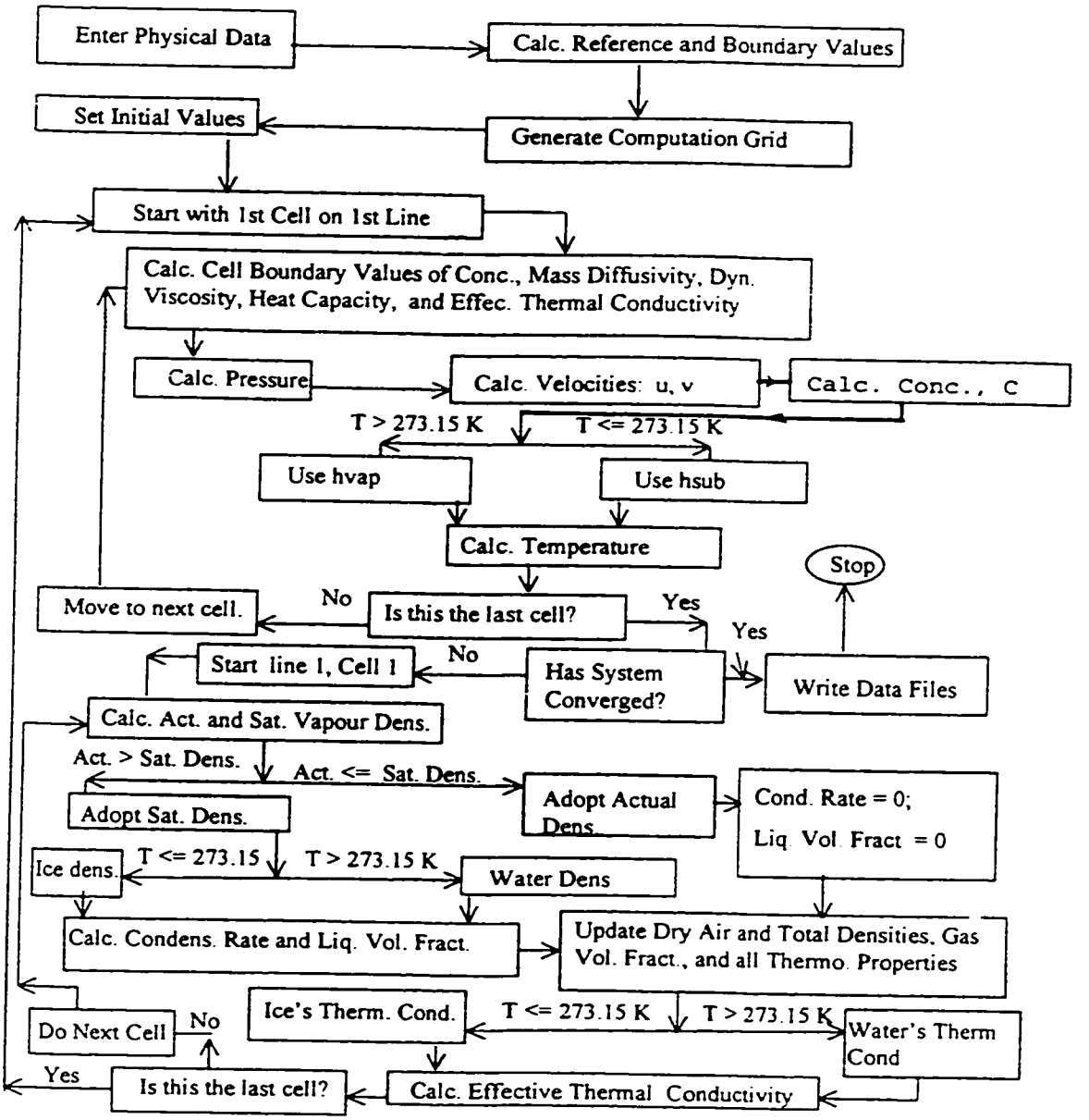


Figure 4.2 : Solution Sequence for Two-dimensional Simultaneous Heat and Mass Transfer Equations.

solved iteratively with successive under-relaxation. (A relaxation factor of 0.9 was used throughout.) The iteration process continues until the pre-set global convergence criteria, discussed later in this section are met.

The steps in the solution process are: (1) input of the physical data; (2) computation of the reference values (from Section B.1); (3) computation of the controlling parameters (from Section B.3); (4) calculation of the boundary values (from Section B.4); and, (5) the "manual" generation of the computation grid.

The initial values are set as follows:

(1) Pressure, temperature, and concentration profiles are made linear based on the inlet and exit values;

(2) all thermophysical coefficients are set to their reference values;

(3) the total density throughout the field is set constant and equal to the value at the inlet;

(4) the gas phase volume fractions are all made equal to the porosity; and

(5) the entire field is assumed to be dry (i.e., the liquid volume fractions and the condensation rates are all set equal to zero).

For the first cell on the first horizontal grid line:

(1) Calculate the values of C, $D_v$, $\mu$, $\rho_g$, $C_{pg}$, and $\lambda_{eff}$ on the grid cell boundaries using the relations provided in Sections 4.3 and 3.6;

(2) Solve for the total pressure from the pressure distribution equation (4.18);

(3) Calculate the cell velocities from Equations 4.14 to 4.17;

(4) Calculate the vapour concentration from Equation 4.19;

(5) If the current cell temperature, T, is greater than 273.15 K, use $h_{vap}$ from Equation 3.48 (otherwise use $h_{sub}$ from Equation 3.49) in Equation 4.20 to solve for the updated value of T.

(6) Repeat the calculations in (1) to (5) for the second up to the last cell on the line (in succession). Do the same computations for the cells on the second line and proceed until the last cell on the last line is covered.

The global flow quantities are calculated using the formulae given in Equations 4.22 to 4.29, and the global balances are checked as shown in Equations 4.30 to 4.32.

The moisture distribution and the coefficients are then updated using the latest values of the field variables. From the first cell on the first line to the last cell on the last line, in succession as before, the following computations are carried out:

(7) The computed vapour density ($\rho_v$) is given by the product of the total density ($\rho_g$) and the concentration (C), while the saturation vapour density ($\rho_{sv}$) is obtained using the vapour pressures calculated from Equations 3.28 and 3.29. If $\rho_v$ is greater than $\rho_{sv}$, then the latter density is adopted as the actual vapour density and the condensation rate is calculated from Equation 4.21, otherwise the former density is adopted as the actual vapour density, and both the condensation rate and the liquid volume fraction are set to zero.

(8) If there is condensation in the cell and the temperature is above 273.15 K, then the density of water is used in the non-dimensional form of Equation 3.31 to obtain the liquid volume fraction. The density of ice is used when the temperature is 273.15 K and below.

(9) The volume fraction of the gaseous components is obtained

from Equation 4.6.

(10) The density of dry air is computed from Equation 4.8 after obtaining the partial pressure of water vapour from Equation 4.9 and the partial pressure of dry air from Equation 4.7.

(11) Equation 4.10 gives the total density of the moist air.

(12) Equations B.82, B.83, and B.84 are used to calculate the specific heat capacities of dry air, water vapour and moist air, respectively.

(13) Vapour diffusivity in medium is given by Equation B.85.

(14) Viscosities of dry air, water vapour, and moist air are calculated from Equations B.86, B.87, and B.90, respectively.

(15) Thermal conductivities for dry air, water vapour, and moist air are obtained using Equations B.91, B.92, and B.93, respectively. These thermal conductivities are combined in Equation 4.12 to determine the effective thermal conductivity. (The thermal conductivity of water is used if the cell temperature is above 273.15 K ($0^{o}C$), otherwise the value for ice is used.)

With the updated coefficients and thermodynamic values, the computational procedure is repeated starting from level (1).

After each iteration, the global conservation of heat and mass is checked. This is done by comparing the flowrates at inlet and exit. Condensation rates and latent heats are also factored into the arithmetic. The flowrates, moisture condensation and latent heats are computed as shown below. The recorded flowrates are double the values obtained from the computations which are based on half the domain.

At the inlet (j = 1), the bulk air flowrate, $Q_g$, is

$$Q_{g,in} = (\rho_{go} V_o D) \sum_{i=1}^{k_3} \overline{\rho}_{g,j} \overline{v}_j (\overline{x}_{i-1} - \overline{x}_i) \tag{4.22}$$

($k_3$ is the number of grid cells within the opening)

At the outlet (j = M+1), the bulk air flowrate is

$$Q_{g,out} = (\rho_{go} V_o D) \sum_{i=1}^{N-1} \overline{\rho}_{g,j-1} \overline{v}_{j-1} (\overline{x}_{i-1} - \overline{x}_i) \tag{4.23}$$

(M and N are the number of interior or non-boundary cells in the y and x directions, respectively.)

At the inlet (j = 1), the total vapour flowrate, $Q_v$, is given by

$$\begin{aligned} Q_{v,in} = & \sum_{i=1}^{k_3} \left[ (\rho_{go} V_o D) (\Delta C \overline{C}_j + C_{out}) \overline{\rho}_{g,j} \overline{v}_j (\overline{x}_{i-1} - \overline{x}_i) \right] \\ & - \sum_{i=1}^{k_3} \left[ (\rho_{go} D_{vo} \Delta C) \overline{\rho}_{g,j} \overline{D}_{v,j} \left. \frac{\partial \overline{C}}{\partial \overline{y}} \right|_j (\overline{x}_{i-1} - \overline{x}_i) \right] \end{aligned} \tag{4.24}$$

At the outlet (j = M+1), the total vapour flowrate is

$$\begin{aligned} Q_{v,out} = & \sum_{i=1}^{N-1} \left[ (\rho_{go} V_o D) (\Delta C \overline{C}_{j-1} + C_{out}) \overline{\rho}_{g,j-1} \overline{v}_{j-1} (\overline{x}_{i-1} - \overline{x}_i) \right] \\ & - \sum_{i=1}^{N-1} \left[ (\rho_{go} D_{vo} \Delta C) \overline{\rho}_{g,j-1} \overline{D}_{v,j-1} \left. \frac{\partial \overline{C}}{\partial \overline{y}} \right|_{j-1} (\overline{x}_{i-1} - \overline{x}_i) \right] \end{aligned} \tag{4.25}$$

At the inlet (j = 1), the total thermal energy transfer rate, $H_s$, is

$$H_{s,in} = \sum_{i=1}^{k_3} \left[ (\rho_{go} C_{pgo} V_o D) (\Delta T \bar{T}_j + T_{out}) \bar{\rho}_{g,j} \bar{C}_{pg,j} \bar{v}_j (\bar{x}_{i-1} - \bar{x}_i) \right]$$
$$- \sum_{i=1}^{k_3} \left[ (\lambda_{effo} \Delta T) \bar{\lambda}_{eff,j} \left. \frac{\partial \bar{T}}{\partial \bar{y}} \right|_j (\bar{x}_{i-1} - \bar{x}_i) \right] \qquad (4.26)$$
$$- \sum_{i=k_3+1}^{N-1} \left[ \frac{\Delta T \, D}{\left( \frac{1}{h_n} + \frac{y_p}{\lambda_p} \right)} (\bar{T}_j - \bar{T}_{in}) (\bar{x}_{i-1} - \bar{x}_i) \right]$$

(The third term on the RHS of Equation 4.26 is the modification required to account for heat conduction through the plasterboard.)

At the outlet (j = M+1), the total thermal energy transfer rate is

$$H_{s,out} = \sum_{i=1}^{N-1} \left[ (\rho_{go} C_{pgo} V_o D) (\Delta T \bar{T}_{j-1} + T_{out}) \bar{\rho}_{g,j-1} \bar{C}_{pg,j-1} \bar{v}_{j-1} (\bar{x}_{i-1} - \bar{x}_i) \right]$$
$$- \sum_{i=1}^{N-1} \left[ (\lambda_{effo} \Delta T) \bar{\lambda}_{eff,j-1} \left. \frac{\partial \bar{T}}{\partial \bar{y}} \right|_{j-1} (\bar{x}_{i-1} - \bar{x}_i) \right] \qquad (4.27)$$

The total condensation rate in the flow domain, $Q_c$, is obtained by the following summation process:

$$Q_c = \sum_{j=1}^{M-1} \sum_{i=1}^{N-1} \left[ \left( \frac{D_{vo} \rho_{go} \Delta C}{D^2} \times D^2 \right) \bar{m}_{(iv,jv)} (\bar{y}_{j-1} - \bar{y}_j) (\bar{x}_{i-1} - \bar{x}_i) \right] \qquad (4.28)$$

Note that iv = i and jv = j, numerically. But (iv,jv) refers to cell center coordinates, whereas i and j refer to cell boundary locations of the same cell for the staggered grid system.

The total latent heat rate, $H_L$, in the domain is given by

$$H_L = \sum_{j=1}^{M-1} \sum_{i=1}^{N-1} \left[ \left( h_{vap} \frac{D_{vo} \rho_{go} \Delta C}{D^2} \times D^2 \right) \bar{m}_{(iv,jv)} (\bar{y}_{j-1} - \bar{y}_j)(\bar{x}_{i-1} - \bar{x}_i) \right] \quad (4.29)$$

The global balances between inlet and exit are assessed as follows.

Bulk air:

$$R_g = \frac{(Q_{g,in} - Q_{g,out} - Q_c)}{Q_{g,in}} \times 100\% \quad (4.30)$$

Vapour:

$$R_m = \frac{(Q_{v,in} - Q_{v,out} - Q_c)}{Q_{v,in}} \times 100\% \quad (4.31)$$

Thermal energy:

$$R_h = \frac{(H_{s,in} - H_{s,out} + H_L)}{H_{s,in}} \times 100\% \quad (4.32)$$

The numerical schemes and procedures used aim to make the values of $R_g$, $R_m$, and $R_h$ as small as possible. Small values are an indication of the accuracy of the schemes used. During the initial stages of this research project it was established that if an inaccurate scheme was used in the discretization of the equations, no amount of grid refinement would improve the global balances. It was found that the control volume approach in combination with the QUICK scheme gave the best results. Hence these were adopted.

The rate of convergence during the iteration processes was controlled by a relaxation factor. Generally, a large factor should lead to faster convergence. However, for the highly non-linear systems of equations in this project it was found that factors greater than 1 almost always led to divergence and total collapse of the process. A factor of 0.9 proved to be a good compromise between the rate and the realisation of

convergence.

The values of $R_g$, $R_m$, and $R_h$ obtained were unpredictable for the different sets of boundary conditions, making it impossible to use them directly to set the convergence criteria. As mentioned before, the values of $R_g$, $R_m$, and $R_h$ are controlled by the numerical schemes and procedures used. For the control volume approach, in combination with the QUICK scheme, the values ranged between $10^{-8}$% and 2%. For example, in a given case, $R_g$ may be $10^{-8}$% when $R_m$ is 2%, and $R_h$ may fall somewhere between the two.

The convergence criterion was based on the deviations in the "R-values" from the previous iteration. The percentage change in each R between successive iterations was monitored and if the R with the largest change changed by less than $10^{-5}$%, then the iteration process was considered to have converged and was terminated.

To improve the results, the domain grid system was refined until no significant changes occurred in the global flowrate values at convergence. The details for each case are provided in the relevant sections.

A horizontal width must be provided for the computational half-domain. The vertical "boundary" defining this width must be located where the effect of the opening is not felt; that is, no heat or mass should cross this boundary in the ideal situation. At this boundary, the pressure, concentration, and temperature gradients in the horizontal direction are all set equal to zero.

The extent of the influence of the opening depends on the opening size and the pressure difference across the insulation. It was established that a half-domain width five times the thickness (or depth) of the insulation provided the desired conditions for the most extreme case considered in

this research project (i.e., an opening length of 40 mm with a pressure difference of 30 Pa, in the extreme). For this case, the gradients in the horizontal direction at the extreme right boundary were about $10^{-4}$ times the gradients at the opening. Hence it was decided that this was the horizontal distance at which to set the gradients to zero for all cases considered.

Darcy's law must apply everywhere in this variable-velocity field. To ensure that this condition was fulfilled, the cell Reynolds number for the cell with the highest absolute velocity was calculated and examined for each case. Any cases whose highest cell Reynolds numbers exceeded 1.0 would be discarded entirely. The cell at the edge of the opening always had the largest absolute velocity.

### 4.5 The "Quasi-transient" Numerical Solution Procedure

The literature review (Chapter 2) revealed that some field variables continue to change after the "quasi-steady-state" is realised in a transient analysis [Modi and Benner (1985, Part I), Wijeysundera (1992), and Hokoi and Kumaran (1993)]. This suggests that this state is just a temporary stage that lasts for a limited period. The ideal way to study the evolution of the field variables with time would be to use the transient forms of the governing equations. However, the stability requirements for systems with transient non-linear equations often dictate the use of very small time-steps, making the prediction of the effects of long-term moisture accumulation in the insulation a rather unproductive exercise. Tien and Vafai (1990) used a time-step of 17.9 seconds, while Chen et al. (1997a) used a time-step of 5 seconds. Most researchers have therefore proceeded only up to the quasi-steady stage, in spite of using the fully-transient formulation.

The second objective of this research project, stated in Chapter 2, is to establish a numerical procedure which can

accelerate the simulation exercise after the quasi-steady stage. The numerical procedure will be called the "Quasi-transient Solution Procedure".

After the quasi-steady stage has been reached, the liquid or frost content, through its influence on the effective thermal condutivity, appears to be the main driving force for the gradual changes that occur in the other field variables, and the quasi-transient procedure capitalises on this fact. In the procedure, the quasi-steady condensation/ablimation rates are assumed to prevail throughout the next time step (say, one hour), so that the total quantity and distribution of the condensate at the end of the time step is estimated simply by multiplying the rate at each location by the time step, then adding the products to the current moisture contents. The new local moisture contents and distribution, including the current profiles of all other field variables, are then fed into the simulation program and an iteration process is implemented. At the end of the iteration, new values for the field variables and transfer rates emerge. Each stage utilises the condensation rates and field variables obtained from the immediate previous stage. Figure 4.3 illustrates the "time-stepping" procedure for the quasi-transient method. In this way, the field variables and transfer rates can be tracked using big time steps. Two examples in Chapter 5 will verify the validity of this procedure.

To the best of the author's knowledge, this is the first time such a technique has been applied to finding the solution of a condensation problem.

The models and solution procedures developed in Chapters 3 and 4 will be validated in Chapter 5 using one semi-analytical and two experimental examples. All the three examples are investigations done by other researchers.

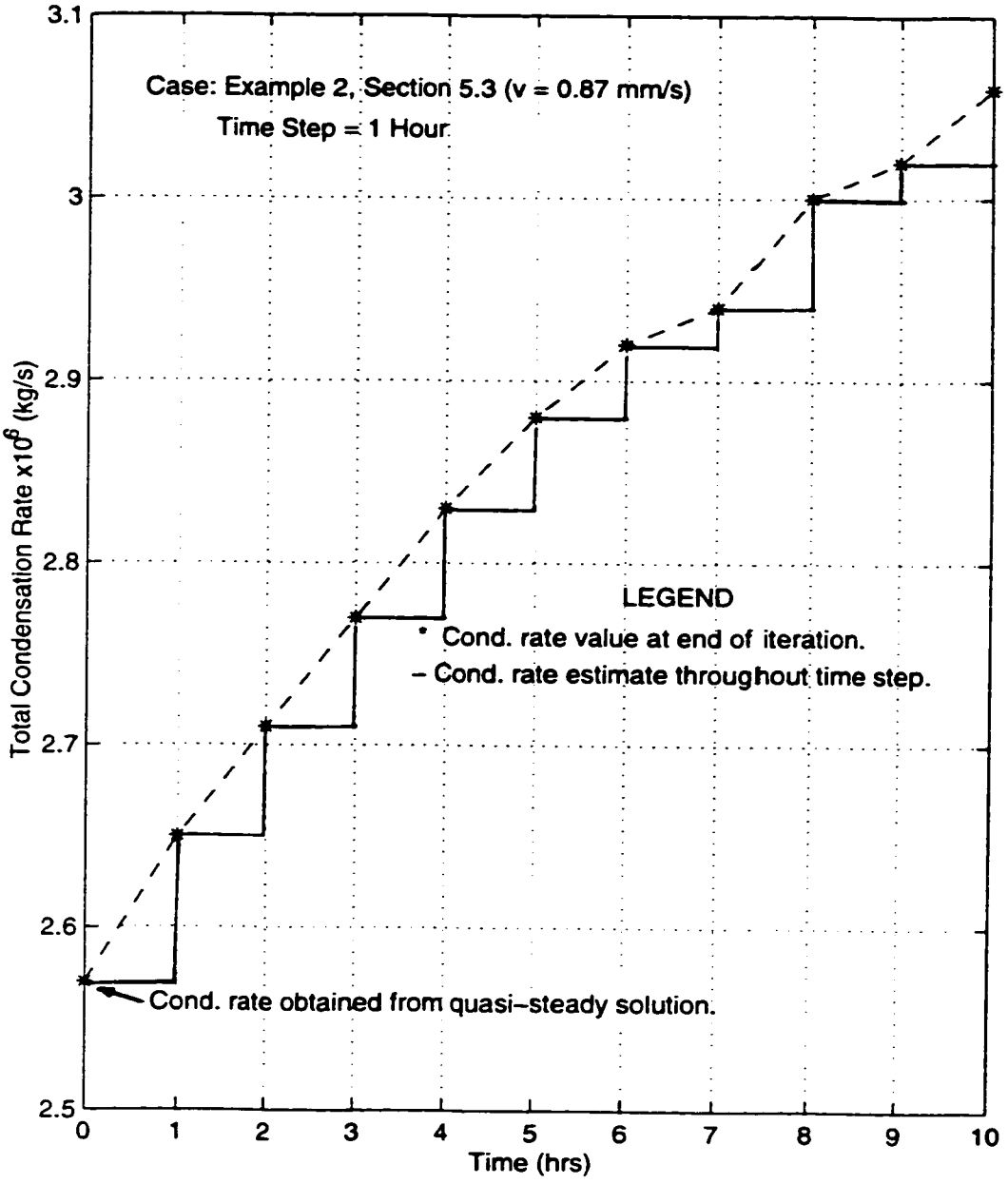


Figure 4.3. Time–stepping Procedure for the Quasi–transient Method.

# CHAPTER 5

# MODEL VALIDATION

## 5.1 Introduction

Three examples are considered for the validation of the mathematical and numerical models developed in Chapters 3 and 4:

(1) The first example is a one-dimensional problem which was solved semi-analytically by Ogniewicz and Tien (1981).

(2) The second example uses the one-dimensional versions of the model equations to simulate the experimental results obtained by Yu (1986).

(3) The third example uses the experimental results obtained by Chen, H., Besant, R.W., and Tao, Y. (1997) to illustrate the performance of SMARC in two dimensions, and shows that the model can be used to obtain the quasi-steady state transfer rates directly, i.e., without going through the traditional fully-transient formulation. (The condensation rates thus obtained can be used to predict long-term moisture accumulation in the insulation.)

## 5.2 Example 1 [Ogniewicz and Tien (1981)]: 1-D Quasi-steady Solution Using SMARC

### 5.2.1 Problem Description

This is a one-dimensional quasi-steady problem representing a porous slab exposed to different humid environments on both sides or boundaries as illustrated in Figure 5.1. The entire slab is initially dry, with unsaturated inlet and outlet conditions. The exit temperature is below the freezing point while the inlet temperature is above freezing point. The air velocity is creeping (i.e., $Re_K < 1$) and is assumed to be

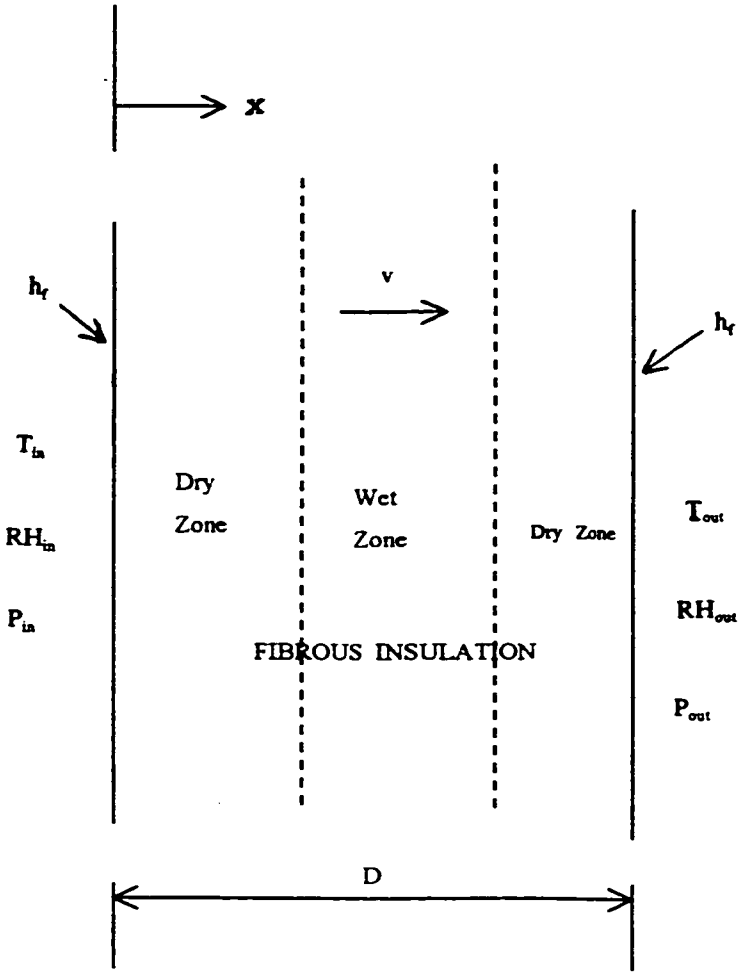


Figure 5.1 : Flow-field and Boundary Conditions for Example 1 [Ogniewicz and Tien, 1981].

constant. All thermophysical properties are assumed to be constant. At the low velocity considered, both the advective and diffusive terms are significant.

Ogniewicz and Tien used a semi-analytical method to solve the problem. The wet-dry interfaces were located by searching for locations in the flow domain where the saturation conditions were satisfied. Solutions in the dry or "no condensation" regions (where heat and mass are not coupled) were obtained analytically. In the wet region, where condensation occurred, the source term was eliminated between the energy and vapour conservation equations. Despite all the simplifying assumptions (e.g., constant velocity and constant thermophysical properties), the solution method used in the wet region was so complex that extending it to more realistic cases, such as variable velocities, variable thermophysical properties and two dimensions, would be extremely difficult. The reader is referred to the paper for details of the solution method.

This example was selected for consideration in this investigation not for validating the heat and mass transfer models and inputs, but mainly to show that, with the same inputs, SMARC is easier to apply than the semi-analytical solution method and yet it gives results which compare well with those obtained by Ogniewicz and Tien (1981).

### 5.2.2 Governing Equations and Other Relations

In the governing equations, the second derivatives of the diffusion and conduction terms have been modified to facilitate the application of the control volume method. That is, for a general function f, $\frac{d^2f}{dx^2}$ is written as $\frac{d}{dx}\left(\frac{df}{dx}\right)$.

The following relations are used in the conversion of variables from dimensional to non-dimensional forms:

$$\bar{x} = \frac{x}{D}; \quad \bar{T} = \frac{T - T_{out}}{\Delta T}; \quad \bar{C} = \frac{C - C_{out}}{\Delta C}; \quad \bar{\dot{m}} = \frac{D^2}{D_v \rho_g \Delta C}\dot{m};$$
$$\bar{\rho}_v = \frac{\rho_v - \rho_{v,out}}{\rho_{v,in} - \rho_{v,out}}; \quad \bar{\epsilon} = \frac{\epsilon}{\epsilon_o},$$

where $\Delta T = T_{in} - T_{out}$ and $\Delta C = C_{in} - C_{out}$.

The non-dimensional vapour conservation equation is then written as

$$PeLe \frac{d\bar{C}}{d\bar{x}} = \frac{d}{d\bar{x}}\left(\frac{d\bar{C}}{d\bar{x}}\right) - \bar{\dot{m}} \tag{5.1}$$

and the non-dimensional energy conservation equation is written as

$$Pe \frac{d\bar{T}}{d\bar{x}} = \frac{d}{d\bar{x}}\left(\frac{d\bar{T}}{d\bar{x}}\right) + \frac{h_{vap}\Delta C}{Le C_{pg}\Delta T}\bar{\dot{m}} \tag{5.2}$$

where $Pe = \frac{\rho_g C_{pg} V_o D}{\lambda_o}$ (5.3)

is the Peclet number, and

$$Le = \frac{\lambda_o}{\rho_g C_{pg} D_v} \tag{5.4}$$

is the Lewis number.

The finite difference approximations (FDA) adopted for the governing equations are based on the control volume formulation. A staggered grid system is used, with flow variables being computed at the cell centers (marked with "iv") while the fluxes and velocities are computed at the cell boundaries (marked with "i"). Refer to Section 4.3 for details.

The finite difference approximation for the vapour

conservation equation is

$$PeLe\left.\frac{d\bar{C}}{d\bar{x}}\right|_{iv} - \frac{1}{(\bar{x}_{i-1}-\bar{x}_i)}\left[\left.\frac{d\bar{C}}{d\bar{x}}\right|_{i-1} - \left.\frac{d\bar{C}}{d\bar{x}}\right|_{i}\right] + \bar{m}_{iv} = 0 \qquad (5.5)$$

and the FDA for the energy conservation equation is

$$Pe\left.\frac{d\bar{T}}{d\bar{x}}\right|_{iv} - \frac{1}{(\bar{x}_{i-1}-\bar{x}_i)}\left[\left.\frac{d\bar{T}}{d\bar{x}}\right|_{i-1} - \left.\frac{d\bar{T}}{d\bar{x}}\right|_{i}\right] - \frac{h_{vap}\Delta C}{LeC_{pg}\Delta T}\bar{m}_{iv} = 0 \qquad (5.6)$$

The advective gradients, $\left.\frac{d\bar{C}}{d\bar{x}}\right|_{iv}$ and $\left.\frac{d\bar{T}}{d\bar{x}}\right|_{iv}$, are estimated using the QUICK scheme [Leonard, 1979] which is discussed in Section 4.3. The condensation rate is determined from the one-dimensional form of Equation 3.30. That is, for a cell centred at "iv",

$$\dot{m}_{iv} = \frac{1}{x_{i-1}-x_i} V_o(\rho_{v,i}-\rho_{sv,iv}) \qquad (5.7)$$

In non-dimensional form, this becomes

$$\bar{m}_{iv} = \left[\frac{D^2}{D_v\rho_g\Delta C}\frac{V_o(\rho_{v,in}-\rho_{v,out})}{D}\right]\frac{(\bar{\rho}_{v,i}-\bar{\rho}_{sv,iv})}{(\bar{x}_{i-1}-\bar{x}_i)} \qquad (5.8)$$

Now $C = \frac{\rho_v}{\rho_g}$, (5.9)

i.e., $\Delta C \cdot \bar{C}_{iv} + C_{out} = \frac{(\rho_{v,in}-\rho_{v,out})\bar{\rho}_{v,iv}+\rho_{v,out}}{\rho_g}$

or $\bar{\rho}_{v,iv} = \frac{\rho_g(\Delta C\cdot\bar{C}_{iv}+C_{out})-\rho_{v,out}}{(\rho_{v,in}-\rho_{v,out})}$ (5.10)

Since $\rho_g$ is constant in the problem, $\bar{\rho}_v$ can be substituted for concentration $\bar{C}$ in the graphs of results, as was done by Ogniewicz and Tien (1981).

$\bar{\rho}_{sv}$ is calculated from the saturation condition as follows:

$$\rho_{sv} = \frac{P_{sv}}{R_v T_n}$$

where $T_n = \Delta T \cdot \bar{T}_{iv} + T_{out}$. (The computation of $P_{sv}$ is given in Section 3.5.6.)

Also, $\rho_{sv} = (\rho_{v,in} - \rho_{v,out})\,\bar{\rho}_{sv,iv} + \rho_{v,out}$.

Therefore, $(\rho_{v,in} - \rho_{v,out})\,\bar{\rho}_{sv,iv} + \rho_{v,out} = \frac{P_{sv}}{R_v T_n}$.

That is,

$$\bar{\rho}_{sv,iv} = \frac{\left(\frac{P_{sv}}{R_v T_n} - \rho_{v,out}\right)}{(\rho_{v,in} - \rho_{v,out})} \qquad (5.11)$$

Details of the FDAs for the convective boundary conditions are provided in Sections C.1 and C.5.

At the inlet,

$$-\left.\frac{d\bar{C}}{d\bar{x}}\right|_{\bar{x}=0} = LeBi\,(1-\bar{C}(0)) \qquad (5.12)$$

and

$$-\left.\frac{d\bar{T}}{d\bar{x}}\right|_{\bar{x}=0} = Bi\,(1-\bar{T}(0)) \qquad (5.13)$$

where the Biot number,

$$Bi = \frac{h_f D}{\lambda_o} \qquad (5.14)$$

At the outlet,

$$-\left.\frac{d\bar{C}}{d\bar{x}}\right|_{\bar{x}=1} = LeBi\,(\bar{C}(1)-0) \qquad (5.15)$$

and

$$-\left.\frac{d\bar{T}}{d\bar{x}}\right|_{\bar{x}=1} = Bi\,(\bar{T}(1)-0) \qquad (5.16)$$

It is essential to check for a global balance of the flow quantities in order to ascertain convergence. The global flowrates of air, heat, and mass are calculated as shown below. At the inlet cell, i=1 and iv=1. At the exit cell, i=M and iv=M (M is the number of grid cells in the flow domain).

For a constant total density ($\rho_g$) and a constant flow velocity ($V_o$), the bulk air flowrates at the inlet and the outlet are constant, and are given by

$$Q_{g,in} = Q_{g,out} = \rho_g V_o \ (kg/s\text{-}m^2) \tag{5.17}$$

The vapour flowrate at the inlet (i=1) is

$$\begin{aligned} Q_{v,in} &= \rho_g V_o C_i - \rho_g D_v \left.\frac{dC}{dx}\right|_i \\ &= \rho_g V_o (\Delta C \cdot \bar{C}_i + C_{out}) - \frac{\rho_g D_v \Delta C}{D} \left.\frac{d\bar{C}}{d\bar{x}}\right|_i \ (kg/s\text{-}m^2) \end{aligned} \tag{5.18}$$

At the outlet (i=M), the vapour flowrate is

$$\begin{aligned} Q_{v,out} &= \rho_g V_o C_{i-1} - \rho_g D_v \left.\frac{dC}{dx}\right|_{i-1} \\ &= \rho_g V_o (\Delta C \cdot \bar{C}_{i-1} + C_{out}) - \frac{\rho_g D_v \Delta C}{D} \left.\frac{d\bar{C}}{d\bar{x}}\right|_{i-1} \end{aligned} \tag{5.19}$$

At the inlet (i=1), the total heat energy transfer rate is given by

$$H_{s,in} = \rho_g C_{pg} V_o T_i - \lambda_o \left.\frac{dT}{dx}\right|_i$$

$$= \rho_g C_{pg} V_o (\Delta T \cdot \bar{T}_i + T_{out}) - \frac{\lambda_o \Delta T}{D} \left.\frac{d\bar{T}}{d\bar{x}}\right|_i \quad (W/m^2) \tag{5.20}$$

At the outlet (i=M), the total heat transfer rate is

$$H_{s,out} = \rho_g C_{pg} V_o T_{i-1} - \lambda_o \left.\frac{dT}{dx}\right|_{i-1} \quad (W/m^2)$$

$$= \rho_g C_{pg} V_o (\Delta T \cdot \bar{T}_{i-1} + T_{out}) - \frac{\lambda_o \Delta T}{D} \left.\frac{d\bar{T}}{d\bar{x}}\right|_{i-1} \tag{5.21}$$

The total rate of condensation in the flow domain is given by

$$Q_c = \sum_{iv=1}^{M} \dot{m}_{iv} \Delta x$$

$$= \frac{\rho_g D_v \Delta C}{D} \sum_{iv=1}^{M} \bar{m}_{iv} \Delta \bar{x} \tag{5.22}$$

and the total rate of latent heat generation is given by

$$H_L = h_{vap} \sum_{iv=1}^{M} \dot{m}_{iv} \Delta x$$

$$= h_{vap} \frac{\rho_g D_v \Delta C}{D} \sum_{iv=1}^{M} \bar{m}_{iv} \Delta \bar{x} \tag{5.23}$$

($h_{sub}$ is used in place of $h_{vap}$ in Equation 5.23 wherever the temperature is less or equal to 273.15 K.)

### 5.2.3 Physical Data

To gauge the performance of SMARC, by comparing with the results obtained by Ogniewicz and Tien, the same inputs must be used, regardless of their validity. The input parameters, given below, are all constant in this example.

$\rho_g = 1.2\ kg/m^3$;

$C_{pg} = 1000\ J/kg\text{-}K$;

$\epsilon_g = 0.98$;

$\epsilon_o = 1$;

$D_{va} = 2.5 \times 10^{-5}\ m^2/s$;

$D_v \approx \epsilon_g \times D_{va} = 2.45 \times 10^{-5}\ m^2/s$;

$\lambda_o = 0.05\ W/m\text{-}K$;

$\alpha_o = \dfrac{\lambda_o}{\rho_g C_{pg}} \approx 4.0 \times 10^{-5}\ m^2/s$;

$h_{vap} = 2.5 \times 10^6\ J/kg$;

$h_{sub} = 2.8 \times 10^6\ J/kg$;

$\rho_l = 1000\ kg/m^3$;

$\rho_{ice} = 920\ kg/m^3$;

$D = 0.15$ m;

$V_o = 5 \times 10^{-4}$ m/s;

$h_f = 10$ W/m$^2$-K;

$T_{in} = 30°C$ (303 K);

$T_{out} = -10°C$ (263 K);

$RH_{in} = 80\%$;

$RH_{out} = 20\%$;

$$Le = \frac{\alpha_o}{D_v} \approx 1.7;$$

$$Pe = \frac{V_o D}{\alpha_o} = 1.8;$$

$$Bi = \frac{h_f D}{\lambda_o} = 30.$$

In order to apply SMARC, a pressure difference must be applied across the domain. If it is assumed that this flow satisfies Darcy's law, then the equivalent pressure difference is determined from the velocity.

That is, $V_o = -\frac{K}{\mu}\frac{\Delta P}{D}$.

Taking a typical value for the permeability of fiberglass to be $K = 5 \times 10^{-10}\ m^2$ [Vafai and Whitaker (1986), Vafai and Tien (1989)], and the viscosity of air at about 15°C to be $\mu = 1.776 \times 10^{-5}\ kg/m\text{-}s$, the pressure difference across the insulation is $\Delta P = 2.664\ Pa$. The pressures, densities and concentrations for the boundaries are obtained using the relations in Section B.2.

### 5.2.4 Numerical Solution Procedure

The solution procedure for this example is similar to the procedure described in Section 4.4, except that this example uses constant coefficients, is one-dimensional, and comprises only two equations.

Convective boundaries (Equations 5.12 to 5.16) and 400 grid points were used in the numerical solution. Grid refinement to more than 400 yielded an insignificant change in the magnitudes of the global flowrates. For example, when the number of grid cells was increased from 400 to 450, the total condensation rate changed by less than 0.01%. The changes in the global air flowrate, the total heat transfer rate at the exit, and the total latent heat transfer rate were even

smaller. Two cases were considered; the "dry" solution included the vapour but ignored the source terms (i.e., the condensation rate and latent heat terms), while the "wet" case included the source terms. The former case was considered in order to compare the results with those in Ogniewicz and Tien's publication, otherwise the case is not physically realistic.

The solution procedure is summarised in Figure 5.2. To start the iteration process, for both the dry and wet cases, the field temperatures and the field concentrations were set equal to the values at the outlet. For the wet case only, the initial condensation rates and liquid volume fractions were set equal to zero in the entire domain.

The concentration and temperature fields are represented by Equations 5.5 and 5.6, respectively. The global rates are obtained from Equations 5.17 to 5.23, and the global balances are checked using Equations 4.30 to 4.32 in Section 4.4.

The computed vapour density (Equation 5.10) is compared to the saturation value (Equation 5.11) and the adoption of one of them follows the procedure described in Section 4.4. If need be, the condensation rate is calculated from Equation 5.8 and the liquid volume fraction rate from Equation 3.31. The convergence criteria are the same as for the general system, described in Section 4.4.

### 5.2.5 Comparison of Results

The results obtained using SMARC were compared to those obtained by Ogniewicz and Tien (1981), which they plotted as their Figure 2. For the figure, they arbitrarily allocated values to the Lewis number (2.0), the Peclet number (1.0) and the Biot number (infinity, or $10^6$ for computation purposes here). It will be shown later in this section that such an arbitrary allocation of values to the controlling parameters

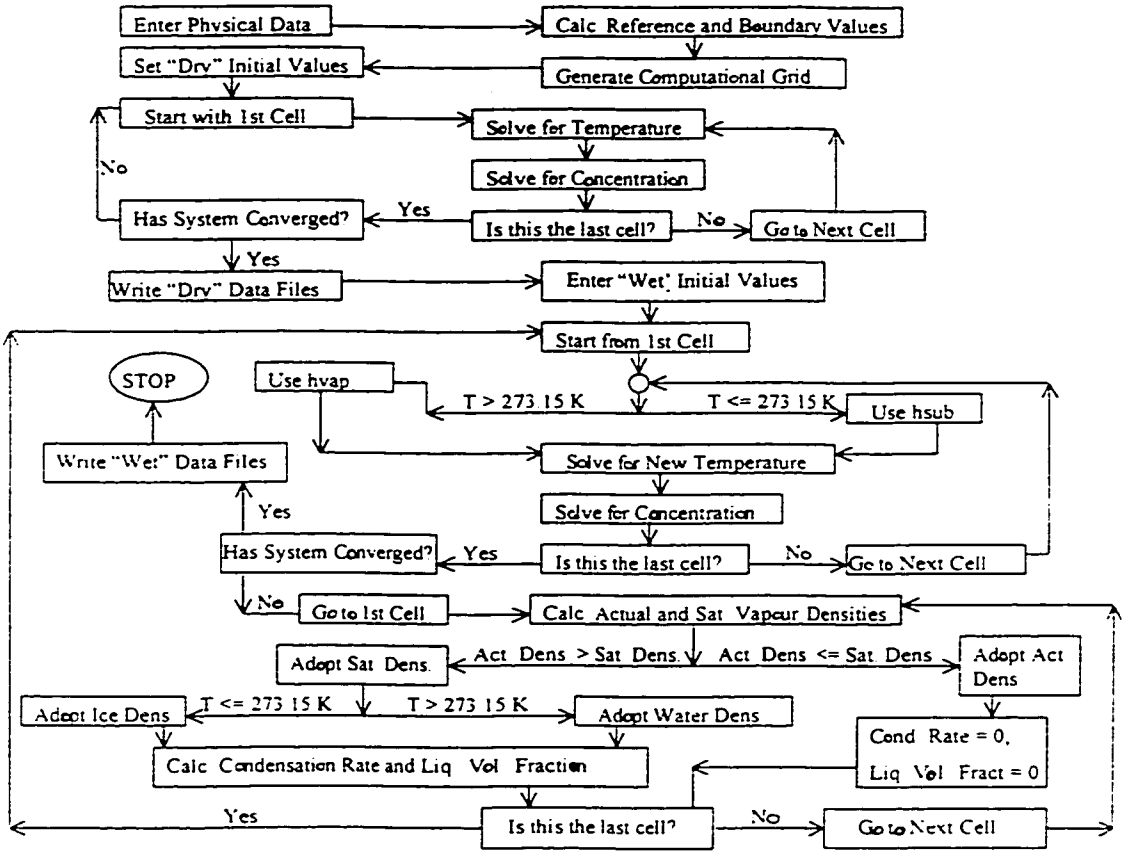


Figure 5.2 : Solution Sequence for the Simultaneous Heat and Mass Transfer Equations in Example 1 [Ogniewicz and Tien, 1981].

may lead to serious errors. The same arbitrary numbers have been used in this simulation in order to compare the results from SMARC with Ogniewicz and Tien's results. The appropriate values of the dimensionless numbers are thereafter applied to show what the results ought to have been.

Table 5.1 shows two sets of results; the "dry" or "no condensation" results are obtained with the assumption that the vapour is convected through the assembly without condensing, and the "wet" results take condensation into account. In the table, for both the dry and wet cases, there is a global imbalance of about 30% for the vapour. This imbalance is caused by the imposition of mismatched dimensionless numbers (i.e., Pe, Le, and Bi).

Figure 5.3 shows the profiles of the actual vapour densities, the saturation vapour densities, and the densities obtained for the dry or "no condensation" case for both SMARC and Ogniewicz and Tien's data. SMARC has, to an acceptable extent, reproduced Ogniewicz and Tien's results.

Figure 5.4 shows that:

(1) SMARC captures the three zones - a wet zone sandwiched between two dry zones - and very accurately locates the wet-dry interfaces; and

(2) the shapes of the two graphs are similar and the magnitudes of the condensation rates are close, except at the wet-dry interfaces where SMARC provides a more gradual change in the condensation rates while Ogniewicz and Tien's profile gives the impression that there exist discontinuities (i.e., sudden changes) in the condensation rates near the interfaces.

A comparison of the actual vapour density and the "no condensation" vapour density curves in Figure 5.3 shows that the condensation process takes water vapour from the gaseous phase, resulting in the curve dropping. During this

condensation process, latent heat energy is released and the temperature profile rises as shown by Figure 5.5.

Table 5.1. Computation Results Obtained with Ogniewicz and Tien's Dimensionless Parameters (Pe=1.0, Le=2.0, Bi=$10^6$).

| | Dry System | Wet System |
|---|---|---|
| Bulk Air Flowrate (x$10^{-6}$ kg/s-m$^2$) | 600 | 600 |
| Vapour Flowrate at Inlet (x$10^{-6}$ kg/s-m$^2$) | 13.2 | 13.7 |
| Vapour Flowrate at Exit (x$10^{-6}$ kg/s-m$^2$) | 9.1 | 6.2 |
| Total Condensation Rate (x$10^{-6}$ kg/s-m$^2$) | N/A | 3.4 |
| % of Total Inlet Vapour Condensed | N/A | 24.7 |
| Error in Moisture/Vapour Global Balance (%) | 31.0 | 29.9 |
| Heat Flux at Inlet (W/m$^2$) | 189.6 | 188.0 |
| Heat Flux at Exit (W/m$^2$) | 178.9 | 184.5 |
| Total Latent Heat Rate (W) | N/A | 8.4 |
| Error in Thermal Energy Balance (%) | 5.6 | 6.1 |

Table 5.2 contains the results obtained when the non-dimensional numbers are calculated from the appropriate relations; that is, the Peclet number (1.8) from Equation 5.3, the Lewis number (1.7) from Equation 5.4, and the Biot number

(30.0) from Equation 5.14. In Table 5.2, unlike in Table 5.1, the global balances of vapour and heat fluxes for both wet and dry cases have been achieved (almost!), the worst case being a difference of 0.69% between the inlet and outlet energy transfer rates for the wet system. For the wet system, the heat flux at the exit now exceeds the heat flux at the inlet as would be expected. It is also noted that 29.0% of the vapour which enters the system is condensed and the latent heat generated is 5.4% of the total heat flux at the exit.

Figures 5.6 to 5.8 compare profiles obtained with SMARC using Ogniewicz and Tien's values for dimensionless numbers to profiles obtained with SMARC using the "appropriate" values. There is a general shift of vapour density profiles (Figure 5.6) and temperature profiles (Figure 5.8) to the right due to the higher Peclet number. The exit values in both figures are now visibly above zero, this being an indication of convective boundary conditions. The much-reduced value of the Biot number is mainly responsible for the dramatic change in exit conditions. Increasing the Biot number makes the exit values drop, causing near-Dirichlet boundary conditions seen in Ogniewicz and Tien's profiles. At the inlet, increasing or decreasing the Biot number has the opposite effect; the inlet values increase when the Biot number is increased. The wet region for the balanced system (Figure 5.7) has been shifted to the right, and the peak condensation rate is higher than in the unbalanced case (Figure 5.4). There is more condensation in the balanced system (Table 5.2) than in the unbalanced system (Table 5.1).

Comparing the results in Table 5.1 to the results in Table 5.2 reveals how dramatically results can become distorted when a controlling parameter is arbitrarily varied - i.e., without due regard for other determining parameters.

Table 5.2. Computation Results Obtained with "Appropriate" Dimensionless Parameters (Pe=1.8, Le=1.7, Bi=30.0).

| | Dry System | Wet System | % Diff. |
|---|---|---|---|
| Bulk Air Flowrate ($x10^{-6}$ kg/s-$m^2$) | 600 | 600 | 0.0 |
| Vapour Flowrate at Inlet ($x10^{-6}$ kg/s-$m^2$) | 12.5 | 12.7 | +1.6 |
| Vapour Flowrate at Exit ($x10^{-6}$ kg/s-$m^2$) | 12.5 | 9.0 | -28.0 |
| Total Condensation Rate ($x10^{-6}$ kg/s-$m^2$) | N/A | 3.7 | N/A |
| % of Total Inlet Vapour Condensed | N/A | 29.0 | N/A |
| Error in Moisture/Vapour Global Balance (%) | 0.12 | 0.10 | N/A |
| Heat Flux at Inlet ($W/m^2$) | 185.9 | 184.9 | -0.54 |
| Heat Flux at Exit ($W/m^2$) | 185.9 | 194.0 | +4.36 |
| Total Latent Heat rate (W) | N/A | 10.5 | N/A |
| Error in Thermal Energy Balance (%) | 0.0 | 0.69 | N/A |

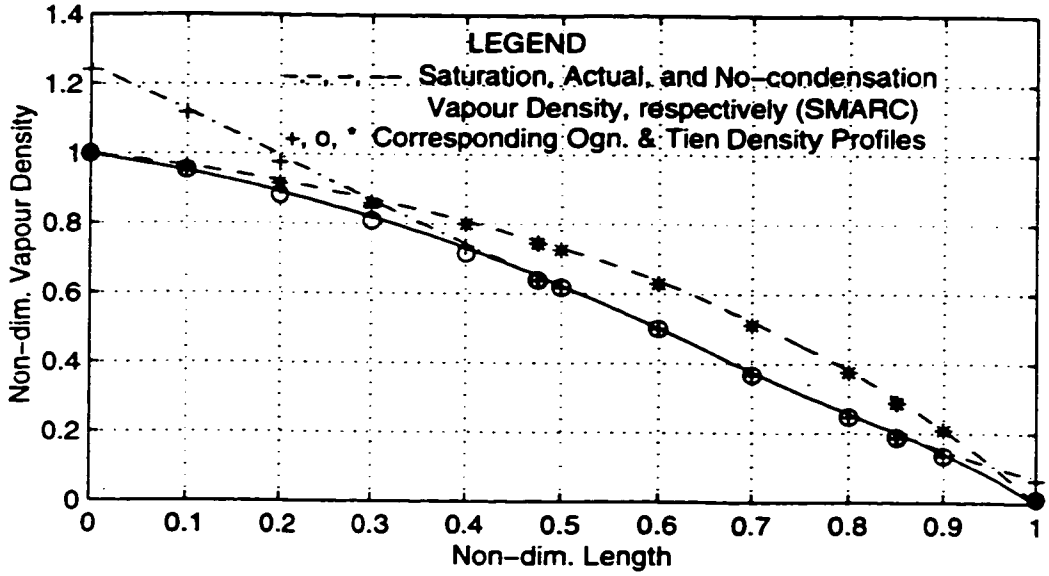


Figure 5.3. Vapour Density Profiles for Pe=1.0, Le=2.0, Bi=$10^6$.

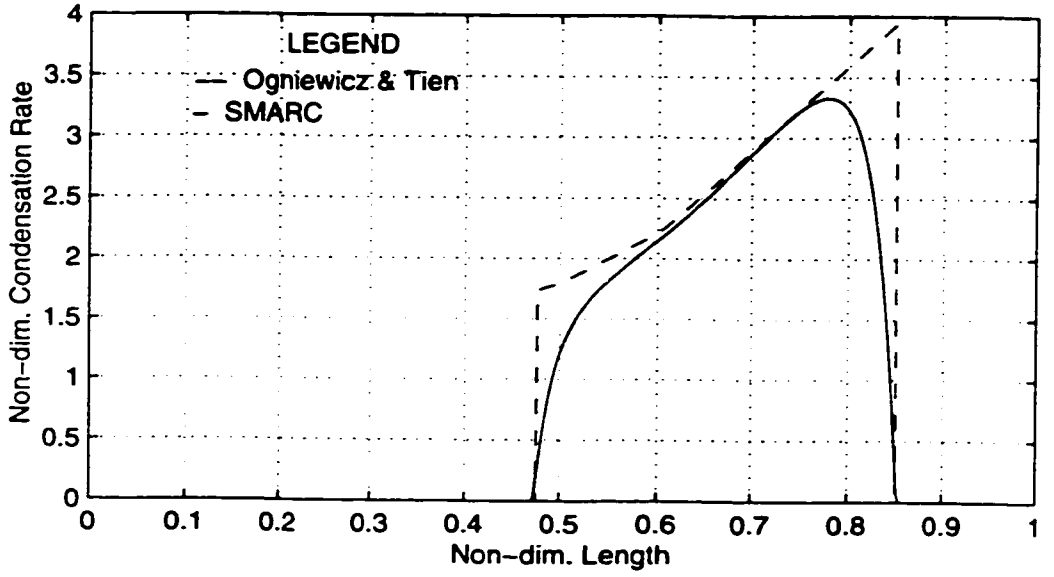


Figure 5.4. Condensation Rate Profiles for Pe=1.0, Le=2.0, Bi=$10^6$.

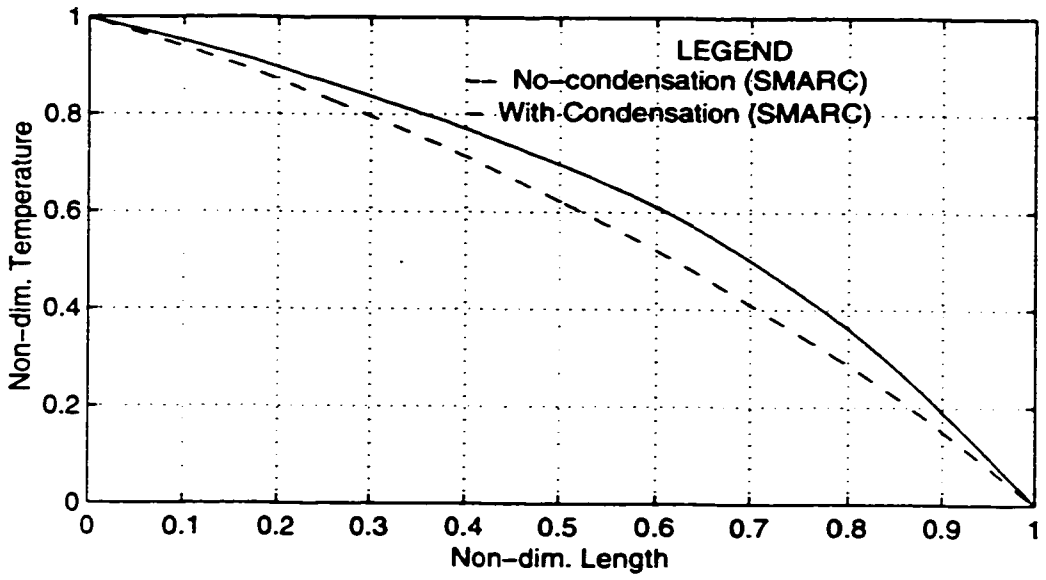


Figure 5.5. Temperature Profiles for Pe=1.0, Le=2.0, Bi=$10^6$.

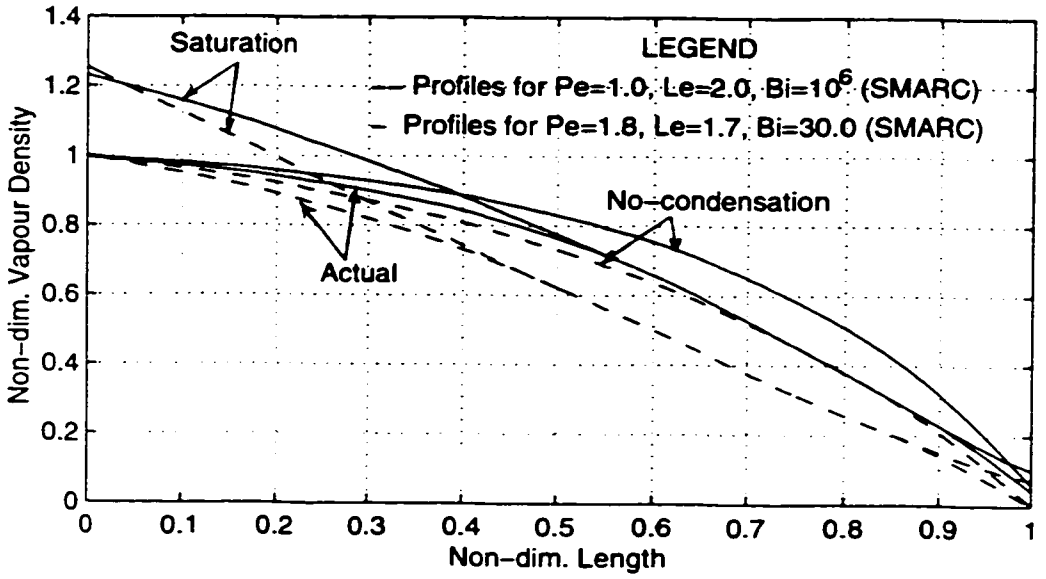


Figure 5.6. Density Profiles for Two Sets of Dimensionless Numbers.

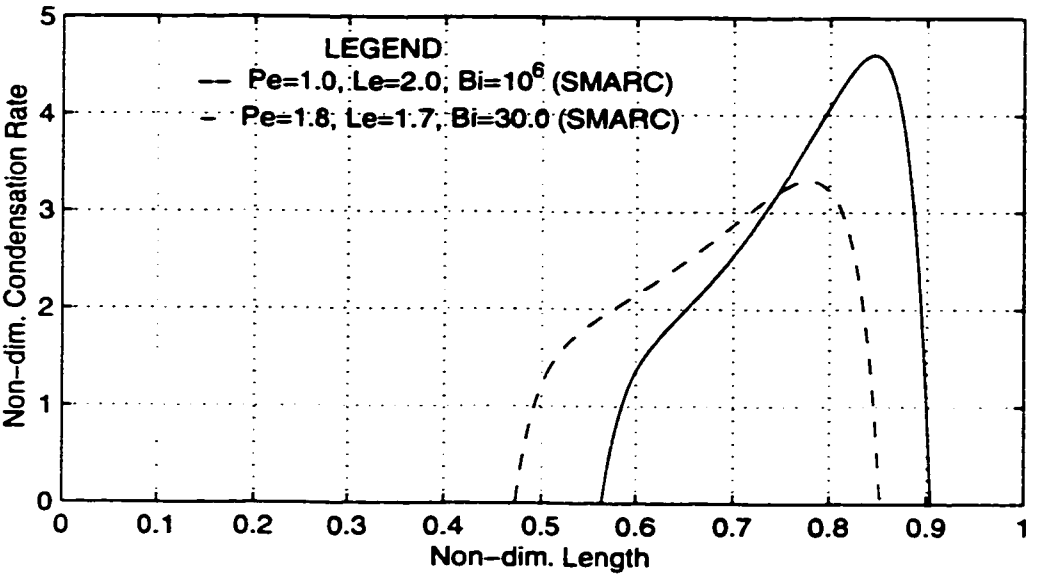


Figure 5.7. Condensation Rate Profiles for Two Sets of Dimensionless Numbers.

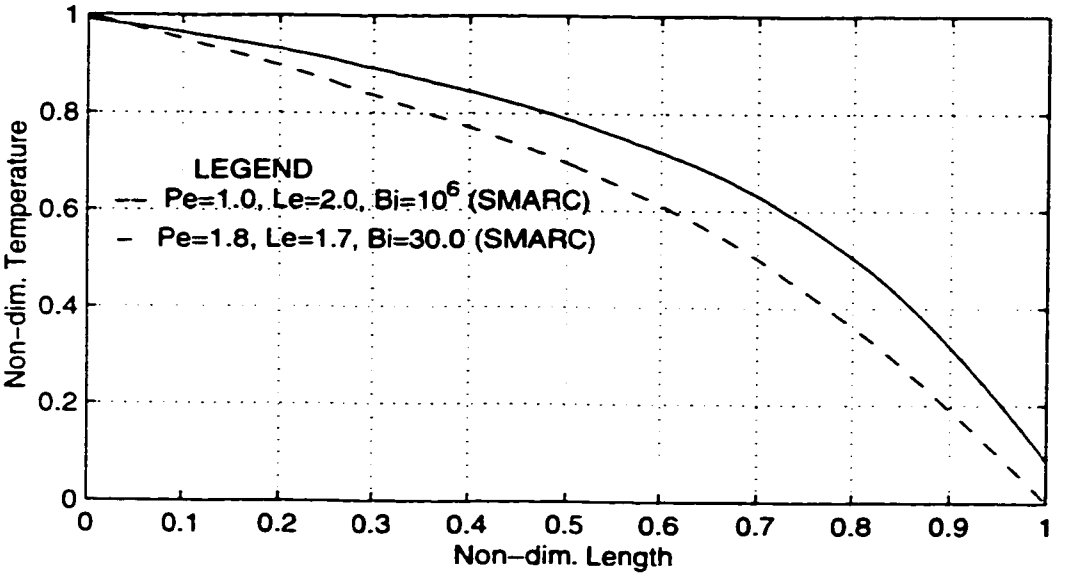


Figure 5.8. Temperature Profiles for Two Sets of Dimensionless Numbers.

### 5.2.6 Summary of Results

SMARC is an easy-to-use alternative to the semi-analytical solution method applied by Ogniewicz and Tien to this quasi-steady problem.

(1) The profiles of the actual vapour density, the saturation vapour density, and the "no condensation" vapour density have been reproduced accurately (Figure 5.3).

(2) The wet-dry interfaces have been accurately located (Figure 5.4).

(3) The condensation rate profile is remarkably similar in shape and magnitude to that obtained by Ogniewicz and Tien (1981). Minor differences occur near the wet-dry interfaces where SMARC presents a more gradual change in the condensation rate than Ogniewicz and Tien's results (Figure 5.4). Physically, what would be expected is a gradual change in the condensation rate from zero, not a step change.

(4) It is important to use physically-appropriate values for the dimensionless numbers. (Compare Figure 5.3 to 5.6 and Figure 5.4 to 5.7.)

## 5.3 Example 2 [Yu, R.C.H. (1986)]: 1-D Validation of SMARC and the Quasi-transient Procedure

### 5.3.1 Introduction

Yu (1986) carried out experimental investigations on transient moisture accumulation in a one-dimensional cellulose insulation slab. An exposed layer of cellulose was subjected to a temperature difference, a pressure difference, and a vapour concentration difference during the tests. "Cellulose insulation is manufactured from waste newsprint. It consists of short-fiber cellulosic material treated with chemicals to control flamability, fungi growth, corrosivity and odor emission. It is soft, fluffy and contains numerous minute air spaces to resist heat flow. Two types are available: loose-fill (for blowing and pouring) and spray-on. Its effective thermal conductivity is about 0.04 W/m-K at 24°C and the porosity is about 0.91." [Yu, 1986].

Yu found that during each test the accumulation of moisture in the insulation caused the temperature profile to decrease from the initial profile. Measurement of final temperatures showed that there was an inflection on the profile which occurred around the freezing point of water. It was observed that substantial moisture deposition occurred below the freezing point, and that the freezing point shifted towards the exit as the exfiltration rate was increased.

This example has been selected for simulation:

(1) to illustrate how SMARC and the quasi-transient procedure can be used to show the shift with time in the temperature profile, including the formation of inflections, towards the final experimental profile;

(2) to show that moisture accumulation rates obtained with SMARC can be used to make reasonable predictions of long-term total moisture contents in the insulation; and

(3) to show that moisture accumulation affects the total heat transfer rate at the exit.

### 5.3.2 Problem Description and Experimental Procedure

The flow-field and the boundary conditions for Yu's problem are shown schematically in Figure 5.9. The insulation test slab consisted of eight equal blocks or layers as shown in Figure 5.10. Each layer was 12.7 mm long with a volume of $3.66 \times 10^{-5}$ $m^3$ (i.e., with a cross-sectional area of $2.88 \times 10^{-3}$ $m^2$) and a dry weight of $1.46(\pm 0.01) \times 10^{-3}$ kg since the density of dry insulation was 40 $kg/m^3$. The data acquisition system used consisted of a MetraByte DASH-8 A-D Converter, a MetraByte Universal Expansion Interface (Model No. EXP-16) and an IBM PC. Seven equally-spaced thermocouple probes were inserted into the middle of one side of the test section "to measure the temperature profile across the cellulose insulation". The thermocouples were not calibrated, resulting in a temperature-measurement uncertainty of ±1 K with the DASH-8 equipment. The thermocouple positioning uncertainty was thought to be ±1 mm in the lower seven insulation layers and ±3 mm in the top layer. At the end of each test, a gravimetric analysis was carried out to determine the moisture content of each layer (in % by dry mass). Five tests were carried out for each of the four exfiltration rates; 0.4 ACH (Air Changes per Hour), 0.6 ACH, 0.9 ACH, and 1.2 ACH. The corresponding nominal velocities for the air change rates were 0.30 mm/s, 0.43 mm/s, 0.66 mm/s, and 0.87 mm/s. Measurements from the five tests were used to compute the mean and standard deviation of the moisture content for each exfiltration rate.

In the experiments, air was forced through the slab in one direction for a period specified for each of the four air exfiltration rates. Yu's intention was to convect the same quantity of air, with the same inlet relative humidity,

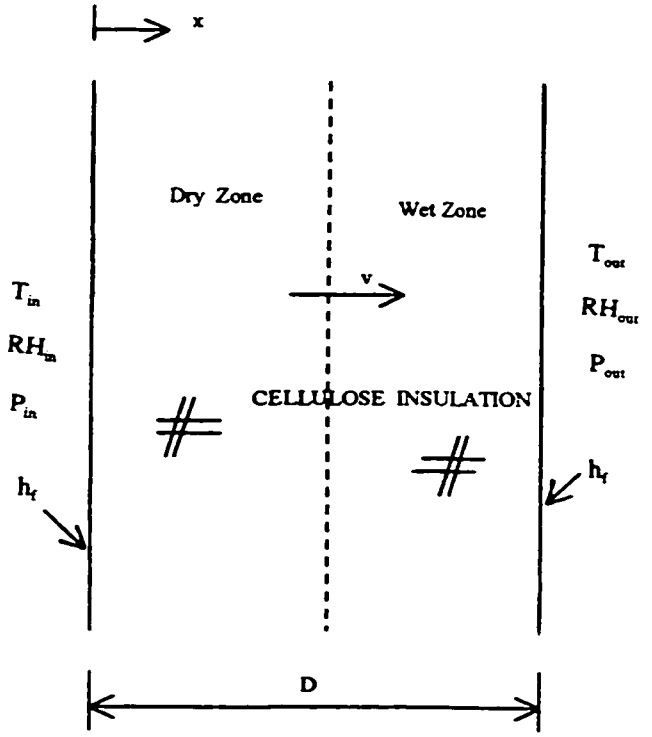


Figure 5.9 : Flow-field and Boundary Conditions for Example 2 [Yu, 1986].

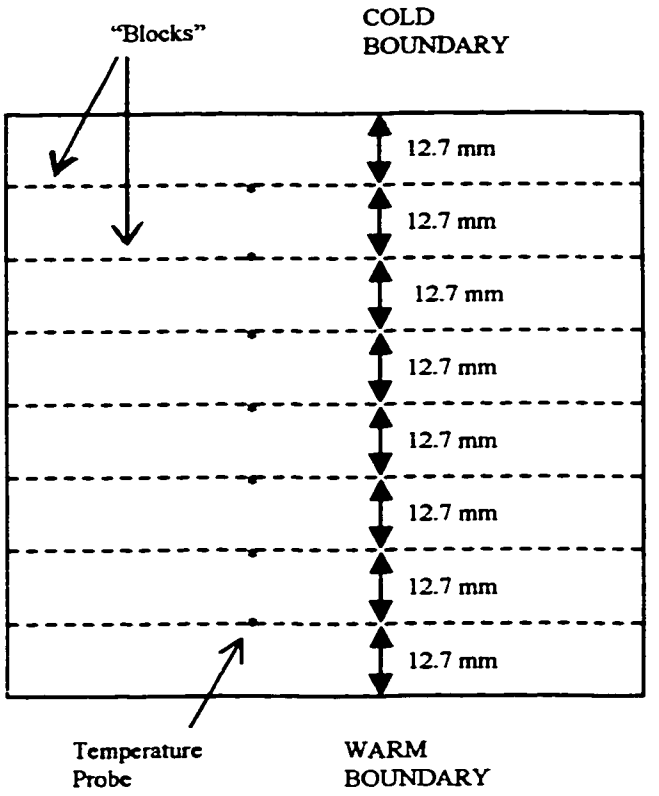


Figure 5.10 : Location of Temperature Probes in Example 2 [Yu, 1986].

through the test insulation, i.e.,

ACH x (time duration of the test) = constant.

"The main item of interest was to determine the effect of exfiltration rate on the moisture distribution and the rate of accumulation within the cellulose" [Yu, 1986]. The exfiltration rate was measured by a tracer gas technique where time decay of tracer gas concentration gave a direct measure of the exfiltration rate. The durations chosen to achieve the stated goal were as follows:

(1) 504 hours (21 days) for 0.4 ACH (i.e., a nominal velocity of 0.30 mm/s);

(2) 336 hours (14 days) for 0.6 ACH (i.e., a nominal velocity of 0.43 mm/s);

(3) 224 hours (9.3 days) for 0.9 ACH (i.e., a nominal velocity of 0.66 mm/s); and

(4) 168 hours (7 days) for 1.2 ACH (i.e., a nominal velocity of 0.87 mm/s).

The following boundary conditions were maintained for all the experiments: inlet temperature = 298 K; exit temperature = 243 K; inlet relative humidity = 40%; and the exit relative humidity = 100% (assumed).

The "initial" temperature readings were taken about 24 hours after the experiments were started. At the end of each test period, the final temperature readings were recorded. A gravimetric analysis was done to obtain the quantity and distribution of the moisture accumulated in the insulation. Yu did not record the rate of moisture accumulation, as this is a difficult measurement to do directly.

### 5.3.3 Numerical Simulation Procedure

In order to simulate Yu's experimental results:

(1) one-dimensional versions of the numerical model equations developed in Chapters 3 and 4 were used;

(2) the transient behaviour of the system was tracked using the new "quasi-transient" method discussed in Section 4.5;

(3) the thermophysical properties of moist air were varied fully with temperature and moisture content since preliminary investigations revealed that the results improved dramatically when the properties were varied;

(4) the boundary conditions for both heat and mass transfer were assumed to be forced-convective; and

(5) assuming Darcy flow conditions, the nominal velocities were used to calculate the approximate pressure differences across the flow domain, so that SMARC could be used to keep track of the moisture quantities and their distribution.

However, for the numerical procedure, the use of a constant pressure difference results in the variation of the velocity in the direction of flow, and the velocity profile shifting with time. The variations in the direction of flow occur because of the effect of temperature on the total air density. For mass to be conserved, a high air density due to a low temperature is compensated for by a low velocity; that is, $\rho_1 v_1 = \rho_2 v_2$. The velocity profile shifts with time because, as the temperature profile shifts, the temperature-dependent dynamic viscosity changes too, causing the velocity calculated from the Darcy equation to shift in the opposite direction to the temperature profile. This phenomenon will be revisited in Section 5.3.9.

The one-dimensional versions of the general two-dimensional equations and relations, developed in Chapters 3 and 4, are given below in non-dimensional form.

The mass continuity equation is:

$$\frac{d}{d\bar{x}}(\bar{\rho}_g \bar{u}) + \frac{D_{vo}\Delta C}{V_o D}\bar{m} = 0 \qquad (5.24)$$

The vapour conservation equation is:

$$\frac{V_o D}{D_{vo}}\bar{\rho}_g \bar{u}\frac{d\bar{C}}{d\bar{x}} - \frac{d}{d\bar{x}}\left(\bar{D}_v \bar{\rho}_g \frac{d\bar{C}}{d\bar{x}}\right) - \Delta C\,\bar{C}\bar{m} + (1-C_{out})\bar{m} = 0 \qquad (5.25)$$

The energy conservation equation is:

$$\frac{V_o D}{\alpha_{effo}}\bar{\rho}_g \bar{C}_{pg}\bar{u}\frac{d\bar{T}}{d\bar{x}} - \frac{d}{d\bar{x}}\left(\bar{\lambda}_{eff}\frac{d\bar{T}}{d\bar{x}}\right) - h_{vap}\frac{D_{vo}}{\alpha_{effo}C_{pgo}}\frac{\Delta C}{\Delta T}\bar{m} = 0 \qquad (5.26)$$

The Darcy "momentum" quation is:

$$\bar{u} = -\frac{K\Delta P}{\mu_o V_o D}\frac{1}{\bar{\mu}_g}\frac{d\bar{p}}{d\bar{x}} \qquad (5.27)$$

The pressure distribution equation is obtained by substituting the momentum equation (5.27) into the mass conservation equation (5.24) to obtain:

$$\frac{d}{d\bar{x}}\left(\frac{\bar{\rho}_g}{\bar{\mu}_g}\frac{d\bar{P}}{d\bar{x}}\right) - \frac{D_{vo}\mu_o}{K}\frac{\Delta C}{\Delta P}\bar{m} = 0 \qquad (5.28)$$

The condensation rate is given by SMARC:

$$\bar{m} = -\frac{V_o D}{D_{vo}} \frac{\rho_{vo}}{\rho_{go}} \frac{1}{\Delta C} \frac{d}{d\bar{x}} (\bar{\rho}_v \bar{u}) \tag{5.29}$$

The finite difference approximations for Equations 5.24 to 5.29 are based on the QUICK scheme discussed in Section 4.3. A staggered grid system is used.

Approximations for the forced-convective boundary conditions for the inlet and the exit are discussed in Sections C.1 and C.5, respectively.

At the inlet (i = 1), the heat flux is given by

$$-\lambda_{eff,i} \left.\frac{dT}{dx}\right|_i = h_{f,in}(T_{in} - T_i), \tag{5.30}$$

or

$$-\bar{\lambda}_{eff,i} \left.\frac{d\bar{T}}{d\bar{x}}\right|_i = Bi_{in}(1 - \bar{T}_i) \tag{5.31}$$

where $Bi = \frac{h_f D}{\lambda_{eff,o}}$ is the Biot number and $h_f$ is the forced-convective heat transfer coefficient in $W/m^2$-K.

At the exit (i = M+1), the heat flux is given by

$$-\lambda_{eff,i-1} \left.\frac{dT}{dx}\right|_{i-1} = h_{f,out}(T_{i-1} - T_{out}), \tag{5.32}$$

or

$$-\bar{\lambda}_{eff,i-1} \left.\frac{d\bar{T}}{d\bar{x}}\right|_{i-1} = Bi_{out}(\bar{T}_{i-1} - 0) \tag{5.33}$$

where M is the total number of grid cells.

From Equation 3.50,

$$\frac{h_f}{h_m} = \rho_g C_{pg}\left(\frac{\alpha_{eff}}{D_v}\right)^{\frac{2}{3}} = \rho_{go} C_{pgo} \overline{\rho}_g \overline{C}_{pg}\left(\frac{\alpha_{effo}}{D_{vo}} \frac{\overline{\lambda}_{eff}}{\overline{\rho}_g \overline{C}_{pg} \overline{D}_v}\right)^{\frac{2}{3}} \tag{5.34}$$

or

$$h_m = \frac{h_f}{\rho_{go} C_{pgo} \overline{\rho}_g \overline{C}_{pg}\left(\frac{\alpha_{effo}}{D_{vo}} \frac{\overline{\lambda}_{eff}}{\overline{\rho}_g \overline{C}_{pg} \overline{D}_v}\right)^{\frac{2}{3}}} \tag{5.35}$$

where $h_m$ is the forced-convective mass transfer coefficient in m/s.

At the inlet (i = 1), the vapour flux is given by

$$-D_{v,i} \left.\frac{dC}{dx}\right|_i = h_m (C_{in} - C_i), \tag{5.36}$$

or

$$-\left.\frac{d\overline{C}}{d\overline{x}}\right|_i = \frac{h_f D}{\lambda_{effo}} \frac{\alpha_{effo}}{D_{vo}} \frac{1}{\overline{\rho}_{g,i} \overline{C}_{pg,i} \overline{D}_{v,i}} \frac{(1-\overline{C}_i)}{\left(\frac{\alpha_{effo}}{D_{vo}} \frac{\overline{\lambda}_{eff,i}}{\overline{\rho}_{g,i} \overline{C}_{pg,i} \overline{D}_{v,i}}\right)^{\frac{2}{3}}} \tag{5.37}$$

At the exit (i = M+1), the vapour flux is given by

$$-D_{v,i-1} \left.\frac{dC}{dx}\right|_{i-1} = h_m (C_{i-1} - C_{out}), \tag{5.38}$$

or

$$-\left.\frac{d\bar{C}}{d\bar{x}}\right|_{i-1} = \frac{h_f D}{\lambda_{effo}} \frac{\alpha_{effo}}{D_{vo}} \frac{1}{\bar{\rho}_{g,i-1}\bar{C}_{pg,i-1}\bar{D}_{v,i-1}} \times$$

$$\frac{(\bar{C}_{i-1} - 0)}{\left(\frac{\alpha_{effo}}{D_{vo}} \frac{\bar{\lambda}_{eff,i-1}}{\bar{\rho}_{g,i-1}\bar{C}_{pg,i-1}\bar{D}_{v,i-1}}\right)^{\frac{2}{3}}} \qquad (5.39)$$

where M is the total number of grid cells.

The global conservation of thermal energy and matter are checked at the end of each solution process using the relations given below.

The bulk air flux at the inlet (i = 1) is given by

$$Q_{g,in} = (\rho_{go} V_o)\, \bar{\rho}_{g,i}\, \bar{u}_i \qquad (5.40)$$

The bulk air flux at the exit (i = M+1) is

$$Q_{g,out} = (\rho_{go} V_o)\, \bar{\rho}_{g,i-1}\, \bar{u}_{i-1} \qquad (5.41)$$

The vapour flux at the inlet (i = 1) is

$$Q_{v,in} = \rho_{go} V_o \bar{\rho}_{g,i} \bar{u}_i (\Delta C \bar{C}_i + C_{out}) - \frac{\rho_{go} D_{vo} \Delta C}{D} \bar{\rho}_{g,i} \bar{D}_{v,i} \left.\frac{d\bar{C}}{d\bar{x}}\right|_i \qquad (5.42)$$

The vapour flux at the outlet (i = M+1) is

$$Q_{v,out} = \rho_{go} V_o \bar{\rho}_{g,i-1} \bar{u}_{i-1} (\Delta C \bar{C}_{i-1} + C_{out}) - \frac{\rho_{go} D_{vo} \Delta C}{D} \bar{\rho}_{g,i-1} \bar{D}_{v,i-1} \left. \frac{d\bar{C}}{d\bar{x}} \right|_{i-1} \quad (5.43)$$

The thermal energy flux at the inlet (i = 1) is

$$H_{s,in} = \rho_{go} C_{pgo} V_o \bar{\rho}_{g,i} \bar{C}_{pg,i} \bar{u}_i (\Delta T \bar{T}_i + T_{out}) - \frac{\lambda_{effo} \Delta T}{D} \bar{\lambda}_{eff,i} \left. \frac{d\bar{T}}{d\bar{x}} \right|_i \quad (5.44)$$

The thermal energy flux at the outlet (i = M+1) is

$$H_{s,out} = \rho_{go} C_{pgo} V_o \bar{\rho}_{g,i-1} \bar{C}_{pg,i-1} \bar{u}_{i-1} (\Delta T \bar{T}_{i-1} + T_{out}) - \frac{\lambda_{effo} \Delta T}{D} \bar{\lambda}_{eff,i-1} \left. \frac{d\bar{T}}{d\bar{x}} \right|_{i-1} \quad (5.45)$$

The total condensation rate for the flow field is given by

$$Q_c = \frac{\rho_{go} D_{vo} \Delta C}{D} \sum_{iv=1}^{M-1} \bar{m}_{iv} \Delta \bar{x} \quad (5.46)$$

The total latent heat generated is

$$H_L = h_{vap} \frac{\rho_{go} D_{vo} \Delta C}{D} \sum_{iv=1}^{M-1} \bar{m}_{iv} \Delta \bar{x} \quad (5.47)$$

The global balances are calculated as outlined in Section 4.4.

The cross-transport terms (Soret and Dufour effects) are not

included in the governing equations, but their magnitudes are estimated after the solutions are obtained. This is done in order to determine their significance relative to the main transport terms.

The Soret mass flux at the inlet (i = 1) is given by

$$Q_{s,in} = -\frac{D_{so}\rho_{go}\Delta T}{D}\overline{D}_{s,i}\overline{\rho}_{g,i}(\Delta C\overline{C}_i + C_{out})\left.\frac{d\overline{T}}{d\overline{x}}\right|_i \qquad (5.48)$$

The Soret mass flux at the outlet (i = M+1) is

$$Q_{s,out} = -\frac{D_{so}\rho_{go}\Delta T}{D}\overline{D}_{s,i-1}\overline{\rho}_{g,i-1}(\Delta C\overline{C}_{i-1} + C_{out})\left.\frac{d\overline{T}}{d\overline{x}}\right|_{i-1} \qquad (5.49)$$

The Dufour heat flux at the inlet (i = 1) is given by

$$H_{d,in} = -\frac{D_{do}\rho_{go}C_{pvo}\Delta C}{D}\overline{D}_{d,i}\overline{\rho}_{g,i}\overline{C}_{pv,i}\left.\frac{d\overline{C}}{d\overline{x}}\right|_i \qquad (5.50)$$

The Dufour heat flux at the outlet (i = M+1) is

$$H_{d,out} = -\frac{D_{do}\rho_{go}C_{pvo}\Delta C}{D}\overline{D}_{d,i-1}\overline{\rho}_{g,i-1}\overline{C}_{pv,i-1}\left.\frac{d\overline{C}}{d\overline{x}}\right|_{i-1} \qquad (5.51)$$

### 5.3.4 Physical Data

The physical data used in the simulation are mostly specific to this example and are listed here.

Nominal velocties: **0.30, 0.43, 0.66, *and* 0.87 *mm/s*.**

Boundary temperatures: $T_{in}$ = **298 *K*,** $T_{out}$ = **243 *K***

Boundary relative humidities: $RH_{in}$ = 40%, $RH_{out}$ = 100%

Insulation slab thickness: D = 0.102 m

Porosity of cellulose = 0.91

Specific gas constant for dry air = 287 J/kg-K

Specific gas constant for water vapour = 462 J/kg-K

The equations relating the thermophysical properties of air, water and ice to temperature are listed in Section 3.6. The equations are for the effective thermal conducivity of air, the diffusion coefficient of water vapour in air, the specific heat capacity of air at constant pressure, the dynamic viscosity of air, the latent heat of vaporization of water, and the latent heat of sublimation of ice.

No value was found in the literature for the permeability of cellulose. However, the exact value is not important because permeability is only used as a parameter to convert the known flow nominal velocities to equivalent pressure differences using Darcy's law. Assuming an isotropic cellulose and a permeability of $5 \times 10^{-10}$ $m^2$, the extreme case which is an exit temperature of 243 K and a nominal velocity of 0.87 mm/s gives a Darcy Reynolds number of $1.81 \times 10^{-3}$, which is well within the requirement for Darcy flow. Hence the value of permeability adopted for the cellulose insulation in this investigation is $5 \times 10^{-10}$ $m^2$. The equivalent pressure differences based on this permeability and a reference temperature of 273.15 K are 1.04 Pa for a nominal velocity of 0.30 mm/s, 1.49 Pa for a nominal velocity of 0.43 mm/s, 2.29 Pa for a nominal velocity of 0.66 mm/s, and 3.01 Pa for a nominal velocity of 0.87 mm/s.

The only information to go by in the search for appropriate convective heat transfer coefficients, $h_f$, for the inlet and the exit, are the "initial" temperature readings taken by Yu after about 24 hours from the beginning of the experiments.

The value of $h_f$ influences the temperature at the boundary. Increasing the inlet value of $h_f$ raises the temperature profile, while increasing its value at the exit lowers the profile. A Biot number tending to infinity at the exit gives Dirichlet exit temperature conditions. To determine the values of $h_f$ at the inlet and the exit to suit each nominal velocity, the quasi-transient procedure, described in detail in Section 4.5, was executed with a time step of 1 hour for a total of 24 hours, and the resulting temperature profile was then compared to Yu's "initial" profile. The values of $h_f$ were adjusted and the quasi-transient procedure repeated until the "best" fit of Yu's profile was realised. The "best" fit was judged by a low absolute error, coupled with the requirement that the entire simulation temperature profile had to lie within the measurement uncertainty of temperature (i.e., ±1 K). Table 5.3 gives the values of $h_f$ adopted for the different nominal velocities.

Table 5.3. Inlet and Exit Forced-convective Heat Transfer Coefficients for Different Nominal Velocities.

| Nominal Velocity (mm/s) | $h_{f,in}$ ($W/m^2$-K) | $h_{f,out}$ ($W/m^2$-K) | Absolute Error (%) on 24-hr profile |
|---|---|---|---|
| 0.30 | 2.7 | 18.0 | 7.8 |
| 0.43 | 7.5 | 3.5 | 7.4 |
| 0.66 | 2.0 | 4.0 | 4.4 |
| 0.87 | 1.0 | 2.3 | 4.3 |

The reference values of the thermophysical properties

discussed in this section are based on 273.15 K, 50% rh, and 101325 Pa, and are given in Section B.1, except for the following:

$$\lambda_{effo} = 3.613 \times 10^{-2}\ W/m\text{-}K$$

$$D_{vo} = 2.017 \times 10^{-5}\ m^2/s$$

5.3.5 Parameter Sensitivity Test Results

The properties of air, water and ice vary with temperature according to the equations given in Section 3.6. When air cools from 298 K to 243 K, its thermal conductivity decreases by about 16.3%, the dynamic viscosity decreases by about 14.2%, the vapour diffusion coefficient decreases by about 29.2%, and the specific heat capacity at constant pressure decreases by 1.05%. The value of the latent heat of vaporization of water increases by 2.5% when the temperature drops from 298 K to 273 K. The latent heat of sublimation of ice increases by 0.14% between 273 K and 253 K, then it remains approximately constant as the temperature decreases to 233 K. The small variations with temperature of the specific heat capacity, the latent heat of vaporization, and the latent heat of sublimation, may justify the use of constant values in computations involving these parameters in the temperature range 298 K to 243 K.

The effects of changing the variable parameters, one at a time by ±10%, on the heat and mass transfer rates was examined. This sensitivity study of the numerical model used a nominal velocity of 0.66 mm/s and examined the effects of changing the effective thermal conductivity, the diffusion coefficient of water vapour in air, the ratio of the permeability to the dynamic viscosity of air, the specific heat capacity of air at constant pressure, the latent heat of vaporization of water, and the latent heat of sublimation of ice.

The heat and mass transfer results are presented in Table 5.4,

while the effect of changing the parameters on the temperature and condensation rate profiles are shown in Figures 5.11 to 5.22.

Changing the effective thermal conductivity by ±10% changes the transfer rates by 2.42% at most. Figure 5.11 shows that the temperature profile is more sensitive to changes in the effective thermal conductivity in the dry region than in the wet region, and increasing this parameter causes the temperature profile to shift to lower levels. Figure 5.12 shows that the wet region expands towards the inlet when the effective thermal conductivity is increased.

Changing the diffusion coefficient of water vapour in air by ±10% changes the heat and mass transfer rates by 1.91% at most. Figure 5.13 indicates that the temperature profile is most sensitive to changes in the diffusion coefficient around the wet-dry interface. The effect of changing the diffusion coefficient on the condensation rate profile is more pronounced than its effect on the temperature profile, as seen in Figure 5.14. The wet region expands as the diffusion coefficient decreases.

Changing the ratio of the permeability to the dynamic viscosity by ±10% does not affect the heat and mass transfer results at all. It also has no effect on the temperature profile (Figure 5.15) and the condensation rate profile (Figure 5.16).

When the specific heat capacity of air is changed by ±10%, the heat and mass transfer rates change by 8.82% at most, this being the change in the total heat transfer rate at the exit. This large change occurs because the specific heat capacity is a factor in the dominant advective term of the total heat transfer rate (Equation 5.45). The temperature profile, shown in Figure 5.17, and the condensation rate profile, shown in Figure 5.18, are sensitive to the changes in the specific heat

capacity in both the dry and wet regions. Increasing the specific heat capacity by ±10% raises the temperature profile and causes the wet-dry interface to shift towards the exit, decreasing both the total condensation rate and the latent heat released by about 4%.

A ±10% change in the latent heat of vaporization of water does not affect the total heat and mass transfer rates (Table 5.4), the temperature profile (Figure 5.19), and the condensation rate profile (Figure 5.20).

When the latent heat of sublimation of ice is changed by ±10%, the largest change (8.6%) occurs in the latent heat released; all other transfer rates change by 2% at most. The effect of the change on the temperature profile (Figure 5.21) is negligible and concentrated in the wet region as expected. The effect on the condensation rate profile (Figure 5.22) is quite small, with the wet-dry interface shifting slightly towards the inlet when the latent heat of sublimation is decreased.

Figures 5.11 to 5.22 and Table 5.4 indicate that the simulation model is most sensitive to changes of ±10% in the effective thermal conductivity and the specific heat capacity. Sensitivity is least to changes in the ratio of the permeability to the dynamic viscosity and to changes in the latent heat of vaporization. To obtain accurate simulation results, the models for the effective thermal conductivity and the specific heat capacity should therefore have the smallest uncertainties. The other parameters can have uncertainties of up to ±10% in their models without the simulation results being affected significantly.

To obtain the results in the following subsections, the governing equations and other relations in non-dimensional form, given in Section 5.3.3, with the physical data given in Section 5.3.4, are solved iteratively with a successive under-relaxation factor of 0.9. The general procedure for the quasi-

steady solution is described in Section 4.4, and the effect of moisture accumulation is captured by the quasi-transient technique described in Section 4.5. 100 uniform grid cells were used. Further grid refinement to 150 cells changed the global flowrates by less than 0.05%. For each nominal velocity, the quasi-transient solution was advanced in time until the total condensation rate remained nearly constant.

### 5.3.6 Temperature Profiles

Figures 5.23, 5.24, 5.25 and 5.26 show the temperature profiles for the four nominal velocities considered in this example. In each case the values of $h_{f,in}$ and $h_{f,out}$ given in Table 5.3 are used in the simulation. The quasi-steady solution, labelled as "1 sec." is first obtained, to be used as the starting profile for the quasi-transient investigation. In this example the quasi-transient time step is one hour.

Investigation revealed that the temperature profile shifts to lower temperature levels as the moisture accumulates with time. The movement of the profile is relatively rapid in the early stages. In later stages, as moisture accumulates and spreads, there is less change in temperature profiles with time. The quasi-steady profile is monotonic, but an inflection appears after several hours and becomes more visible with time. In all cases, the inflection occurs around the freezing point of water. Each of the figures (5.23 to 5.26) shows the predicted temperature profile at a few selected times. The final (long-term) measured temperature profiles are plotted on the figures to show that the drop in the profiles and the transformation of the inflections continue as long as the moisture accumulates with time. It is expected that if the quasi-transient solution is effected for longer times there would be further decreases in the temperature profiles and further alterations of the shapes of the inflections, hopefully giving good agreement with the final measured

Table 5.4. Parameter Sensitivity Study Results for a Nominal Velocity of 0.66 mm/s. (VC is the percentage of inlet vapour condensed, $Q_C$ is the total condensation rate, $H_{s,out}$ is the total heat transfer rate at the exit, and $H_L$ is the latent heat released.)

| Parameter | VC (%) | $Q_C$ ($\times 10^{-6}$ kg/s) | $H_{s,out}$ (W) | $H_L$ (W) |
|---|---|---|---|---|
| $0.9\lambda_{eff}$ | 56.7 | 3.63 | 253.2 | 10.3 |
| $1.0\lambda_{eff}$ | 57.7 | 3.72 | 255.2 | 10.5 |
| $1.1\lambda_{eff}$ | 57.9 | 3.75 | 256.8 | 10.6 |
| $0.9D_v$ | 58.3 | 3.72 | 255.0 | 10.5 |
| $1.0D_v$ | 57.7 | 3.72 | 255.2 | 10.5 |
| $1.1D_v$ | 56.6 | 3.68 | 255.2 | 10.4 |
| $0.9K/\mu_g$ | 57.7 | 3.72 | 255.2 | 10.5 |
| $1.0K/\mu_g$ | 57.7 | 3.72 | 255.2 | 10.5 |
| $1.1K/\mu_g$ | 57.7 | 3.72 | 255.2 | 10.5 |
| $0.9C_{pg}$ | 58.7 | 3.81 | 232.7 | 10.8 |
| $1.0C_{pg}$ | 57.7 | 3.72 | 255.2 | 10.5 |
| $1.1C_{pg}$ | 56.0 | 3.57 | 277.3 | 10.1 |
| $0.9h_{vap}$ | 57.7 | 3.72 | 255.2 | 10.5 |
| $1.0h_{vap}$ | 57.7 | 3.72 | 255.2 | 10.5 |
| $1.1h_{vap}$ | 57.7 | 3.72 | 255.2 | 10.5 |
| $0.9h_{sub}$ | 58.9 | 3.79 | 254.5 | 9.67 |
| $1.0h_{sub}$ | 57.7 | 3.72 | 255.2 | 10.5 |
| $1.1h_{sub}$ | 56.8 | 3.65 | 255.8 | 11.4 |

profiles. Comparing the profiles for the different nominal velocities at a given time shows that the location of the inflection is nearer to the exit for higher exfiltration rates. This is seen clearly from the profiles for 24 hours. The intersection of a 24-hour profile with a 273.15 K line is

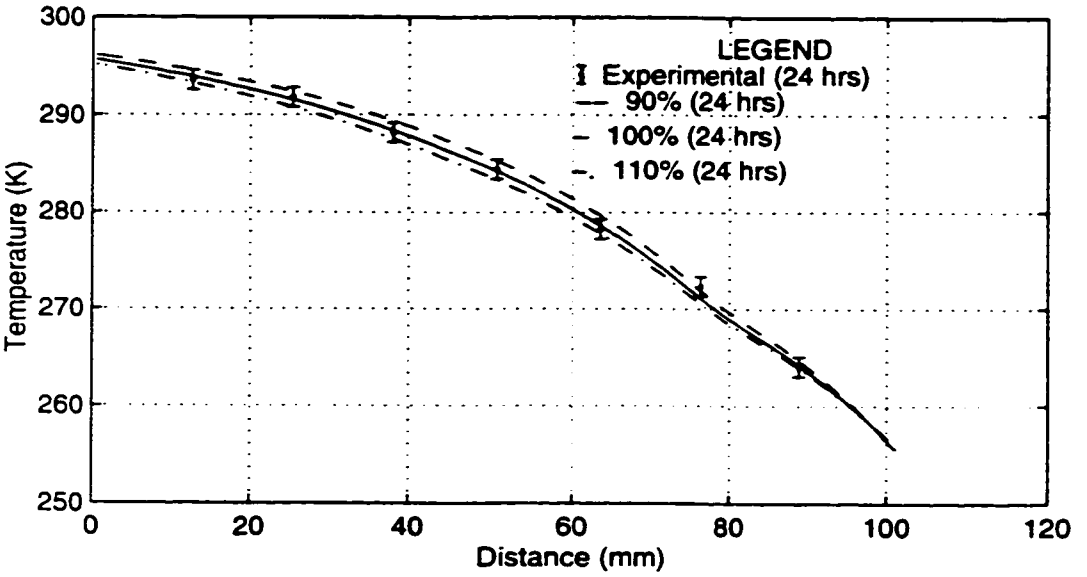


Figure 5.11. Temperature Profiles for 90%, 100%, and 110% of the Effective Thermal Conductivity. (v=0.66 mm/s)

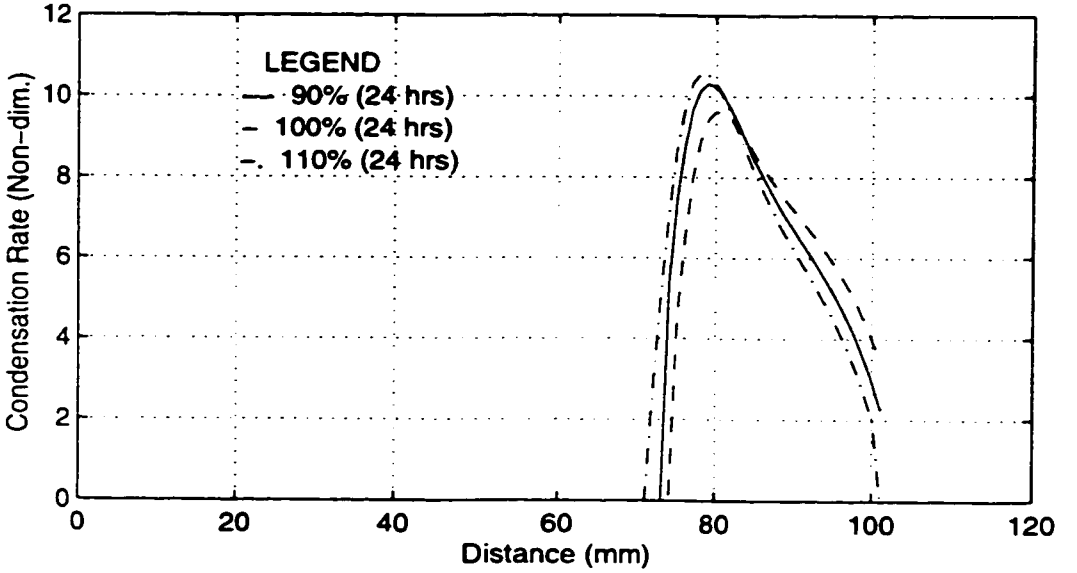


Figure 5.12. Condensation Rate Profiles for 90%, 100%, and 110% of the Effective Thermal Conductivity. (v=0.66 mm/s)

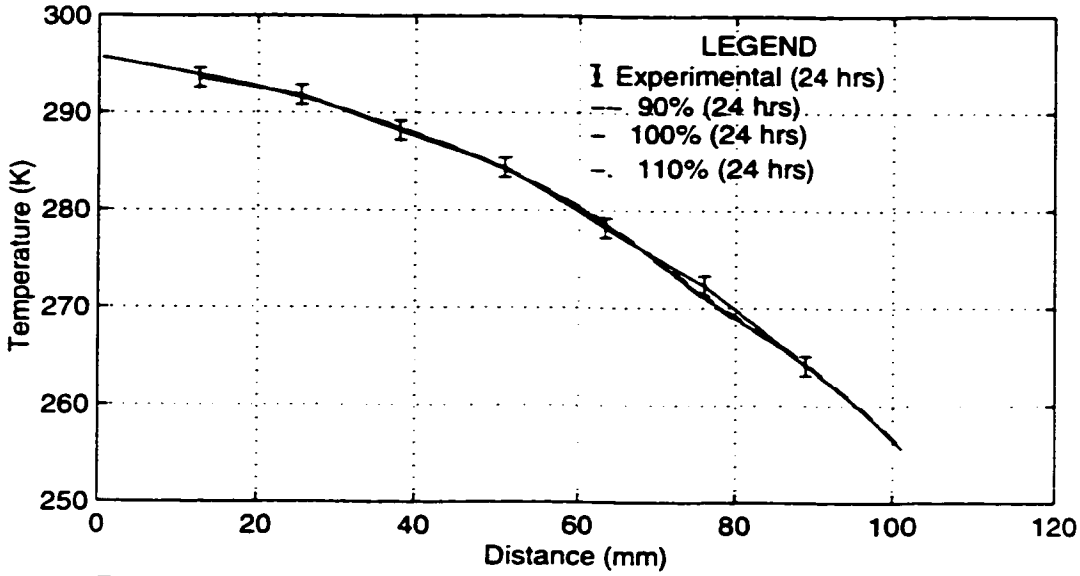


Figure 5.13. Temperature Profiles for 90%, 100%, and 110% of the Diffusion Coefficient of Water Vapour in Air. (v=0.66 mm/s)

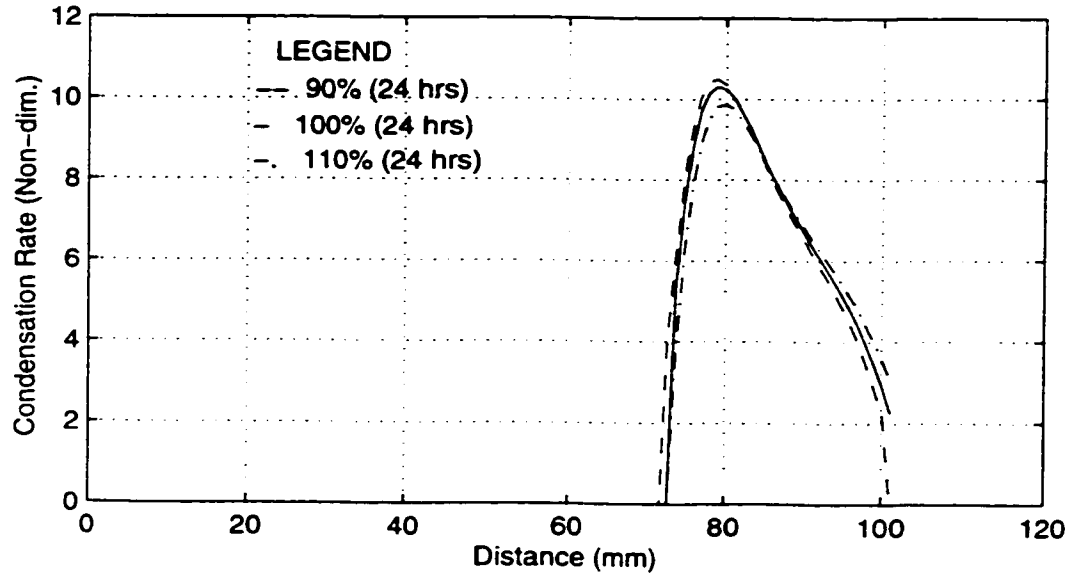


Figure 5.14. Condensation Rate Profiles for 90%, 100%, and 110% of the Diffusion Coefficient of Water Vapour in Air. (v=0.66 mm/s)

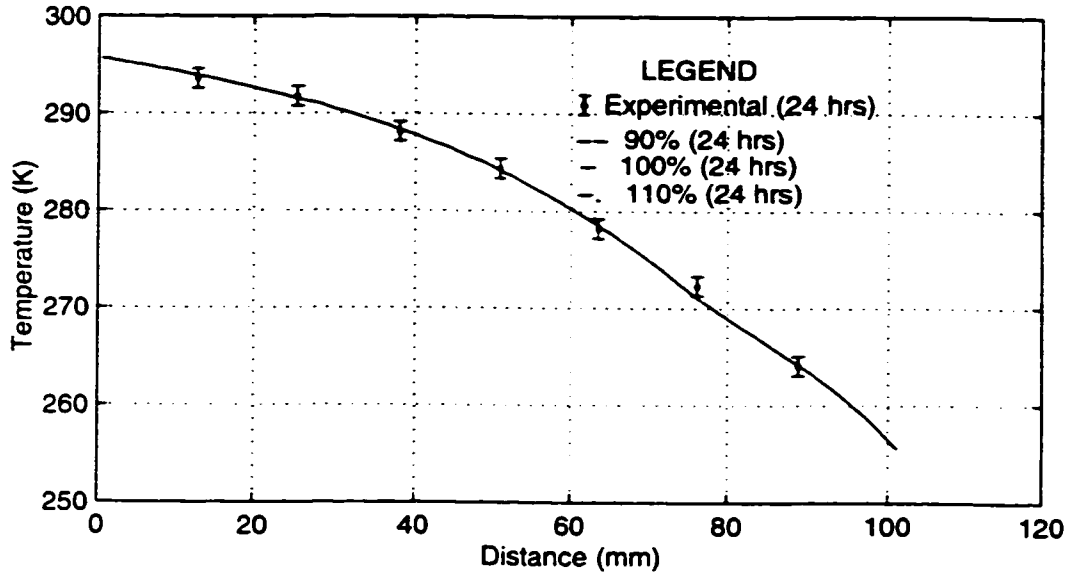


Figure 5.15. Temperature Profiles for 90%, 100%, and 110% of the Ratio of Permeability to Dynamic Viscosity of Air. (v=0.66 mm/s)

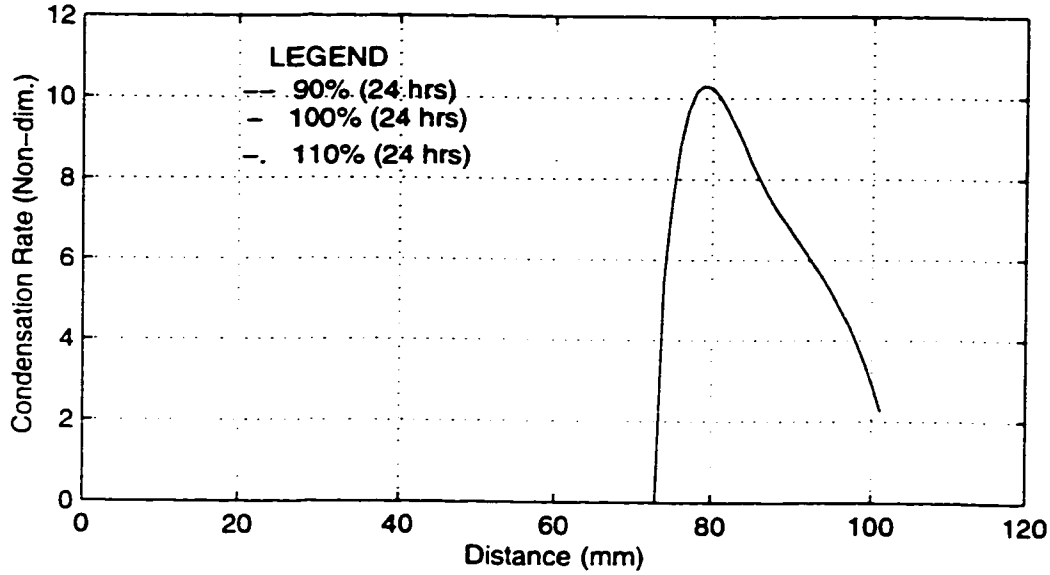


Figure 5.16. Condensation Rate Profiles for 90%, 100%, and 110% of the Ratio of Permeability to Dynamic Viscosity of Air. (v=0.66 mm/s)

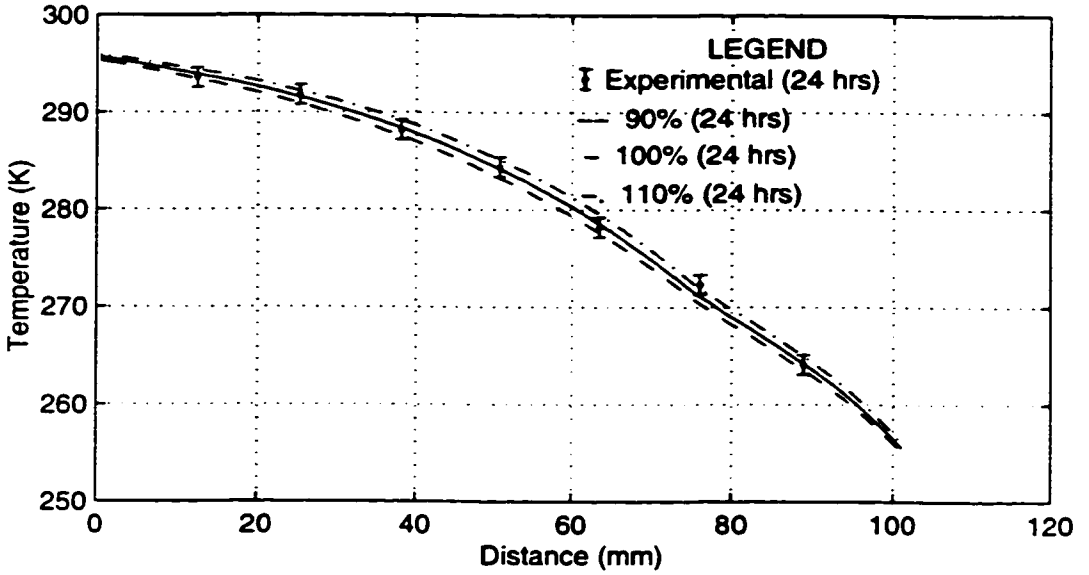


Figure 5.17. Temperature Profiles for 90%, 100%, and 110% of the Specific Heat Capacity of Air. (v=0.66 mm/s)

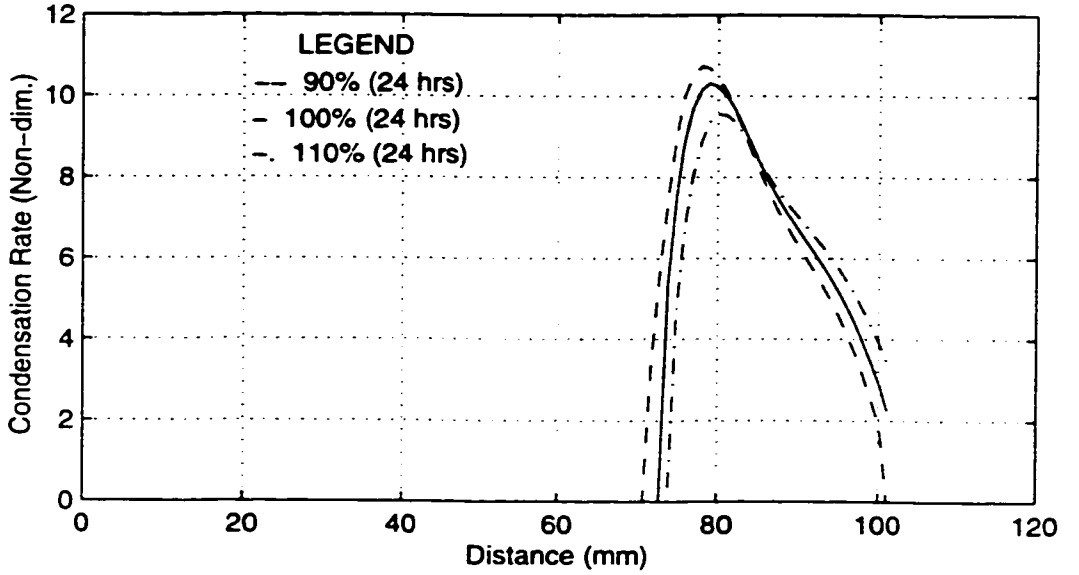


Figure 5.18. Condensation Rate Profiles for 90%, 100%, and 110% of the Specific Heat Capacity of Air. (v=0.66 mm/s)

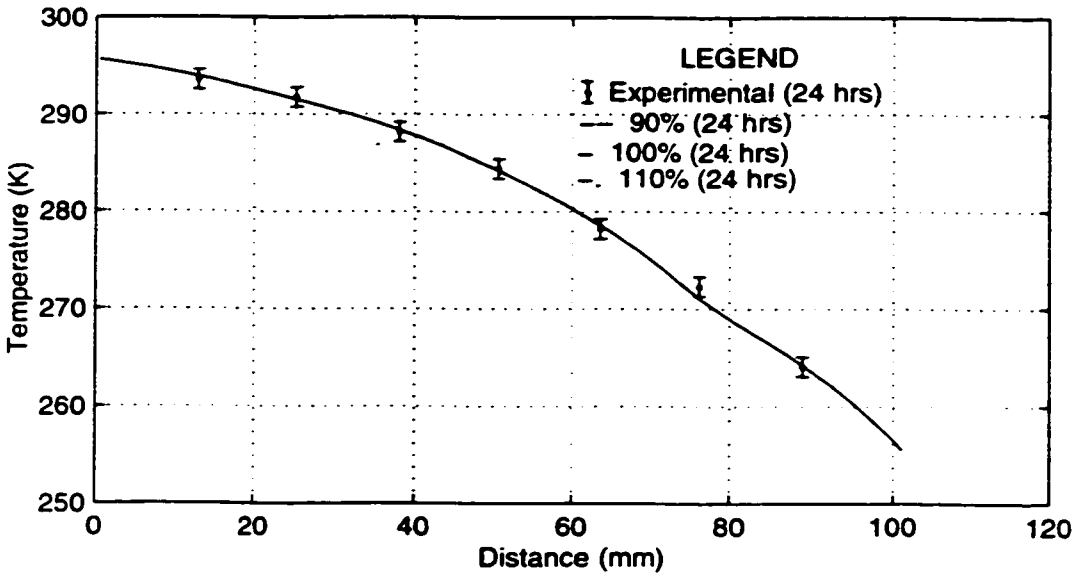


Figure 5.19. Temperature Profiles for 90%, 100%, and 110% of the Latent Heat of Vaporization of Water. (v=0.66 mm/s)

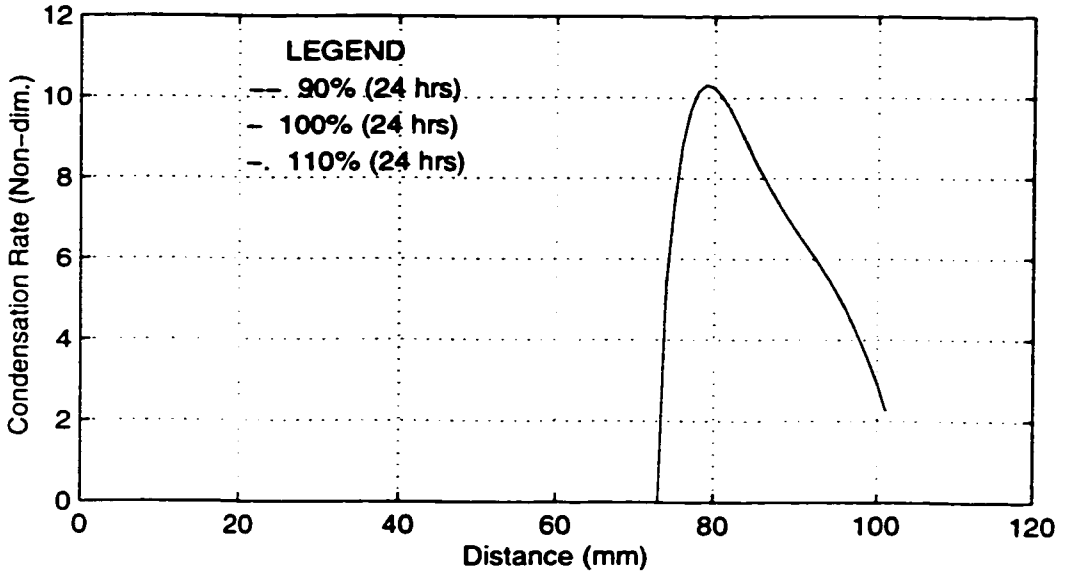


Figure 5.20. Condensation Rate Profiles for 90%, 100%, and 110% of the Latent Heat of Vaporization of Water. (v=0.66 mm/s)

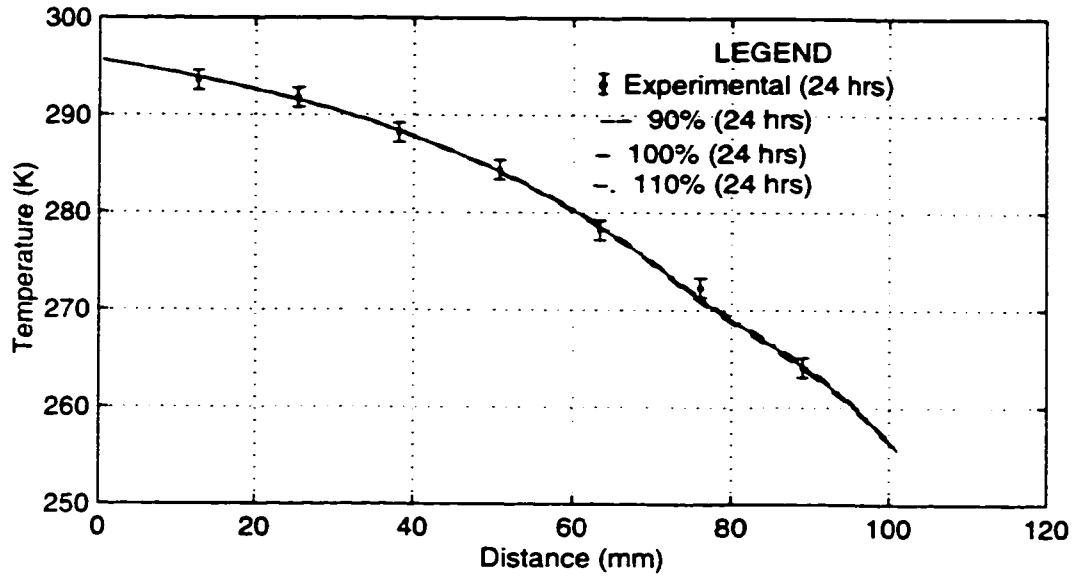


Figure 5.21. Temperature Profiles for 90%, 100%, and 110% of the Latent Heat of Sublimation of Ice. (v=0.66 mm/s)

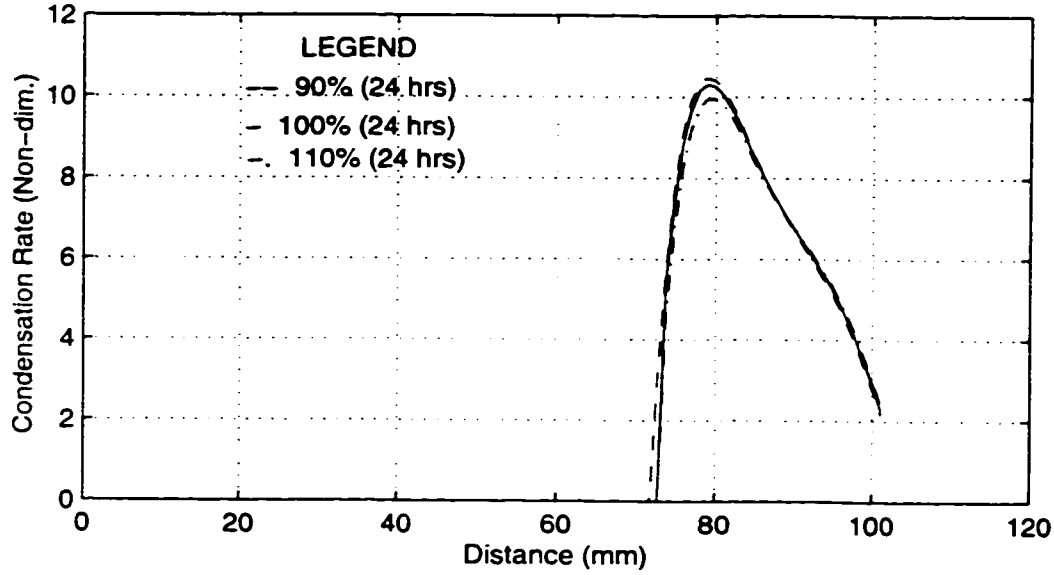


Figure 5.22. Condensation Rate Profiles for 90%, 100%, and 110% of the Latent Heat of Sublimation of Ice. (v=0.66 mm/s)

closer to the exit for higher exfiltration rates. The intersection occurs at 55 mm in Figure 5.23, 69 mm in Figure 5.24, 72 mm in Figure 5.25, and 83 mm in Figure 5.26.

Existing literature does not contain much on shifting temperature profiles and the formation of inflections. Both phenomena occur after the quasi-steady stage, but experimental investigations have mostly focussed on moisture accumulation, and not on temperature profiles. Numerical investigations, on the other hand, have mostly dealt with the transient evolution of profiles from an artificial dry state to, at most, the quasi-steady stage - a period of just about one hour in real time according to Vafai and Sarkar (1986) and Tao et al. (1991a). However, Modi and Benner (1985, Part I) reported that the temperature profile changes gradually after the quasi-steady stage, and that condensation may cause a drop in the temperature profile while increasing the heat flux.

### 5.3.7 Moisture Distribution Profiles

Figure 5.27 shows that the wet region expands towards the inlet with time. In the figure, the wet-dry interface for the quasi-steady stage is located at a distance of 83 mm from the inlet. This interface shifts to 77 mm from the inlet after 12 hours, then to 73 mm after 24 hours. This phenomenon is well documented in several research papers, two examples of which are by Tao et al. (1991a) and Wijeysundera et al. (1996). In time, the entire insulation slab may become wet. The location of the wet-dry interface at a given time depends also on the exfiltration rate. The interface is closer to the exit for higher rates. Figure 5.28 shows the distances, from the inlet, of the locations of the interfaces after 24 hours: 58 mm for a nominal velocity of 0.30 mm/s; 70 mm for a nominal velocity of 0.43 mm/s; 73 mm for a nominal velocity of 0.66 mm/s; and 82 mm for a nominal velocity of 0.87 mm/s. These locations coincide approximately with the locations of the inflections

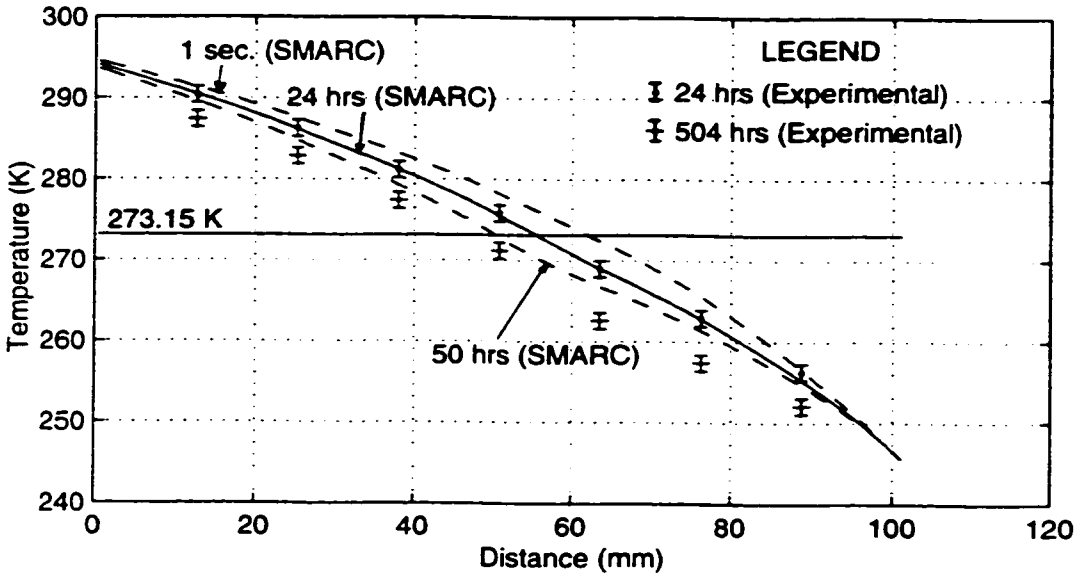


Figure 5.23. Temperature Profiles for v=0.30 mm/s

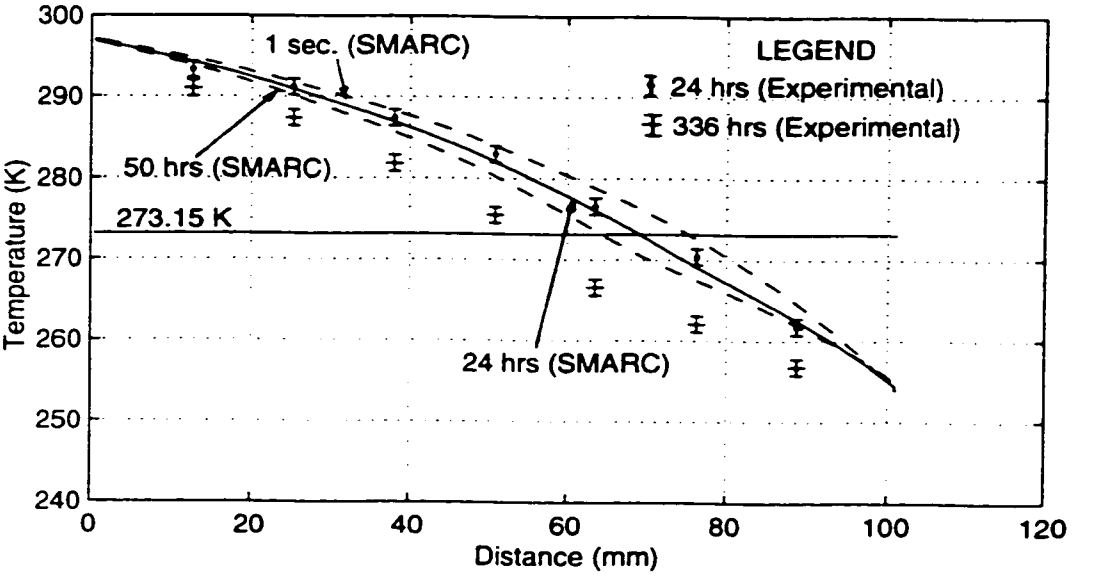


Figure 5.24. Temperature Profiles for v=0.43 mm/s

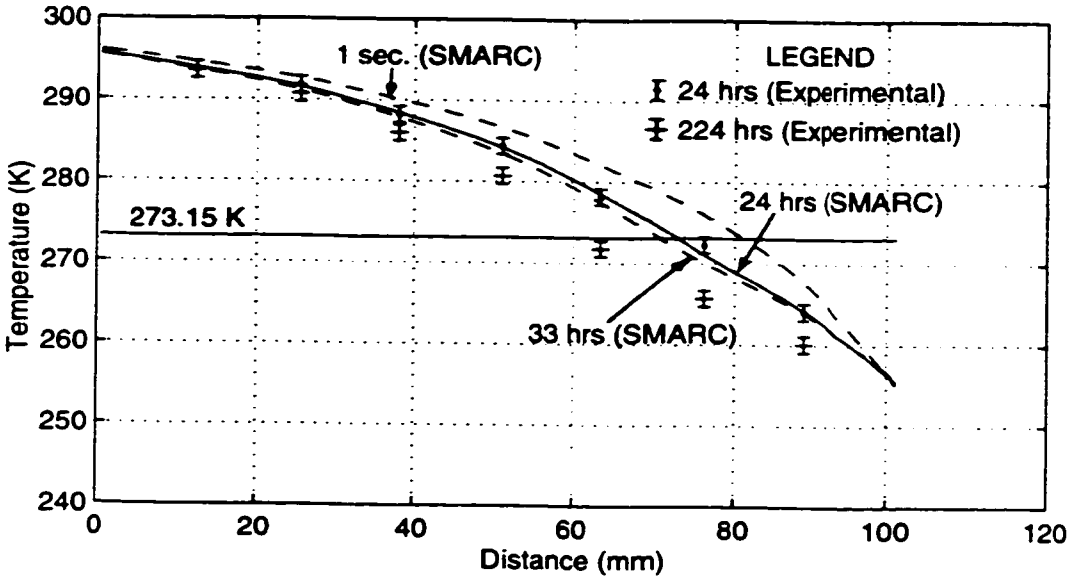


Figure 5.25. Temperature Profiles for v=0.66 mm/s

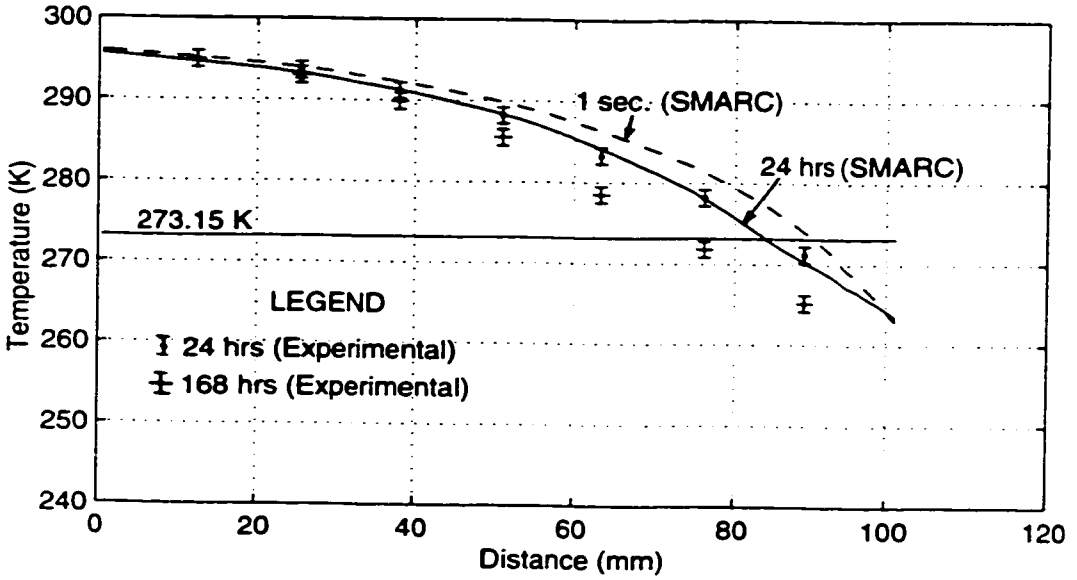


Figure 5.26. Temperature Profiles for v=0.87 mm/s

on the temperature profiles after a period of 24 hours (Section 5.3.6).

The total condensation rate in the insulation increases with time, rapidly in the initial stages and then gradually later, as shown in Figure 5.29. The nearly-constant rates for later times can be used for predicting the long-term moisture contents. Table 5.5 compares long-term moisture contents predicted by SMARC with Yu's experimental results for the same durations. Predicted moisture contents (MC) are computed from the formula:

$$\begin{aligned} MC\ (\%) = MC1 + &[\text{Average Total Condensation Rate } (kg/s\text{-}m^2) \\ &\times \text{Cross-Sectional Area of Insulation Slab } (m^2) \\ &\times \text{Total Time } (s) \times 100] \\ &/[\text{Dry Mass of Insulation Slab } (kg)] \end{aligned}$$

where MC1 is the total moisture content at the time when the condensation rates become nearly-constant, the "average total condensation rate" is the nearly-constant rate for subsequent times and "total time" is the total time during which the condensation rate is nearly-constant.

Generally, the total condensation rate increases with the exfiltration rate. However, a high exfiltration rate also increases the local temperatures in the insulation. The local saturation vapour pressures increase with the local temperatures, thus reducing the differences between the local actual vapour densities and the local saturation vapour densities. The local condensation rates computed using SMARC are thereby reduced, and regions closer to the inlet may become dry if the local saturation vapour densities exceed the local actual vapour densities. Hence the total condensation rate may start declining after a certain exfiltration rate is exceeded. This explains why the total condensation rate for a nominal velocity of 0.87 mm/s is less than the rate for a nominal velocity of 0.66 mm/s. It is expected that at some

higher exfiltration rate the insulation would experience the total "dry-out" reported by Ojanen and Kumaran (1996).

Table 5.5 shows poor experimental and simulation results for a nominal velocity of 0.30 mm/s. Percentage measurement and simulation errors are usually large when the measured or computed quantities are small in magnitude. In Yu's experiments, the low nominal velocity of 0.30 mm/s was realised not by forced convection but by buoyancy effects (i.e., natural convection). The simulation model in this project neglects natural convection entirely, and this may be the cause of the large discrepancy between the experimental and the simulation results for the nominal velocity of 0.30 mm/s. However, the discrepancies in Table 5.5 compare quite favourably with results from other investigations [Mitchel et al. (1995a), Simonson et al. (1996)].

Figure 5.30 shows that, for each of the nominal velocities, the total liquid content increases approximately linearly for the durations represented in the plots. Similar findings were reported by Wijeysundera and Hawlader (1992), who found by experiment that the increase was approximately linear initially, followed by a decrease much later. They considered durations between 200 and just over 600 hours, and, for all of them, the total liquid content increased approximately linearly with time.

The amount of vapour condensed, as a percentage of the amount of vapour at the inlet, increases with time due to increasing total condensation rates. The percentages are lower for higher exfiltration rates because, although the quantity of condensed vapour increases in absolute terms, the increase in the quantity of vapour at the inlet due to advection is much higher. The following percentages were recorded:

(1) an increase from 62.5% to 73.3% during the first 50 hours for a nominal velocity of 0.30 mm/s;

(2) an increase from 49.5% to 58.8% during the first 50 hours for a nominal velocity of 0.43 mm/s;

(3) an increase from 48.0% to 58.1% during the first 33 hours for a nominal velocity of 0.66 mm/s; and

(4) an increase from 32.5% to 41.4% during the first 26 hours for a nominal velocity of 0.87 mm/s.

Table 5.5. Comparison Between Experimental Results [Yu, 1986] and Numerical Predictions by SMARC of Long-term Moisture Contents.

| Nom. Vel. (mm/s) | Total Time (hrs) | Experimental Results | | SMARC Results | | % Diff. Between SMARC & Exp. |
|---|---|---|---|---|---|---|
| | | Moist. Cont. (%) | Std. Dev. | Av. Cond. Rate ($x10^{-5}$ kg/s) | Moist. Cont. (%) | |
| 0.30 | 504 | 106.0 | 7.8 | 0.298 | 132.2 | +24.7 |
| o.43 | 336 | 87.0 | 1.7 | 0.285 | 84.0 | -3.45 |
| 0.66 | 224 | 78.0 | 1.9 | 0.376 | 73.9 | -5.26 |
| 0.87 | 168 | 42.0 | 3.2 | 0.328 | 48.0 | +14.3 |

### 5.3.8 Latent Heat and Total Heat Transfer Rate at the Exit

Condensation generates latent heat which goes into increasing the total heat transfer rate at the exit. As the total condensation rate in the insulation increases with time, so does the total heat transfer rate at the exit.

For a nominal velocity of 0.30 mm/s, the quasi-steady exit heat transfer rate is 127.8 $W/m^2$. This increases to 133.8 $W/m^2$ after 50 hours. Over the same period, the contribution of

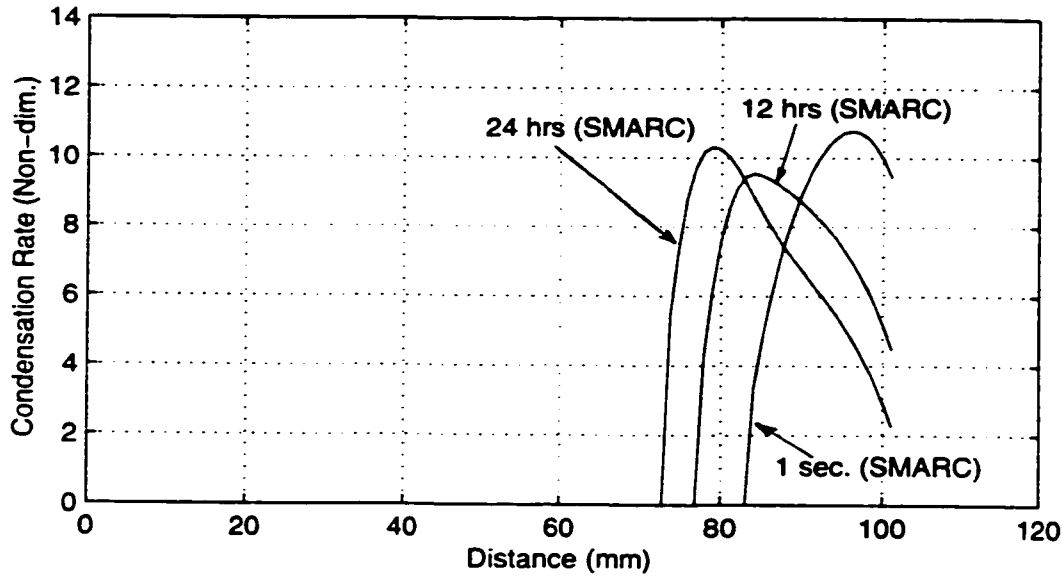


Figure 5.27. Expansion of Wet Region (v=0.66 mm/s)

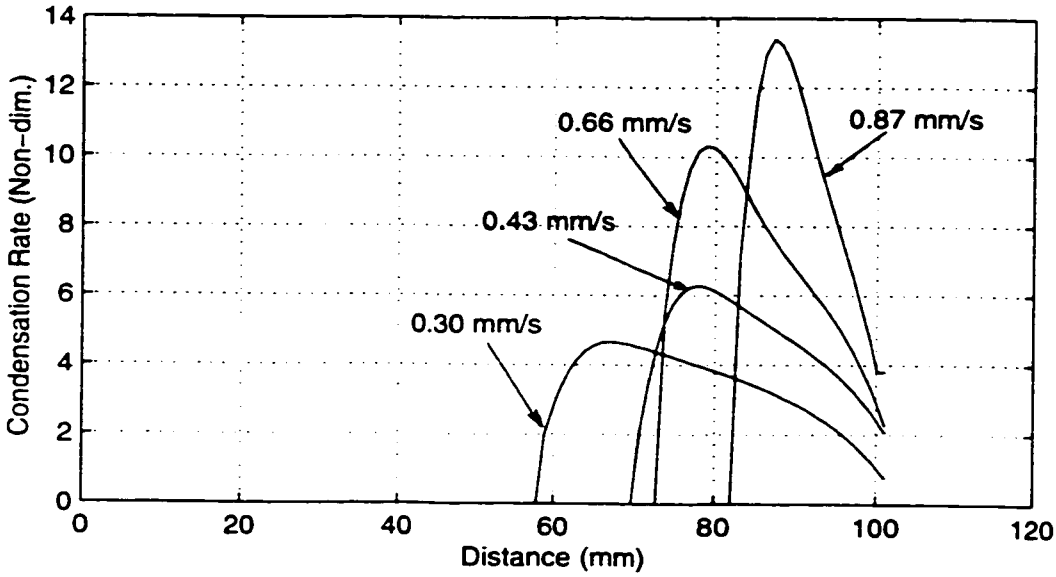


Figure 5.28. Wet-dry Interfaces for 24 Hours

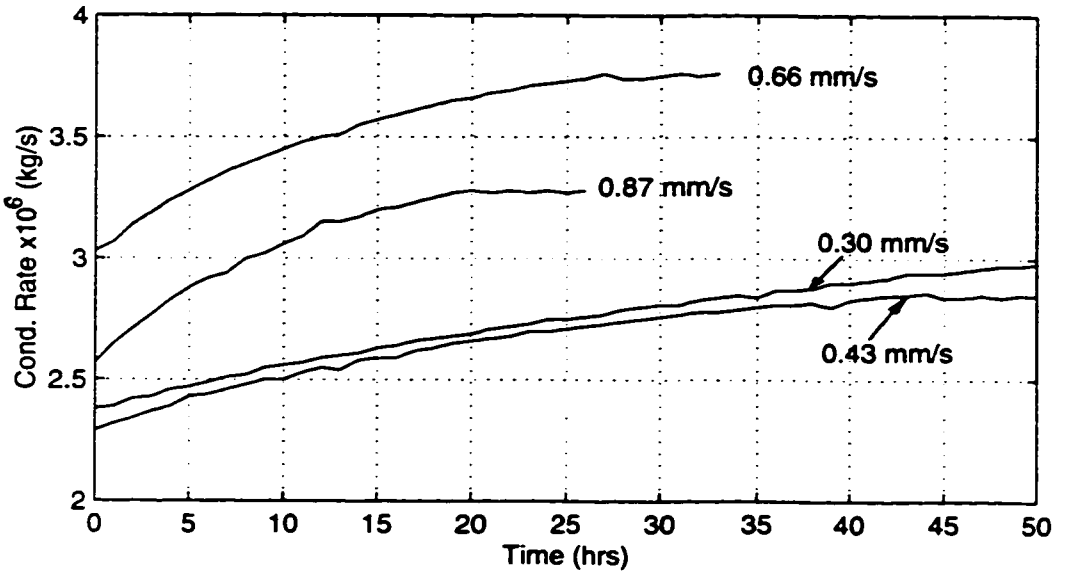


Figure 5.29. Variation of Total Condensation Rate with Time.

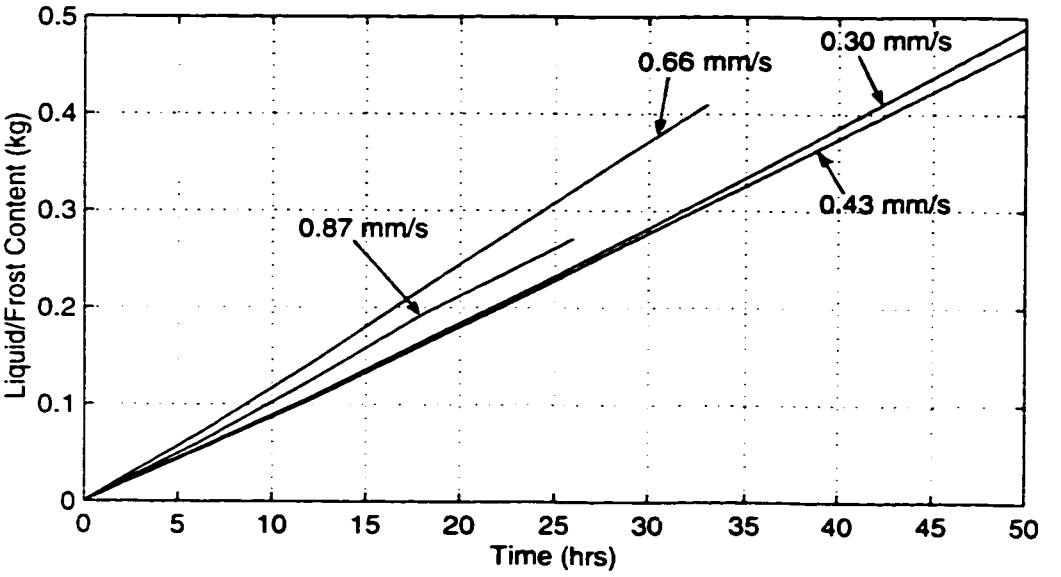


Figure 5.30. Variation of Total Liquid/Frost Content with Time.

latent heat to the total transfer rate increases from 5.27% to 6.32%.

For a nominal velocity of 0.43 mm/s, the quasi-steady exit heat transfer rate is 169.8 $W/m^2$, increasing to 175.6 $W/m^2$ after 50 hours. During the same period the contribution of latent heat to the total transfer rate at the exit increases from 3.82% to 4.61%.

For a nominal velocity of 0.66 mm/s, the quasi-steady exit heat transfer rate is 249.5 $W/m^2$ and increases to 256.2 $W/m^2$ after 33 hours. The contribution of latent heat to the total transfer rate increases from 3.44% to 4.16% over the same period.

For a nominal velocity of 0.87 mm/s, the quasi-steady exit heat transfer rate is 316.4 $W/m^2$, increasing to 321.6 $W/m^2$ after 26 hours. The contribution of latent heat to the total transfer rate increases from 2.30% to 2.90% over the same period.

The latent heat released is small compared to the total heat transfer rate, contributing less than 7% of the total.

5.3.9 General Observations

(1) Considering a nominal velocity of 0.87 mm/s, there is a 15% decrease in the magnitude of the field velocity between the inlet and the exit. This is due to the requirements for mass conservation. The bulk air density is higher at the exit due to the low temperature. The flow velocity decreases towards the exit to compensate for the increase in density and conserve mass. The velocity profile also shifts with time as the temperature profile shifts, but in the opposite direction to that of the temperature profile. This is because of the temperature-dependent dynamic viscosity in the denominator of the right hand side of Darcy's law. (It was observed that the pressure gradient remained nearly constant in the domain.)

(2) The Soret and Dufour terms are negligible compared to the advection and diffusion/conduction terms in the governing equations. A comparison of terms at the inlet and the exit revealed that the Soret mass flux is of the order of $10^{-12}$ to $10^{-11}$ kg/s-m$^2$ compared to $10^{-6}$ to $10^{-3}$ kg/s-m$^2$ for convection. The Dufour heat fluxes were of the order of $10^{-10}$ to $10^{-9}$ W/m$^2$ compared to $10^{+1}$ to $10^{+2}$ W/m$^2$ for convective heat fluxes.

(3) The varying of the properties of air with temperature and moisture content was extremely important in this investigation because inflections on the temperature profiles were not observed before the variations were effected. Shapiro and Motakef (1990) stated that varying the thermophysical properties of air would have reduced the discrepancies between their experimental and simulation results. The specific heat capacity, the thermal conductivity, the mass diffusion coefficient of vapour in air, and the dynamic viscosity are strong functions of temperature and have profiles similar to the temperature profile, including inflections wherever they occur.

(4) In the model for the effective thermal conductivity (Section 3.6, Equation 3.47), the second term accounts solely for the contribution of the liquid/frozen phase. Since this term is added directly to the other terms, the wet/frozen interfaces are distinctly marked by sudden changes in the magnitudes of the effective conductivity. Although the liquid and frost exist in minute quantities, their much larger thermal conductivities, relative to the values for air and vapour, ensure that changes in the effective thermal conductivity due to condensate/frost mask the changes due to air temperature and vapour content. Benner and Modi (1986) reported that the effective thermal conductivity in their investigation increased rapidly initially, then decreased, and eventually levelled off to a pseudo-steady-state value directly proportional to the moisture gain.

(5) Other investigations with SMARC and the quasi-transient procedure using different boundary conditions show that:

(i) three zones (dry-wet-dry) may occur if the inlet and exit boundary relative humidities are both less than 100% and the exit temperature is below 273.15 K - also shown by Example 1 (Ogniewicz and Tien, 1981) and Motakef and El-Masri (1986);

(ii) the entire insulation slab may be wet if both the inlet and exit boundaries are saturated (i.e., at 100% rh), even if both boundaries are above 273.15 K (Wijeysundera, 1992, and Tien and Vafai, 1990); and

(iii) if both boundaries are at 100% rh and the inlet is above the freeezing point, say at 298 K, while the exit is below the freezing point, say at 243 K, so that the entire slab is wet/frozen, an inflection will eventually develop on the temperature profile at the freezing point due to a sudden change in the magnitude of the effective thermal conductivity caused by the change in the condensation/frosting rate.

5.3.10 Physical Interpretation of Results

Condensation commences when there exists a region within the insulation slab where the local vapour pressures exceed the saturation values for the local temperatures. The quasi-steady or "initial" solution is a function of the boundary conditions and is used to identify the frozen or wet region if there is one. As the liquid or frost accumulates with time in this region, the second term in the effective thermal conductivity model (Equation 3.47) increases due to increasing liquid/frost volume fraction. A large effective thermal conductivity means that thermal energy is conducted at a faster rate from the location and the local temperature drops. As the local temperature drops, the temperature gradient between the location and other locations upstream increases, resulting in higher conduction rates from the upstream locations. The

higher conduction rates cause the temperatures to drop even in regions which may still be dry. When the local temperature drops, the saturation vapour pressure and, therefore, the saturation vapour density decreases. A decrease in the saturation vapour density has two possible effects: either a bigger difference is created between the saturation vapour density and the actual vapour density, increasing the condensation rate in regions which are already wet; or new regions may become saturated, and thereby the wet zone encroaches upon regions which were previously dry. The cycle of events is repeated when the boosted local liquid content increases the effective thermal conductivity further. The net result is that the temperature profile drops continuously as moisture builds up in the insulation.

The shape of the temperature profile is determined by the relative magnitudes of the effective thermal conductivities for adjacent grid cells, much in the same way that the magnitudes of the thermal conductivities of the materials in a composite solid experiencing pure conduction determine the temperature profile. At the wet-dry interface (Figures 5.27 and 5.28), the term $\epsilon_l \lambda_l$ is suddenly introduced, while at the wet-frozen interface $\epsilon_l \lambda_l$ is suddenly converted to $\epsilon_i \lambda_i$ ( "i" for ice). The density of ice is lower than the density of water, and the thermal conductivity of ice is higher than the thermal conductivity of water. Hence changes in the effective thermal conductivity at the wet-frozen interfaces are usually larger than changes at the wet-dry interfaces. Changes at the dry-frozen interfaces are the largest of all types. If a change in the effective thermal conductivity is sufficiently large, then the accompanying change in the rate of conduction may create an inflection on the temperature profile. This explains why an inflection only emerges and grows later in a condensation process, and why an inflection is more likely to occur at a dry-frozen interface than at a wet-dry or a wet-

frozen interface.

The cases which have been considered in this example show that the local condensation rates decrease as the exits are approached (Figure 5.28). This is partly due to the continuous decrease in the difference between the actual vapour density and the saturation vapour density, some of the vapour having been condensed out of the air at the upstream locations. A dry zone may appear before the exit if the actual vapour density falls to, or below, the saturation level. This is most likely to occur if the exit boundary relative humidity is less than 100%.

### 5.3.11 Summary and Conclusions

SMARC and the quasi-transient technique have been used successfully for solving Yu's problem, which is a forced-convective, multiphase, one-dimensional problem involving condensation. The quasi-steady solution is obtained directly based on the boundary conditions, instead of using the traditional fully-transient methods which use an artificial dry state as the initial state. The effect of moisture accumulation on the field variables, such as temperature, has been investigated by the quasi-transient technique.

The temperature profiles and the moisture contents for the long term, predicted by SMARC and the quasi-transient method, compare quite well with the experimental results. Except for the case with the lowest nominal velocity (i.e., 0.30 mm/s), all predictions are within the measurement uncertainties.

The variation of the properties of air with temperature and moisture content improves the accuracy of the moisture results and is absolutely necessary for the creation of inflections on the temperature profiles.

After the quasi-steady stage, the conduction term, the condensation rate term, and the latent heat term become very

important in the equations because they determine the evolution of the field variables. (The dominating role of the advection term does not extend beyond the quasi-steady stage.) The role played by the effective thermal conductivity is crucial and its modelling merits further research, so that simulation moisture results may be improved.

In conclusion, SMARC and the quasi-transient technique have proved to be easy-to-apply, very effective tools for the prediction of long-term moisture contents in porous insulation.

## 5.4 Example 3 [Chen, H., Besant, R.W., and Tao, Y. (1997a, 1997b)]: 2-D Validation of SMARC and the Quasi-transient Procedure

### 5.4.1 Introduction

This example illustrates the application of SMARC to two-dimensional problems, and demonstrates that SMARC can be used to obtain the quasi-steady state solution directly, i.e., without going through a fully- transient solution procedure as is customary. The experimental results obtained by Chen et al. (1997) are compared with simulation results obtained using SMARC. Chen et al.'s stated aim: "It is this quasi-steady heat and water vapour transfer process that is the main focus of this paper ..." By comparing experimental and simulation results for temperature profiles, moisture accumulation profiles and the heat conduction rate through the cold boundary, it will be shown that SMARC and the quasi-transient procedure can accurately predict the experimental results for the duration of the tests that Chen et al. conducted.

### 5.4.2 Problem Description and Experimental Procedure

Chen et al.'s test cell, shown in Figure 5.31, was 600 mm high by 135 mm wide by 275 mm deep. It was bounded by a constant-temperature warm plate on the left and a constant-temperature

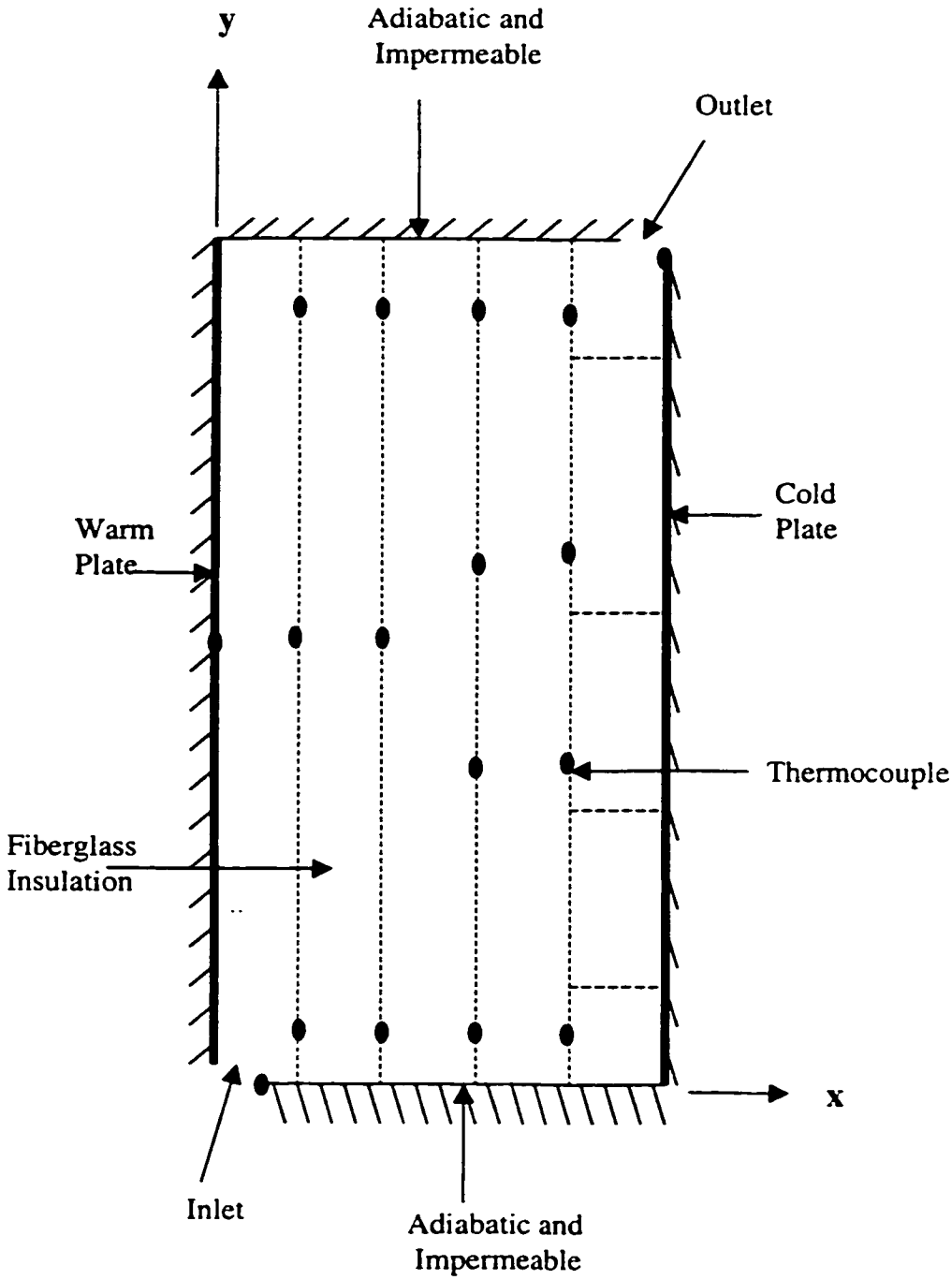


Figure 5.31. Schematic of Experimental Test Cell [ Chen et. al., 1997a]

cold plate on the right, with the horizontal top and bottom boundaries being both impermeable and adiabatic.

The inlet slot was located at the bottom left corner of the cell. It had a length h which was 4% of the width of the test cell and a depth of 275 mm. The exit slot, with the same dimensions as the inlet slot, was located at the top right corner.

The space between the warm and cold plates was filled with five layers of commercially-available medium density fiberglass insulation with total dimensions 275 mm by 600 mm by 135 mm. The measured dry density of the insulation was about 50 kg/m$^3$. The layer of insulation adjacent to the warm plate was 38 mm thick while the other four were each 25 mm thick. After settlement, the boundaries of the layers were located at approximately the following distances from the warm plate: 0 mm, 37 mm, 61 mm, 86 mm, 110 mm, and 135 mm. To measure temperature, a total of 38 thermocouples (type T, calibrated, uncertainty ±0.2°C) were placed between the fiberglass layers, at the inlet/outlet slots, and on the cold plate heat flux meter. The temperature measurement uncertainty was usually ±0.5°C.

The layer adjacent to the cold plate (110 mm to 135 mm from the warm plate), which experienced the largest accumulation of condensate/frost, was pre-cut into five pieces to facilitate the gravimetric determination of the profile of the moisture accumulated within it after 3.5 hours. The boundaries of the five pieces were located at the following heights: 0 mm, 81 mm, 181 mm, 338 mm, 519 mm, and 600 mm. The centers of the five pieces occurred at heights 40.5 mm, 131 mm, 259.5 mm, 428.5 mm, and 559.5 mm, respectively.

A large layer of polyethylene wrap was located on the cold plate to facilitate the collection of the frost deposited on the plate. The polyethylene layer was also pre-cut along the

boundaries of the five pieces of insulation forming the layer adjacent to the cold plate. In this way, it was possible to pull out this layer from the test cell at the end of each test.

The electrically-heated warm plate forming the left boundary of the test cell was maintained at 21.5°C, with an uncertainty of ±1°C. The cold plate forming the right boundary of the test cell was part of a heat exchanger designed to cool the plate to a temperature of -20°C. The heat exchanger consisted of a coolant which removed the heat from the plate, and a heat flux meter to measure the average rate at which the heat was removed by the coolant. The heat flux meter was mounted within the plate and was calibrated, with a measurement uncertainty of ±4.0 $W/m^2$.

The relative humidity of the air at the inlet slot was measured by a calibrated relative humidity sensor (uncertainty ±2% rh), while the volumetric air flowrate was set using a mass flow controller with an uncertainty of ±0.8% of its full range (20 L/min.).

Before each test, the insulation samples were oven-dried at 110°C for 14 hours, then cooled for 4 hours to room temperature while wrapped in polyethylene to prevent contact with moist ambient air. Moisture accumulation at the end of a test was determined by comparing the weight of the oven-dried samples, taken before the test, to the weight including the moisture/frost, taken after the test. The moisture measurement uncertainty was thought to be within ±1% moisture content by dry mass.

### 5.4.3 Numerical Simulation: Equations, Assumptions, Physical Data and Implementation

To simulate the experimental results, the model equations developed in Chapter 3 and Appendix A were applied to the

domain shown in Figure 5.31. The conditions and assumptions given in Sections 3.4 and 3.5 apply to this problem too, except that in this case the medium is not isotropic and the Darcy momentum equations are modified to incorporate the permeabilities used by Chen et al. The finite difference approximations for the equations and boundaries are given in Chapter 4 and Appendix C, respectively. The inlet boundary is assumed to be Dirichlet, while the exit boundary is convective and "free". "Free" here means that the constant-temperature cold plate and the top impermeable and adiabatic boundary are allowed to freely influence the temperature conditions at the exit slot since the slot is small and borders the two other boundaries. Chen et al. made no mention at all of the exit relative humidity value, not even in their numerical model. The assumption made in this numerical investigation is that the last numerical grid cell on the cold plate, at the exit boundary, has a relative humidity of 100%. This assumption proves to be valid because in the final solution this location experiences frosting conditions. The relative humidity assumed at this location and the adiabatic and impermeable top boundary then freely influence the vapour concentration values across the exit boundary in the same manner as for temperature.

In the experimental test cell the slot width was 5.4 mm and the depth was 275 mm. The air flowrates used were 5 L/min., 10 L/min., and 15 L/min. For this two-dimensional simulation project, the slot dimensions are adjusted to 5.4 mm wide by 1000 mm deep. The corresponding equivalent air flowrates for the new dimensions are 18.18 L/min. ($3.03 \times 10^{-4}$ $m^3/s$), 36.36 L/min. ($6.06 \times 10^{-4}$ $m^3/s$), and 54.54 L/min. ($9.09 \times 10^{-4}$ $m^3/s$), respectively.

In the experiments, the desired air flowrate was simply introduced into the test cell through the inlet port. In the numerical simulation, pressure differences which give

approximately the same flowrates have to be found. By imposing trial pressure differences across the test cell and solving the system of equations by the procedure described in Section 4.4, it was determined that air flowrates of $3.03 \times 10^{-4}$ $m^3/s$, $6.06 \times 10^{-4}$ $m^3/s$, and $9.09 \times 10^{-4}$ $m^3/s$ are achieved (approximately) by pressure differences of 22 Pa, 44 Pa, and 66 Pa, respectively.

The parameters (physical data) used in the numerical simulation are summarised below.

Inlet relative humidities: 60%, 70%, 77%, 84%.

Inlet air temperature: 21.5°C.

Warm plate temperature: 21.5°C.

Cold plate temperature : -20°C.

Density of dry insulation: 50 $kg/m^3$.

Porosity of fiberglass insulation: 0.98.

The insulation used in the experiments was not isotropic and the directional permeabilities measured by Chen et al. were $K_x = (1.28 \pm 0.05) \times 10^{-9}$ $m^2$ and $K_y = (2.16 \pm 0.09) \times 10^{-9}$ $m^2$.

The measured directional effective thermal conductivities for dry insulation at 21.5°C were $\lambda_{eff-x} = (0.035 \pm 0.002)$ W/m-K and $\lambda_{eff-y} = (0.034 \pm 0.002)$ W/m-K. For this simulation project, the value adopted for 21.5°C is $\lambda_{eff} = 0.034$ W/m-K. However, SMARC uses variable thermophysical properties and it is therefore essential to distinguish between the thermal conductivities of the solid and the fluid elements in the porous medium. For dry air at 21.5°C, $\lambda_a = 0.0255$ W/m-K (Equation 3.44). Substituting the values of thermal conductivity given above and a porosity $\epsilon = 0.98$ into Equation 3.47 gives the thermal conductivity of the solid elements in the fiberglass insulation as $\lambda_s = 0.451$ W/m-K.

The numerical solution procedure for this example is described in detail in Section 4.4. A control volume approach, with a staggered grid system, is adopted in the discretization of the model equations. Grid refinement to improve accuracy is done along all the four boundaries since in these regions the gradients of the field variables may be high. The finite difference approximations used for the boundaries (Appendix C) are also less accurate than the QUICK scheme which is applied to the interior grid cells. Refining the grid along the boundaries helps improve the accuracy of the boundary FDAs. The number of grid cells used in the x and y directions were 65 and 71, respectively. The successive under-relaxation factor used for the iterative solution was 0.9. The quasi-transient procedure, described in detail in Section 4.5, was implemented for a 30-minute time-step up to a total time of 3.5 hours.

### 5.4.4 Results and Discussion

Figure 5.32 shows that the velocities are high at the narrow inlet but diminish rapidly once the air clears the entrance. The velocities later increase rapidly when the air converges towards the narrow exit slot (Figure 5.33), leaving in a vertical direction. The flow direction in the main body of the cell is mostly vertical, i.e., perpendicular to the near-horizontal pressure contours at the center of the test cell (Figure 5.34). Temperatures are high, and the temperature gradients are low, in about one-half of the cell neighbouring the inlet and the warm plate (Figure 5.35). The temperature gradients increase towards the cold plate and are highest at the exit slot where the contours have the highest concentration.

#### (a) Temperature Profiles

In the numerical simulation, attempts were made to get as many grid cell centers as possible to coincide with the boundaries

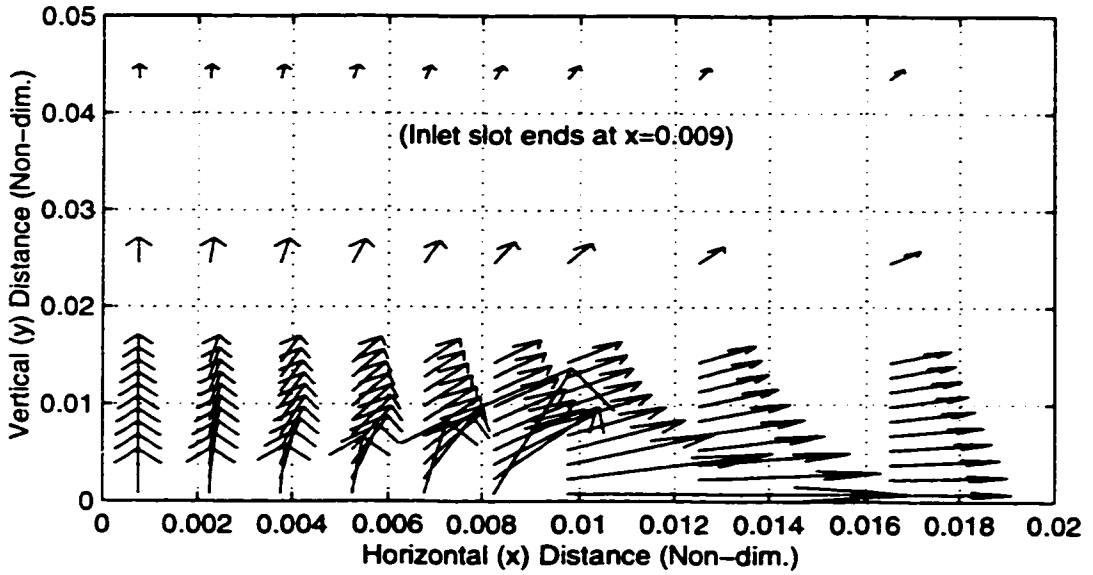


Figure 5.32. Typical Velocity Vectors at Inlet
(Flowrate=36.4 L/min., Inlet RH=84%, Time=3.5 hrs)

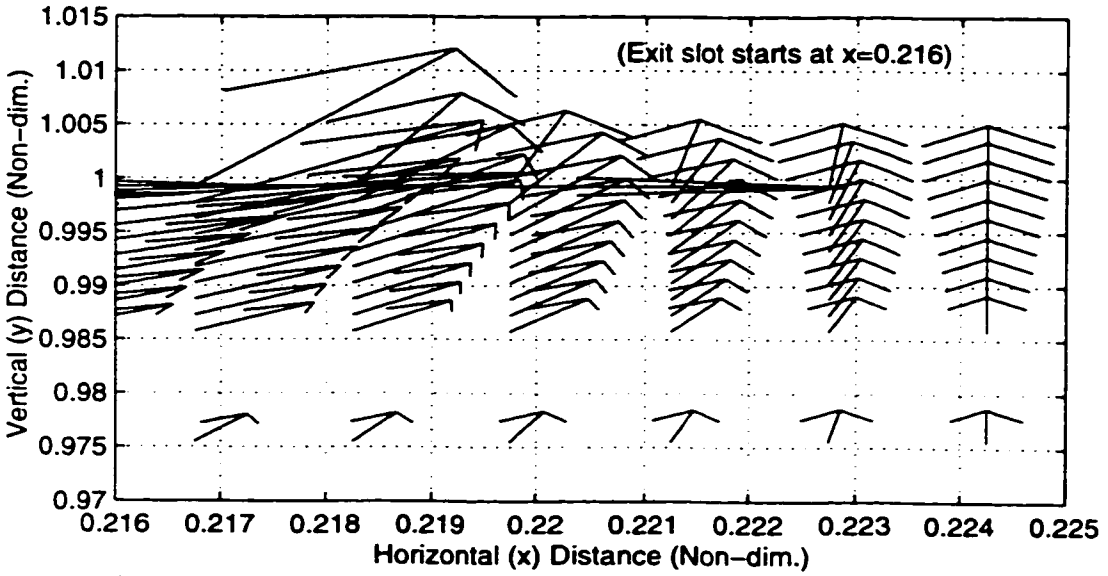


Figure 5.33. Typical Velocity Vectors at Exit
(Flowrate=36.4 L/min., Inlet RH=84%, Time=3.5 hrs)

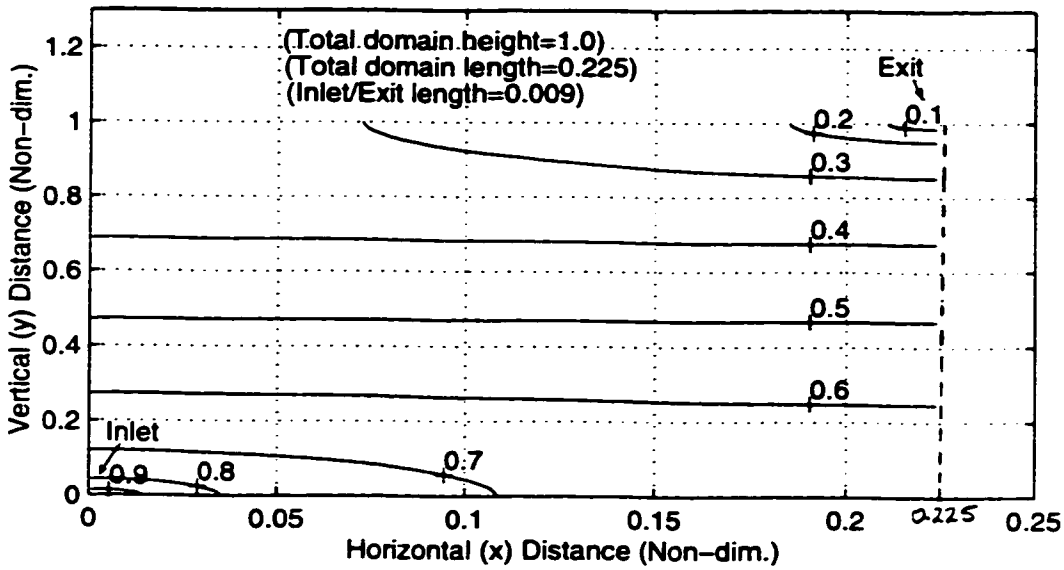


Figure 5.34. Typical Pressure Contours (Non-dim.)
(Flowrate=36.4 L/min., Inlet RH=84%, Time=3.5 hrs)

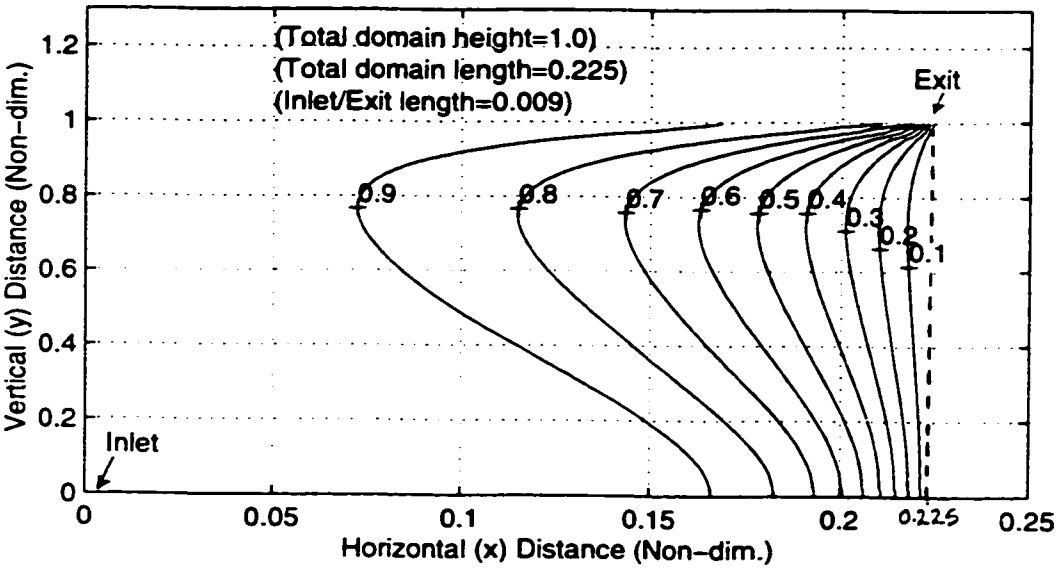


Figure 5.35. Typical Temperature Contours (Non-dim.)
(Flowrate=36.4 L/min., Inlet RH=84%, Time=3.5 hrs)

of the five insulation layers along which the thermocouples were located. In the experimental work, Chen et al. stated that there was an uncertainty with regard to the positioning of the thermocouples which was estimated to be less than 2% of the total length in both the x and y directions.

The following were the approximate locations of the thermocouples:

(1) On (or next to) the warm plate (x≈0 mm), two thermocouples were located at y≈30 mm and y≈300 mm;

(2) Along x≈37 mm, three thermocouples were located at y≈30 mm, y≈300 mm , and y≈570 mm;

(3) Along x≈61 mm, three thermocouples were located at y≈30 mm, y≈300 mm, and y≈570 mm;

(4) Along x≈86 mm, four thermocouples were located at y≈30 mm, y≈210 mm, y≈390 mm, and y≈570 mm;

(5) Along x≈110 mm, four thermocouples were located at y≈30 mm, y≈210 mm, y≈390 mm, and y≈570 mm; and

(6) One thermocouple was placed on the cold plate (x=135 mm), at the centre (y≈300 mm).

Figures 5.36 to 5.40 show temperature profiles in the insulation along the boundaries of the layers, given as x-distances in (1) to (6) above, for specified inlet relative humidities and air flowrates. The simulation profiles are shown with full lines while the thermocouple measurements are marked with error bars. Because of the short duration considered, the simulation temperature profiles for all the times (from the quasi-steady state to 3.5 hours) are indistinguishable from each other. For a given air flowrate and a given relative humidity, the temperature profiles at x-levels removed from the warm plate show that the temperature along an x-level decreases steadily with y-distance for nearly

three quarters of the distance, after which it rises rather steeply towards the top impermeable and adiabatic boundary or the exit slot. The initial decrease occurs because, in the center of the test cell, the air flow is nearly parallel to the plate so that there is hardly any temperature change due to mixing of air streams, yet thermal energy is conducted towards the cold plate from the level. As the top boundary or the exit slot is approached, the air streams converge towards the narror slot, and the mixing of warm air from levels close to the warm plate with colder air from levels closer to the cold boundary causes the temperatures at the latter levels to rise. Level x=0.224 (134.4 mm) represents the centers of the grid cells along the cold plate. The temperature at this level is affected by the mixing process near the exit slot and rises as shown in the figures, unlike the plate temperature which is constant.

A comparison of Figures 5.36, 5.37, and 5.38 reveals that increasing the inlet relative humidity while keeping the air flowrate constant raises the temperatures in the insulation. The increase in temperature is due to an increase in the latent heat from condensation. From Figures 5.36, 5.39, and 5.40, it is observed that keeping the relative humidity constant, while increasing the air flowrate, increases the temperatures. The temperatures increase because the advection heat transfer rate increases.

Discrepancies between simulation and experimental results are largest near the exit slot, where the air flowrates and the temperature gradients are very high. The numerical model performs poorly probably because at such high gradients some of the assumptions made in the model, like Darcy's law and negligible effect from natural convection, may be breaking down. (Chen et al.'s simulation work experienced the same problem.) The absolute errors in the simulation of the temperature profiles are:

(i) 4% for Figure 5.36 (36.4 L/min., 60% inlet RH);

(ii) 4% for Figure 5.37 (36.4 L/min., 70% inlet RH);

(iii) 4% for Figure 5.38 (36.4 L/min., 84% inlet RH);

(iv) 4% for Figure 5.39 (54.5 L/min., 60% inlet RH); and

(v) 2% for Figure 5.40 (18.2 L/min., 60% inlet RH).

The absolute errors given above are approximations since the problem of matching the thermocouple locations to the locations of the grid-cell centers arises in the computations.

(b) Moisture Profiles

In the experiments, moisture measurements were made mainly for the five-piece insulation layer adjacent to the cold plate (i.e., between x=110 mm and 135 mm), where significant condensation/frosting occurred. These measurements were compared with the numerical results obtained by adding the moisture in all the grid cells within each piece. Moisture data were recorded for each quasi-transient time. Figure 5.41 shows the simulation moisture content profiles for different times and the experimental profile for 3.5 hours. The trends are the same: moisture content (% by dry mass) in the layer decreases with distance up to the fourth piece, then increases sharply in the fifth piece which includes the exit. In a large part of the layer before the exit is reached, the air flow is nearly parallel to the cold plate. There is hardly any injection of moisture from the other insulation layers. At each piece, some vapour is condensed so that the piece immediately downstream to it receives air with a smaller vapour concentration. Less vapour concentration leads to a smaller condensation rate and less moisture accumulation, unless the temperature drops drastically between the two adjacent pieces. Near the exit the converging streams of moist air increase the vapour concentrations and the condensation

rates in this layer, in spite of the increase in temperatures discussed earlier.

In the experiments it took more than one hour for the cold boundary to drop from 21.5°C to -20°C, where it was then maintained for the rest of the experiment. It took approximately another one hour after the cold boundary reached -20°C for the quasi-steady stage to be reached. Vafai and Sarkar (1986) and Tao et al. (1991a) reported that the quasi-steady state is attained after about one hour from an initial dry state. This time applies when the boundary conditions are fixed before the air is introduced into the test cell. The simulation procedures used in this investigation assume fixed boundary conditions so that the quasi-steady solution is a function of the steady boundaries. The fact that the cold boundary was transient for more than one hour in Chen et al.'s experiments introduces serious uncertainties when their moisture results after 3.5 hours are to be compared with the simulation results. It is expected that it would take a longer time to attain a given moisture content by experiment than by simulation. The experimental temperature profile would also lag the simulation profile. Indeed, in Figure 5.41 the simulation moisture profile for 3 hours is a better match for the 3.5 hours experimental profile than the simulation profile for 3.5 hours is. The experimental moisture results have an uncertainty of ±1% (by dry mass).

Table 5.6 shows that, for a fixed air flowrate, increasing the inlet relative humidity increases the total condensation rate and also increases the percentage of the vapour (at inlet) which condenses. For a given relative humidity, increasing the air flowrate increases the total condensation rate. The percentage of the inlet vapour which condenses decreases with increasing flowrate because the increase due to advection is relatively larger. Otherwise the absolute quantity of vapour which condenses increases with air flowrate. The increase of

the condensation rate with relative humidity was also reported by Modi and Benner (1985, Part I), Vafai and Tien (1989), Mitchel et al. (1995a), and Ojanen and Kumaran (1996). Ojanen and Kumaran (1996) also reported that the total condensation rate increased with the exfiltration rate, then decreased before abruptly dropping to zero or "drying out".

In the experiments, the pieces of polyethylene sheet between the five pieces of insulation and the cold plate were pulled out and weighed so that the amount of frost deposited on the cold plate could be estimated. The numerical simulation uses the control volume approach where it is assumed that the frost is deposited anywhere within the grid cell adjacent to the cold plate, and there is no way to distinguish between the quantities of frost deposited on the cold plate, on the fibers, and on previously-deposited frost. Therefore, no

Table 5.6. Moisture Accumulation Results for the Insulation Layer Adjacent to the Cold Plate (x=110 to 135 mm).

| Air Flowrate | | Inlet Rel. Hum. (%) | Vapour Condensed (% of inlet) | Total Cond. Rate | |
|---|---|---|---|---|---|
| L/min. | ($x10^{-6}$) kg/s | | | ($x10^{-6}$) kg/s | % Increase |
| 18.2 | 367 | 60 | 73.0 | 2.63 | - |
| | | 84 | 77.6 | 3.90 | +48.3 |
| 36.4 | 721 | 60 | 55.0 | 4.09 | - |
| | | 70 | 57.6 | 5.03 | +23.0 |
| | | 84 | 60.7 | 6.32 | +54.5 |
| 54.5 | 1072 | 60 | 44.3 | 5.05 | - |
| | | 77 | 47.2 | 6.76 | +33.9 |

prediction was attempted for the amount of moisture deposited

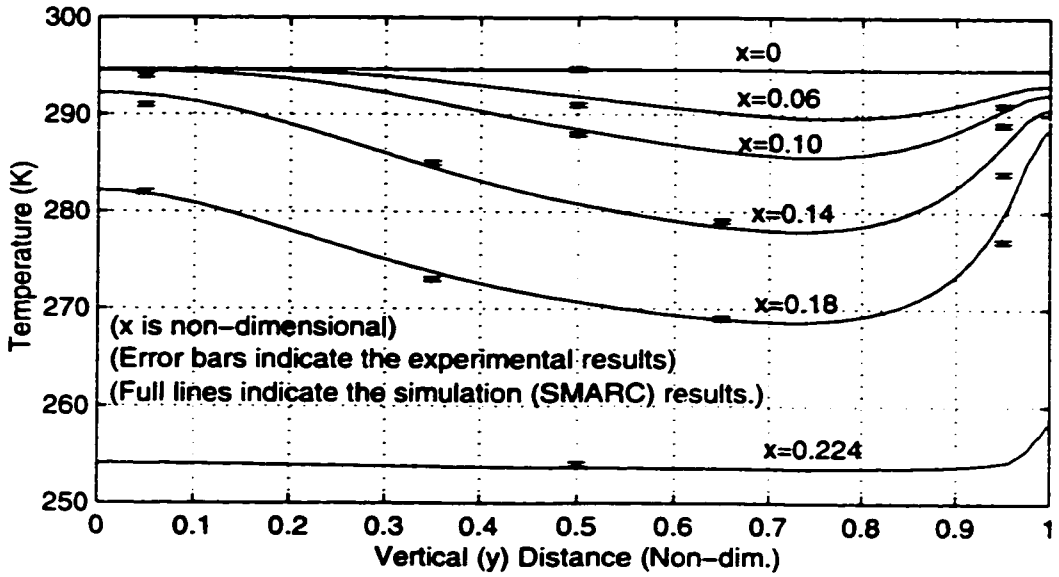


Figure 5.36. Experimental and Simulation (SMARC) Temperature Profiles for a 36.4 L/min. Flowrate, a 60% Inlet RH, and a Time of 3.5 Hours.

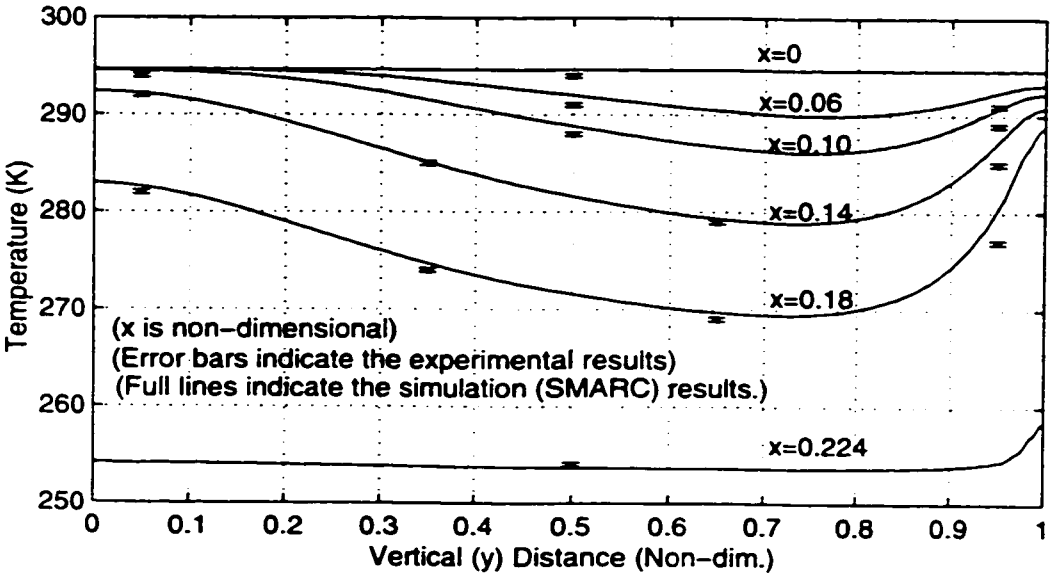


Figure 5.37. Experimental and Simulation (SMARC) Temperature Profiles for a 36.4 L/min. Flowrate, a 70% Inlet RH, and a Time of 3.5 Hours.

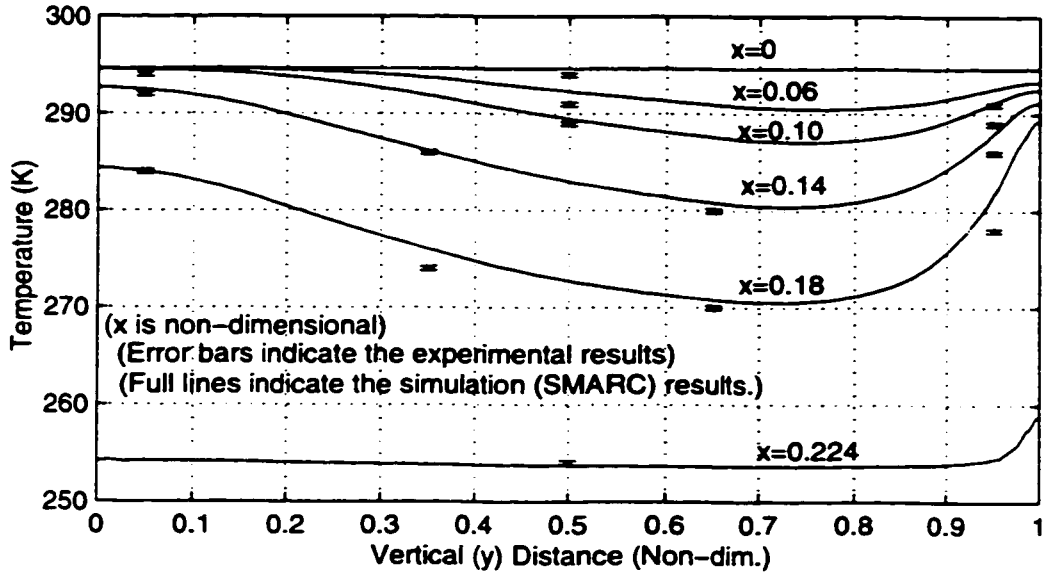


Figure 5.38. Experimental and Simulation (SMARC) Temperature Profiles for a 36.4 L/min. Flowrate, a 84% Inlet RH, and a Time of 3.5 Hours.

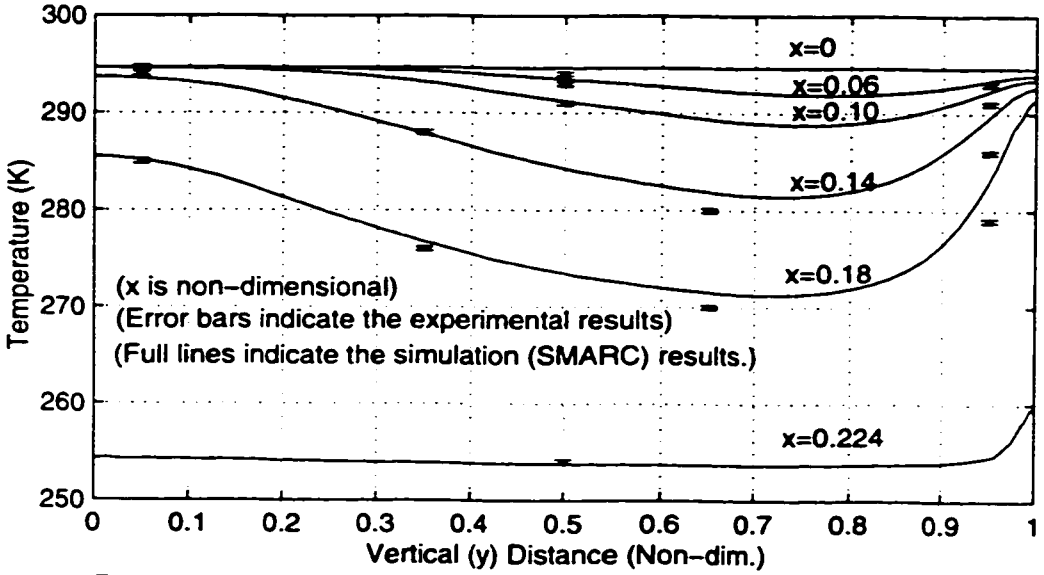


Figure 5.39. Experimental and Simulation (SMARC) Temperature Profiles for a 54.5 L/min. Flowrate, a 60% Inlet RH, and a Time of 3.5 Hours.

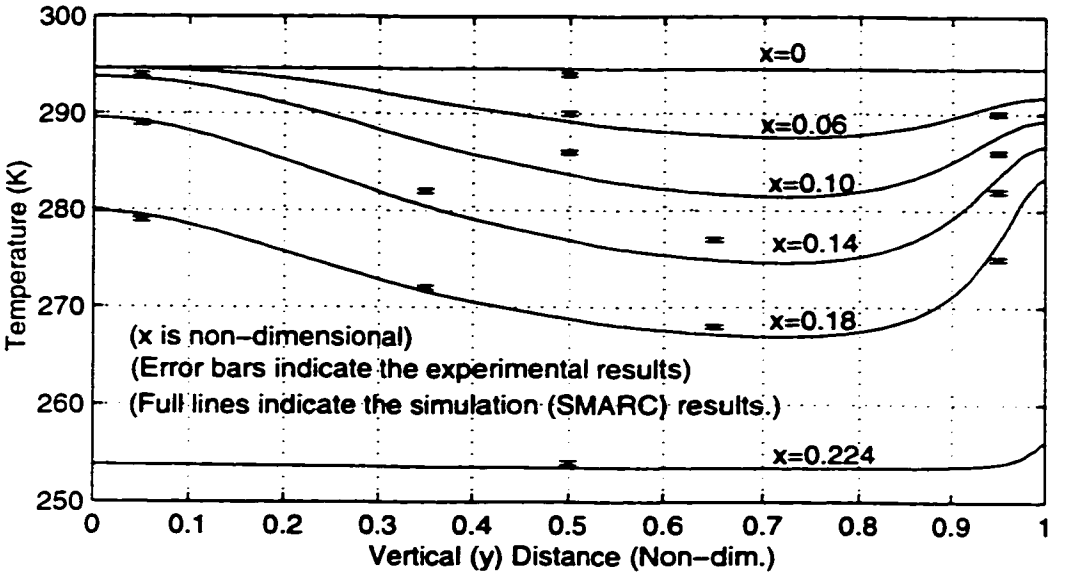


Figure 5.40. Experimental and Simulation (SMARC) Temperature Profiles for a 18.2 L/min. Flowrate, a 60% Inlet RH, and a Time of 3.5 Hours.

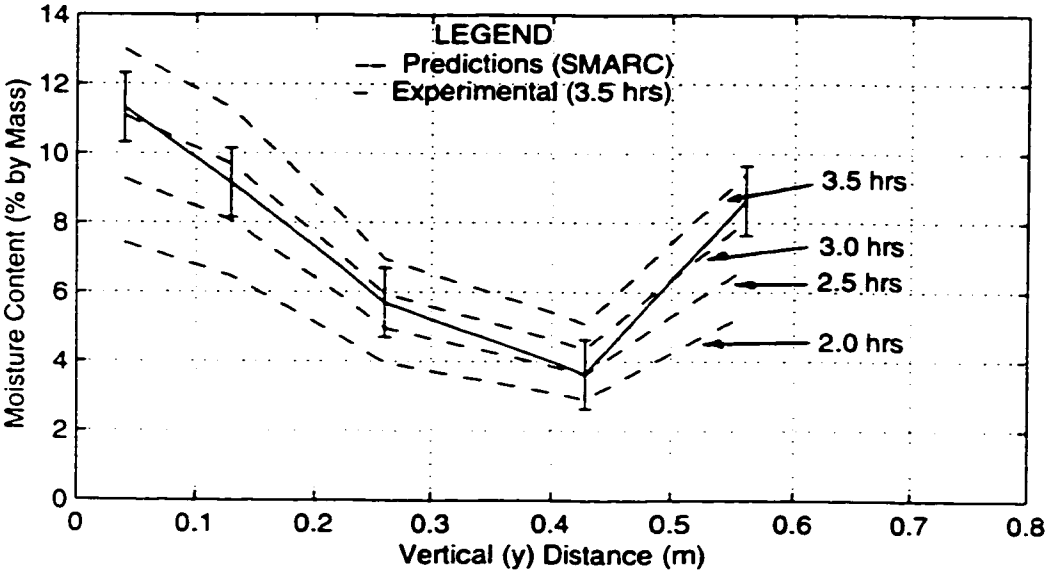


Figure 5.41. Moisture Accumulation Profiles for x-distance from 110 mm to 135 mm. (Flowrate=36.4 L/min., Inlet RH=84%)

on the cold plate only.

(c) Heat Transfer Rates

In the experiments, the heat flux meter gave a reading which was the average for the entire cold plate. In the simulation, the average heat flux for the whole plate is computed from the relationship

$$q'_{av.} \approx \frac{\int_0^D q'(y)\,dy}{D} \tag{5.52}$$

where

$$q'(y) = -\lambda_{eff}(y)\left[\left.\frac{\partial T}{\partial x}\right|_{x=135\ mm}\right](y)$$

In the control volume formulation used, the temperature gradient at the cold plate is estimated by computing its value between the cold plate surface and the center of the grid cell adjacent to the plate. The grid is refined and clustered next to the plate to improve the accuracy of this estimation.

Table 5.7 compares the average conduction heat fluxes through the cold plate obtained from simulation to the measured values (Chen et al., 1997). The measurement uncertainty was ±8% of the value or ±4 W/m$^2$, whichever was larger.

All the simulation results, except those for an air flowrate of 18.2 L/min., are within the experimental uncertainty (i.e., ±8% difference). Chen et al.'s simulation results for 18.2 L/min. were also the worst. The large disparity may be due to combined natural and forced convection occurring in the experiment at low flowrates whereas the model neglects natural convection.

Table 5.8 gives the heat fluxes into and out of the test cell and the latent heat rates due to condensation in the

insulation.

Table 5.7. Experimental and Simulation Average Heat Conduction Rates Through the Cold Plate.

| Air Flowrate (L/min.) | Relative Humidity (%) | Exp. Results ($W/m^2$) | Simulation Results ($W/m^2$) | Difference (%) |
|---|---|---|---|---|
| 18.2 | 60 | 47.9 | 33.8 | +29.4 |
| | 84 | 51.9 | 38.3 | +26.2 |
| 36.4 | 60 | 48.1 | 49.2 | -2.3 |
| | 70 | 49.3 | 52.2 | -5.9 |
| | 84 | 56.4 | 56.2 | +0.4 |
| 54.5 | 60 | 60.6 | 61.4 | -1.3 |
| | 77 | 62.5 | 67.5 | -7.8 |

The heat conduction rate from the warm plate is negligible compared to the total heat transfer rate into the test cell. This is because the temperature gradient at the plate is small. The significance of the conducted heat diminishes when the relative humidity is increased because the temperature in the insulation rises due to the latent heat released, making the temperature gradient at the plate even smaller. For a given relative humidity, the significance of the conducted heat energy at the warm plate decreases with increase in the air flowrate because the temperatures in the insulation increase, reducing the temperature gradients at the warm plate. Besides, the advection component of the total heat flux increases, further diminishing the relative contribution of conduction from the warm plate.

For the conditions considered in this investigation, the heat

conduction rate through the cold plate accounts for between 10.8% and 18.7% of the total transfer rate from the test cell. Latent heat accounts for between 4.2% and 8.7% of the total transfer rate. The percentage due to conduction increases with relative humidity because the rise in temperatures in the insulation increases the temperature gradients at the cold plate. The percentage due to latent heat increases because condensation rates increase with relative humidity. When the air flowrate is increased but the relative humidity is maintained constant, both the percentages due to latent heat and conduction transfer rate through the cold plate decrease because of the much larger increase due to advection heat transfer. Otherwise both conduction and latent heat transfer rates increase in absolute terms.

Table 5.8. Simulation Heat Transfer Rates Into and Out of the Test Cell. (W.P=Warm Plate, C.P.=Cold Plate, L.H.=Latent Heat)

| Air Flowrate | | Inlet RH (%) | Heat Into Test Cell | | Heat Out of Test Cell | | |
|---|---|---|---|---|---|---|---|
| L/min. | kg/s ($x10^{-6}$) | | Total (W) | W.P. (% of Tot.) | Total (W) | C.P. (% of Tot.) | L.H (% of Tot.) |
| 18.2 | 367 | 60 | 113.5 | 1.81 | 120.5 | 16.8 | 6.1 |
| | | 84 | 113.3 | 1.52 | 123.5 | 18.7 | 8.7 |
| 36.4 | 721 | 60 | 219.8 | 0.39 | 231.8 | 12.7 | 5.0 |
| | | 70 | 219.8 | 0.36 | 233.7 | 13.4 | 6.0 |
| | | 84 | 219.6 | 0.32 | 236.3 | 14.3 | 7.3 |
| 54.5 | 1072 | 60 | 325.5 | 0.11 | 341.6 | 10.8 | 4.2 |
| | | 77 | 325.5 | 0.10 | 345.6 | 11.7 | 5.4 |

### 5.4.5 Sources of Error

There are three types of errors which affect the accuracy with which the experimental results are simulated. These are experimental errors, numerical errors, and "matching" errors.

Experimental errors were addressed by Chen et al. through the specification of measurement uncertainties. At low flowrates, the numerical errors are relatively large and cause the simulation model to perform poorly. At the low flowrates the problem becomes one involving combined flow. That is, natural convection becomes significant relative to forced convection and both transfer mechanisms should then be included in the model in order to obtain good results. "Matching" errors were of most concern in the course of this investigation. It is extremely difficult to match all thermocouple positions in the experiment with the centers of numerical grid cells simultaneously. The same difficulty applies to the boundaries of the various layers and pieces of insulation, all of which need to be matched when estimating the moisture contents. The use of the control volume approach with staggered grids in the numerical scheme also ensures that it is only possible to plot the field variables at the grid cell centers.

### 5.4.6 Conclusion

This example has shown that SMARC with the quasi-transient procedure may be used as a reasonably reliable and effective alternative to the fully-transient method when solving two-dimensional forced-convective problems with high exfiltration rates for the quasi-steady state and later times. The simulation temperature profiles, moisture profiles, and conduction heat transfer rates through the cold plate compare quite well with the experimental results, except when the local air speeds, heat transfer rates and moisture accumulation rates are small, and also in regions where the local temperature gradients and local velocity gradients are

very large.

## 5.5 Summary

The three examples in this chapter have validated the Saturation Method for the Approximation of the Rate of Condensation (SMARC) and the quasi-transient numerical procedure for one and two-dimensional problems. It has been shown that varying the thermophysical properties with temperature is important; it improves the results for the temperature profile and the moisture condensation rates.

SMARC and the quasi-transient procedure will be used in the next chapter to investigate the problem of condensation at slits in open attic insulation.

# CHAPTER 6

# MOISTURE DEPOSITION IN ATTIC FIBROUS INSULATION

## 6.1 Introduction

In this chapter, conditions which promote the deposition of moisture in the vicinity of leakage sites in the attic insulation are investigated. The geometry considered is the slit and the flow domain and boundaries are shown in Figure 3.3. Investigations are carried out for different opening sizes, pressure differences, inlet and exit relative humidities, and different exit temperatures. The inlet temperature is fixed at 293 K and the insulation material is fiberglass with a porosity value of 0.97. Properties of the materials in the flow domain are given in Section A.2.

The full model equations for the simultaneous air, heat and mass transfer developed in Chapter 3 are applied. The Soret and Dufour effects are excluded since it was shown in Chapter 5 that these are insignificant in comparison to the main transport terms. The exclusion of natural convection from the investigation is justified by the analysis given in Appendix E, where it is shown that the maximum possible Darcy-modified Rayleigh number for the highest temperature difference considered in this project is too small to cause convective instabilities in the far-field of the flow domain. Inlet boundary conditions are assumed to be Dirichlet, while the exit conditions are forced convective for both heat and mass transfer.

The flow domain is symmetrical and, therefore, the numerical solution was applied to only half the domain, with a slit leghth of 1 m. The control volume approach and the QUICK scheme were applied in the iterative solution of the equations which were discretized and solved as described in Chapter 4.

Three levels of refinement were used in the x-direction; the finest grid was within the slit, followed by a less fine grid up to a distance x=0.2 m, and the remaining length (up to x=0.5 m), where the gradients of temperature and pressure were lowest, had the least refinement. It had been determined that in all the cases considered the gradients became quite low after a distance x=0.2 m. Uniform grids were used in the y-direction since the distance is short compared to the x-direction. Grid refinement was done until the globally-balanced heat and mass transfer rates changed by less than 0.5% with any further refinement. The total number of grid cells in each direction and within each refinement level in the x-direction, required to achieve this condition, depended mainly on the temperature and pressure gradients. Regions with high gradients required finer grids than low-gradient regions, hence the grids were finest in the y-direction and within the slit in the x-direction. Tests carried out with the highest pressure difference (30 Pa) and the highest temperature difference (60 K) showed that a total of 91 grid cells in each direction gave sufficient refinement. The 91x91 grid for the half-domain was then used in all the numerical simulations. In the x-direction, the number of grid cells within a half-slit depended on the slit width: 10 grid cells in 3 mm; 18 grid cells in 7 mm; 20 grid cells in 11 mm; 24 grid cells in 15 mm; and 27 grid cells in 20 mm. 41 grid cells, in each case, were located between x=0 m and x=0.2 m, the remaining cells, from a total of 91, being distributed uniformly between x=0.2 m and x=0.5 m.

The quasi-steady solution method, validated in Chapter 5, is used to study how the boundary conditions influence moisture condensation; then a set of boundary conditions is selected to investigate how moisture accumulation affects the field variables beyond the "initial" or quasi-steady stage. The latter investigation is carried out using the new quasi-

transient procedure described in Section 4.5.

In this chapter the field variables, the condensation rates, the liquid contents, the heat transfer rates at the exit, and the latent heats are examined for specific cases. The reader is referred to Chapter 7 for general estimates of bulk air flowrates and total heat transfer rates.

## 6.2 Quasi-steady Results for Slits

All the results in this chapter were obtained for a slit length of 1 m.

### 6.2.1 Typical Profiles of Field Variables

Figure 6.1 shows typical inlet velocity vectors. The magnitudes are largest close to the edge of the opening, while the directions are perpendicular to the pressure contours. Figure 6.2 shows typical temperature contours (isotherms). High air flowrates at the inlet enhance thermal penetration into the fiberglass; the penetration is indicated by the upward curvature of the temperature contours. Indeed, the extent of the influence of the opening can be gauged by how much into the flow-field the contours are curved. In regions which are remote from the opening, the effect of the opening is negligible and the temperature contours are approximately horizontal, this being an indication that conduction is the dominant mode of heat transfer in the "remote" regions.

The contours of other variables which are temperature-dependent (i.e., total air density, specific heat capacity at constant pressure, saturation vapour density, dynamic viscosity, vapour diffusion coefficient, and thermal conductivity) are similar to the contours of temperature. It was found that the variation in properties over the temperature range 298 K to 233 K was at most 34% (for the vapour diffusion coefficient). Vapour distribution in the flow-field depends mainly on the air-flow characteristics. The

actual vapour density contours run along the pressure contours in regions where there is no condensation (Figure 6.3). However, in regions with condensation the actual vapour density contours and the saturation vapour density contours coincide and run along the temperature contours (Figure 6.3). The "wet" region can be identified in Figure 6.3 by this coincidence of the saturation and actual vapour densities. The condensate volume fraction contours, shown in Figure 6.4, also give an approximation of the extent of the wet zone; the "kinks" on the contours mark the liquid-frost interface or the 273.15 K (0°C) temperature contour. Regions with liquid volume fractions less than $10^{-6}$ would be considered to contain adsorbed moisture rather than condensate [Langlais, 1982].

6.2.2 Effect of Increasing the Pressure Difference

Table 6.1 shows that increasing the pressure difference increases the air flowrate, the total condensation rate, the total heat transfer rate at the exit, and the total latent heat rate.

High air flowrates:

(1) increase the total heat transfer rate at both the inlet and exit by increasing the advective component; and

(2) introduce vapour into the fiberglass insulation at a fast rate, resulting in increased vapour densities/concentrations and, hence, increased total condensation rates and increased total latent heat rates.

However, the increase in the total condensation rate is not indefinite because, as shown in Example 2 (Section 5.3), at certain high air flowrates the wet zone starts shrinking and eventually dries out completely at much higher flowrates.

A comparison between Figures 6.5 and 6.6 shows that the pressure difference also affects the moisture distribution in

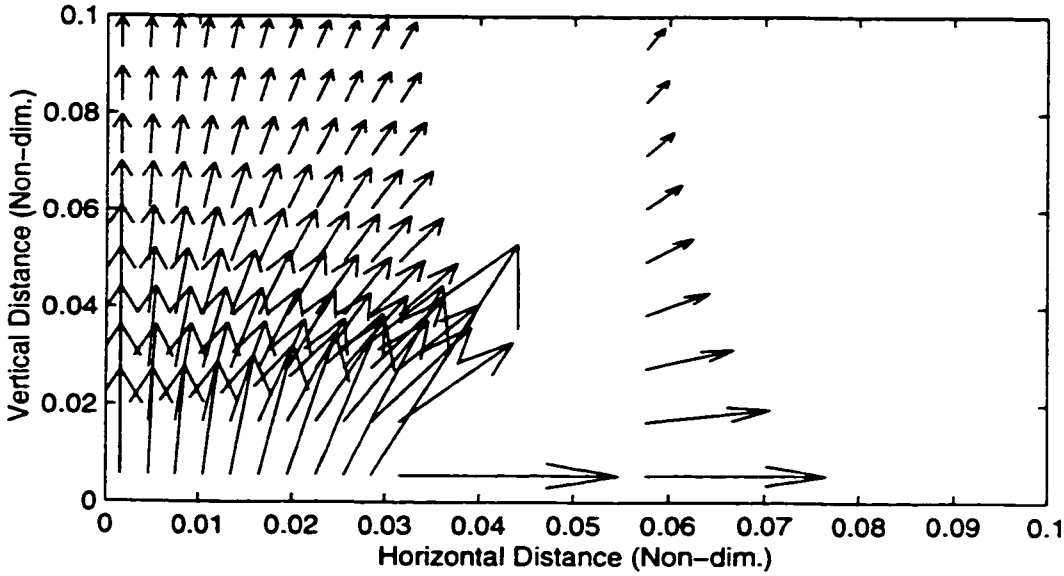


Figure 6.1. Typical Inlet Velocity Vectors.
(Slit Width = 6 mm, Pressure Difference = 8 Pa)

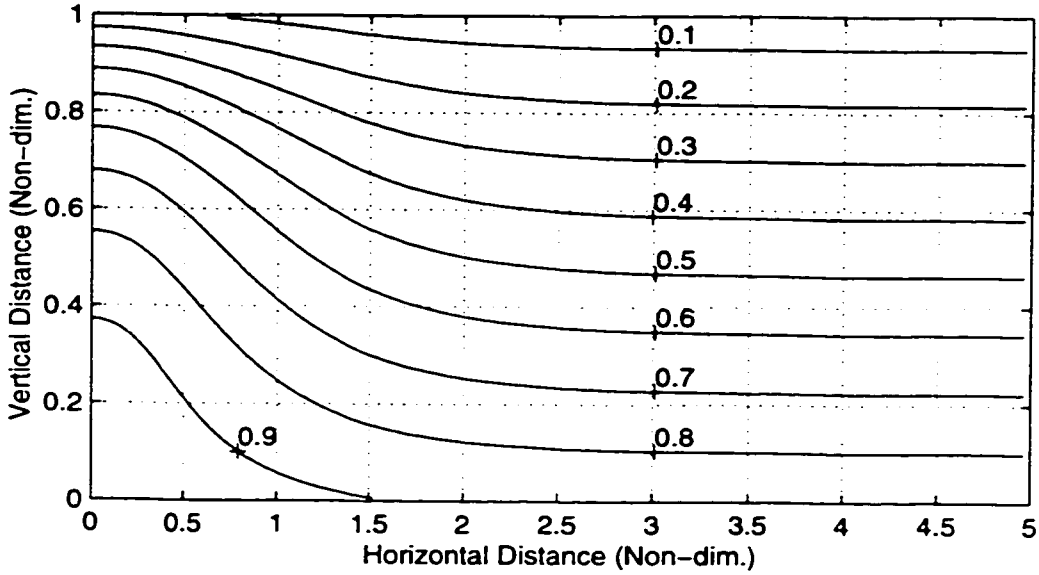


Figure 6.2. Typical Temperature Contours (Non-dim.).
(Slit Width = 6 mm, Pressure Difference = 8 Pa, Exit Temp. = 233 K)

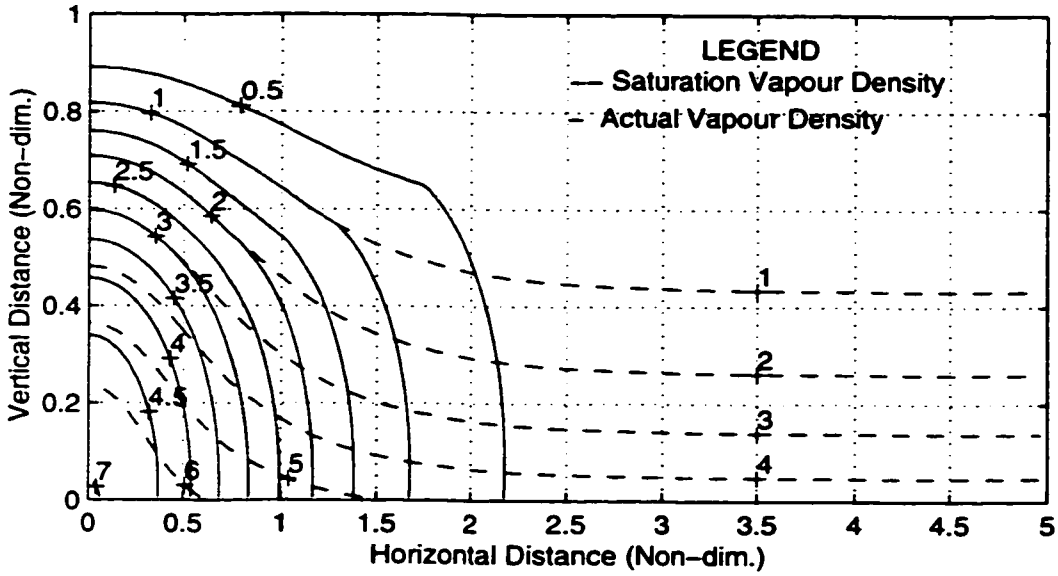


Figure 6.3. Typical Vapour Density Contours (Non-dim.).

(Slit Width=6 mm, Press. Diff.=8 Pa, Ex. Temp.=233 K, In. RH=70%, Ex. RH=100%)

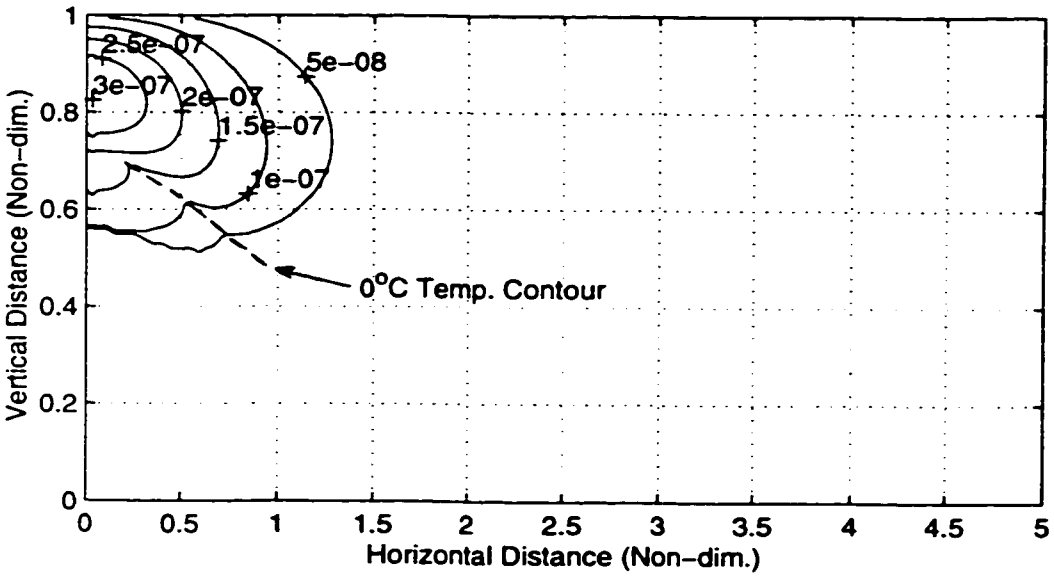


Figure 6.4. Typical Condensate Volume Fraction Contours (Non-dim.).

(Slit Width=6 mm, Press. Diff.=8 Pa, Ex. Temp.=233 K, In. RH=70%, Ex. RH=100%)

the insulation, besides increasing the total condensation rate. As the pressure difference increases, the wet-dry interface shifts towards the exit. This shift occurs because of increased thermal penetration (Figure 6.2) which delays the attainment of saturation conditions as the air flows through the insulation. A similar occurrence was experienced with the one-dimensional case (Example 2, Section 5.3).

Table 6.1. Effect of Pressure Difference on Quasi-steady Heat and Mass Transfer Rates: Exit Temperature is 233 K, Slit Width is 6 mm, Inlet Relative Humidity is 70%, and Exit Relative Humidity 100%. ($Q_{g,out}$ is exit bulk air flowrate, $Q_c$ is total condensation rate, $H_{s,out}$ is exit total heat transfer rate, and $H_L$ is total latent heat released.)

| Press. Diff., $\Delta P$ (Pa) | Mass Flowrates | | Heat Transfer Rates | |
|---|---|---|---|---|
| | $Q_{g,out}$ ($\times 10^{-6}$) kg/s | $Q_c$ ($\times 10^{-6}$) kg/s | $H_{s,out}$ (W) | $H_L$ (W) |
| 2 | 48.0 | 0.35 | 36.8 | 1.00 |
| 8 | 186.1 | 1.46 | 78.0 | 4.07 |
| 14 | 322.1 | 2.49 | 119.7 | 6.90 |
| 20 | 457.7 | 3.44 | 161.6 | 9.49 |
| 30 | 683.6 | 4.82 | 231.4 | 13.23 |

From Table 6.1 it is noted that, for each 1 Pa increase in the pressure difference:

(1) the average increase in the air flowrate at the exit is $22.7 \times 10^{-6}$ kg/s (47% of the value for 2 Pa);

(2) the average increase in the total condensation rate is $0.16 \times 10^{-6}$ kg/s (45.7% of the value for 2 Pa);

(3) the average increase in the total heat transfer rate at the exit is 6.95 W (18.9% of the value for 2 Pa); and

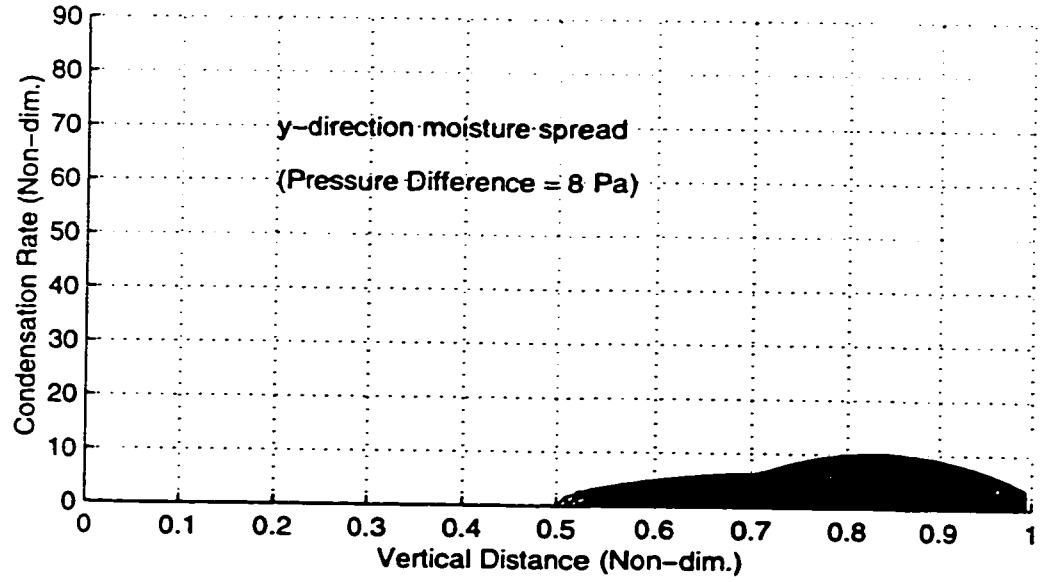


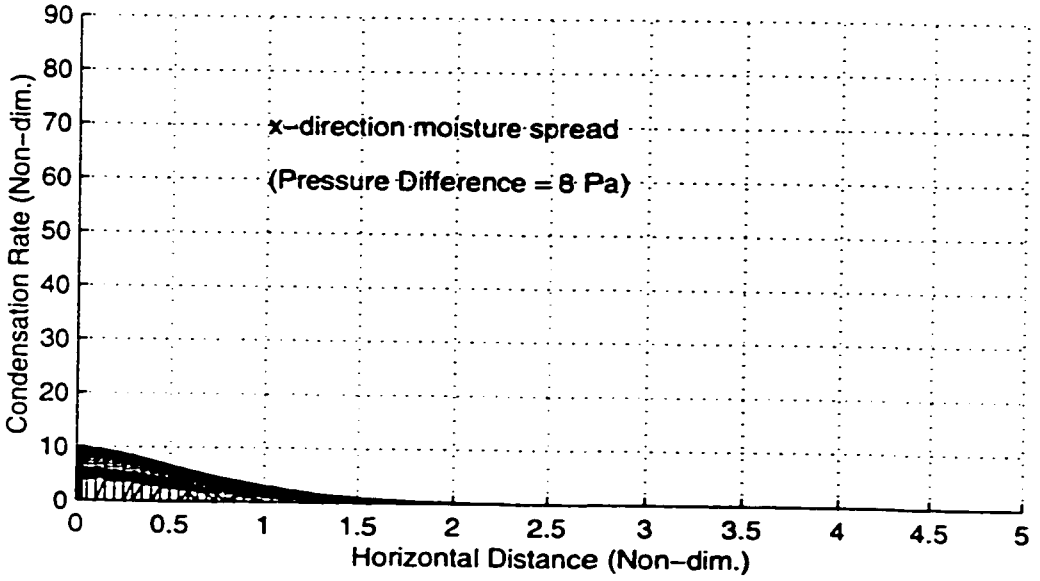


Figure 6.5. Condensation Rate Profiles (x and y direction) for 8 Pa.
(Slit Width=6 mm, Exit Temp.=233 K, Inlet RH=70%, Exit RH=100%)

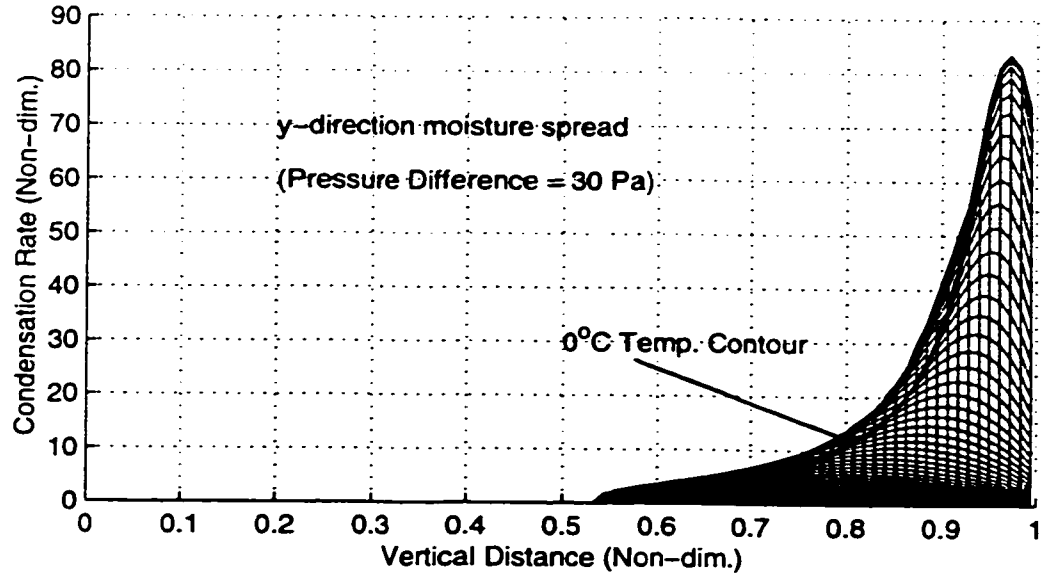


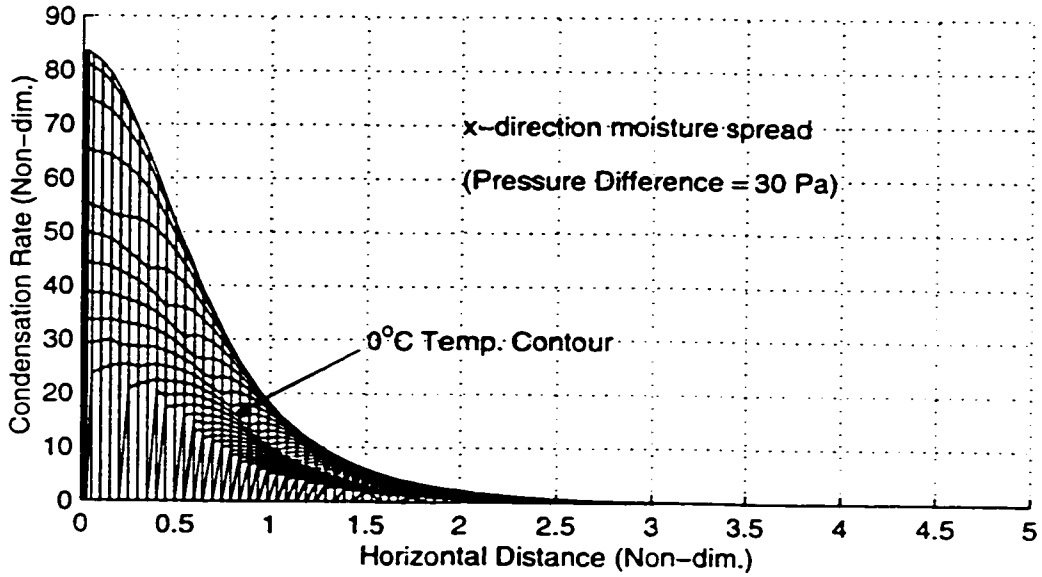


Figure 6.6. Condensation Rate Profiles (x and y direction) for 30 Pa.
(Slit Width=6 mm, Exit Temp.=233 K, Inlet RH=70%, Exit RH=100%)

(4) the average increase in the total latent heat transfer is 0.45 W (45% of the value for 2 Pa).

Ojanen and Kumaran (1996) reported that the total condensation rate increased with the exfiltration rate before decreasing, and then dropping abruptly to zero or "drying out".

### 6.2.3 Effect of Increasing the Inlet Relative Humidity

Increasing the inlet relative humidity increases the vapour density in the flow domain. Some regions which would not be saturated with vapour at a lower inlet relative humidity become saturated, the wet zone expands towards the inlet as seen when Figures 6.7 and 6.8 are compared, and the peak of the condensation rate profile drops.

In Table 6.2, the difference between the exit total heat transfer rate, $H_{s,out}$, and the total latent heat rate, $H_L$, (i.e., $H_{s,out}-H_L$) decreases very little as the inlet relative humidity is increased. This difference represents the total heat transfer rate at the inlet; its small decrease indicates that the increase in $H_{s,out}$ when the inlet relative humidity, $RH_{in}$, increases, is largely due to the increase in the latent heat rate, $H_L$. It is not expected that the inlet temperature gradient and the advective heat would be greatly affected by the inlet relative humidity. The bulk air flowrate at the exit, $Q_{g,out}$, decreases with increasing $RH_{in}$ due to the increase in the total condensation rate, while the bulk air in-flowrate is approximately constant. The increase in the total rate of condensation is not obvious from Figures 6.7 and 6.8, but comes out when a summation of the local rates is done.

Computations based on Table 6.2 show that, on average, for each 1% increase in the inlet relative humidity:

(1) the bulk air flowrate at the exit, $Q_{g,out}$, decreases by $0.04 \times 10^{-6}$ kg/s (0.02% of the value for 40% rh);

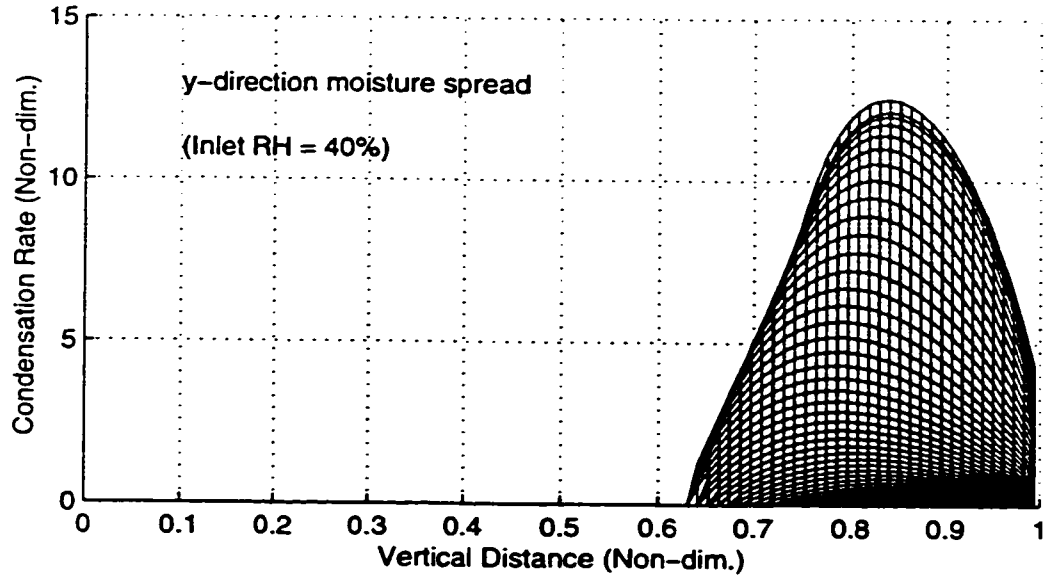


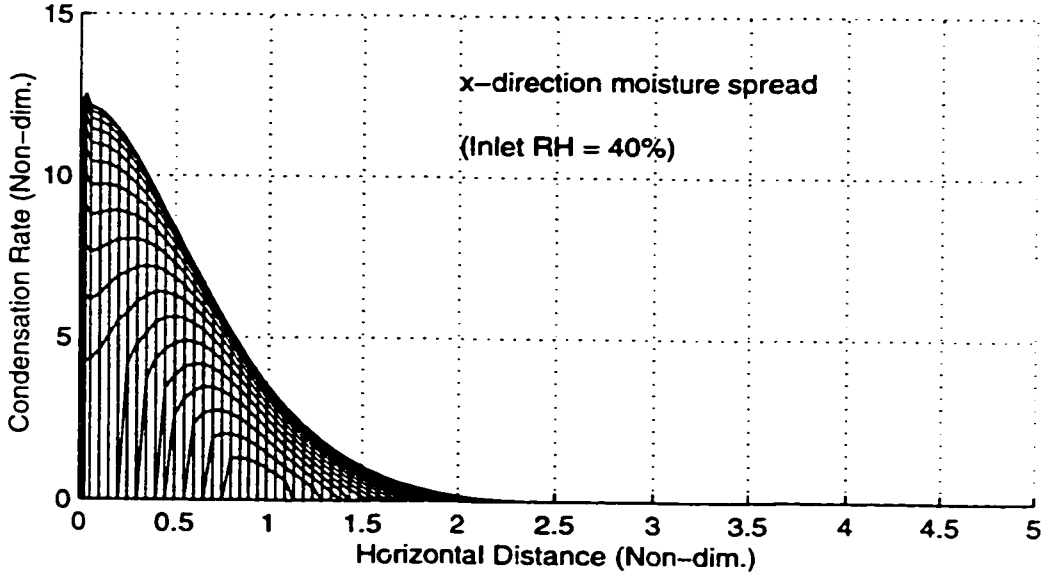


Figure 6.7. Condensation Rate Profiles (x and y direction) for 40% Inlet RH. (Slit Width=6 mm, Press. Diff.=8 Pa, Exit Temp.=233 K, Exit RH=100%)

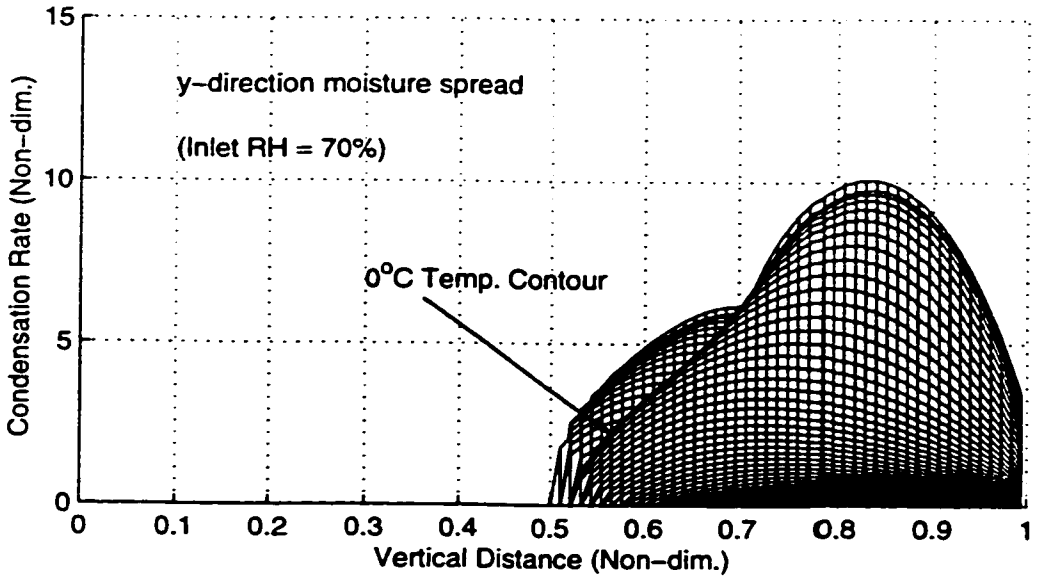


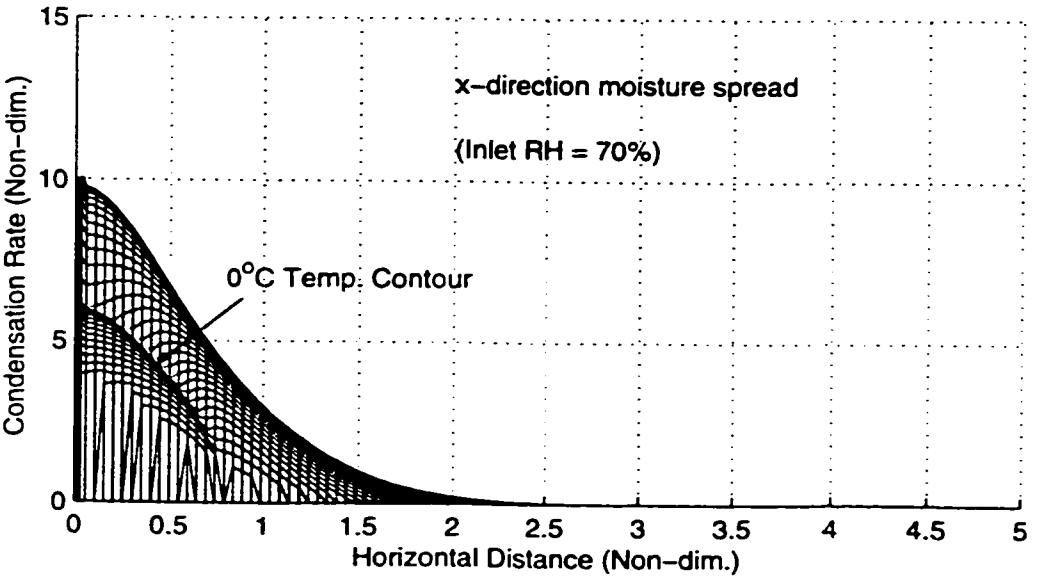


Figure 6.8. Condensation Rate Profiles (x and y direction) for 70% Inlet RH. (Slit Width=6 mm, Press. Diff.=8 Pa, Exit Temp.=233 K, Exit RH=100%)

(2) the total condensation rate, $Q_c$, increases by $0.024 \times 10^{-6}$ kg/s (3.3% of the value for 40% rh);

(3) the total heat transfer rate at the exit, $H_{s,out}$, increases by 0.044 W (0.06% of the value for 40% rh); and

(4) the latent heat rate, $H_L$, increases by 0.066 W (3.2% of the value for 40% rh).

Table 6.2. Effect of Inlet Relative Humidity on Quasi-steady Heat and Mass Transfer Rates: Exit Temperature is 233 K, Slit Width is 6 mm, Pressure Difference is 8 Pa, and Exit Relative Humidity is 100%. ($Q_{g,out}$ is exit bulk air flowrate, $Q_c$ is total condensation rate, $H_{s,out}$ is exit total heat transfer rate, and $H_L$ is total latent heat released.)

| Inlet RH, $RH_{in}$ (%) | Mass Flowrate | | Heat Transfer rate | |
|---|---|---|---|---|
| | $Q_{g,out}$ ($\times 10^{-6}$) kg/s | $Q_c$ ($\times 10^{-6}$) kg/s | $H_{s,out}$ (W) | $H_L$ (W) |
| 40 | 187.3 | 0.73 | 76.7 | 2.07 |
| 50 | 186.9 | 0.97 | 77.2 | 2.75 |
| 60 | 186.5 | 1.21 | 77.6 | 3.42 |
| 70 | 186.1 | 1.46 | 78.0 | 4.07 |
| 80 | 185.7 | 1.70 | 78.4 | 4.71 |

Modi and Benner (1985, Part I), Vafai and Tien (1989), Mitchel et al. (1995a), and Ojanen and Kumaran (1996), all reported increases in the condensation rates when the inlet relative humidity was increased.

Inlet relative humidities in conditioned spaces normally range from 35% to 70%, depending on the purpose of the building. The total condensation rate in Table 6.2 increases by about 100% when the inlet relative humidity is increased from 40% to 70%. This is quite a significant increase. The International Agency

Annex XIV (1991) recommends the limiting of indoor relative humidities to less than 70% to prevent the growth of mold. This limit also helps reduce the amount of condensate in the insulation if there are leakage paths. It is therefore important to study the effects of varying the inlet relative humidity.

The effect of varying the exit relative humidity from 20% to 100% was also studied. As expected, the effect of the variation on the heat and mass transfer rates was found to be negligible. Only the magnitude of the local condensation rate at the exit appeared to be affected, but negligibly.

### 6.2.4 Effect of Increasing the Slit Width

The sizes and locations of slits in a building envelope vary greatly and are mostly beyond the control of anyone. Most of the slits are very small; a 6 mm wide slit would be considered to be large. Computations with small slits and small pressure differences tended to incur large percentage numerical errors, seen in poor global balance numbers with respect to moisture. To investigate whether there is any correlation between slit width and the heat and mass transfer rates, and at the same time minimise the impact of computational errors on the results, large slit widths of up to 40 mm were used.

Increasing the slit width increases the bulk air flowrate. Water vapour is introduced into the insulation in larger quantities, resulting in higher vapour densities. Regions which would otherwise be below vapour saturation levels become saturated and both the total condensation rate and latent heat rate increase. The total heat transfer rate at the exit increases mainly due to increased advection of warm air .

Figures 6.9 and 6.10 show the effect of increasing the slit width on moisture distribution. The local condensation rates increase in magnitude, but the wet-dry interface shifts

slightly towards the exit due to increased thermal penetration caused by the higher bulk air flowrate. Temperatures in the insulation rise, and the local saturation vapour pressures and saturation densities increase, delaying the onset of condensation in regions near the inlet. This explanation is similar to the one given in Section 6.2.2 for increasing the pressure difference. However, the effects of the two variables have to be investigated separately because, unlike the pressure difference, the variations in slit width cause the heat and mass transfer rates to vary in a non-linear way, as can be determined from the data in Table 6.3, so that no constant value can be assigned as a change due to unit increase in the slit width. Moreover, the magnitudes of the impact of the two variables on heat and mass transfer rates are different; the effect of increasing the slit width by 1 mm is much smaller than the effect of increasing the pressure difference by 1 Pa. For the range of data given in Table 6.3 the values given below may be used as representative rough estimates.

(1) The bulk air flowrate, $Q_{g,out}$, increases by approximately $4.4 \times 10^{-6}$ kg/s (2.4% of the value for 6 mm) per mm increase in the slit width.

(2) The total condensation rate, $Q_c$, increases by approximately $0.034 \times 10^{-6}$ kg/s (2.3% of the value for 6 mm) per mm increase in the slit width.

(3) The total heat transfer rate at the exit, $H_{s,out}$, increases by 1.36 W (1.7% of the value for 6 mm) per mm increase in the slit width.

(4) The latent heat released, $H_L$, increases by 0.09 W (2.2% of the value for 6 mm) per mm increase in the slit width.

The increases in the transfer rates per mm increase in the slit width actually decrease gradually with increasing slit

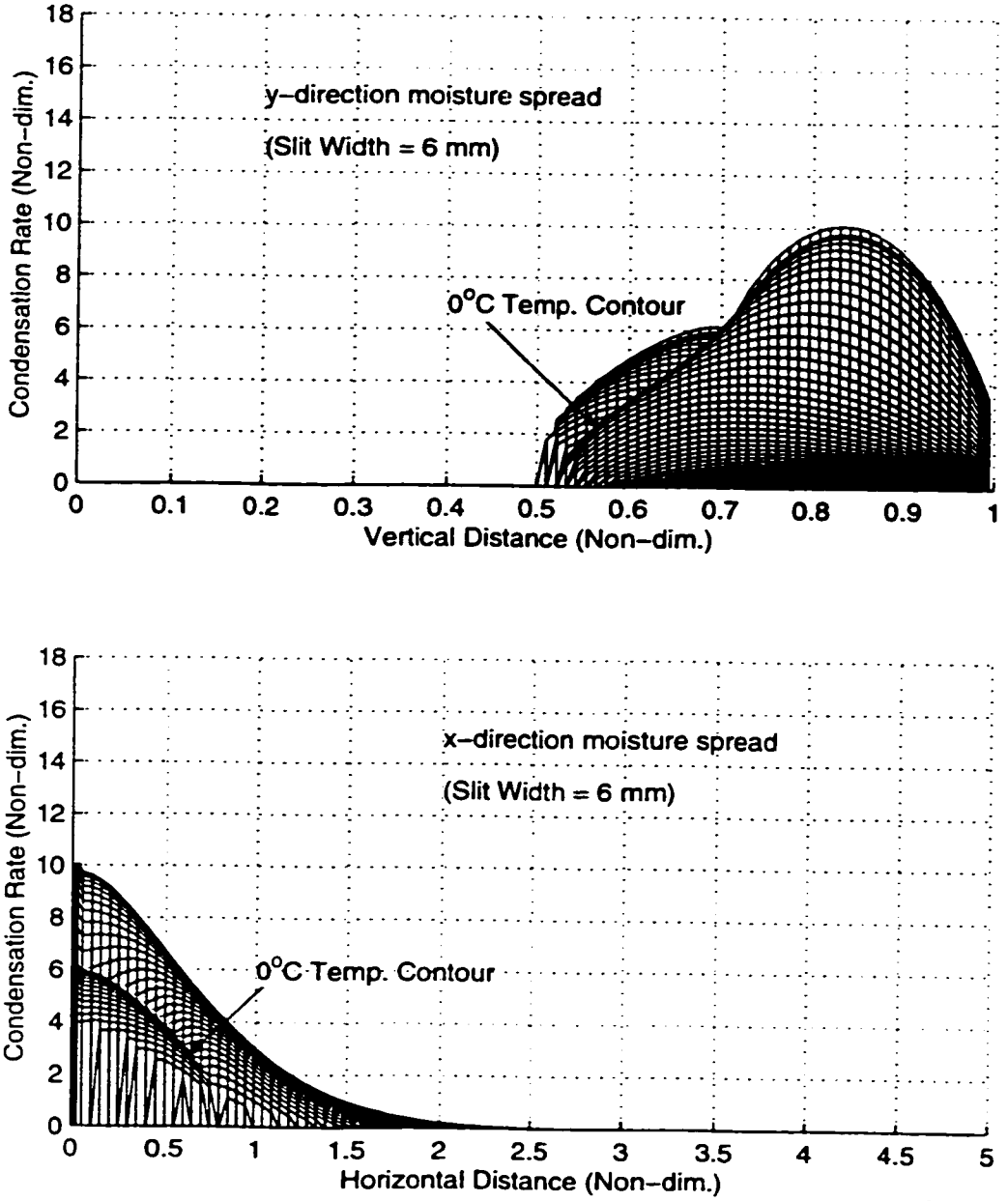


Figure 6.9. Condensation Rate Profiles (x and y direction) for 6 mm Slit Width. (Press. Diff.=8 Pa, Exit Temp.=233 K, Inlet RH=70%, Exit RH=100%)

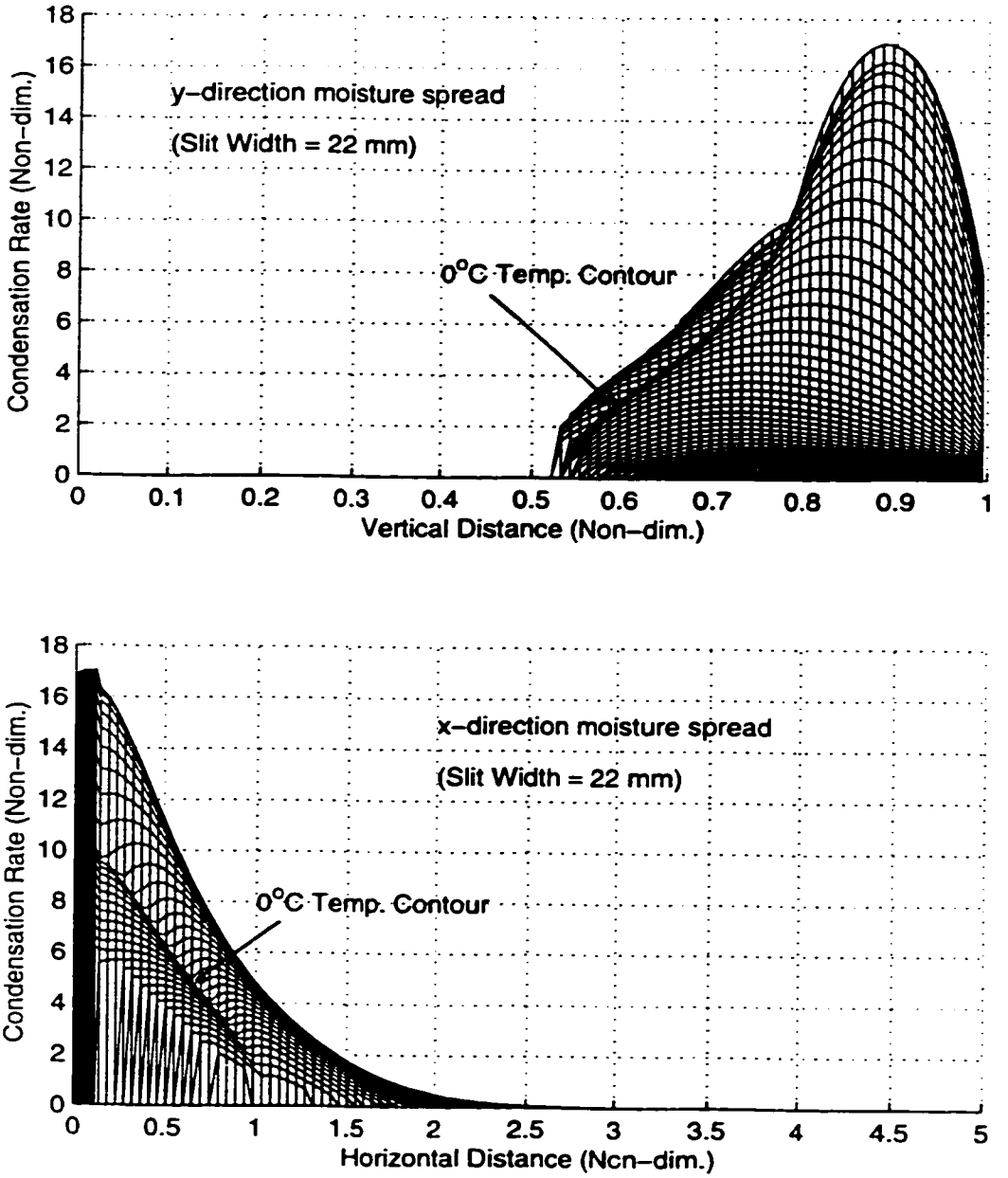


Figure 6.10. Condensation Rate Profiles (x and y direction) for 22 mm Slit Width. (Press. Diff.=8 Pa, Exit Temp.=233 K, Inlet RH=70%, Exit RH=100%)

width. Bulk air flowrates for different opening areas and pressure differences can be estimated more accurately from the power law pressure-flow relationship given in Chapter 7.

Table 6.3. Effect of Slit Width on Quasi-steady Heat and Mass Transfer Rates: Exit Temperature is 233 K, Pressure Difference is 8 Pa, Inlet Relative Humidity is 70%, and Exit Relative Humidity is 100%. ($Q_{g,out}$ is exit bulk air flowrate, $Q_c$ is total condensation rate, $H_{s,out}$ is exit total heat transfer rate, and $H_L$ is total latent heat released.)

| Slit Width, dl (mm) | Mass Flowrates | | Heat Transfer Rates | |
|---|---|---|---|---|
| | $Q_{g,out}$ ($\times 10^{-6}$) kg/s | $Q_c$ ($\times 10^{-6}$) kg/s | $H_{s,out}$ (W) | $H_L$ (W) |
| 6 | 186.1 | 1.46 | 78.0 | 4.07 |
| 14 | 235.1 | 1.84 | 93.0 | 5.12 |
| 22 | 270.6 | 2.11 | 103.9 | 5.86 |
| 30 | 300.9 | 2.34 | 113.2 | 6.49 |
| 40 | 335.2 | 2.60 | 123.7 | 7.18 |

### 6.2.5 Effect of Lowering the Exit Temperature

For a fixed inlet or room temperature, decreasing the exit or attic temperature (i.e., increasing the temperature difference across the domain) brings larger portions of the domain under cold temperatures with low saturation vapour densities. Hence the region experiencing condensation or ablimation expands in both x and y directions, increasing the local and total condensation rates and the latent heat rate. The total heat transfer rate at the exit increases due to both the larger temperature gradients and the increased latent heat rate. Figures 6.11 and 6.12 show the increase in the condensation rate and the expansion of the wet zone associated with decreasing the exit temperature from 263 K (Figure 6.11) to

233 K (Figure 6.12).

Table 6.4 contains data obtained for different exit temperatures. In spite of the increase in the total condensation rate, the bulk air flowrate at the exit still manages a modest increase. This may be due to the bulk air densities being higher for the lower exit temperatures. The data in the table give the following average increases in the transfer rates for each 1 K decrease in the exit temperature:

(1) an increase of $0.050 \times 10^{-6}$ kg/s (0.03% of the value for 273 K) in $Q_{g,out}$;

(2) an increase of $0.035 \times 10^{-6}$ kg/s (70% of the value for 273 K) in $Q_c$;

(3) an increase of 0.41 W (0.7% of the value for 273 K) in $H_{s,out}$; and

(4) an increase of 0.1 W (76% of the value for 273 K) in $H_L$.

Modi and Benner (1985, I and II) also observed that the condensation rate increased with the temperature difference.

When the temperature difference is increased, the conduction component of the total heat transfer rate increases nearly proportionally, but the total heat transfer rate itself increases by a smaller percentage. This is because the advection component, which is larger than the conduction component hardly increases. However, for small slit widths and small pressure differences, the contribution due to conduction is bigger and the effect of increasing the temperature difference becomes more significant.

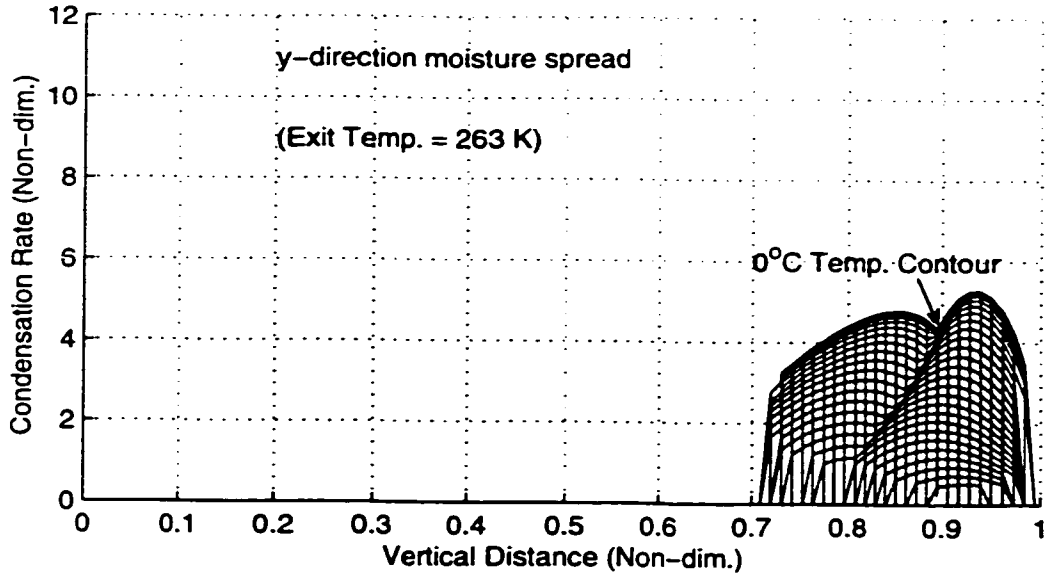


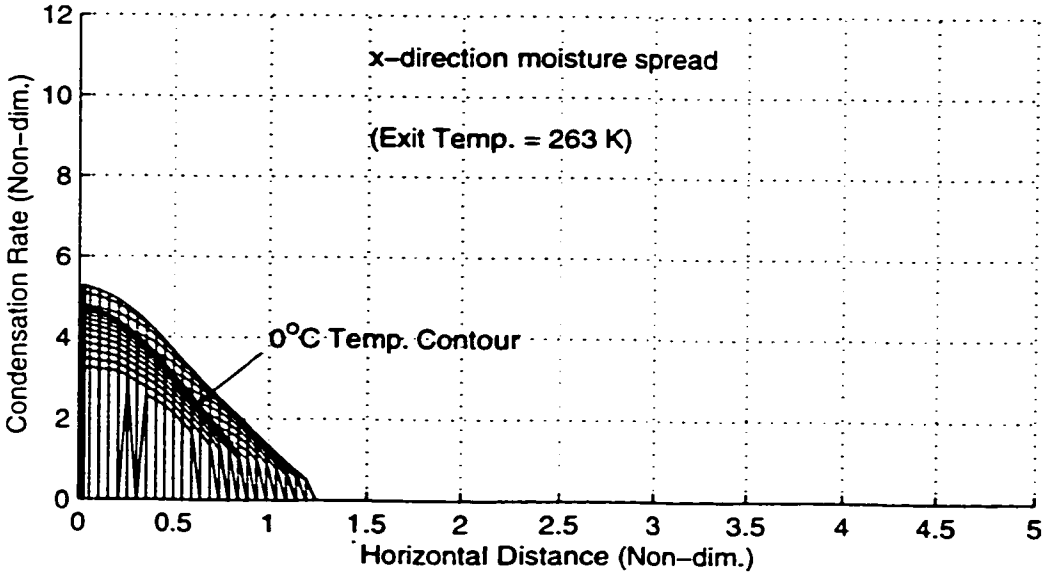


Figure 6.11. Condensation Rate Profiles (x and y direction) for 263 K Exit Temp. (Slit Width=6 mm, Press. Diff.=8 Pa, Inlet RH=70%, Exit RH=100%)

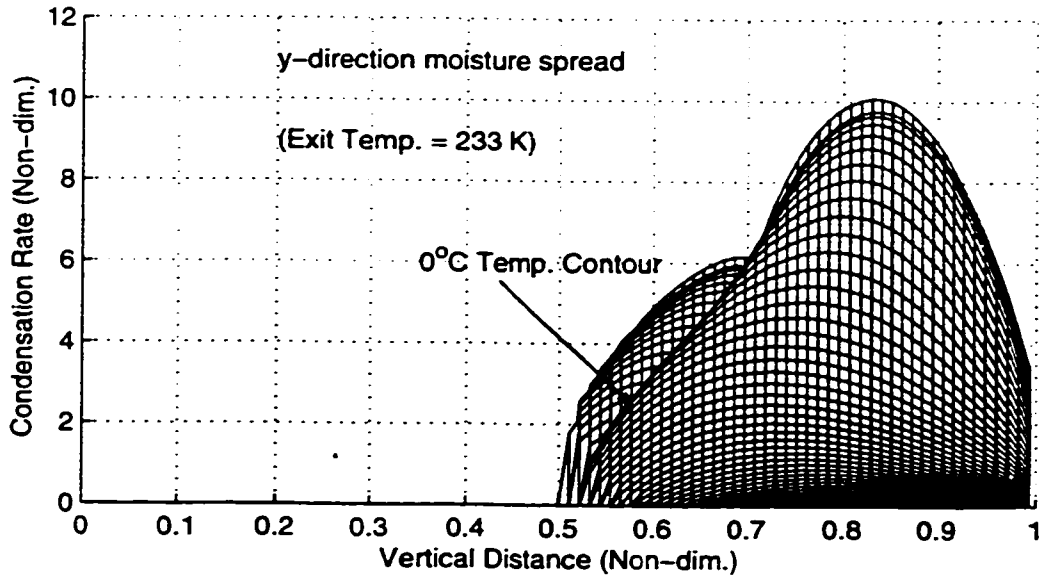


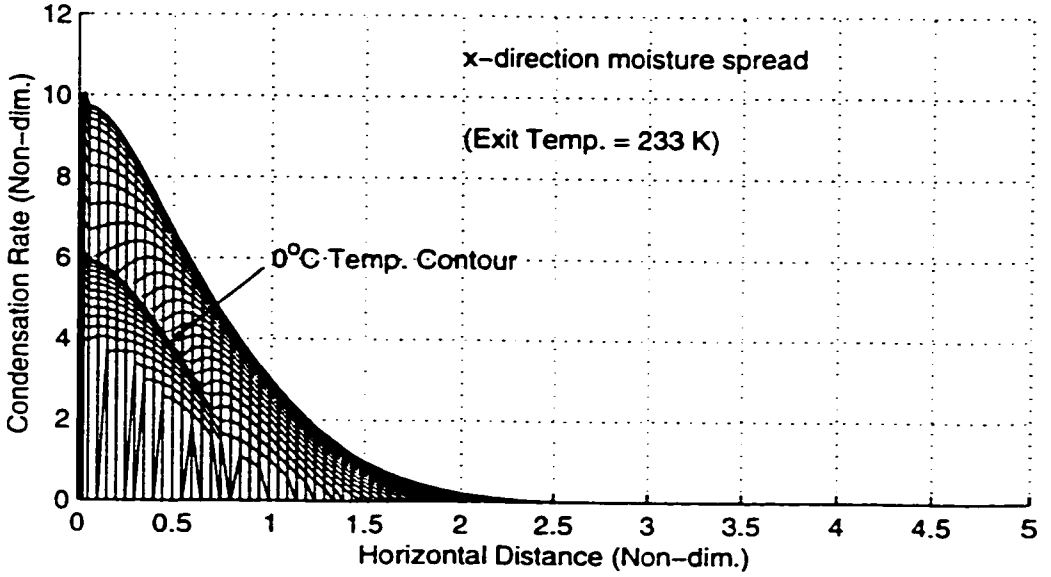


Figure 6.12. Condensation Rate Profiles (x and y direction) for 233 K Exit Temp. (Slit Width=6 mm, Press. Diff.=8 Pa, Inlet RH=70%, Exit RH=100%)

Table 6.4. Effect of Exit Temperature on Quasi-steady Heat and Mass Transfer Rates: Pressure Difference is 8 Pa, Slit Width is 6 mm, Inlet Relative Humidity is 70%, and Exit Relative Humidity is 100%. ($Q_{g,out}$ is exit bulk air flowrate, $Q_c$ is total condensation rate, $H_{s,out}$ is exit total heat transfer rate, and $H_L$ is total latent heat released.)

| Exit Temp., $T_{out}$ (K) | Mass Flowrates | | Heat Transfer Rates | |
|---|---|---|---|---|
| | $Q_{g,out}$ ($\times 10^{-6}$) kg/s | $Q_c$ ($\times 10^{-6}$) kg/s | $H_{s,out}$ (W) | $H_L$ (W) |
| 273 | 184.1 | 0.05 | 61.8 | 0.13 |
| 263 | 184.8 | 0.36 | 65.8 | 0.95 |
| 253 | 185.2 | 0.80 | 70.1 | 2.19 |
| 243 | 185.6 | 1.18 | 74.2 | 3.27 |
| 233 | 186.1 | 1.46 | 78.0 | 4.07 |

## 6.3 Effect of Moisture Accumulation

After the quasi-steady stage, moisture becomes the key factor, affecting all the field variables either directly or indirectly as it spreads and increases in quantity. The mechanics of this process were discussed fully in Section 5.3.10.

The data in Table 6.5 show the effects of moisture accumulation on heat and mass transfer rates over a 30-hour period for a set of boundary conditions: a 6 mm wide slit, an 8 Pa pressure difference, a 233 K exit temperature, a 70% inlet relative humidity, and a 100% exit relative humidity. The table shows that, over 30 hours:

(1) the bulk air flowrate at the exit increases slightly, from $186.1 \times 10^{-6}$ to $187.3 \times 10^{-6}$ kg/s (i.e., by 0.6%);

(2) the percentage of inlet vapour which condenses increases,

from 76.5% to 80.4% (i.e., by 5.1%);

(3) the total condensation rate increases, from $1.46 \times 10^{-6}$ to $1.54 \times 10^{-6}$ kg/s (i.e., by 5.5%);

(4) the total heat transfer rate at the exit increases, from 78.1 W to 79.3 W (i.e., by 1.5%); and

(5) the total latent heat increases, from 4.07 W to 4.24 W (i.e., by 4.2%), representing an increase from 5.21% to 5.35% of the total rate of heat transfer at the exit.

Figures 6.9, 6.13, and 6.14 show the moisture distribution profiles for three different times; 0 hours (i.e., the quasi-steady state); 6 hours; and 18 hours. It is observed that the wet-dry interface advances gradually with time towards the inlet [Tao et al. (1991a), Wijeysundera et al. (1996)]. Given sufficient time, it is expected that this interface would eventually reach the inlet. The slight increase with time in the total condensation rate is mainly due to the expansion of the wet zone, since the bulk of the magnitudes of the local condensation rates tend to decrease with time.

In Figure 6.14, high condensation rates occur just after the wet-dry interface, creating a high peak. The sudden drop in the local rates after the peak is an indication that the differences between the local actual vapour densities and the local saturation vapour densities decrease sharply, and continue to do so towards the exit as most of the vapour is condensed upstream. The increase in the total condensation rate is responsible, mainly, for the increases in the total latent heat and the total heat transfer rate at the exit. The increase in the total condensation rate also accounts for the increase in the percentage of inlet vapour which is condensed. The mechanics of the complex processes which occur as the moisture accumulates were discussed in detail in Section 5.3.10.

Table 6.5. Effect of Moisture Accumulation with Time on Heat and Mass Transfer Rates: Slit Width is 6 mm, Pressure Difference is 8 Pa, Exit Temperature is 233 K, Inlet RH is 70%, and Exit RH is 100%. ($Q_{g,out}$ is bulk air flowrate at exit, VC is percentage of inlet vapour which condenses, $Q_c$ is total condensation rate, MC is total liquid/frost content, $H_{s,out}$ is total heat transfer rate at exit, and $H_L$ is total latent heat released.)

| Time (hrs) | $Q_{g,out}$ ($\times 10^{-6}$) kg/s | VC (%) | $Q_c$ ($\times 10^{-6}$) kg/s | MC (kg) | $H_{s,out}$ (W) | $H_L$ (W) |
|---|---|---|---|---|---|---|
| 0 | 186.1 | 76.5 | 1.46 | 7.3e-7 | 78.1 | 4.07 |
| 6 | 186.4 | 78.2 | 1.49 | 0.016 | 78.4 | 4.13 |
| 12 | 186.7 | 79.3 | 1.51 | 0.033 | 78.6 | 4.18 |
| 18 | 186.9 | 79.8 | 1.52 | 0.049 | 78.9 | 4.20 |
| 24 | 187.1 | 79.9 | 1.53 | 0.066 | 79.1 | 4.22 |
| 30 | 187.3 | 80.4 | 1.54 | 0.083 | 79.3 | 4.24 |

As time advances, the local effective thermal conductivities increase in accordance with Equation 3.47, the main effect being exerted by the accumulation of liquid or ice. Figures 6.15 and 6.16 show the effective thermal conductivity profiles for 6 and 18 hours.

Figures 6.4 and 6.17 show the contours of the moisture volume fractions for 0, 6, and 18 hours. In Figure 6.4, the quasi-steady state, the moisture volume fractions would be considered as adsorbed quantities since they are less than $10^{-6}$ [Langlais et al., (1982)]. After 6 hours the moisture volume fractions are of the order of $10^{-3}$. After 18 hours, the wettest regions have moisture volume fractions as high as order $10^{-2}$. The contours also show that the wet region expands in all directions, and not just towards the inlet.

Figure 6.18 shows that the moisture accumulation profile is approximately linear with time. This linear relationship was also found by Wijeysundera and Hawlader (1992).

## 6.4 Summary of Results

In this chapter, it was seen that the exit temperature was the most influential factor in moisture deposition, followed by the pressure difference, the inlet relative humidity, the slit width, and the exit relative humidity, in that order. Decreasing the exit temperature from 273 to 233 K increased the total condensation rate by 2820%; increasing the pressure difference from 2 to 30 Pa increased the total condensation rate by 1277%; increasing the inlet relative humidity from 40% to 80% increased the total condensation rate by 132%; increasing the slit width from 6 to 40 mm increased the total condensation rate by 78%; and increasing the exit relative humidity from 20% to 100% increased the total condensation rate by a mere 3.5%.

It was also seen that all heat and mass transfer rates increase with time in the presence of accumulating moisture. The rates of change of the transfer rates are small, but this means that the moisture not only accumulates, it does so at a faster rate with time if the boundary conditions are sustained, making the moisture problem worse.

In Chapter 7, general mathematical and graphical relations which can be used for a quick estimate of the bulk air flowrates and heat transfer rates for given boundary conditions will be presented.

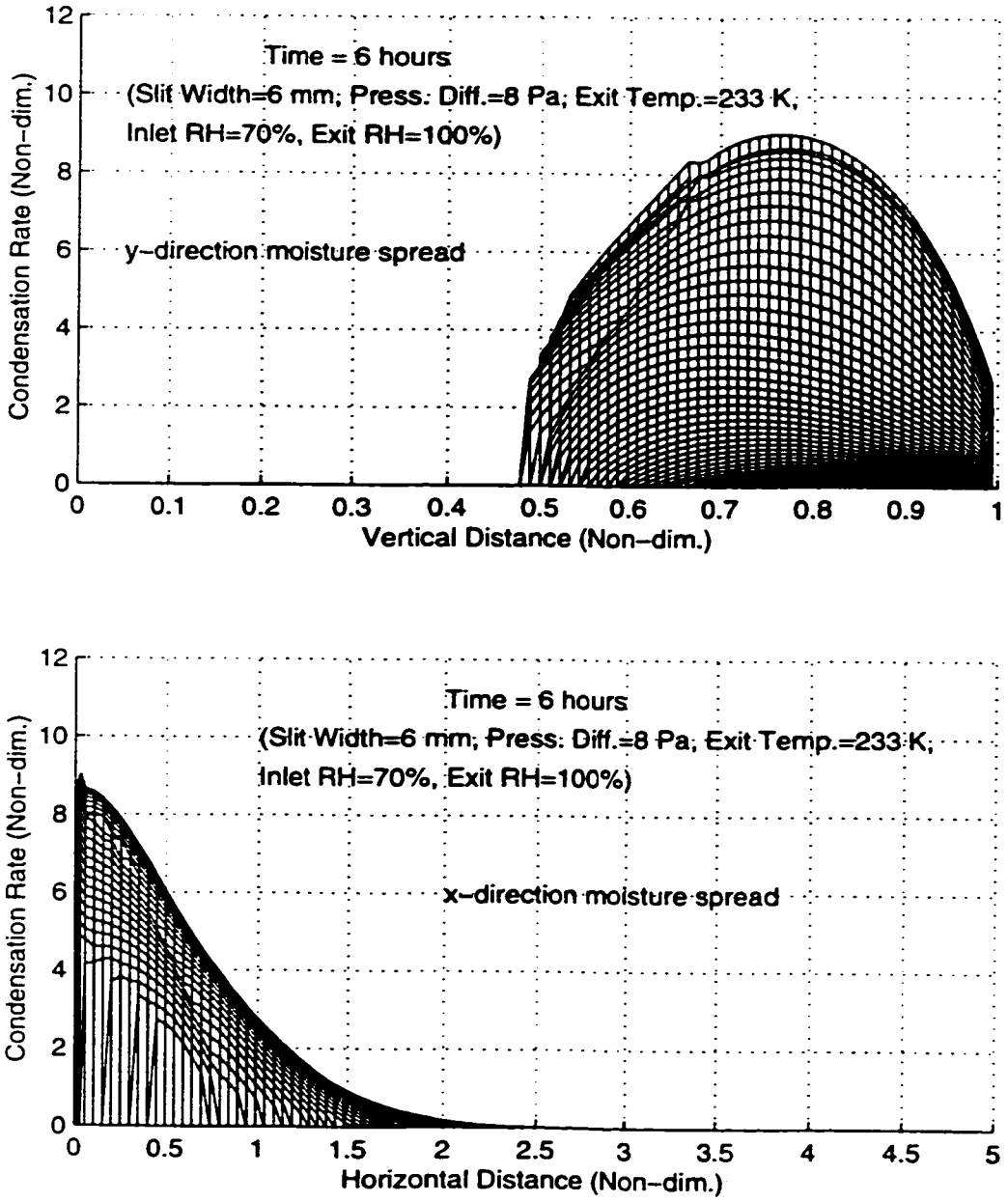


Figure 6.13. Condensation Rate Profiles (x and y direction) after 6 Hours.

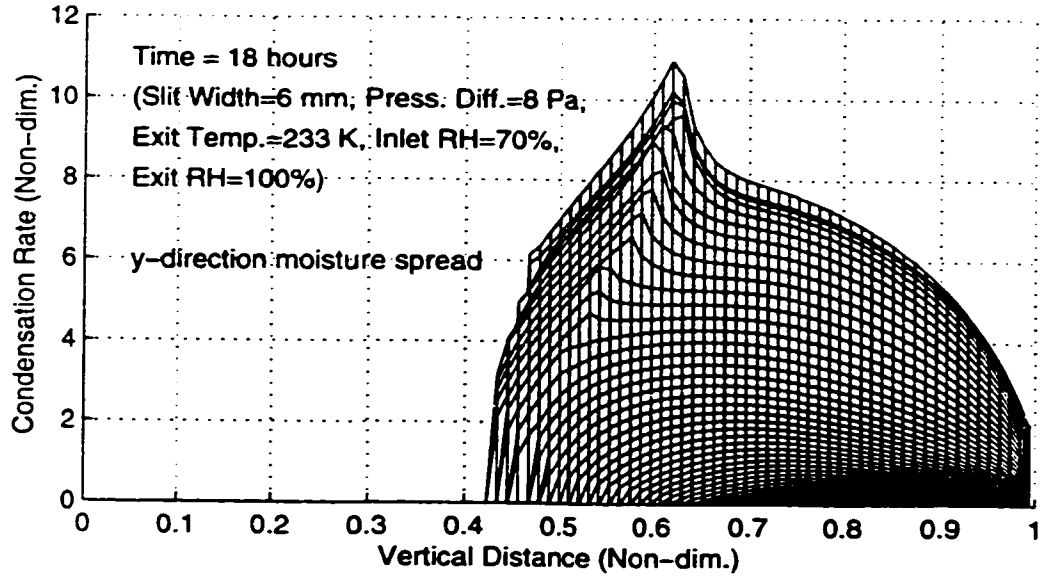


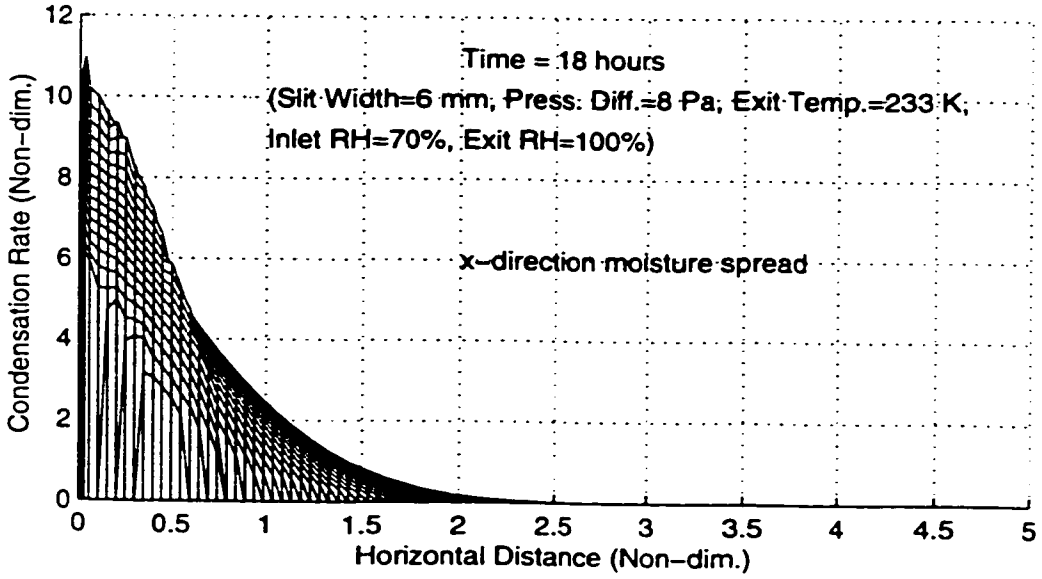


Figure 6.14. Condensation Rate Profiles (x and y direction) after 18 Hours.

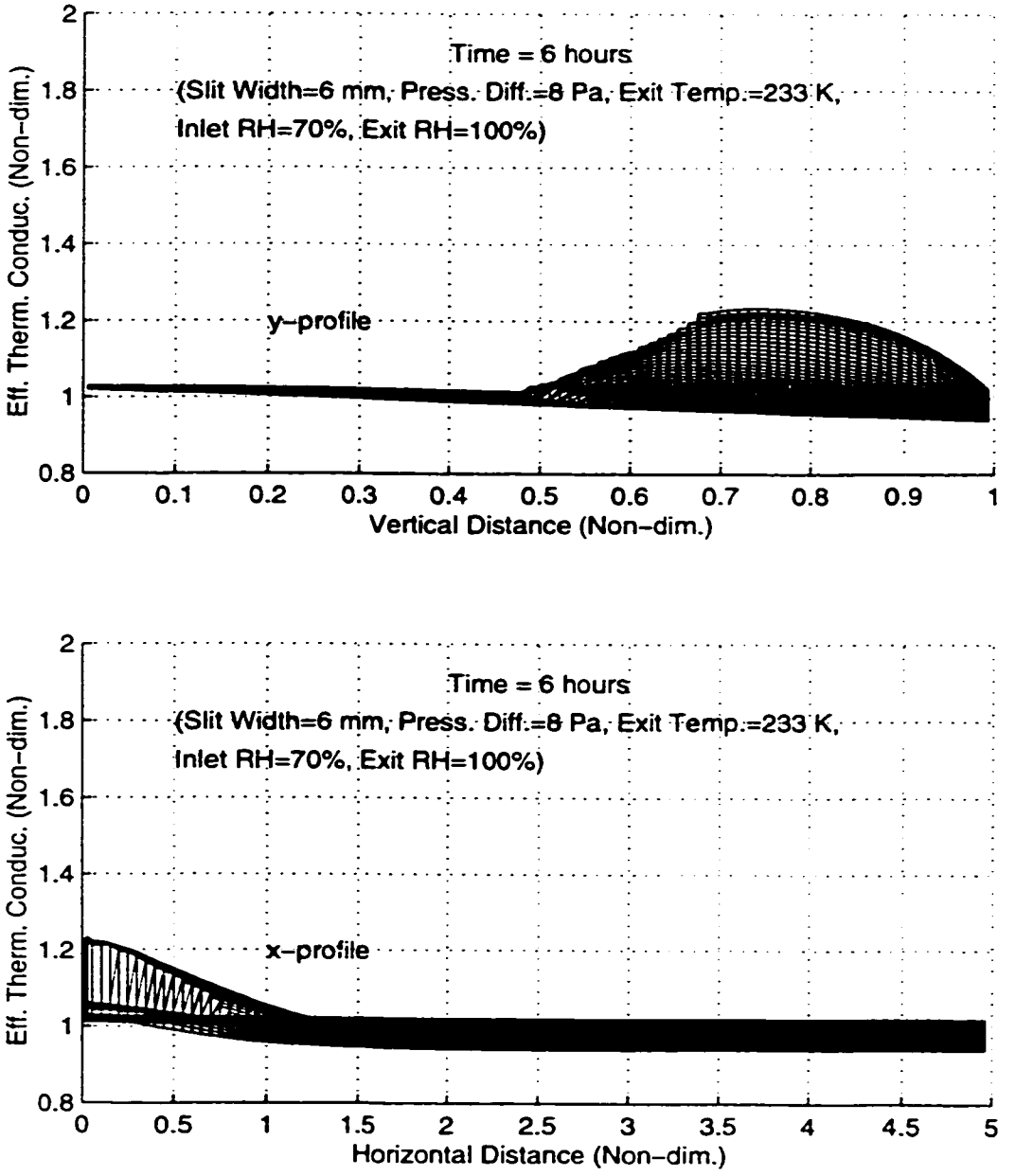


Figure 6.15. Effective Thermal Conductivity Profiles (x and y direction) after 6 Hours.

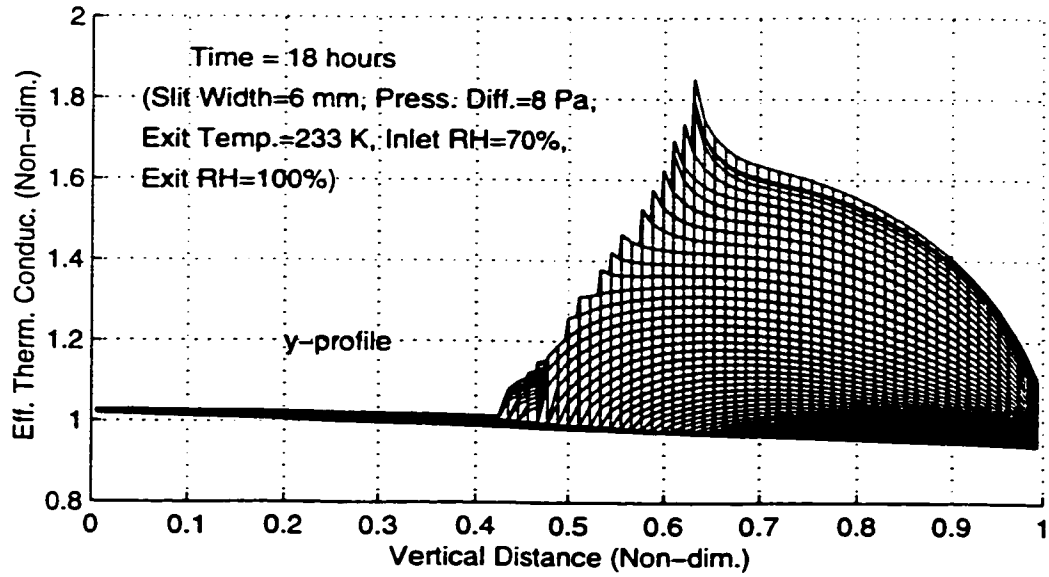


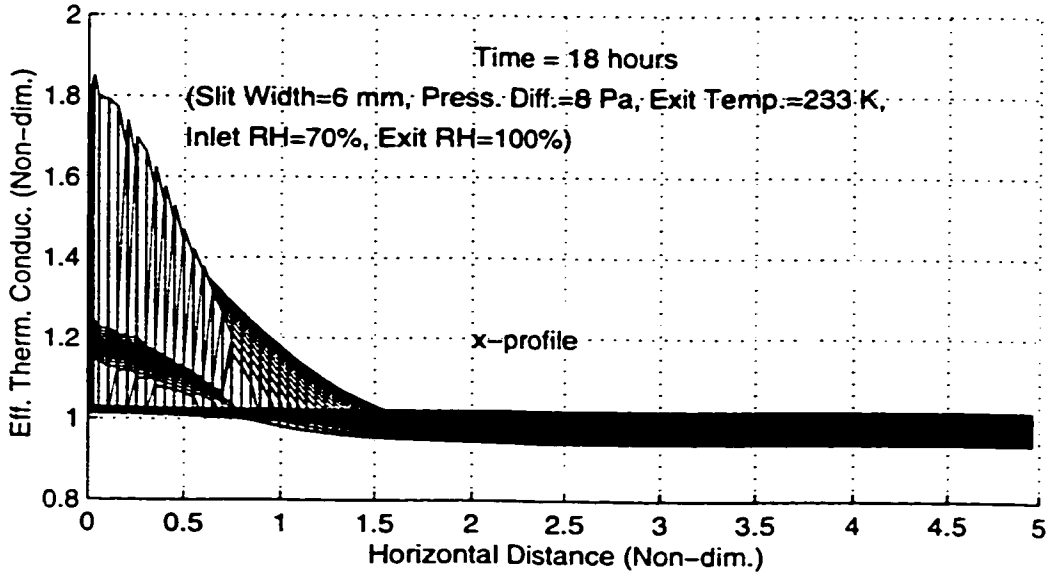


Figure 6.16. Effective Thermal Conductivity Profiles (x and y direction) after 18 Hours.

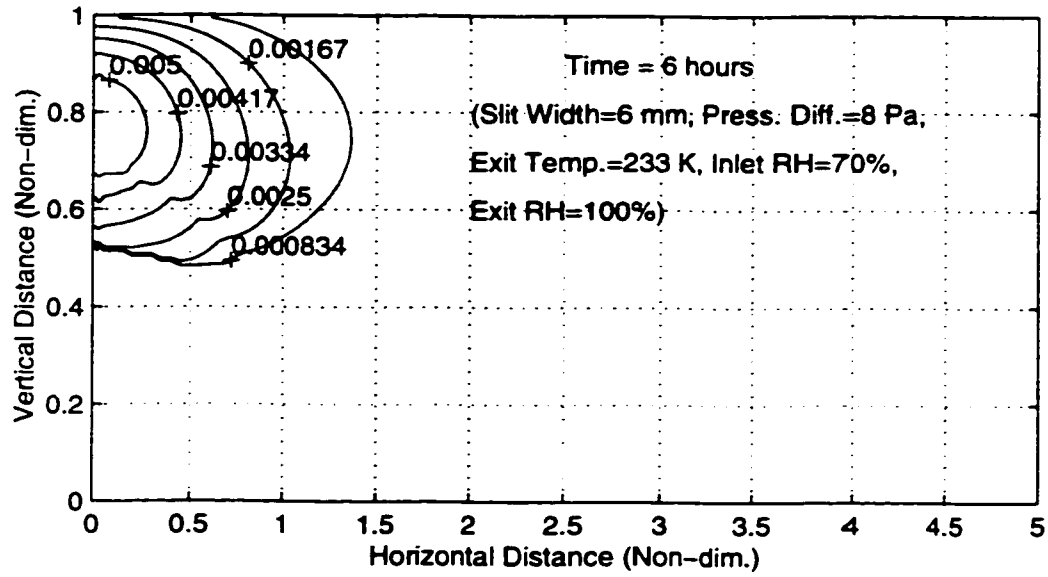


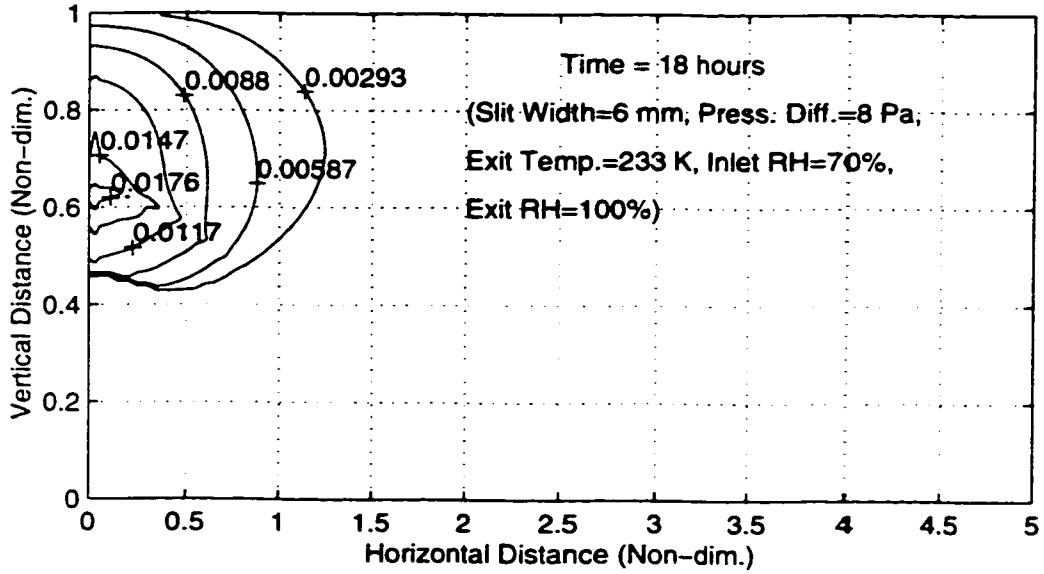


Figure 6.17. Condensate/Ablimate Volume Fraction Contours for 6 and 18 Hours.

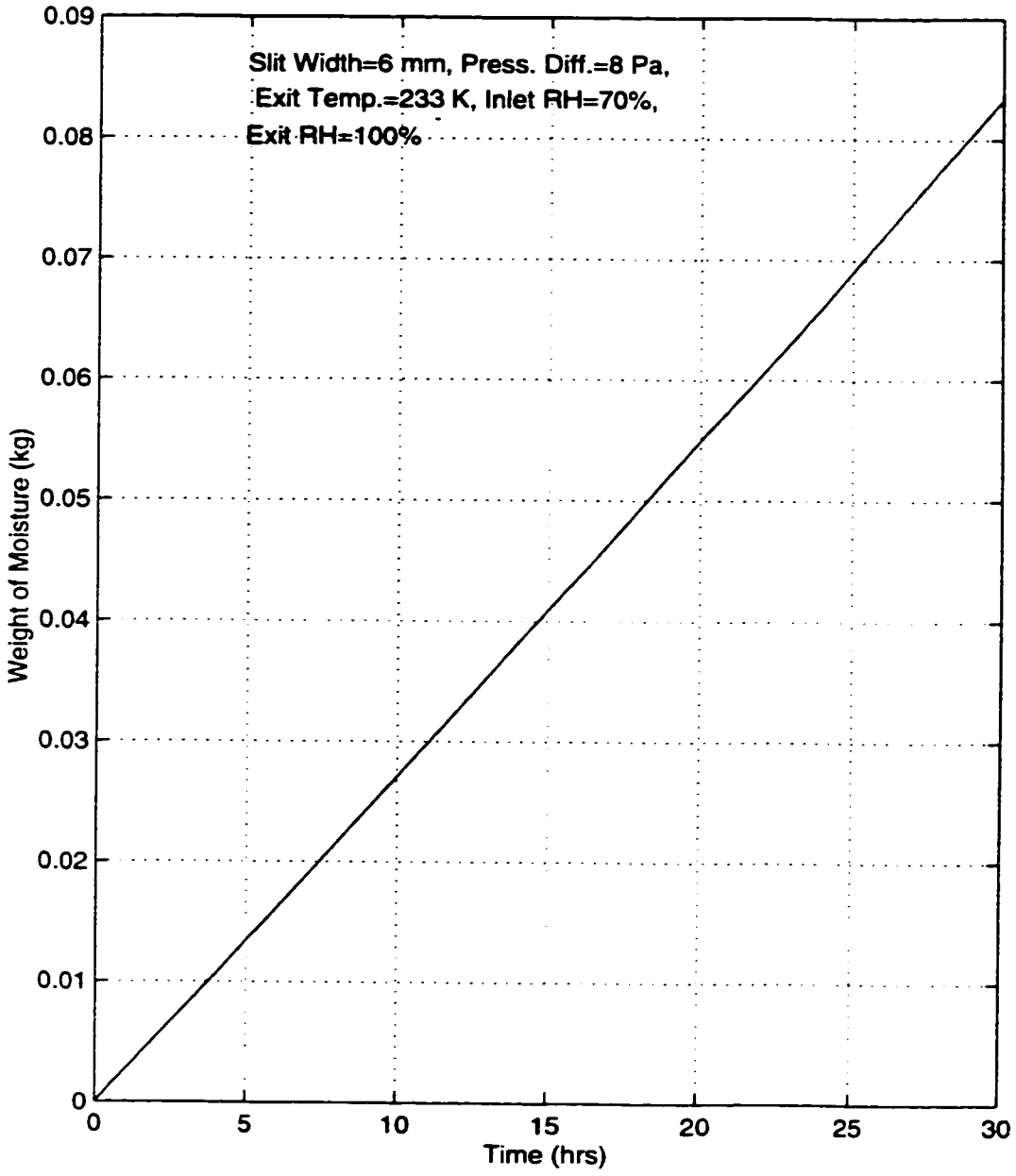


Figure 6.18. Variation of Total Weight of Moisture in the Insulation with Time.

# CHAPTER 7

# ESTIMATION OF BULK AIR FLOWRATES AND HEAT TRANSFER RATES IN SLITS AND ROUND HOLES IN ATTIC FIBROUS INSULATION

## 7.1 Introduction

Bulk air flowrates through openings in building envelopes depend on the pressure differences across the envelope, the dimensions and shapes of the openings, and the Reynolds Number of the flow. This relationship may be expressed by an orificial model in the form

$$Q_a = C_d A_{eff}\left(\frac{2\Delta P}{\rho_a}\right)^{0.5} \quad m^3/s$$

$$= C_d A_{eff}(2\rho_a \Delta P)^{0.5} \quad kg/s \qquad (7.1)$$

where $Q_a$ is the rate of flow of air through the opening, $A_{eff}$ is the effective or equivalent area of the opening, and $C_d$ is a discharge coefficient which depends on the size, shape and nature of the opening, and on the Reynolds number appropriate to the flow.

Flow in small openings such as cracks can also be expressed by a power law pressure-flow relationship:

$$Q_a = C_F(\Delta P)^n \qquad (7.2)$$

The flow coefficient, $C_F$, depends on the geometry (size, shape) and nature of the opening, and also on the nature of the flow. The index, n, relates the flowrate to the applied pressure difference.

The power law relationship is frequently used for the leakage characteristics of entire buildings and rooms, where the index, n, ranges in value from 0.5 (for turbulent flow) to

1.0 (for fully-developed laminar flow) [Walker and Wilson, 1998].

In this chapter the intention is to find the values of $C_F$ and n for leakages through slits and round holes in the attic insulation. This is done by computing the flowrates for different opening sizes and pressure differences across the insulation slab. The heat transfer rates through the cracks and holes are determined for different attic (exit) temperatures. Relations developed for the values of $C_F$ and n may be useful to practicing engineers who may need to estimate transfer rates through holes and cracks in the building envelop without having to carry out measurements or calculations.

## 7.2 Flow Domain and Governing Equations

Consider the flow domain shown in Figure 3.3. For the range of variables used in Chapter 6, it was observed that condensation had a negligible effect on the bulk air and heat transfer rates at the inlet. At the exit, condensation caused a variation of less than 2% in the bulk air flowrates and a variation of less than 5% in the total heat transfer rate for a given exit temperature. These are small percentages and reasonable estimates of the total transfer rates can be arrived at by considering the "dry" results.

The inlet transfer rates may be estimated by solving the governing equations for the "dry" system; i.e., the condensation rate and latent heat rate terms are removed from the mass conservation and energy conservation equations, respectively, while the vapour conservation equation is entirely excluded. The governing equations, therefore, become the steady state forms of the equations, the solution of which result in the same transfer rates at the inlet and the exit.

The model equations which were developed in Chapter 3 are used

for slits. Axisymmetric flow (i.e., flow through round holes) is modelled by the relations presented in Appendix D. The equations, with variable thermophysical properties of dry air, are solved by the procedures which were discussed in Chapter 4. All the reference values of properties are based on a temperature of 273.15 K and a pressure of one atmosphere. The room temperature is fixed at 293 K. For isothermal flow, the entire flow domain is assumed to be at 293 K. The inlet boundary is Dirichlet, while the exit boundary is forced-convective with a convective heat transfer coefficient of 10 $W/m^2$-K [Ogniewicz and Tien, 1981]. It is found that 30 grid cells in the y-direction and 70 in the x-direction provide sufficient accuracy for the dry system. The number of grid cells was determined by refining the grid until any further refinement produced a change of less than 0.5% in the balanced global heat and mass transfer rates.

## 7.3 Results and Discussion

Tabulated data for the different opening sizes, pressure differences, and exit temperatures are given in Appendix F.

The slit widths used are 6 mm, 14 mm, 22 mm, 30 mm and 40 mm. Assuming a slit length of 1 m, the corresponding opening areas are 0.006 $m^2$, 0.014 $m^2$, 0.022 $m^2$, 0.030 $m^2$, and 0.040 $m^2$, respectively.

The hole diameters used are also 6 mm, 14 mm, 22 mm, 30 mm and 40 mm. The corresponding opening areas are 28 $mm^2$, 154 $mm^2$, 380 $mm^2$, 707 $mm^2$, and 1257 $mm^2$, respectively.

The pressure differences used are 2, 8, 14, 20 and 30 Pa, while the exit temperatures are 293 K (for isothermal flow), 273 K, 263 K, 253 K, 243 K, and 233 K. The temperatures, not just the temperature differences, are listed because these are needed for the computation of the thermophysical properties of dry air.

### 7.3.1 Results for Slits

All computations are based on a slit length of 1 m.

The velocity vectors and temperature contours are similar to Figures 6.1 and 6.2, respectively. The contours of air density, specific heat capacity, effective thermal conductivity and viscosity are similar to the temperature contours (Figure 6.2) since these properties are functions of temperature only.

For isothermal flow, the pressure field satisfies Laplace's equation (i.e., $\nabla^2 P = 0$), giving the typical contours shown in Figure 7.1. Data generated from the model (Appendix F) show that the air flowrates increase marginally as the exit temperatures decrease. Hence it is not expected that the pressure contours will be distorted significantly by the temperature field. When the opening width is varied from 6 mm to 40 mm, with different exit temperatures and pressure differences, the air flowrates increase by between 83 and 87%. Increasing the pressure difference from 2 to 30 Pa, over the entire range of considered exit temperatures and opening areas, causes the air flowrates to increase by between 1293 and 1400%, the latter value being for isothermal flow.

The values of $C_F$ and n for different opening sizes are obtained by plotting the logarithm of the pressure difference, $\Delta P$, against the logarithm of the flowrate, Q, in Equation 7.2.

The plots of pressure difference against air flowrate for different slit widths are given in Figure 7.2. These plots are for isothermal flow. Temperature has little effect on the flowrates. Figure 7.3 shows that, for a given slit width, decreasing the exit temperature from 293 to 233 K does not increase the air flowrates substantially. Figure 7.2 can be used to estimate the flowrate for a given pressure difference and a slit width.

The variation of $C_F$ with slit geometric area for different exit temperatures is shown in Figure 7.4, while Figure 7.5 gives the corresponding n values. The value of $C_F$ increases with the geometric area of the opening, but decreases as the exit temperature increases. Investigations revealed that the value of n for isothermal flow is always 1.0, regardless of the temperature adopted for the computation of the thermodynamic and thermophysical properties. As the temperature difference increases (i.e., as the exit temperature decreases), the value of n for a given opening area decreases. For a given exit temperature, n decreases with increasing opening area, except in the isothermal case where n remains constant at 1.0. However, for all practical purposes the value of n may be rounded off to 1. This is not unexpected since the value of n for fully-developed laminar flow is 1, and Darcy flow is within the laminar range.

Equating the right hand side of Equation 7.1 to the right hand side of Equation 7.2, the expression for the effective area is obtained as

$$A_{eff} = \frac{C_F}{C_d (2\rho_a)^{0.5}} (\Delta P)^{n-0.5} \qquad (7.3)$$

The effective areas are computed for a standard discharge coefficient, $C_d$, of 0.60 and an air density, $\rho_a$, of 1.205 $kg/m^3$, this being the density of dry air at 293 K. For each opening area, with the values of $C_F$ and n obtained earlier in this chapter, the effective areas are determined for the range of pressure differences under consideration.

Figure 7.6 contains plots of pressure difference against effective area for different slit geometric areas and isothermal flow. The effective areas are smaller than the geometric areas due to the resistance to flow provided by

the fibrous insulation. Figure 7.7 uses two different geometric areas to show that the effective area is only a weak function of the exit temperature.

The total heat transfer rate into the flow domain is calculated at the inlet (i.e., y = 0) from Equation 4.26.

In the equation, $k_3$ is the number of computational grid cells within the opening on the horizontal axis. All parameters in the equation are calculated at the entrance to the insulation slab (i.e., at the lower horizontal boundaries of the grid cells on the first grid-line).

Heat transfer data for different exit temperatures, slit widths, and pressure differences are presented in Appendix F. It is found that at a given pressure difference and a given slit width, a plot of the exit temperatures against the total heat transfer rates is a straight line; i.e., the relationship between the temperature difference and the heat transfer rate may be expressed in linear form as

$$H_s = C_{cond}\Delta T + H_{adv} \qquad (7.4)$$

where $C_{cond} \equiv \frac{\lambda_{eff} A}{D}$, $H_{adv} \equiv C_{adv} A$; A is the opening area and $C_{adv}$ is the advective heat transfer rate per unit area of the slit.

The first term on the right-hand-side of Equation 7.4 represents the contribution of conduction heat transfer to the total heat transfer rate. This term may be called the "conduction heat transfer component". $C_{cond}$ has units W/K and may be referred to as the "conduction heat transfer coefficient". This first term has a value which is different from that obtained for pure conduction (i.e., with no bulk air flow) because it represents conduction with a temperature field which has been distorted by the advecting fluid. For a slit, $C_{cond}$ increases with increasing geometric area, but it decreases with increasing pressure difference (i.e., as

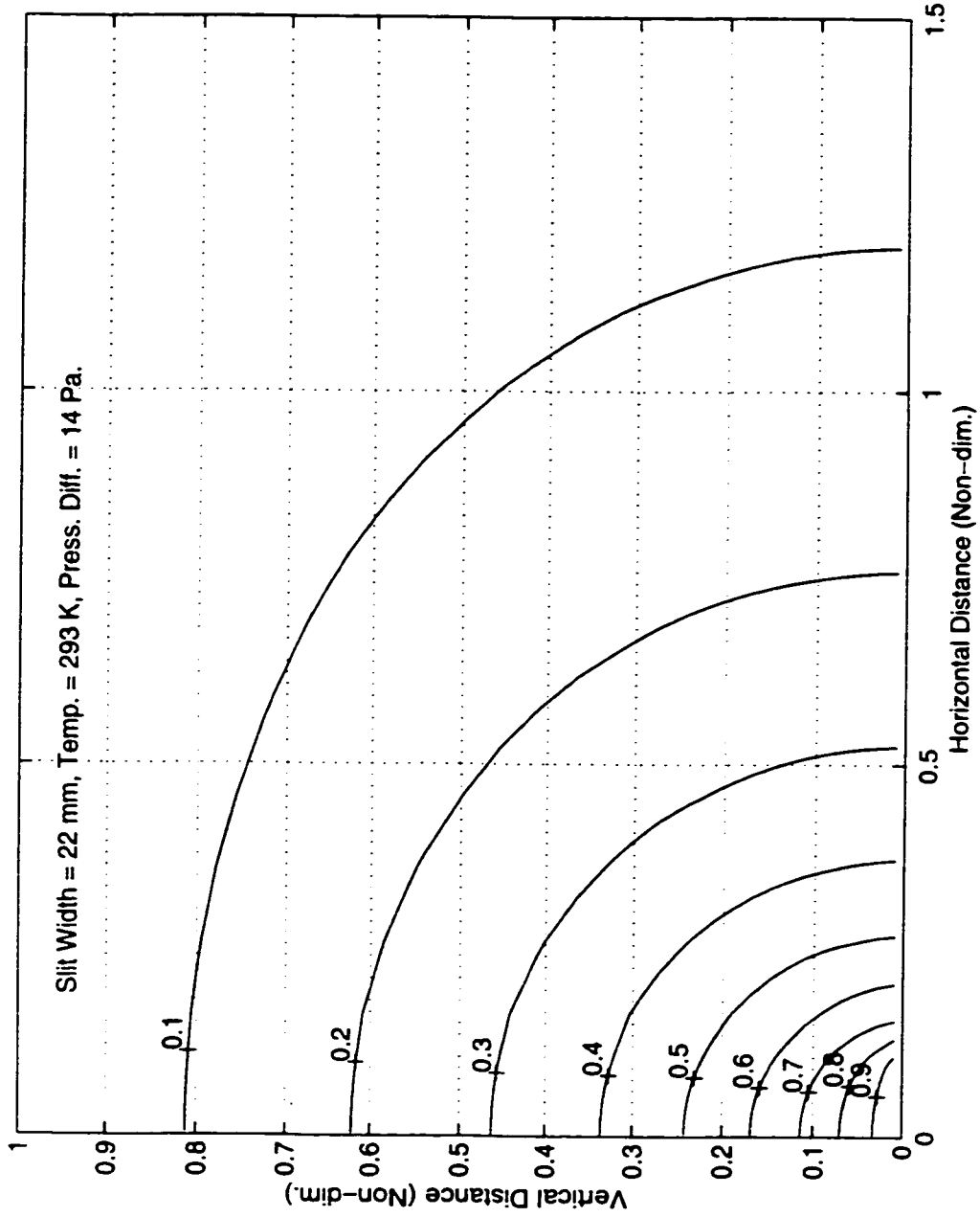


Figure 7.1. Typical Pressure Contours (Non-dim.) for Isothermal Flow.

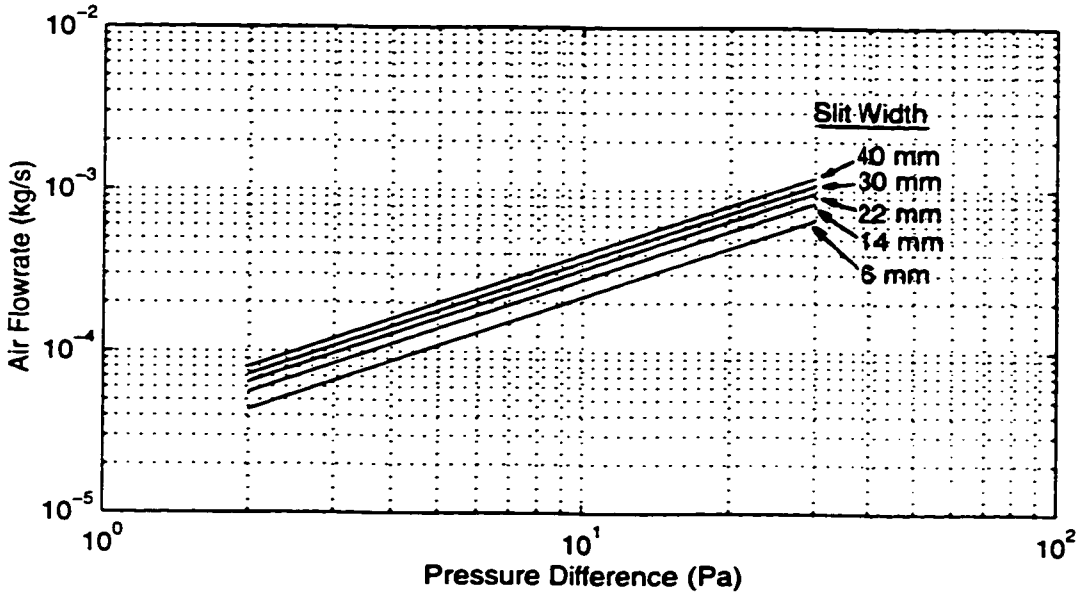


Figure 7.2. Isothermal (293 K) Air Flowrates for Slits.

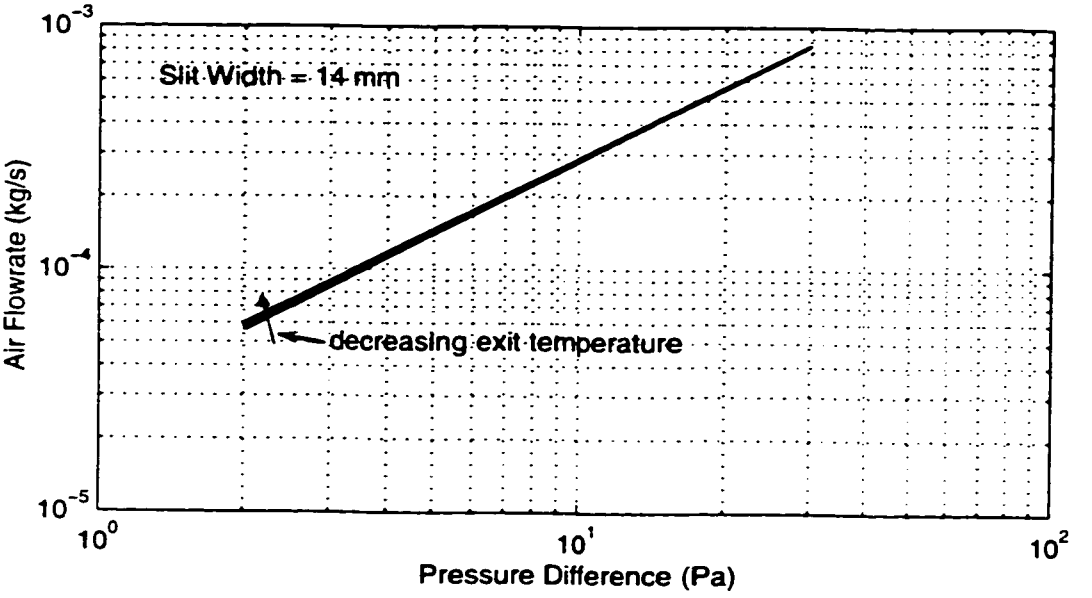


Figure 7.3. Air Flowrates for Different Exit Temperatures.

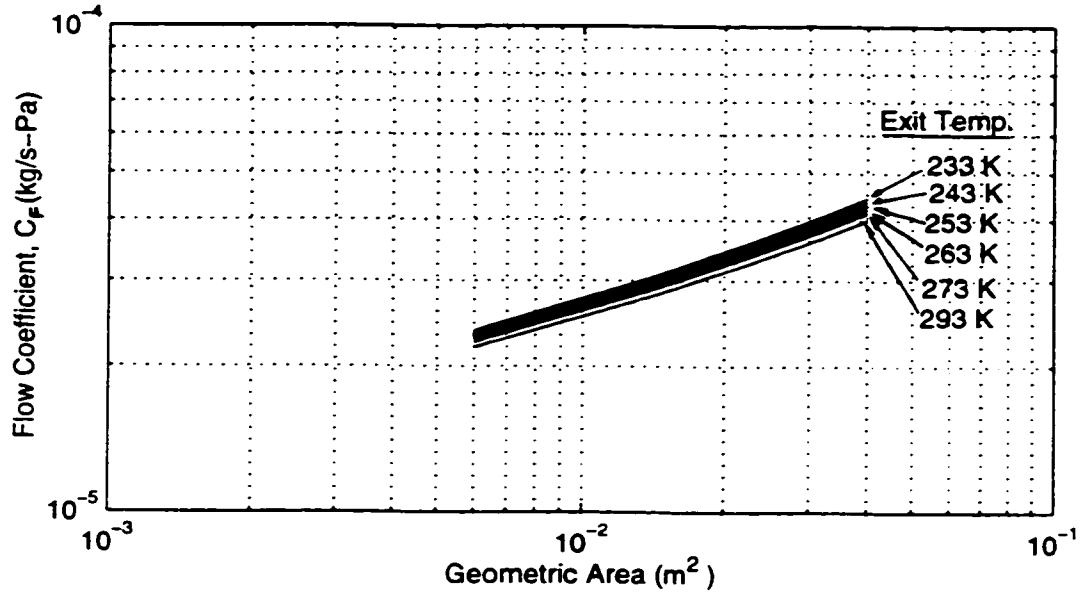


Figure 7.4. Flow Coefficients ($C_F$) for Slits.

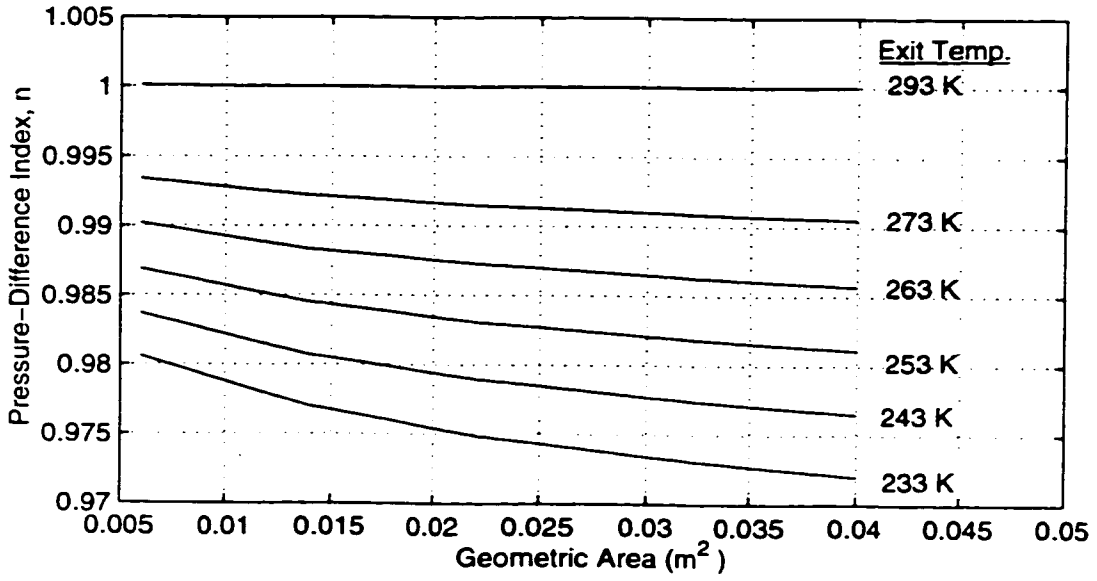


Figure 7.5. Pressure-Difference Indices, n, for Slits.

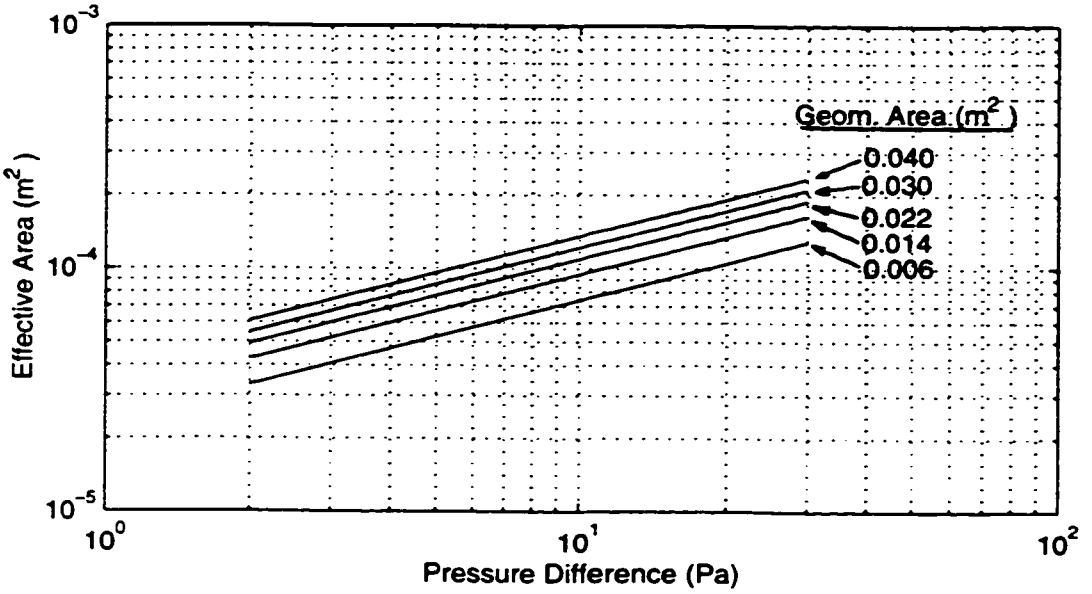


Figure 7.6. Effective Areas for Slits at 293 K.

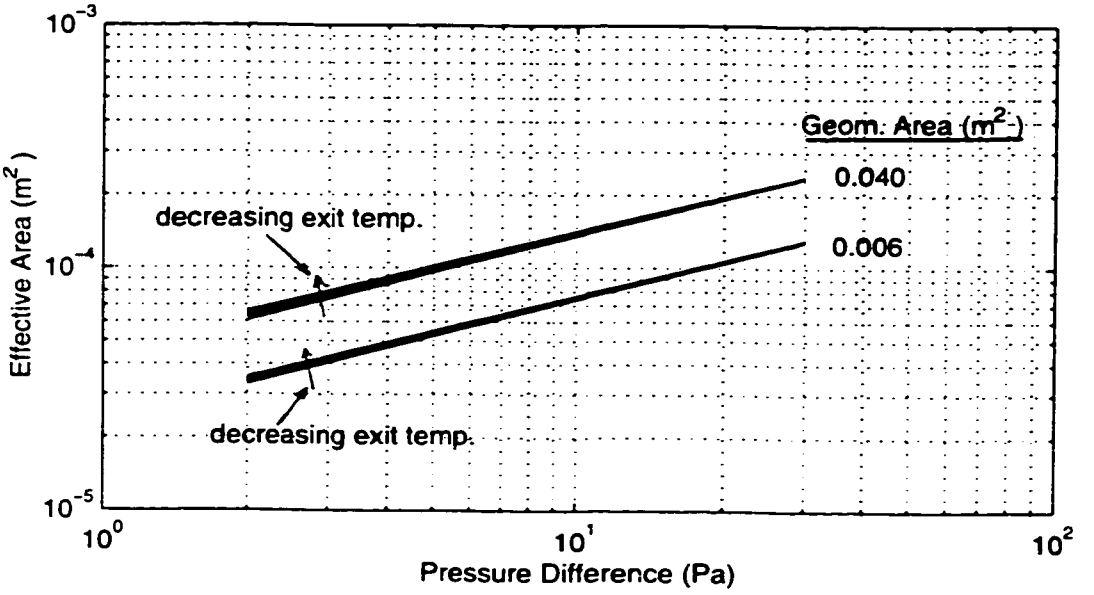


Figure 7.7. Effective Areas for Slits at Other Temperatures.

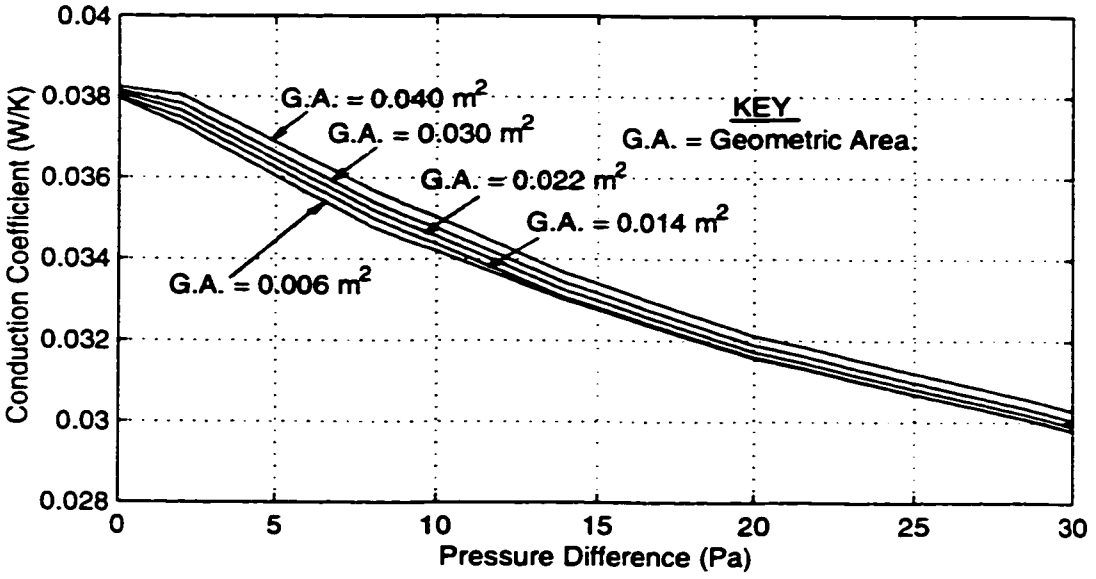


Figure 7.8. Conduction Heat Transfer Coefficients for Slits.

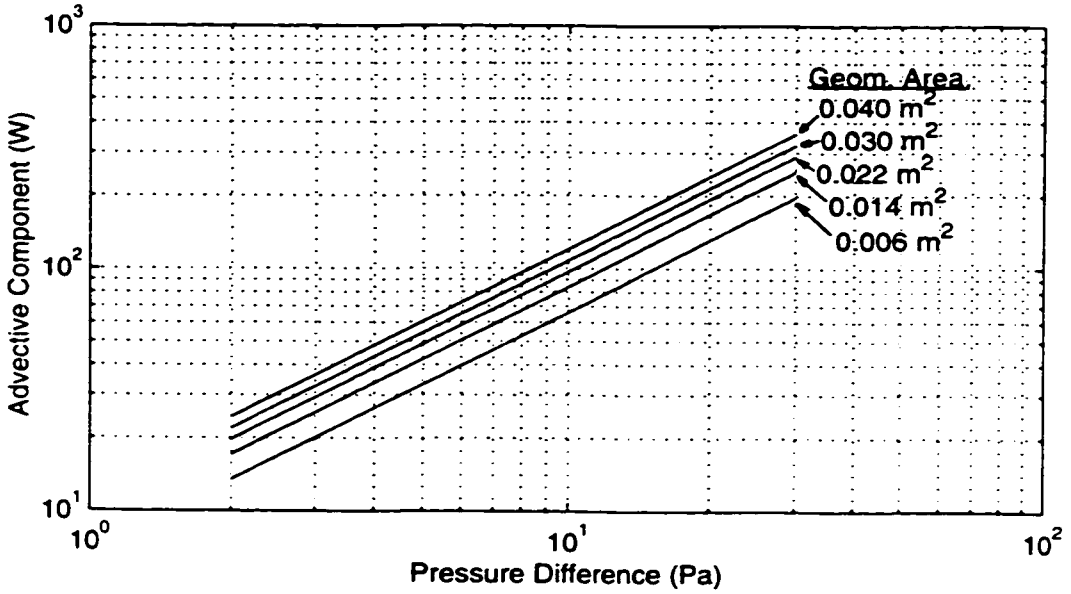


Figure 7.9. Advective Heat Transfer Components for Slits.

advection becomes more dominant) as shown in Figure 7.8. Increasing the pressure difference increases the thermal penetration, causing the temperature gradients at the inlet to decrease. This explains why $C_{cond}$, and therefore the conduction component, decreases with pressure difference.

The second term on the right hand side of Equation 7.4 is the contribution due to advection. This will be referred to simply as the "advective heat transfer component" and $C_{adv}$ as the "advective heat flux". $H_{adv}$ increases with both the slit area and the pressure difference as shown in Figure 7.9. When the pressure difference is increased, the increase in the advective component is much larger than the decrease in the conduction component, and the total heat transfer rate, $H_s$, becomes larger.

The approach used in Equation 7.4 is similar to the "lumped" effective thermal conductivities used by some researchers in their experimental work, where one value for the effective thermal conductivity in the insulation slab is computed from the temperature difference across the slab, the slab dimension, and the total heat transfer rate measured at the exit. Examples are Chen et al. (1997), and Modi and Benner (1985).

### 7.3.2 Results for Round Holes (Axisymmetric Flow)

With a few exceptions, the vectors and contours of the flow-field variables for axisymmetric flow are similar to the vectors and contours shown and discussed in Section 7.3.1 for slits. The magnitudes of the air and heat transfer rates are, however, quite different. This section basically gives the results for axisymmetric flow; discussion is limited to areas where results are significantly defferent from those obtained for slits.

Tabulated data for different boundary values are presented in

Appendix F. When the hole diameter is varied from 6 mm (28.3 $mm^2$) to 40 mm (1256.6 $mm^2$), for different exit temperatures and pressure differences, the air flowrates increase by between 845% and 875%. Increasing the pressure difference from 2 to 30 Pa, over the entire range of considered exit temperatures and opening areas, causes the air flowrates to increase by between 1339 and 1400%, the latter value being for isothermal flow.

The plots of pressure difference against air flowrate for different hole diameters are given in Figure 7.10. These plots are for isothermal flow. Data in Appendix F and Figure 7.11 show that temperature has little effect on air flowrate. Figure 7.10 may be used to estimate the air flowrate for a given pressure difference and a hole size.

Figure 7.12 gives the values of $C_F$ for the different hole sizes and exit temperatures, while Figure 7.13 gives the values of n corresponding to those of $C_F$. The value of $C_F$ increases with the geometric area of the opening, but decreases very slightly as the exit temperature increases. Computations based on tabulated data in Appendix F reveal that the value of n for isothermal flow is always 1.0, regardless of the temperature adopted for the computation of the thermodynamic and thermophysical properties. As the temperature difference increases (i.e., as the exit temperature decreases), the value of n for a given hole area decreases. For a given exit temperature, n decreases with increasing hole size, except in the isothermal case where n remains constant at 1.0. However, for all practical purposes the value of n may be rounded to 1. This is not unexpected, for reasons given in Section 7.3.1.

The effective areas are computed for a standard discharge coefficient, $C_d$, of 0.60 and an air density, $\rho_a$, of 1.205 $kg/m^3$, this being the density of dry air at 293 K. For each hole area, with the values of $C_F$ and n obtained earlier and

Equation 7.3, the effective areas are determined for the range of pressure differences under consideration (i.e., 2 to 30 Pa).

The effective areas for different pressure differences and geometric areas are plotted in Figure 7.14. Figure 7.15 uses two different geometric areas to show that the effective area is a very weak function of the exit temperature.

Heat transfer data for different exit temperatures, opening areas, and pressure differences are presented as tables in Appendix F. From the tabulated data it is found that at a given pressure difference and a given hole area, a plot of exit temperatures against the corresponding total heat transfer rates is a straight line. For a hole, unlike for a slit, $C_{cond}$ decreases with increasing geometric area. In a similar manner to slits, $C_{cond}$ decreases with increasing pressure difference (i.e., as advection becomes more dominant) as shown in Figure 7.16.

For holes, $H_{adv}$ increases with both hole area and pressure difference as shown in Figure 7.17.

## 7.4 Summary

The discussion in this chapter has provided confirmation that, for a crack or a hole in the attic fibrous insulation, the bulk air flowrate and the pressure difference have a power law pressure-flow relationship. Values of flow coefficient ($C_F$) and pressure index (n) for different opening areas and temperature differences have been computed.

For both slits and holes, the value of n for isothermal flow is constant and equal to 1. That is, it is independent of the size of the opening. In non-isothermal flow, n decreases as the temperature difference and the opening area increase. However, the deviations of n from 1 for such situations are very small and may be neglected.

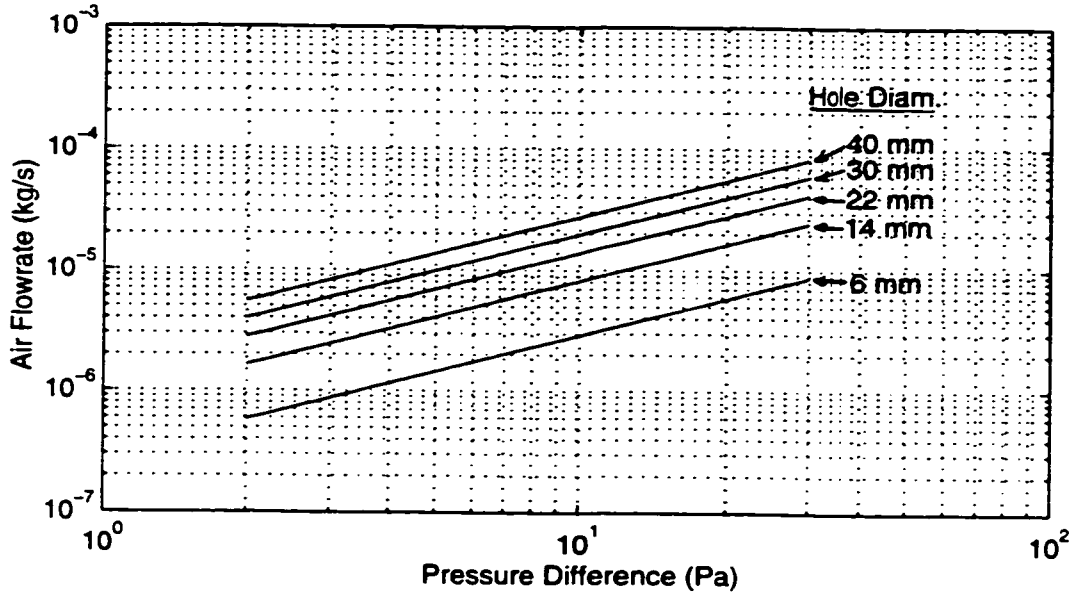


Figure 7.10. Isothermal (293 K) Air Flowrates for Holes.

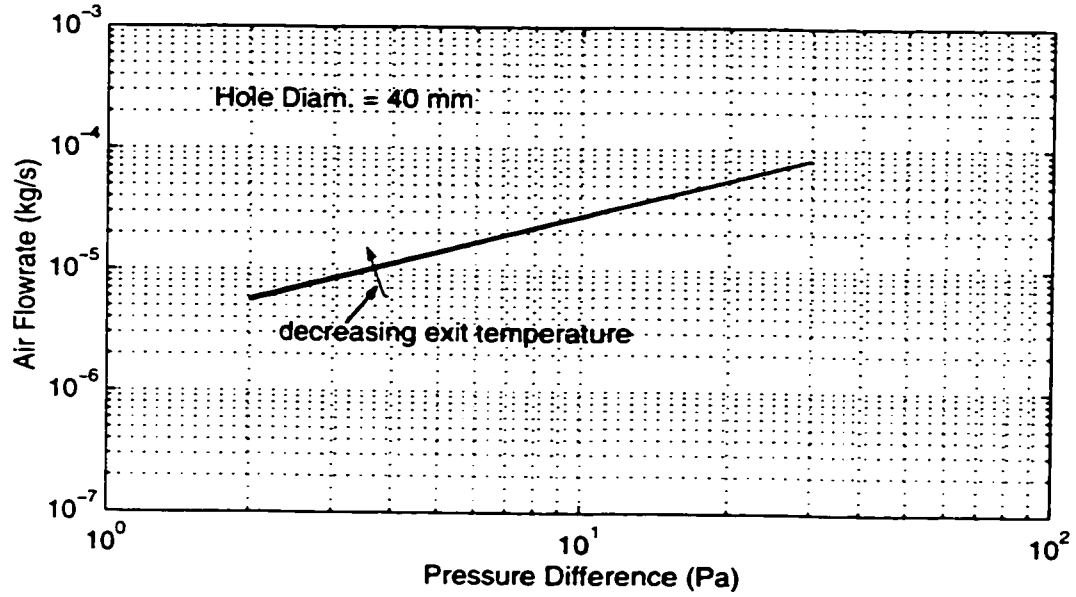


Figure 7.11. Air Flowrates for Different Exit Temperatures (Holes).

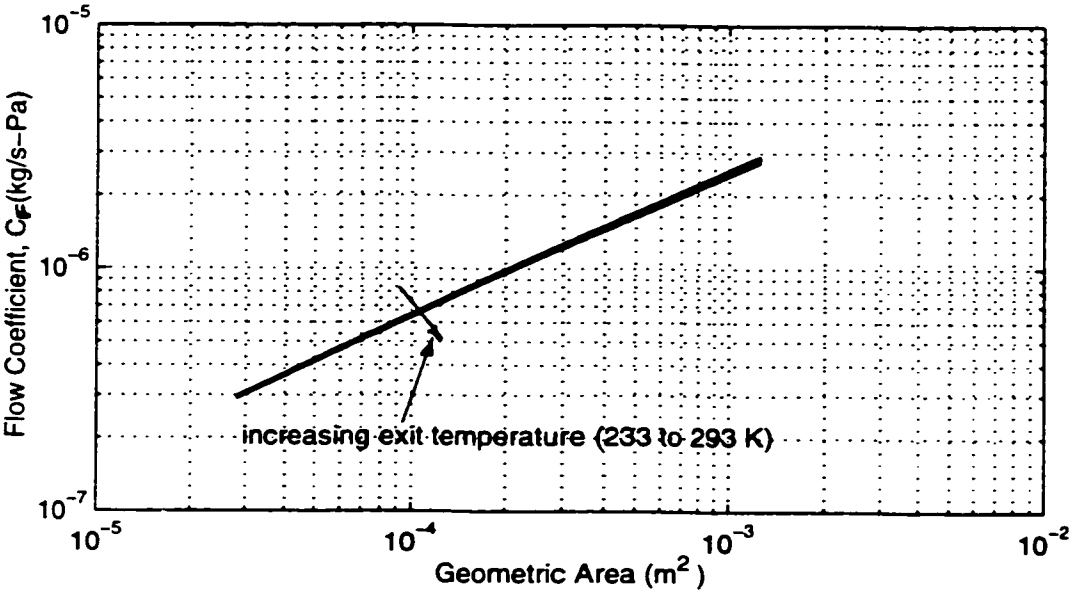


Figure 7.12. Flow Coefficients ($C_f$) for Holes.

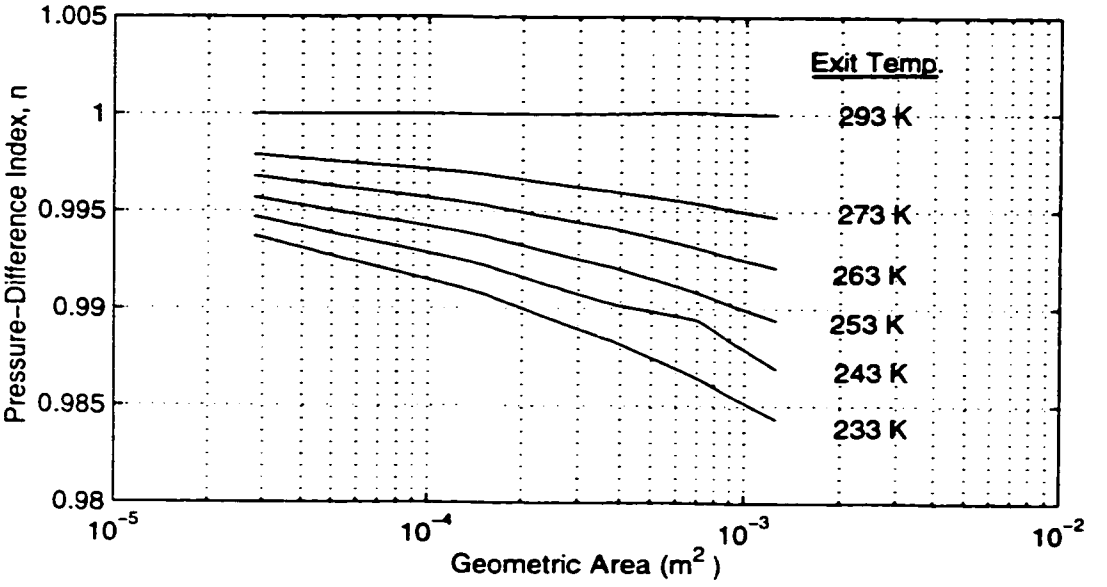


Figure 7.13. Pressure–Difference Indices, n, for Holes.

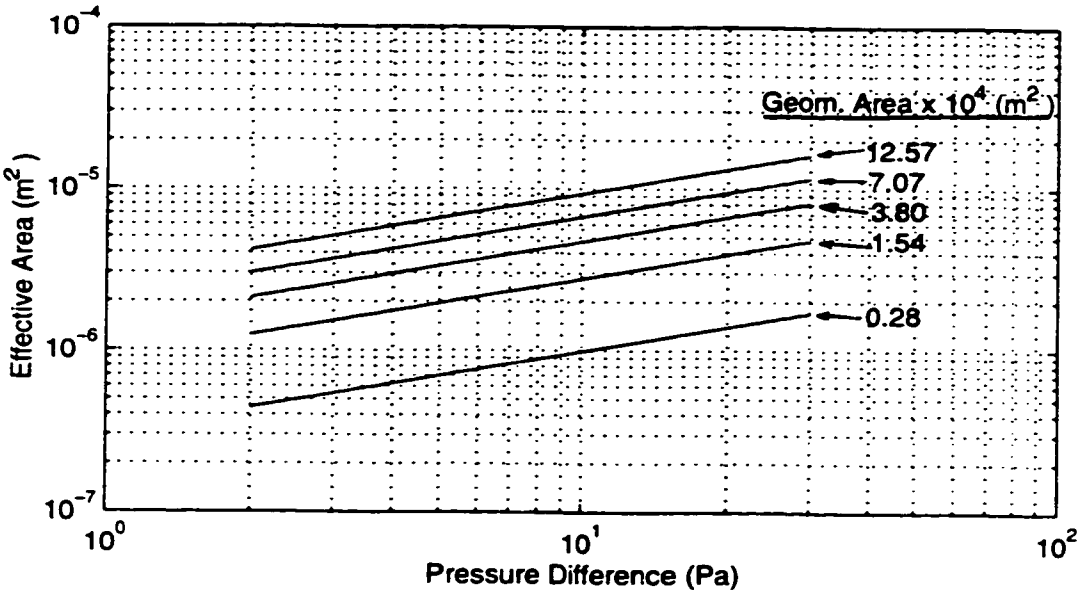


Figure 7.14. Effective Areas for Holes at 293 K.

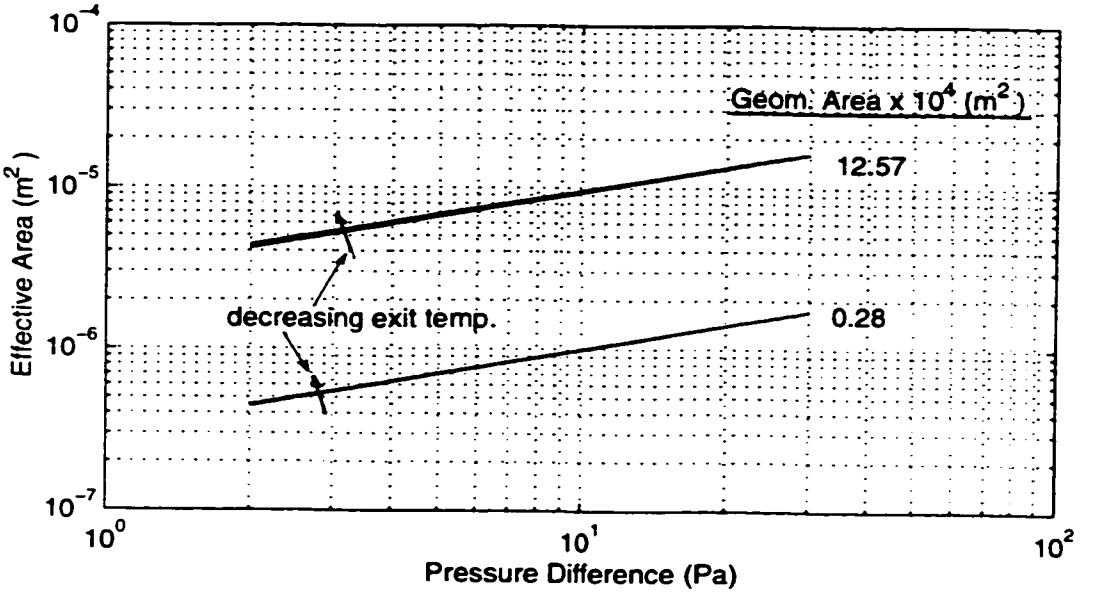


Figure 7.15. Effective Areas for Holes at Other Temperatures.

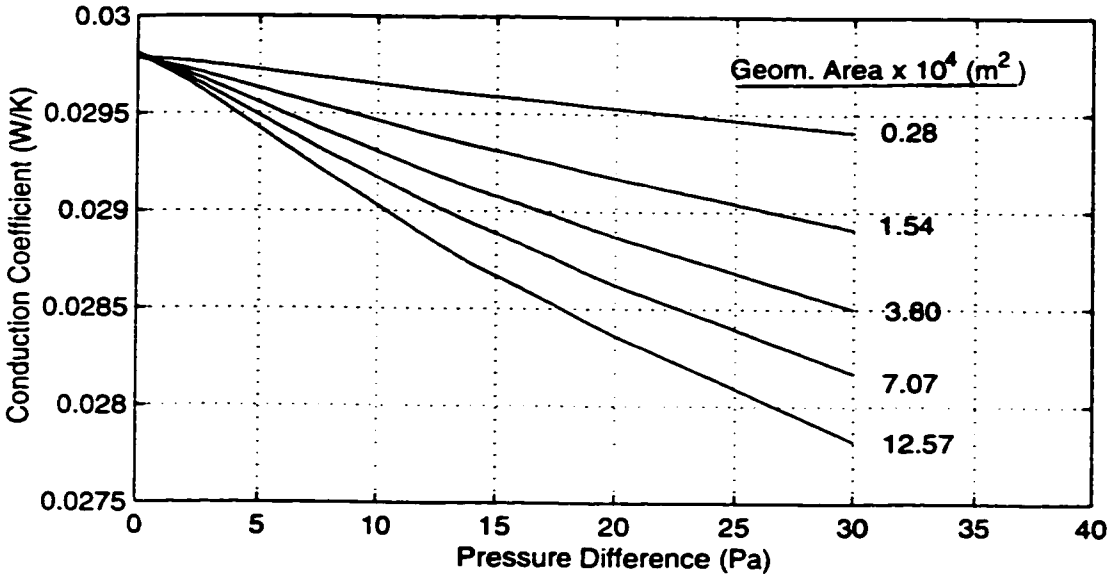


Figure 7.16. Conduction Heat Transfer Coefficients for Holes.

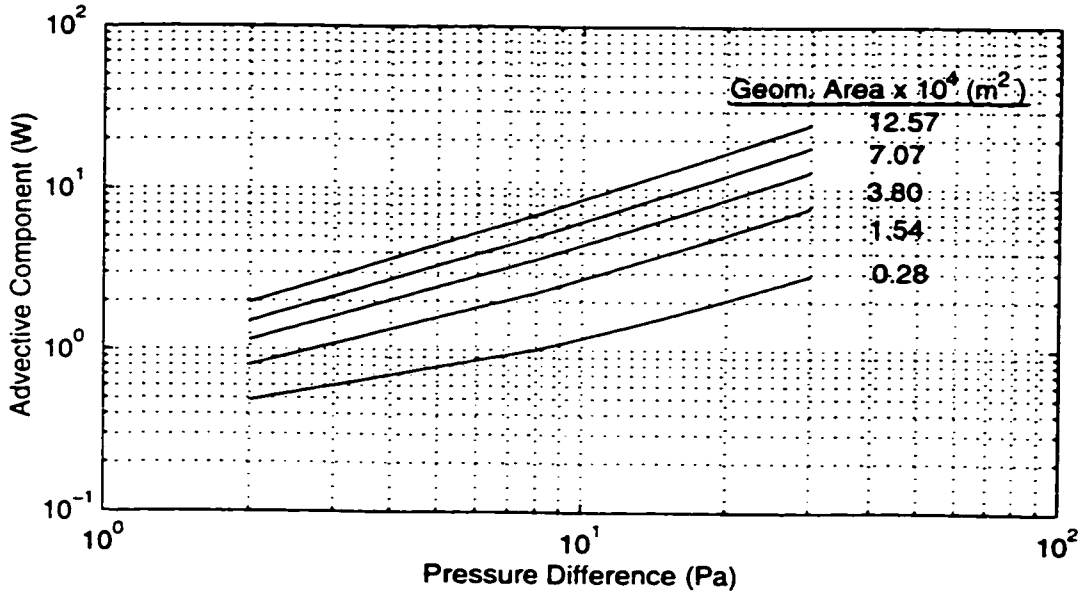


Figure 7.17. Advective Heat Transfer Components for Holes.

The flow coefficient ($C_F$) varies significantly with the opening area but is hardly affected by the temperature. At a given exit temperature, $C_F$ increases with the opening area. When the slit width is increased from 6mm to 40 mm, $C_F$ increases from about $2x10^{-5}$ to about $4x10^{-5}$. Similarly, when the hole diameter is increased from 6mm to 40 mm, $C_F$ increases from about $3x10^{-7}$ to about $3x10^{-6}$.

Computed data show that the total heat transfer rate is linearly related to the temperature difference when only dry air is considered. In this chapter the total heat transfer rate has been presented as the sum of two components:

(1) a component consisting of the product of the "conduction heat transfer coefficient", $C_{cond}$ (W/K), and the temperature difference gives the contribution from thermal conduction; and

(2) a component called the "advective heat transfer component", $H_{adv}$ (W), gives the contribution from the advection of bulk air.

In the case of a slit, $C_{cond}$ decreases with the pressure difference from about 0.038 W/K for a pressure difference of 2 Pa to about 0.030 W/K for a pressure difference of 30 Pa. For a given pressure difference, $C_{cond}$ increases by about 0.001 W/K when the slit width is increased from 6 mm to 40 mm. The advective heat transfer component ($H_{adv}$) increases with both the pressure difference and the slit width; from between 10 W (6 mm width) and 30 W (40 mm width) at 2 Pa to between 200 W (6 mm width) and 350 W (40 mm width) at 30 Pa.

In the case of a hole, $C_{cond}$ decreases with the pressure difference from about 0.0298 W/K for all hole diameters at a pressure difference of 2 Pa to about 0.0294 W/K, 0.0290 W/K, 0.0285 W/K, 0.0282 W/K, and 0.0278 W/K for hole diameters 6 mm, 14 mm, 22 mm, 30 mm, and 40 mm, respectively, at a pressure difference of 30 Pa. The advective heat transfer

component ($H_{adv}$) increases with both the pressure difference and the hole diameter; from between 0.5 W (6 mm diameter) and 2 W (40 mm diameter) at 2 Pa to between 3 W (6 mm diameter) and 25 W (40 mm diameter) at 30 Pa.

It is not known why, at a given pressure difference, the value of $C_{cond}$ increases with increasing slit width but decreases with increasing hole diameter.

Chapter 8 contains a summary of all the important findings in this research project.

# CHAPTER 8

# SUMMARY, CONCLUSIONS AND RECOMMENDATIONS

## 8.1 Summary and Conclusions

A new method for modelling the moisture condensation rate, called the Saturation Method for the Approximation of the Rate of Condensation (SMARC), was introduced. SMARC is an explicit model which directly utilises the known saturation and flow properties of moist air. The quasi-transient procedure was introduced as an alternative solution method to the fully-transient method, which can be used to make long-term predictions of moisture content by using large time steps. SMARC and the quasi-transient procedure were validated using three examples:

(1) Ogniewicz and Tien's (1981) one-dimensional quasi-steady forced convective moisture condensation problem;

(2) Yu's (1986) experimental results for one-dimensional forced convective transient moisture deposition in a cellulose slab; and

(3) Chen et al.'s (1997) two-dimensional problem investigating moisture deposition on a cold plate and the rate of heat conduction through the cold plate.

In Example 1, it was shown that SMARC is easy to use, and accurately reproduces the results which Ogniewicz and Tien obtained by a complex semi-analytical solution procedure.

In Example 2, SMARC and the quasi-transient technique were used successfully to solve Yu's problem, which is a forced-convective, multiphase, one-dimensional problem involving condensation. The quasi-steady solution was obtained directly from the boundary conditions, instead of using the traditional fully-transient methods which use an artificial dry state as

the initial state. The quasi-steady solution was then used as an initial state in the quasi-transient procedure which investigated the effect of long term moisture accumulation on the field variables such as temperature and moisture content. The predicted temperature profiles and the moisture contents for the long term compared quite well with the experimental results. Except for the case with the lowest nominal velocity (i.e., 0.30 mm/s), all predictions were within the measurement uncertainties. It was found that after the quasi-steady stage, the conduction term, the condensation rate term, and the latent heat term become very important in the equations because they determine the evolution of the field variables. The dominating role of the advection term does not extend beyond the quasi-steady stage. The role played by the effective thermal conductivity is crucial and its modelling merits further research, so that simulation moisture results may be improved.

In Example 3, it was proved that SMARC and the quasi-transient procedure can be used as a reliable and effective alternative to the fully-transient method when solving two-dimensional forced-convective problems with high exfiltration rates. The simulation temperature profiles, moisture profiles, and conduction heat transfer rates through the cold plate compared quite well with the experimental results.

During the investigations, it was found that varying the thermophysical properties of air with temperature is important; it improves the results for the temperature profiles and the moisture condensation rates.

After validation, SMARC and the quasi-transient procedure were used to investigate flow through slits in attic fibrous insulation for different boundary conditions. It was found that the exit temperature was the most influential factor in moisture deposition, followed by the pressure difference, the

inlet relative humidity, the slit width, and the exit relative humidity, in that order. Decreasing the exit temperature from 273 to 233 K increased the total condensation rate by 2820%; increasing the pressure difference from 2 to 30 Pa increased the total condensation rate by 1277%; increasing the inlet relative humidity from 40% to 80% increased the total condensation rate by 132%; increasing the slit width from 6 to 40 mm increased the total condensation rate by 78%; and increasing the exit relative humidity from 20% to 100% increased the total condensation rate by a mere 3.5%. Results indicated that the contribution made by the latent heat released to the total heat transfer rate is about 8% at most.

It was also found that all heat and mass transfer rates increase with time in the presence of accumulating moisture. Although the rates of change of the transfer rates are small, their increase with time means that the moisture not only accumulates, it does so at a faster rate with time if the boundary conditions are sustained, making the moisture problem worse.

The dry results for flow through slits and holes in attic insulation were used to investigate the power law pressure-flow relationship for slits and round holes and the correlations between heat transfer rate and the boundary conditions. The following findings were made.

(1) For both slits and holes, the value of the pressure index, n, for isothermal flow is constant and equal to 1. In non-isothermal flow, n decreases as the temperature difference and the opening area increase, but the deviations of n from 1 for such situations are very small and may be neglected.

(2) The flow coefficient ($C_F$) varies significantly with the opening area but is hardly affected by the temperature. At a given exit temperature, $C_F$ increases with the opening area.

(3) The total heat transfer rate is linearly related to the temperature difference when only dry air is considered and can be written as the sum of two components:

(i) a component consisting of the product of the "conduction heat transfer coefficient", $C_{cond}$ (W/K), and the temperature difference, which gives the contribution from thermal conduction; and

(ii) a component called the "advective heat transfer component", $H_{adv}$ (W), which gives the contribution from the advection of bulk air.

8.2 Recommendations

In the course of the investigations, it became certain that moisture and heat transfer results improved when variable thermophysical properties of air were used. Without the variable thermophysical properties, it was not possible to capture phenomena like the inflections on the temperature profiles which appear whenever there is a sudden and large change in the magnitude of the condensation rates. Such sudden changes are usually associated with phase changes. The variation of the thermophysical properties of air with temperature is straightforward and simple to apply. The inclusion of moisture content in the property models is, however, not easy at all, and the existing methods for this inclusion are very approximate and theoretical. It is recommended here that the properties of air be varied, at least with temperature, for any research work involving temperature gradients.

The key factor in the evolution of the field variables for wet systems is the effective thermal conductivity. The parallel model for the effective thermal conductivity used in this project is the simplest model available. To bridge the gap between simulation and experimental condensation rates, more

effort should be invested in finding alternative, probably better, models for this property.

Finally, in spite of SMARC's remarkable performance, the author believes that more work needs to be done to improve the model, especially for high flowrates and high temperature gradients when, as seen in the temperature profiles at the exit in Example 3 (Section 5.4), the model performs poorly.

# BIBLIOGRAPHY


ASHRAE Fundamentals Handbook (SI) (1997). American Society of Heating, Refrigerating and Air-Conditioning Engineering, Inc., Atlanta, Georgia.

Banklvall, C.G. (1972). (Summary of) Heat Transfer in Fibrous Materials. Document D4:1972, National Swedish Building Research Summaries. Also in J. Testing Evaluation (JTEVA), Vol. 1, No. 3, May 1973, pp 235-243.

Bear, J. (1972). Dynamics of Fluids in Porous Media. American Elsevier Publishing Company Inc.

Bear, J. and Bachmat, Y. (1991). Introduction to Modelling of Transport Phenomena in Porous Media, Vol. 4. Kluwer Academic Publishers.

Bejan, A. (1984). Convection Heat Transfer. John Wiley & Sons Inc.

Benner, S.M. and Modi, D.K. (1986). Moisture Gain of Spray-Applied Insulations and its Effect on Effective Thermal Conductivity - Part II. J. Thermal Insulation, Vol. 9, January 1986, pp 211-223.

Benson, R.S. (1977). Advanced Thermodynamics, 2nd Edition.

Bird, R.B., Stewart, W.E. and Lightfoot, E.N. (1960). Transport Phenomena. Wiley, New York.

CIBSE Guide (1988), Vol. A: Design Data. The Chartered Institution of Building Services Engineers, London (UK).

CIBSE Guide (1988), Vol. C: Reference Data. The Chartered Institution of Building Services Engineers, London (UK).

Chen, H., Besant, R.W. and Tao, Y. (1997a). Two-dimensional Air Exfiltration and Heat Transfer Through Fiberglass Insulation I: Numerical Model and Experimental Facility. HVAC & R Research, Vol. 3, No. 3, pp 197-213.

Chen, H., Besant, R.W. and Tao, Y. (1997b). Two-dimensional Air Exfiltration and Heat Transfer Through Fiberglass Insulation II: Comparisons Between Simulations and Experiments. HVAC & R Research, Vol. 3, No. 3, pp 215-232.

Cox, R.G. (1970). The motion of Long Slender Bodies in a Viscous Fluid. Part I: General Theory. J. Fluid

Mechanics, Vol. 44, pp 791-810.

de Groot, S.R. and Mazur, P. (1962). Non-Equilibrium Thermodynamics. North-Holland Publishing Company, Amsterdam, pg 279.

de Vries, D.A. (1958). Simultaneous Transfer of Heat and Moisture in Porous Media. American Geophysical Union Transactions, Vol. 39, No. 5, pp 909-916.

Epstein, N. and Masliyah, J.H. (1972). Creeping flow Through Clusters of Spheroids and Elliptical Cylinders. Chem. Eng. J., Vol. 3, pp 169-175.

Fletcher, C.A.J. (1988). Computational Techniques for Fluid Dynamics 1 (Fundamental and General Techniques), 2nd Edition. Springer-Verlag, New York Inc.

Fletcher, C.A.J. (1988). Computational Techniques for Fluid Dynamics 2 (Special Techniques for Differential Flow Categories), 2nd Edition. Springer-Verlag, New York Inc.

Hokoi, S. and Kumaran, M.K. (1993). Experimental and Analytical Investigations of Simultaneous Heat and Moisture Transport through Glass Fiber Insulation. J. Thermal Insul. and Bldg Envs, Vol. 16, January 1993, pp 263-292.

Holman, J.P. (1981). Heat Transfer, 5th Edition, pp 492-494. McGraw-Hill Book Company.

Incropera, F.P. and de Witt, D.P. (1990). Fundamentals of Heat and Mass Transfer, 3rd Edition. John Wiley & Sons Inc.

Iribarne, J.V. and Godson, W.L. (1981, Appendix I). Atmospheric Thermodynamics, 2nd Edition, Vol. 6, pg 246. D. Reidel Publishing Company.

Jackson, G.W. and James, D.F. (1986). The Permeability of Fibrous Porous Media. The Canadian Journal of Chemical Engineering, Vol. 64, pp 364-374.

Langlais, C., Hyrien, M. and Karlsfeld, S. (1982). Moisture Migration in Fibrous Insulation Material Under the Influence of a Thermal Gradient. Moisture Migration in Buildings, ASTM STP 779, pp 191-206.

Langlais, C., Arquis, E., and McCaa, D. J. (1990). A Theoretical and Experimental Study of Convective Effects in Loose-fill Thermal Insulation. Insulation Materials: Testing and Applications, ASTM STP 1030, pp 290-318.

Lapwood, E. R. (1948). Convection of a Fluid in a Porous Medium. Proc. Camb. Phil. Soc., Vol. 44, pp 508-521.

Leonard, B.P. (1979). A Stable and Accurate Convective Modelling Procedure Based on Quadratic Upstream Interpolation. Computer Methods in Applied Mechanics and Engineering, Vol.19, pp 59-98.

Luikov, A.V. (1975). Systems of Differential Equations of Heat and Mass Transfer in Capillary-Porous Bodies (Review). Int. J. Heat Mass Transfer, Vol. 18, pp 1-14.

Mason, E.A. and Monchick, L. (1965). Survey of the Equation of State and Transport Properties of Moist Gases. In "Humidity and Moisture", Vol. 3 (Fundamentals and Standards), pp 257-272 (Edited by Wexler, A. and Wildhack, W.A.). Reinhold Publishing Corporation, New York.

Mitchel, D.R., Tao, Y.-X. and Besant, R.W. (1995a). Air Filtration with Moisture and Frosting Phase Changes in Fiberglass Insulation - I. Experiment. Int. J. Heat Mass Transfer, Vol. 38, No. 9, pp 1587-1596.

Mitchel, D.R., Tao, Y.-X. and Besant, R.W. (1995b). Air Filtration with Moisture and Frosting Phase Changes in Fiberglass Insulation - II. Model Validation. Int. J. Heat Mass Transfer, Vol. 38, No. 9, pp 1597-1604.

Modi, D.B. and Benner, S.M. (1985). Moisture Gain of Spray-Applied Insulations and its Effect on Effective Thermal Conductivity - Part I. J. Thermal Insulation, Vol. 8, April 1985, pp 259-277.

Motakef, S. and El-Masri, M.A. (1986). Simultaneous Heat and Mass Transfer with Phase Change in a Porous Slab. Int. J. Heat Mass Transfer, Vol. 29, No.10, pp 1503-1512.

Murata, K. (1995). Heat and Mass Transfer with Condensation in a Fibrous Insulation Slab Bounded on One Side by a Cold Surface. Int. J. Heat Mass Transfer, Vol. 38, No. 17, pp 3253-3262.

Muskat, M. (1946). The Flow of Homogeneous Fluids Through Porous Media, First Edition. McGraw-Hill Book Company Inc.

Nield, D. A. (1968). Onset of Thermohaline Convection in a Porous Medium. Water Resources Res., Vol. 4, pp 553-560.

Nield, D. A. and Bejan A. (1992). Convection in Porous Media. Springer-Verlag New York Inc.

Ogniewicz, Y. and Tien, C.L. (1981). Analysis of Condensation in Porous Insulation. Int. J. Heat Mass Transfer, Vol. 24, pp 421-429.

Ojanen, T. and Kumaran, K. (1996). Effect of Exfiltration on the Hygrothermal Behaviour of a Residential Wall Assembly. J. Thermal Insul. and Bldg Envs., Vol. 19, January 1996, pp 215-227.

Patankar, S.V. (1980). Numerical Heat Transfer and Fluid Flow. Hemisphere Publishing Corporation.

Philip, J.R. and de Vries, D.A. (1957). Moisture Movement in Porous Materials under Temperature Gradients. American Geophysical Union Transactions, Vol. 38, No. 2, pp 222-232.

Reid, R.C., Prausnitz, J.M. and Sherwood, T.K. (1987). The Properties of Gases and Liquids. McGraw-Hill Book Company, New York.

Scheidegger, A. E. (1974). The Physics of Flow Through Porous Media, 3rd Edition. University of Toronto Press.

Shapiro, A.P. and Motakef, S. (1990). Unsteady Heat and Mass Transfer with Phase Change in Porous Slabs: Analytical Solutions and Experimental Results. Int. J. Heat Mass Transfer, Vol. 33, No. 1, pp 163-173.

Silberstein, A., Langlais, C., and Arquis, E. (1990). Natural Convection in Light Fibrous Insulation Materials with Permeable Interfaces: Onset Criteria and its Effects on the Thermal Performances of the Product. Journal of Thermal Insulation, Vol. 14 (July), pp 22-42.

Simonson, C.J., Tao, Y.-X. and Besant, R.W. (1996). Simultaneous Heat and Moisture Transfer in Fiberglass Insulation with Transient Boundary Conditions. ASHRAE Trans., Vol. 102 , No. 1, pp 315-327.

Tao, Y.-X., Besant, R.W. and Rezkallah, K.S. (1991a). Unsteady Heat and Mass Transfer with Phase Changes in an Insulation Slab: Frosting Effects. Int. J. Heat Mass Transfer, Vol. 34, No. 7, pp 1593-1603.

Tao, Y.-X., Besant, R.W. and Rezkallah, K.S. (1991b). Modelling of Frost Formation in a Fibrous Insulation Slab and on an Adjacent Cold Plate. Int. Comm. Heat Mass Transfer, Vol. 18, pp 609-618.

Tenwolde, A. and Rose, W.B. (1996). Moisture Control Strategies for the Building Envelope. J. Thermal Insul.

and Bldg Envs., Vol. 19, Jauary 1996, pp 207-214.

Tien, H.C. and Vafai, K. (1990). A Synthesis of Infiltration Effects on an Insulation Matrix. Int. J. Heat Mass Transfer, Vol. 33, No.6, pp 1263-1280.

Vafai, K. and Sarkar S. (1986). Condensation Effects in a Fibrous Insulation Slab. J. Heat Transfer, Vol. 108, pp 667-675.

Vafai, K. and Tien, H.C. (1989). A Numerical Investigation of Phase Change Effects in Porous Materials. Int. J. Heat Mass Transfer, Vol. 32, No. 7, pp 1261-1277.

Vafai, K. and Whitaker, S. (1986). Simultaneous Heat and Mass Transfer Accompanied by Phase Change in Porous Insulation. Trans. ASME, Vol. 108, pp 132-140.

Walker, I. S. and Wilson, D.J. (1998). Field Validation of Algebraic Equations for Stack and Wind Driven Air Infiltration Calculations. Int. J. Heating, Ventilating, Air-Conditioning and Refrigeration Research (HVAC & R Research), Vol. 4, April 1998, No.2.

Whitaker, S. (1977). Simultaneous Heat, Mass and Momentum Transfer in Porous Media: A Theory of Drying. Advances in Heat Transfer, Vol. 13, pp 119-203.

Wijeysundera, N.E., Hawlader, M.N.A. and Tan, Y.T. (1989). Water Vapour Diffusion and Condensation in Fibrous Insulation. Int. J. Heat Mass Transfer, Vol. 32, pp 1865-1878.

Wijeysundera, N.E., Zheng, B.F., Iqbal, M. and Hauptmann, E.G. (1993-94). Effective Thermal Conductivity of Flat and Round - Pipe Insulations in the Presence of Condensation. J. Thermal Insulation and Bldg Env., Vol. 17, pp 55-77.

Wijeysundera, N.E. and Hawlader, M.N.A. (1992). Effects of Condensation and Liquid Transport on the Thermal Performance of Fibrous Insulations. Int. J. Heat Mass Transfer, Vol. 35, No. 10, pp 2605-2616.

Wijeysundera, N.E. (1992). Effects of Moisture Migration in Insulations under Hot and Humid Conditions. J. Thermal Insulation, Vol. 15, April 1992, pp 319-339.

Wijeysundera, N.E., Zheng, B.F., Iqbal, M. and Hauptmann, E.G. (1996). Numerical Simulation of the Transient Moisture Transfer Through Porous Insulation. Int. J. Heat Mass Transfer, Vol. 39, No. 5, pp 995-1004.

Wilke, C.R. (1950). A Viscosity Equation for Gas Mixtures. J. Chem. Phys., Vol. 18, pg 517.

Wilkes, K. E. and Rucker, J. L. (1983). Thermal Performance of Residential Attic Insulation. Energy and Buildings, Vol. 5, pp 263-277.

Wilkes, K. E., Wendt, R. L., Delmas, A., and Childs, P. W. (1991). Thermal Performance of One Loose-fill Fiberglass Attic Insulation. Insulation Materials: Testing and Applications, 2nd Vol., ASTM STP 1116, pp 275-291.

Wilkes, K. E. and Childs, P. W. (1992). Thermal Performance of Fiberglass and Cellulose Attic Insulations. Thermal Performance of the Exterior Envelopes of Buildings (ASHRAE), Vol. 5, pp 357-367.

Wright, P.G. and Gray, P. (1962). Collision Interference Between Unlike Molecules Transporting Momentum or Energy in Gases. Trans. Faraday Soc. Vol. 58, pg 1.

Yu, R.C.H. (1986). The Effect of Exfiltration Rate on the Transient Moisture Accumulation in Porous Insulation. MSc Thesis (unpublished), Department of Mechanical Engineering, University of Alberta, Canada.

# APPENDIX A

# VARIABLE THERMOPHYSICAL PROPERTIES OF MOIST AIR AND OTHER MATERIAL PROPERTIES

## A.1 Variable Thermophysical Properties of Moist Air

The best way to determine a particular property of moist air would be by direct measurement. Experimental data on the properties of moist air are meager, and whatever little there is has been used, with the experimental data on dry air and pure water vapour, to predict the properties outside of the range of the available experimental data. Even the combination rules for determining the properties of the mixture from those of dry air and pure water vapour are not very satisfactory.

The specific heat capacity, dynamic viscosity, and thermal conductivity of the mixture, and the diffusion coefficient of water vapour in air, all vary with temperature, pressure, and the mixing ratio. In normal living conditions the effect of pressure is negligible compared to the effects of temperature and mixing ratio [Bear, 1972].

Many researchers have considered it sufficient to assume constant thermophysical properties for moist air in their work. They have dwelt more on the effects, on heat and mass transfer, of the intensive properties and boundary types. However, in studies on buildings, the external temperatures may swing by as much as 60°C between winter and summer. From the literature review (Chapter 2), we saw that for such a large variation in temperature, the value of a thermophysical property may change by as much as 20%. It then becomes clear that the effect of varying the intensive properties and changing boundary conditions is best captured by varying the thermophysical properties accordingly. There are many formulae, mostly semi-empirical, for relating the

thermophysical properties of moist air to temperature, pressure and composition.

The measurement of the thermophysical properties of moist air and their dependence on temperature, moisture content and pressure has been slow. The National Bureau of Standards (NBS) circular of 1955 listed semi-theoretical vapour diffusivities, conductivities, viscosities, and thermal diffusion (Soret) coefficients at different temperatures. These properties, as they appear in the circular, are discussed in great detail by Mason and Monchick (1965). The authors also explain how the properties of moist air can be estimated from those of dry air and pure vapour for any mixing ratio. Some of the contents of the NBS circular appear in the 1997 ASHRAE Fundamentals Handbook (SI) and in the book by Reid (1987). It must be mentioned here that the empirical relations that Reid (1987) provides for the dependence of the diffusion coefficients on temperature and pressure are accurate close to a reference temperature, but depart increasingly from the NBS circular values away from the reference point. Benson (1977) gives, among other information, the dependence of the specific heat capacities on temperature.

To the best of the author's knowledge, the data and relations provided in the NBS (1955) circular, Mason and Monchick's (1965) paper, Reid's (1987) book, Benson's (1977) book, and in ASHRAE (1997), have never been used fully by researchers in the simulation of heat and mass transfer processes in fibrous insulation. The common practice has been to assume constant thermophysical properties for dry air (and even moist air) regardless of the temperature range. "Justification" for the assumptions has been found in yet another assumption - that the driving forces (pressure, temperature and concentration gradients) absolutely dominate any effect that the variation in the thermophysical properties might have. In the end, emphasis has been placed on the general trends established by

the boundary conditions rather than on the details of the mechanics of the transfer processes.

The models for the variable thermophysical properties of moist air used in this project are developed in the following sections.

(a) Specific Heat Capacities at Constant Pressure

Benson (1977) gives the dependence of the heat capacity (at constant pressure) of an ideal gas on temperature as

$$C_p = \frac{\bar{R}}{M}[A_1 + 2A_2T + 3A_3T^2 + 4A_4T^3], \qquad (A.1)$$

where, $\bar{R}$ = 8314.3 J/kmol-K, and

M = molecular mass in kg/kmol.

The values of M, $A_1$, $A_2$, $A_3$, and $A_4$ for seven ideal gases are given in the same reference. From these values we obtain the following simplified expressions for Water Vapour, Nitrogen and Oxygen, where T is the temperature in Kelvin.

$$C_{pv} = 1727.3576 + 0.52204T + 6.85660\times10^{-5}T^2 - 3.35606\times10^{-8}T^3 \qquad (A.2)$$

$$C_{pNi} = 992.519 + 0.174658T + 1.7388\times10^{-6}T^2 - 7.8048\times10^{-9}T^3 \qquad (A.3)$$

$$C_{pOx} = 845.2426 + 0.3390T - 1.16553\times10^{-4}T^2 + 1.59950\times10^{-8}T^3 \qquad (A.4)$$

There is no chemical reaction involving dry air. Therefore, its properties will be dominated by the properties of Oxygen and Nitrogen. Hence, as an approximation, it is assumed that dry air consists of 23.29% Oxygen and 76.71% Nitrogen by weight, giving its specific heat capacity, in J/kg-K, as

$$C_{pa} = 0.2329 C_{pOx} + 0.7671 C_{pNi} . \qquad (A.5)$$

Mass-averaging using the mixing ratio gives the predicted heat capacity of moist air as

$$C_{pg} = \frac{\rho_v}{\rho_g} C_{pv} + \frac{\rho_a}{\rho_g} C_{pa} \qquad (A.6)$$

where, $\rho_v$ is the vapour density,

$\rho_a$ is the dry-air density, and

$\rho_g$ is the total density in the space under consideration.

The units of heat capacity in this case are J/kg-K.

(b) Diffusion Coefficients of Water Vapour in Air

Figure A.1 shows a least squares fit of the data in ASHRAE Fundamentals Handbook (1997, SI, pg 6.16). The data is adopted from Mason and Monchick (1965) and covers the temperature range 203 K to 523 K.

The fit gives

$$D_{va} = 1.643 \times 10^{-9} T^{1.695} \qquad (A.7)$$

for the dependence on temperature of the diffusion coefficient of water vapour in open air ($D_{va}$). To obtain the diffusion coefficient in a porous medium ($D_v$), Ogniewicz and Tien (1981) recommended that $D_{va}$ be multiplied by the porosity, $\epsilon$, because in such a medium the gas occupies a volume $\epsilon$ for every unit volume. That is,

$$D_v = \epsilon D_{va} . \qquad (A.8)$$

The units of the diffusion coefficient are $m^2/s$.

(c) Viscosities, $\mu$

Least squares fits of the viscosity data in Mason and Monchick (1965) over the temperature range 193 K to 573 K give

$$\mu_a = 2.543 \times 10^{-7} T^{0.750} \qquad (A.9)$$

and

$$\mu_v = 1.916 \times 10^{-8} T^{1.093} \qquad (A.10)$$

for the viscosities of dry air and water vapour, respectively. The fits are shown in Figures A.2 and A.3, respectively. The units of $\mu$ are kg/m-s or $Ns/m^2$.

One of the simpler formulae for calculating the viscosity of the mixture of water vapour and dry air is due to Sutherland [Wright, P.G. and Gray, P., 1962] and is of the form

$$\mu_g = \frac{\mu_a}{1 + G_{av}\left(\frac{x_v}{x_a}\right)} + \frac{\mu_v}{1 + G_{va}\left(\frac{x_a}{x_v}\right)}. \qquad (A.11)$$

$G_{av}$ and $G_{va}$ are constants for the gas pair dry air-water vapour at a given temperature, and $x_i$ is the mole fraction of a component i.

Wilke (1950) proposed a simple but usually accurate combination scheme for the G factors. This scheme gives

$$G_{av} = \frac{\sqrt{2}}{4}\left(\frac{M_v}{M_a + M_v}\right)^{\frac{1}{2}}\left[1 + \left(\frac{\mu_a}{\mu_v}\right)^{\frac{1}{2}}\left(\frac{M_v}{M_a}\right)^{\frac{1}{4}}\right]^2 \qquad (A.12)$$

and

$$G_{va} = \frac{\sqrt{2}}{4}\left(\frac{M_a}{M_a + M_v}\right)^{\frac{1}{2}}\left[1 + \left(\frac{\mu_v}{\mu_a}\right)^{\frac{1}{2}}\left(\frac{M_a}{M_v}\right)^{\frac{1}{4}}\right]^2 \qquad (A.13)$$

where $M_i$ is the molecular weight of a substance i.

Using $M_{Ox} = 32.00$; $M_{Ni} = 28.02$; $M_a = 28.85$; and

$M_v = 18.02$

gives

$$\frac{x_v}{x_a} = \left(\frac{M_a}{M_v}\right)\left(\frac{\rho_v}{\rho_a}\right) = 1.6015\left(\frac{\rho_v}{\rho_a}\right), \tag{A.14}$$

and

$$\frac{x_a}{x_v} = 0.6244\left(\frac{\rho_a}{\rho_v}\right) . \tag{A.15}$$

(d) Thermal Conductivities, $\lambda$

For thermal conductivities, the expressions

$$\lambda_a = 1.814 \times 10^{-4} T^{0.870} \tag{A.16}$$

and

$$\lambda_v = 1.177 \times 10^{-5} T^{1.281} \tag{A.17}$$

have been obtained by applying least squares fitting to the data for thermal conductivities of dry air and water vapour, respectively. The data are obtained from Mason and Monchick (1965) for the temperature range 193 K to 573 K, and the fits are illustrated in Figures A.4 and A.5, respectively. The combination formula, after Sutherland [Wright, P.G. and Gray, P., 1962], is

$$\lambda_g = \frac{\lambda_a}{1 + G_{av}\left(\frac{x_v}{x_a}\right)} + \frac{\lambda_v}{1 + G_{va}\left(\frac{x_a}{x_v}\right)} \tag{A.18}$$

$G_{av}$ and $G_{va}$ in Equation A.18 take on the same values as those computed for viscosity above, in accordance with Mason and Monchick's (1965) recommendation. $\lambda$ has units W/m-K.

(e) Cross-transport Phenomena and Coefficients

The cross-transport phenomena or coupled processes can be accounted for by extra terms in the vapour and thermal energy conservation equations given in Sections 3.5.2 and 3.5.4, respectively. To the vapour balance equation is added the term

$$\nabla \cdot (D_s \rho_g C \nabla T) \quad ,$$

and to the energy balance equation is added the term

$$\nabla \cdot (D_d C_{pv} \rho_g \nabla C) \quad ,$$

where $D_s$ and $D_d$ are the Soret and Dufour coefficients, respectively.

Cross-diffusion terms are small and are usually neglected. However, the neglecting is done more for the sake of simplicity than anything else, because, though small, the contributions of these phenomena are by no means negligible for many cases. It is indeed necessary to carry out a rough calculation of their magnitudes in any particular application so as to asses the errors due to their being neglected.

The cross-diffusion coefficients are extremely difficult to calculate from theory (i.e., Onsager's or Onsager-Casimir's reciprocal relations or Onsager's law [Bear and Bachmat, 1991]), while experimental data are not available for most of the common gaseous mixtures. de Groot and Mazur (1962) provide that, in gases,

$$\frac{D_s}{D_v} = O(10^{-3} - 10^{-5})\ K^{-1} \quad , \tag{A.19}$$

with

$$D_s \approx 10^{-8} - 10^{-10}\ m^2/s\text{-}K \quad , \tag{A.20}$$

and

$$D_d \approx D_s\ (m^2K/s) \quad , \tag{A.21}$$

where $D_v$, the mass diffusivity, is in $m^2/s$.

Luikov (1975) also gives a similar estimate for $D_s$.

For $H_2O$-air mixtures, the thermal diffusion (Soret) factor depends on both temperature and composition. A search of available literature failed to reveal any experimental value

for the thermal diffusion factor involving $H_2O$. The non-dimensional values tabulated in Mason and Monchick (1965) could be in error by as much as a factor of two, but are good enough for order-of-magnitude assessment. Mason and Monchick state that at low temperatures the $H_2O$ molecules tend to concentrate at the cold boundary rather than at the hot boundary, giving rise to the negative signs in the data at low temperatures. Mason and Monchick do not offer any physical explanation or reference for their explanation of the phenomenon.

Least squares fits on the non-dimensional data for air and $H_2O$ in Mason and Monchick (1965) (Figures A.6 and A.7) give, for the temperature range 193 K to 573 K,

$$\bar{D}_{sa} = -0.0318 + 1.570 \times 10^{-4} T \quad , \tag{A.22}$$

for a mixture where the mole fraction of $H_2O$ tends to zero, and

$$\bar{D}_{sv} = -0.0409 + 2.115 \times 10^{-4} T \quad , \tag{A.23}$$

for a mixture where the mole fraction of $H_2O$ tends to one. $\bar{D}_s$ is the non-dimensional thermal diffusion factor. Thermal diffusion coefficients are estimated relative to the mass diffusion coefficients, $D_v$. By definition,

$$\bar{D}_s = \frac{D_s T}{D_v} \quad . \tag{A.24}$$

Let the reference temperature, $T_0$, be 273.15 K. Then the reference thermal diffusion coefficients (non-dimensional) are:

$$\bar{D}_{sao} = -0.0318 + 1.570 \times 10^{-4} T_o \quad , \tag{A.25}$$

for a mixture where the mole fraction of $H_2O$ tends to zero, and

$$\bar{D}_{svo} = -0.0409 + 2.115 \times 10^{-4} T_o \quad , \tag{A.26}$$

for a mixture where the mole fraction of $H_2O$ tends to one.

For the thermal diffusion coefficients of mixtures of intermediate compositions, appeal is once again made to the now-familiar Sutherland formula and Wilke's combination scheme. Together, and after some manipulation, these give:

$$\bar{D}_s = \frac{\bar{D}_{sa}}{\left(1 + G_{av}\left(1.6015 \frac{\rho_{vo}}{\rho_{ao}} \frac{\bar{\rho}_v}{\bar{\rho}_a}\right)\right)} + \frac{\bar{D}_{sv}}{\left(1 + G_{va}\left(0.6244 \frac{\rho_{ao}}{\rho_{vo}} \frac{\bar{\rho}_a}{\bar{\rho}_v}\right)\right)} \qquad \text{(A.27)}$$

and

$$\bar{D}_{so} = \frac{\bar{D}_{sao}}{\left(1 + G_{avo}\left(1.6015 \frac{\rho_{vo}}{\rho_{ao}}\right)\right)} + \frac{\bar{D}_{svo}}{\left(1 + G_{vao}\left(0.6244 \frac{\rho_{ao}}{\rho_{vo}}\right)\right)} \qquad \text{(A.28)}$$

Wilke's factors $G_{av}$ , $G_{va}$ , $G_{avo}$ , and $G_{vao}$ acquire the same values as those obtained for viscosity. Note that $G_{avo}$ is the value of $G_{av}$ at a temperature $T_o$ while $G_{vao}$ is obtained similarly from $G_{va}$ . $\bar{D}_{so}$ is computed from $\bar{D}_{sao}$ and $\bar{D}_{svo}$ since the latter two are known from Equations A.25 and A.26, respectively.

From the definition of the non-dimensional thermal diffusion factor (Equation A.24), we get

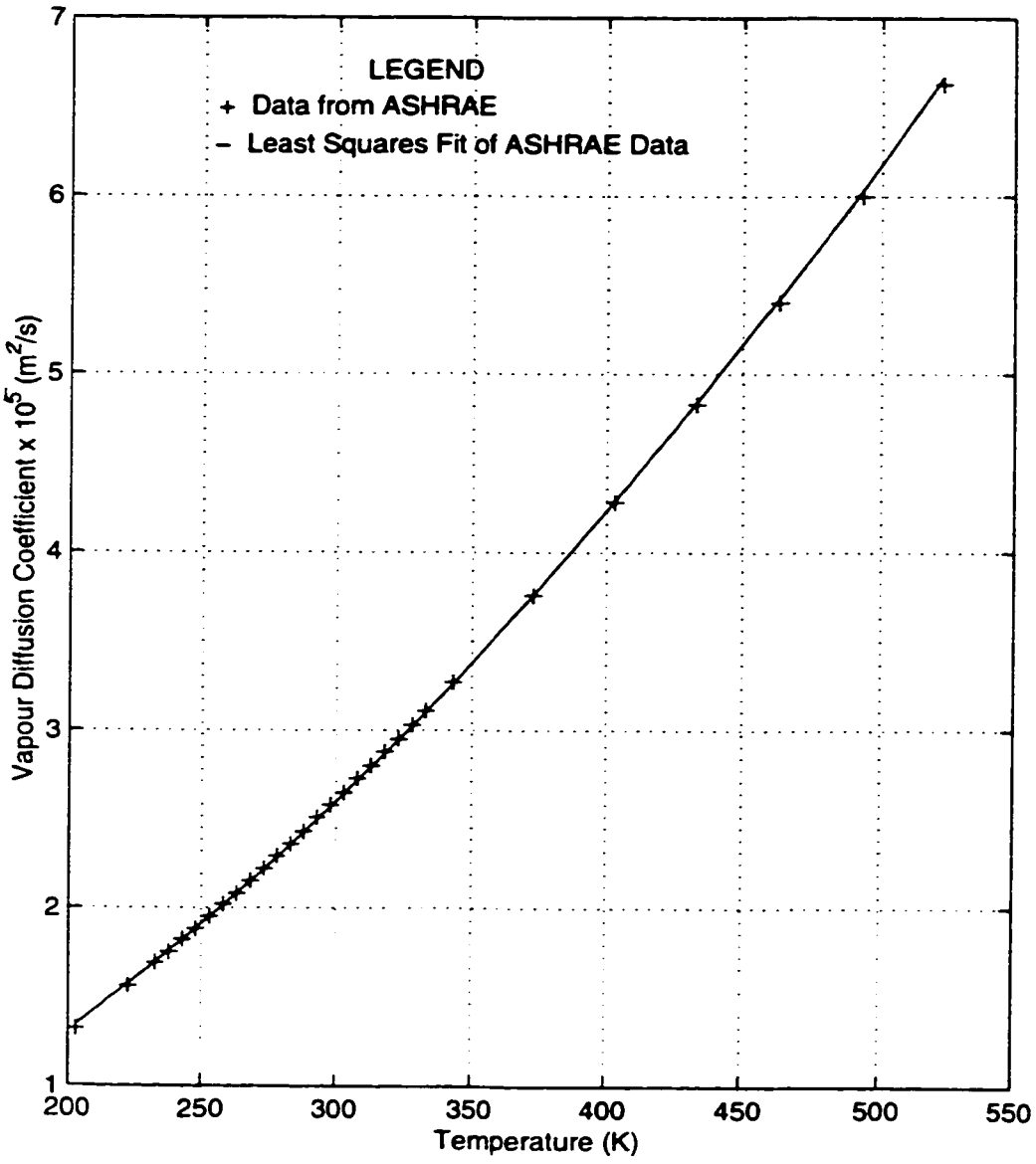


Figure A.1. Diffusion Coefficients of Water Vapour in Air.

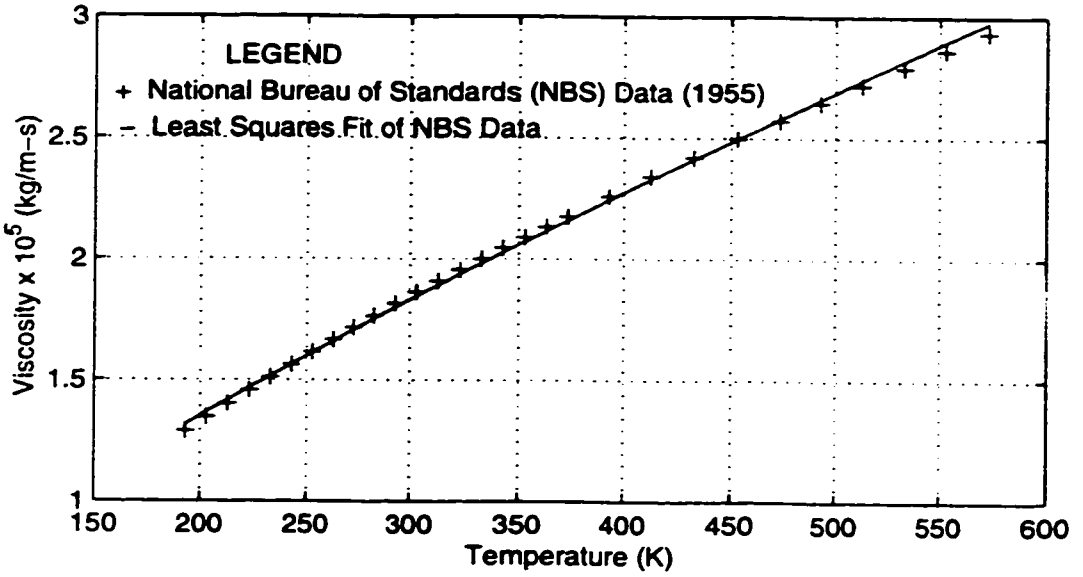


Figure A.2. Dynamic Viscosities of Dry Air.

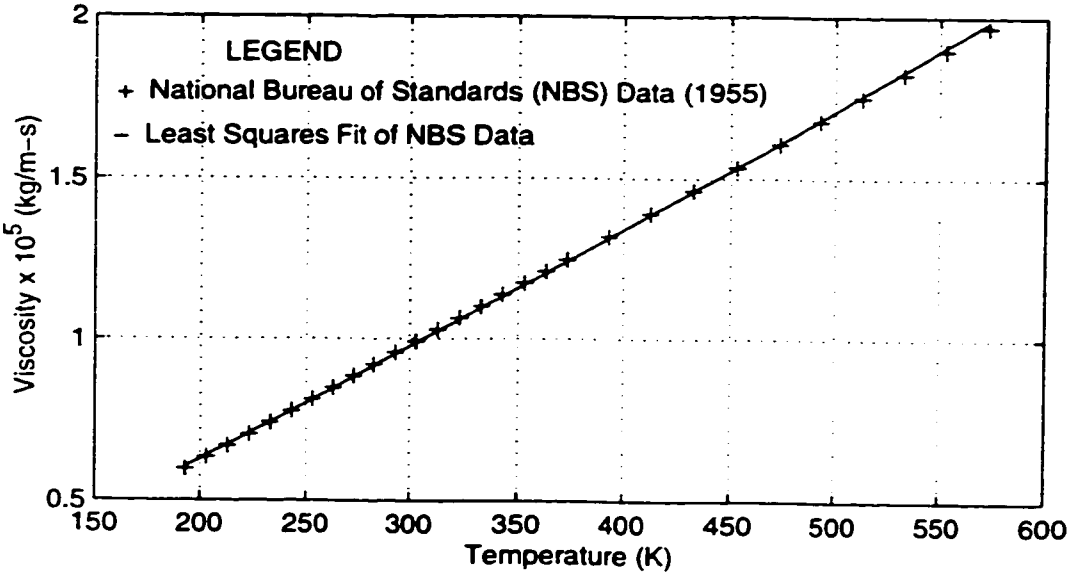


Figure A.3. Dynamic Viscosities of Pure Water Vapour.

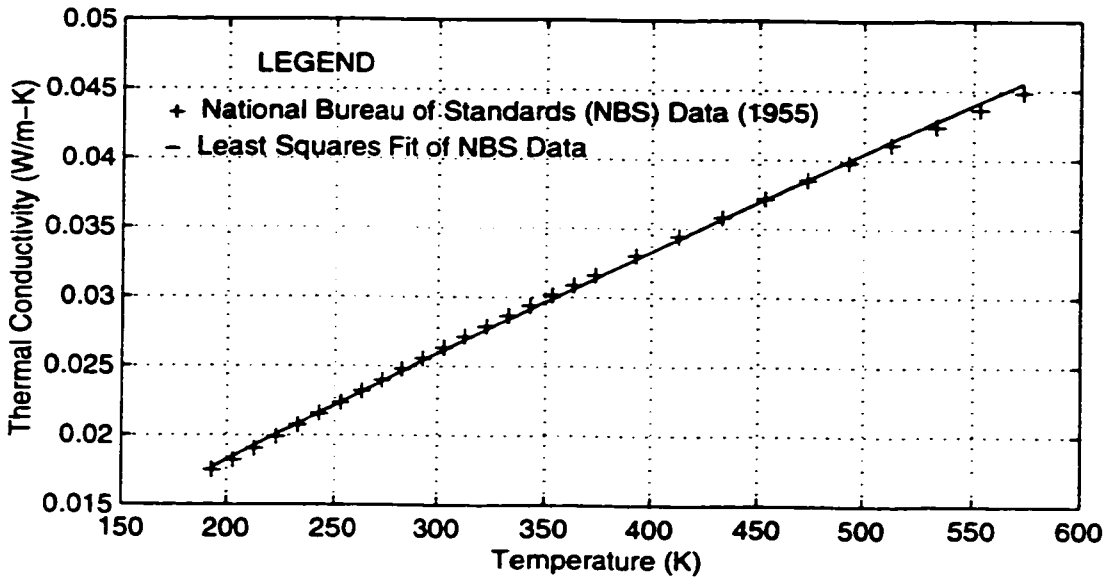


Figure A.4. Thermal Conductivities of Dry Air.

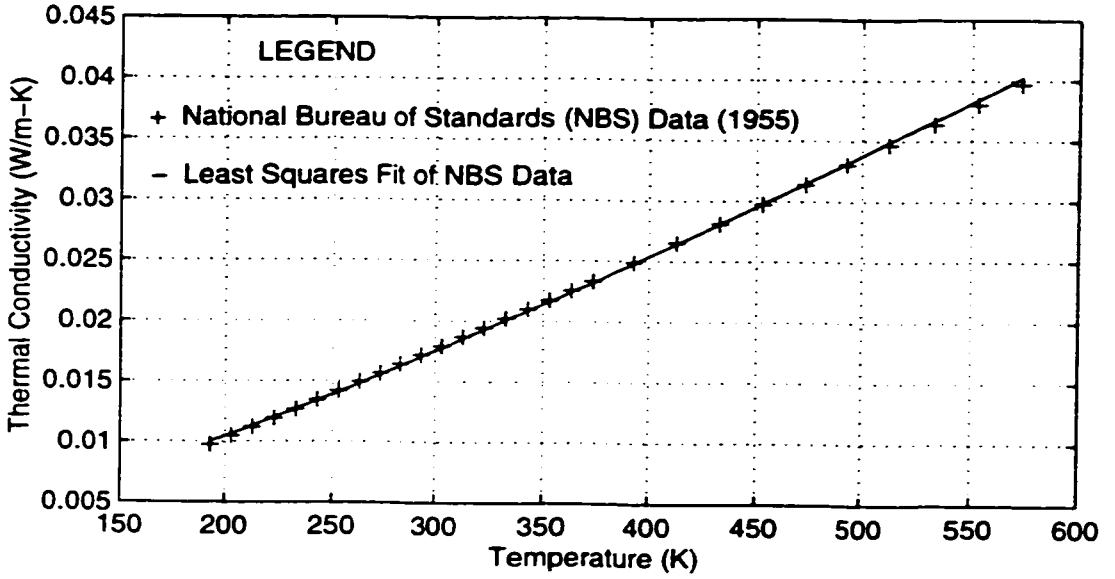


Figure A.5. Thermal Conductivities of Pure Water Vapour.

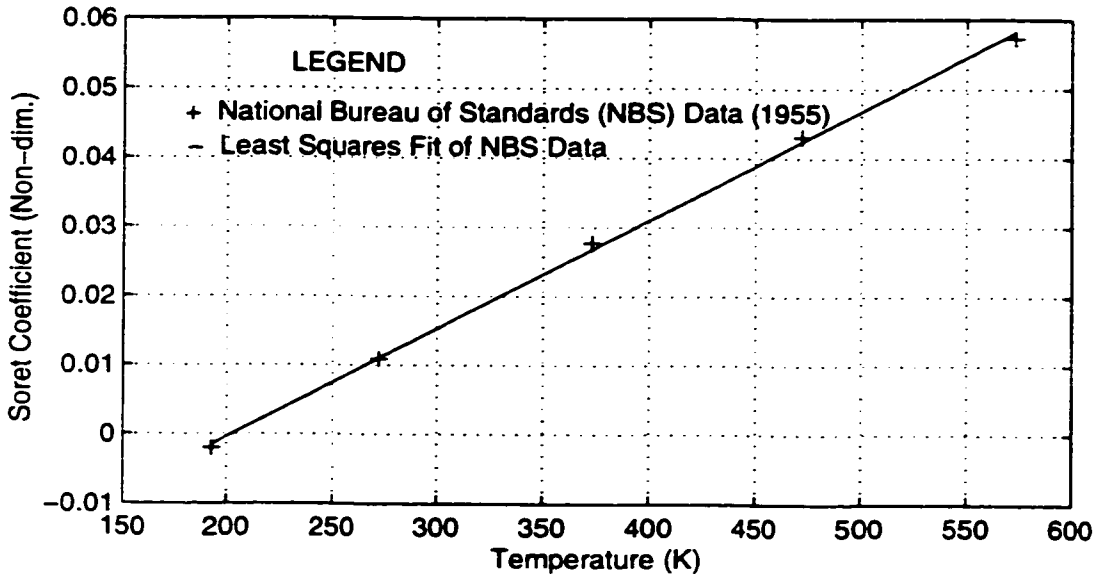


Figure A.6. Soret Coefficients of "Dry Air"

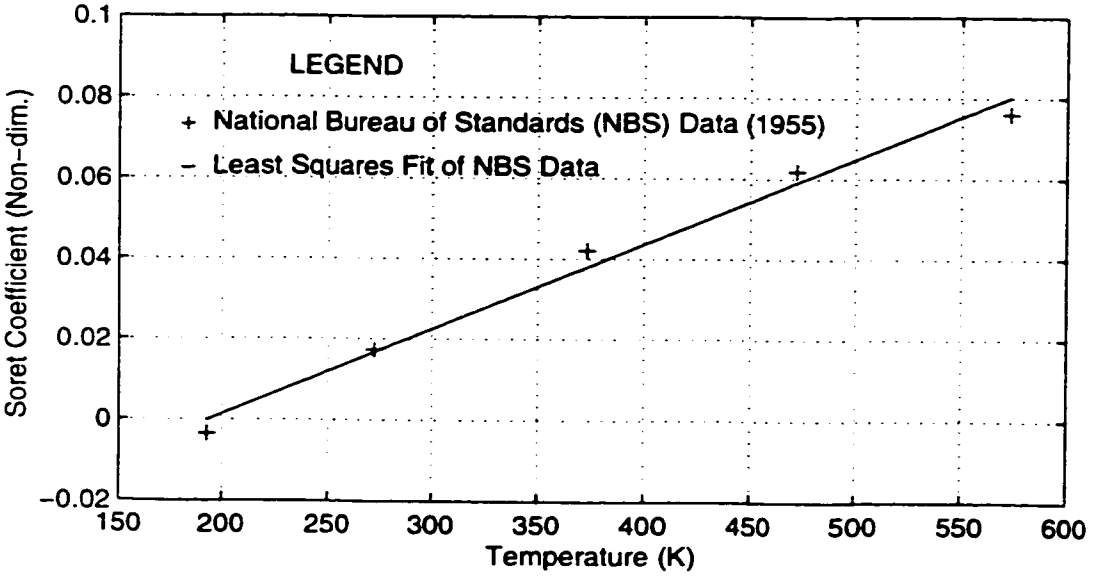


Figure A.7. Soret Coefficients of "Pure Water Vapour"

$$\bar{D}_{so} = \frac{D_{so} T_o}{D_{vo}} \quad . \tag{A.29}$$

Hence

$$D_{so} = \frac{D_{vo} \bar{D}_{so}}{T_o} \ (m^2/s\text{-}K) \tag{A.30}$$

and

$$D_s = D_{so} \bar{D}_s \ (m^2/s\text{-}K) \quad . \tag{A.31}$$

$\bar{D}_{so}$ is obtained from Equation A.28, $D_{vo}$ from Equations A.7 and A.8 (for T = 273.15 K), and $\bar{D}_s$ from Equation A.27.

Finally, the Dufour coefficient , $D_d$, is given by

$$D_d = D_s \ (m^2K/s). \text{ [de Groot and Mazur, 1962]} \tag{A.32}$$

A.2 Other Material Properties

Besides moist air, the porous medium consists of a solid matrix and, sometimes, liquid (water) and/or solid (ice/frost). The properties of the medium are obtained by averaging from the properties of the solid matrix and any liquid or ice that may be present, besides the properties of the moist air. The properties of the solid matrix, the liquid, and the ice do not vary with temperature and pressure as significantly as do the properties of moist air, and, for the sake of simplicity, they are usually taken to be constant. The constant values adopted here have been averaged from the available experimental data. The solid insulation material considered in this project is fiberglass. Cellulose (or paper pulp) is used for the one-dimensional case where model and experimental results are compared. Plasterboard (or gypsum) forms the physical barrier between the interior and the attic insulation. The properties of these elements are listed below.

(a) Fiberglass

Representative properties of fiberglass are taken to be

those of window glass at 293 K. These are:

Conductivity, $\lambda_s$ = 0.78 W/m-K;

Density, $\rho_s$ = 2700 kg/m$^3$; and,

Specific heat capacity, $C_{ps}$ = 840 J/kg-K.

(b) Cellulose (paper pulp)

Cellulose insulation, as a porous medium, is described in Section 5.3.1.

At 300 K the properties of hardwood (oak, maple) are very similar to the properties of the cellulose or paper pulp used in building insulation. The properties of hardwood are therefore adopted for the solid component of the cellulose insulation. These are given in Incropera and de Witt (1990) as

Conductivity, $\lambda_s$ = 0.16 W/m-K;

Density, $\rho_s$ = 720 kg/m$^3$; and,

Specific heat capacity, $C_{ps}$ = 1255 J/kg-K.

(c) Plasterboard (Gypsum)

One-half inch (0.0127 m) thick plasterboard is used as the physical and thermal barrier between the room conditions and the insulation in the attic. At 300 K, from Incropera and de Witt (1990), plasterboard has the following properties:

Conductivity, $\lambda_p$ = 0.17 W/m-K; and,

Density, $\rho_p$ = 800 kg/m$^3$.

(d) Ice or Frost

Incropera and de Witt (1990) give the conductivity and density of ice at 253 K and 273 K. Averaging the values for the two temperatures gives:

Conductivity, $\lambda_i$ = 1.955 W/m-K; and,

Density, $\rho_i$ = 920 kg/m$^3$.

Iribarne and Godson (1981) give tabulated values of specific heat capacity, $C_{pi}$, and heat of sublimation, $h_{sub}$, of ice for a range of temperatures. Least square fits on these data give the following relations:

$$C_{pi} \approx 10.394 T^{0.947} \; J/kg\text{-}K \qquad (A.33)$$

(for values of T between 223 and 273 K); and,

and

$$h_{sub} \approx (3.129 \times 10^6) T^{-0.0176} \; J/kg \qquad (A.34)$$

(for values of T between 253 and 273 K).

Between 233 and 253 K, the value of $h_{sub}$ is approximately constant at 2.839x10$^6$ J/kg.

(e) Liquid (water)

Tien and Vafai (1990) give the thermal conductivity and density of water as :

Conductivity, $\lambda_l$ = 0.603 W/m-K; and,

Density, $\rho_l$ = 1000 kg/m$^3$.

Iribarne and Godson (1981) give tabulated values of specific heat capacity, $C_{pw}$, and heat of vaporisation, $h_{vap}$, of water for a range of temperatures. Least square fits on the data give the following relations:

$$C_{pw} \approx (8.210 \times 10^3) T^{-0.119} \; J/kg\text{-}K \qquad (A.35)$$

(for values of T between 273 and 293 K);

and,

$$h_{vap} \approx (1.175 \times 10^7) T^{-0.276} \; J/kg \qquad (A.36)$$

(for values of T between 273 and 303 K).

(f) Porous Media: Permeability and Porosities

Throughout this project a permeability of $5 \times 10^{-10}$ $m^2$ for fiberglass has been used. The porosities used are 0.97 [Tien and Vafai, 1990] and 0.98 [Ogniewicz and Tien, 1981] for fiberglass and 0.91 [Yu, 1986] for cellulose.

(g) Specific Gas Constants

The universally accepted values of the specific gas constants for dry air, $R_a$, and water vapour, $R_v$, are 287 and 462 J/kg-K, respectively.

A.3 Natural and Forced Convective Heat Transfer Coefficients

The term convection refers to the cummulative transport of heat and mass due to the bulk fluid motion (advection) and the random molecular motion (diffusion) in the presence of a temperature or concentration gradient. Diffusion dominates near a surface where, in accordance with the velocity boundary theory, the fluid velocity is low.

Convective heat and mass transfer may be classified according to the nature of the flow. When the flow is induced by external means, say a fan, pump, or atmospheric winds, we talk of forced convection. When the flow is induced by buoyancy forces due to density differences caused by temperature variations, we talk of free (or natural) convection. Conditions corresponding to mixed (i.e., combined forced and natural) convection often exist.

Convective heat transfer is governed by Newton's law of cooling:

$$q'' = h_f(T_s - T_\infty) \quad , \tag{A.37}$$

where $q''$ is the convective heat flux ($W/m^2$),

$T_s$ is the solid surface temperature, and

$T_\infty$ is the fluid's bulk temperature.

The proportionality constant $h_f$ ($W/m^2$-K) is called the convective heat transfer coefficient, the film conductance or the film coefficient. The value of $h_f$ (or $h_n$ for natural or free convection) depends on the conditions in the boundary layer, which are influenced by the surface geometry, the nature of the fluid motion, and the thermodynamic and transport properties of the fluid. Newton's law of Cooling applies regardless of whether the flow of heat is from the fluid to the solid surface or from the solid surface to the fluid.

Incropera and de Witt (1990) provide the following "typical" values for convective heat transfer coefficients in $W/m^2$-K.

| | |
|---|---|
| Free Convection: | |
| gases | 2 - 25 |
| liquids | 50 - 1000 |
| Forced Convection: | |
| gases | 25 - 250 |
| liquids | 50 - 20000 |

The "problem of convection" is to develop means to determine the convection coefficients, $h_n$, $h_f$ and $h_m$ (for mass transfer). For simple flow situations, the coefficients have been obtained by solving boundary layer equations. The more practical approach would be to calculate the coefficients from empirical relations governing different flow situations. The particular form of these empirical equations is obtained by correlating measured convection heat and mass transfer results in terms of appropriate dimensionless groups.

Available data on values of forced convection heat transfer coefficients relate to flow over solid boundaries. C. L. Tien,

H. C. Tien and their associates have often applied forced convection heat transfer coefficients to situations where the fluid is forced across a boundary and into or out of a porous medium. However, the origins or methods of determination of the values they use is not clear. There is also no evidence of any other group of researchers or individuals, independent of those named above, who have resorted to similar usage. But theirs are about the only results that are available for a comparative evaluation of the results obtained in this research project. For the sake of making comparisons, and for lack of any other - not to mention better - estimates, Tiens' and associates' values, and usage, will be adopted whenever and wherever necessary.

CIBSE Guide, Volume A, 1988, pg A3-6 (Design Data) recommends the following values for natural convection heat transfer coefficients.

downward flow: 1.5 $W/m^2$-K

horizontal flow: 3.0 $W/m^2$-K

upward flow: 4.3 $W/m^2$-K

average value: 3.0 $W/m^2$-K

## A.4 Convective Mass Transfer Coefficient

For simultaneous heat and mass transfer, it is not necessary to independently determine the value of the convection mass transfer coefficient, $h_m$, once the heat transfer coefficient, $h_f$, is known because the two coefficients are related by the Lewis number. The Lewis number gives the ratio of the thermal to the mass diffusivities. That is,

$$Le = \frac{\alpha}{D_v} \quad , \qquad \text{(A.38)}$$

$$\text{where } \alpha = \frac{\lambda_g}{C_{pg}\rho_g} .$$

Then $h_m = \dfrac{h_t}{C_{pg}\rho_g Le^{\frac{2}{3}}}$ (A.39)

[Holman (1981), Incropera and de Witt (1990), pg 356].

# APPENDIX B

## REFERENCE VALUES AND BOUNDARY CONDITIONS

### B.1 Reference Values

The reference values of thermodynamic variables and the thermophysical properties, distinguished with subscript "o" in the non-dimensional equations ( and relations), are used in the solution algorithms. These values are computed at a temperature of 273.15 K, a pressure of 101325 Pa and a relative humidity of 0.5 (50% RH). No liquid or frost is included.

i.e., $T_o$ = 273.15 K;

$P_{go}$ = 101325 Pa; and

$RH_o$ = 50%.

Hence,

$$P_{svo} = 10^{C_1} \quad (where\ C_1 = 12.5380997 - \frac{2663.91}{T_o}) \ ; \tag{B.1}$$

$$P_{vo} = RH_o P_{svo} \ ; \tag{B.2}$$

$$P_{ao} = P_{go} - P_{vo} \ ; \tag{B.3}$$

$$\rho_{vo} = \frac{P_{vo}}{R_v T_o} \ ; \tag{B.4}$$

$$\rho_{ao} = \frac{P_{ao}}{R_a T_o} \ ; \tag{B.5}$$

$$\rho_{go} = \rho_{vo} + \rho_{ao} \ ; \tag{B.6}$$

$$\epsilon_o = 1 \ ; \tag{B.7}$$

$$C_{PNio} = 992.519 + 0.174658 T_o + 1.7388\times10^{-6} T_o^2 - 7.8048\times10^{-9} T_o^3 \ ; \tag{B.8}$$

$$C_{pOxo} = 845.2426 + 0.3390 T_o - 1.16553\times10^{-4} T_o^2 + 1.59950\times10^{-8} T_o^3 \quad ; \qquad (B.9)$$

$$C_{pao} = 0.2329 C_{pOxo} + 0.7671 C_{pNio} \quad ; \qquad (B.10)$$

$$C_{pvo} = 1727.3576 + 0.52204 T_o + 6.85660\times10^{-5} T_o^2 - 3.35606\times10^{-8} T_o^3 \quad ; \qquad (B.11)$$

$$C_{pgo} = \frac{\rho_{ao}}{\rho_{go}} C_{pao} + \frac{\rho_{vo}}{\rho_{go}} C_{pvo} \quad ; \qquad (B.12)$$

$$D_{vo} = (1 - \epsilon_s) 1.643\times10^{-9} T_o^{1.695} \quad ; \qquad (B.13)$$

$$\mu_{ao} = 2.543\times10^{-7} T_o^{0.750} \quad ; \qquad (B.14)$$

$$\mu_{vo} = 1.916\times10^{-8} T_o^{1.093} \quad ; \qquad (B.15)$$

$$G_{avo} = 0.219\left[1 + 0.889\left(\frac{\mu_{ao}}{\mu_{vo}}\right)^{\frac{1}{2}}\right]^2 \quad ; \qquad (B.16)$$

$$G_{vao} = 0.277\left[1 + 1.125\left(\frac{\mu_{vo}}{\mu_{ao}}\right)^{\frac{1}{2}}\right]^2 \quad ; \qquad (B.17)$$

$$\frac{X_{vo}}{X_{ao}} = 1.6015 \frac{\rho_{vo}}{\rho_{ao}} \quad ; \qquad (B.18)$$

$$\frac{X_{ao}}{X_{vo}} = 0.6244 \frac{\rho_{ao}}{\rho_{vo}} \quad ; \qquad (B.19)$$

$$\mu_o = \frac{\mu_{ao}}{1 + G_{avo}\left(1.6015 \frac{\rho_{vo}}{\rho_{ao}}\right)} + \frac{\mu_{vo}}{1 + G_{vao}\left(0.6244 \frac{\rho_{ao}}{\rho_{vo}}\right)} \quad ; \qquad (B.20)$$

$$\lambda_{ao} = 1.814\times10^{-4} T_o^{0.870} \quad ; \tag{B.21}$$

$$\lambda_{vo} = 1.177\times10^{-5} T_o^{1.281} \quad ; \tag{B.22}$$

$$\lambda_{go} = \frac{\lambda_{ao}}{1 + G_{avo}\left(1.6015 \frac{\rho_{vo}}{\rho_{ao}}\right)} + \frac{\lambda_{vo}}{1 + G_{vao}\left(0.6244 \frac{\rho_{ao}}{\rho_{vo}}\right)} \quad ; \tag{B.23}$$

$$\lambda_{effo} = \epsilon_s \lambda_s + (1-\epsilon_s)\lambda_{go} \quad ; \tag{B.24}$$

$$\alpha_{effo} = \frac{\lambda_{effo}}{\rho_{go} C_{pgo}} \quad ; \tag{B.25}$$

$$v_o = \frac{K\Delta P}{\mu_o D} \quad ; \tag{B.26}$$

$$\Delta T = (T_{in} - T_{out}) \quad ; \tag{B.27}$$

$$\Delta C = (C_{in} - C_{out}) \quad ; \tag{B.28}$$

$$\Delta P = (P_{in} - P_{out}) \quad ; \tag{B.29}$$

$$\bar{T}_{ref} = \frac{(T_o - T_{out})}{\Delta T} \quad ; \tag{B.30}$$

(a) Reference Values for Dry Air

Reference values for dry air are computed on the basis of 100% dry air or 0% relative humidity. The values listed below are obtained.

$\rho_{go} = 1.293\ kg/m^3$

$C_{pgo} = 1016.9\ J/kg\text{-}K$

$\lambda_{effo} = 4.659\times10^{-2}\ W/m\text{-}K$

$\mu_o = 1.708\times10^{-5}\ kg/m\text{-}s$

$h_f$ = 10 $W/m^2$-$K$ (adopted from Ogniewicz and Tien, 1981)

$Bi_H$ = 21.5

(b) Reference Values for Moist Air

Here the reference values are computed for an air-water vapour mixture whose relative humidity is 50%. The values shown below are obtained.

$\rho_{go}$ = 1.291 $kg/m^3$

$\rho_{ao}$ = 1.289 $kg/m^3$

$\rho_{vo}$ = $2.418\times10^{-3}$ $kg/m^3$

$C_{pgo}$ = 1018.6 $J/kg$-$K$

$\lambda_{effo}$ = $4.656\times10^{-2}$ $W/m$-$K$

$\mu_o$ = $1.705\times10^{-5}$ $kg/m$-$s$

$D_{vo}$ = $2.150\times10^{-5}$ $m^2/s$

$h_f$ = 10 $W/m^2$-$K$

$Le$ = 1.65

$Bi_H$ = 21.5

B.2 Boundary Conditions

The saturation vapour pressure, the saturation vapour density, the actual vapour density, the dry-air density, the total density, the vapour concentration and the specific heat capacities of the air in the attic and the room are calculated from the respective pressures, temperatures, and relative humidities. Saturation properties are determined by the empirical methods in CIBSE Guide, Volume C, 1988, given in Section 3.5.6, and the specific heat capacities are obtained from Benson's (1977) formulae (Section A.1).

(a) External (Attic) Conditions

Attics are generally not airtight. The attic pressure is therefore assumed to be equal to the atmospheric pressure (which is taken to be 101325 Pa) and the other attic conditions calculated as shown below.

$$P_{sv,out} = 10^{C_1} \quad , \tag{B.31}$$

where, $C_1 = 12.5380997 - \left(\frac{2663.91}{T_{out}}\right)$

(for $T_{out} \leq T_o$ ),

and $C_1 = 33.59051 - 8.2 \log_{10} T_{out}$

$$+ 2.4804 \times 10^{-3} T_{out} - \left(\frac{3142.31}{T_{out}}\right)$$

(for $T_{out} > T_o$ );

$$P_{v,out} = RH_{out} P_{sv,out} ; \tag{B.32}$$

$$P_{a,out} = P_{g,out} - P_{v,out} \quad ; \tag{B.33}$$

$$\rho_{sv,out} = \frac{P_{sv,out}}{R_v T_{out}} \quad ; \tag{B.34}$$

$$\rho_{v,out} = \frac{P_{v,out}}{R_v T_{out}} \quad ; \tag{B.35}$$

$$\rho_{a,out} = \frac{P_{a,out}}{R_a T_{out}} \quad ; \tag{B.36}$$

$$\rho_{g,out} = \rho_{v,out} + \rho_{a,out} \quad ; \tag{B.37}$$

$$C_{out} = \frac{\rho_{v,out}}{\rho_{g,out}} \quad ; \tag{B.38}$$

$$C_{pNi,out} = 992.519 + 0.174658 T_{out}$$

$$+ 1.7388 \times 10^{-6} (T_{out})^2 - 7.8048 \times 10^{-9} (T_{out})^3 \quad ; \tag{B.39}$$

$$C_{pOx,out} = 845.2426 + 0.3390\,T_{out} - 1.16553\times10^{-4}(T_{out})^2 + 1.59950\times10^{-8}(T_{out})^3 \quad ; \quad (B.40)$$

$$C_{pa,out} = 0.2329\,C_{pOx,out} + 0.7671\,C_{pNi,out} \quad ; \quad (B.41)$$

$$C_{pv,out} = 1727.3576 + 0.52204\,T_{out} + 6.85660\times10^{-5}(T_{out})^2 - 3.35606\times10^{-8}(T_{out})^3 \quad ; \quad (B.42)$$

$$C_{pg,out} = \frac{\rho_{a,out}}{\rho_{g,out}} C_{pa,out} + \frac{\rho_{v,out}}{\rho_{g,out}} C_{pv,out} \quad . \quad (B.43)$$

(b) Internal (Room) Conditions

The inlet to the insulation at the opening is assumed to be at room temperature, which is maintained at 293 K. That is, Dirichlet boundary conditions are assumed. The other boundary conditions are then determined as shown below.

$$P_{sv,in} = 10^{C_1} \quad , \quad (B.44)$$

where, $C_1 = 12.5380997 - \left(\frac{2663.91}{T_{in}}\right)$

(for $T_{in} \le T_o$)

and $C_1 = 33.59051 - 8.2\log_{10}T_{in} + 2.4804\times10^{-3}T_{in} - \left(\frac{3142.31}{T_{in}}\right)$

(for $T_{in} > T_o$) ;

$$P_{v,in} = RH_{in}P_{sv,in} \; ; \quad (B.45)$$

$$P_{a,in} = P_{g,in} - P_{v,in} \quad ; \quad (B.46)$$

$$\rho_{sv,in} = \frac{P_{sv,in}}{R_v T_{in}} \quad ; \quad (B.47)$$

$$\rho_{v,in} = \frac{P_{v,in}}{R_v T_{in}} ; \tag{B.48}$$

$$\rho_{a,in} = \frac{P_{a,in}}{R_a T_{in}} ; \tag{B.49}$$

$$\rho_{g,in} = \rho_{v,in} + \rho_{a,in} ; \tag{B.50}$$

$$C_{in} = \frac{\rho_{v,in}}{\rho_{g,in}} ; \tag{B.51}$$

$$C_{pNi,in} = 992.519 + 0.174658\,T_{in} + 1.7388\times10^{-6}(T_{in})^2 - 7.8048\times10^{-9}(T_{in})^3 ; \tag{B.52}$$

$$C_{pOx,in} = 845.2426 + 0.3390\,T_{in} - 1.16553\times10^{-4}(T_{in})^2 + 1.59950\times10^{-8}(T_{in})^3 ; \tag{B.53}$$

$$C_{pa,in} = 0.2329\,C_{pOx,in} + 0.7671\,C_{pNi,in} ; \tag{B.54}$$

$$C_{pv,in} = 1727.3576 + 0.52204\,T_{in} + 6.85660\times10^{-5}(T_{in})^2 - 3.35606\times10^{-8}(T_{in})^3 ; \tag{B.55}$$

$$C_{pg,in} = \frac{\rho_{a,in}}{\rho_{g,in}} C_{pa,in} + \frac{\rho_{v,in}}{\rho_{g,in}} C_{pv,in} . \tag{B.56}$$

## B.3 Controlling Parameters

Controlling parameters are groups made up of property values which remain unchanged during the computation process. Some are standard non-dimensional numbers while others are unique to this project. They are listed below.

$$Pe_H = \frac{V_o D}{\alpha_{effo}} ; \tag{B.57}$$

$$Pe_V = \frac{V_o D}{D_{vo}} ; \tag{B.58}$$

$$Bi_H = \frac{h_f D}{\lambda_{effo}} \quad ; \tag{B.59}$$

$$Bi_V = \frac{h_m D}{D_{vo}} \quad ; \tag{B.60}$$

$$Le = \frac{\alpha_{effo}}{D_{vo}} \quad ; \tag{B.61}$$

$$P1 = \frac{\rho_{ao}}{\rho_{go}} \quad ; \tag{B.62}$$

$$P2 = \frac{\rho_{vo}}{\rho_{go}} \quad ; \tag{B.63}$$

$$P5 = \frac{\rho_{a,out}}{\rho_{g,out}} \quad ; \tag{B.64}$$

$$P6 = \frac{\rho_{v,out}}{\rho_{g,out}} \quad ; \tag{B.65}$$

$$P7 = \frac{\rho_{a,in}}{\rho_{g,in}} \quad ; \tag{B.66}$$

$$P8 = \frac{\rho_{v,in}}{\rho_{g,in}} \quad ; \tag{B.67}$$

$$P12 = \frac{\Delta C}{(Le C_{pgo} \Delta T)} \quad ; \tag{B.68}$$

$$P13 = P12 h_{vap} \text{ or } P12 h_{sub} \quad ; \tag{B.69}$$

$$P14 = \frac{(1 - \epsilon_s)}{\epsilon_o} \quad ; \tag{B.70}$$

$$P19 = \frac{\epsilon_s \lambda_s}{\lambda_{effo}} \quad ; \tag{B.71}$$

$$P201 = \frac{\epsilon_o \lambda_l}{\lambda_{effo}} \quad ; \tag{B.72}$$

$$P202 = \frac{\epsilon_o \lambda_{ice}}{\lambda_{effo}} \quad ; \tag{B.73}$$

$$P21 = \frac{\epsilon_o \lambda_{go}}{\lambda_{effo}} \quad ; \tag{B.74}$$

$$P23 = \frac{C_{pso}}{C_{pgo}} \quad ; \tag{B.75}$$

$$P24 = \frac{C_{pvo}}{C_{pgo}} \quad ; \tag{B.76}$$

$$P27 = \frac{K \Delta P}{\mu_o V_o D} \quad ; \tag{B.77}$$

$$P28 = \frac{D_{vo} \rho_{go} \Delta C}{D^2} \quad . \tag{B.78}$$

## B.4 Non-dimensional Variables

Variable thermophysical coefficients are used in the model equations in this project. These, and the boundary values, have to be written in non-dimensional forms using the definitions given in Section 4.2 before being used with the non-dimensional model equations.

### (a) Non-dimensional Thermophysical Coefficients

Let $T_v = \Delta T \overline{T} + T_{out}$ .

Then,

$$C_{pNi} = 992.519 + 0.174658\,T_v + 1.7388\times10^{-6}\,T_v^{2} - 7.8048\times10^{-9}\,T_v^{3} \quad ; \tag{B.79}$$

$$C_{pOx} = 845.2426 \;\; 0.3390\,T_v - 1.16553\times10^{-4}\,T_v^{2} + 1.59950\times10^{-8}\,T_v^{3} \quad ; \tag{B.80}$$

$$C_{pv} = 1727.3576 + 0.52204\,T_v + 6.85660\times10^{-5}\,T_v^{2} - 3.35606\times10^{-8}\,T_v^{3} \quad ; \tag{B.81}$$

$$\overline{C}_{pa} = \frac{1}{C_{pao}}\left(0.2329\,C_{pOx} + 0.7671\,C_{pNi}\right) \quad ; \tag{B.82}$$

$$\overline{C}_{pv} = \frac{C_{pv}}{C_{pvo}} \quad ; \tag{B.83}$$

$$\overline{C}_{pg} = \frac{\rho_{ao}}{\rho_{go}}\frac{C_{pao}}{C_{pgo}}\frac{\overline{\rho}_a}{\overline{\rho}_g}\overline{C}_{pa} + \frac{\rho_{vo}}{\rho_{go}}\frac{C_{pvo}}{C_{pgo}}\frac{\overline{\rho}_v}{\overline{\rho}_g}\overline{C}_{pv} \quad ; \tag{B.84}$$

$$\overline{D}_v = \frac{1}{D_{vo}}\epsilon_g\left(1.643\times10^{-9}\right)T_v^{1.695} \quad ; \tag{B.85}$$

$$\overline{\mu}_a = \frac{1}{\mu_{ao}}\left(2.543\times10^{-7}\,T_v^{0.750}\right) \quad ; \tag{B.86}$$

$$\overline{\mu}_v = \frac{1}{\mu_{vo}}\left(1.916\times10^{-8}\,T_v^{1.093}\right) \quad ; \tag{B.87}$$

$$G_{av} = 0.219\left[1 + 0.889\left(\frac{\mu_{ao}}{\mu_{vo}}\frac{\overline{\mu}_a}{\overline{\mu}_v}\right)^{\frac{1}{2}}\right]^2 \quad ; \tag{B.88}$$

$$G_{va} = 0.277\left[1 + 1.125\left(\frac{\mu_{vo}}{\mu_{ao}}\frac{\overline{\mu}_v}{\overline{\mu}_a}\right)^{\frac{1}{2}}\right]^2 \quad ; \tag{B.89}$$

$$\bar{\mu}_g = \frac{1}{\mu_o}\left[\frac{\mu_{ao}\bar{\mu}_a}{1 + G_{av}\left(1.6015\,\frac{\rho_{vo}}{\rho_{ao}}\,\frac{\bar{\rho}_v}{\bar{\rho}_a}\right)}\right] ; \qquad (B.90)$$

$$+ \frac{1}{\mu_o}\left[\frac{\mu_{vo}\bar{\mu}_v}{1 + G_{va}\left(0.6244\,\frac{\rho_{ao}}{\rho_{vo}}\,\frac{\bar{\rho}_a}{\bar{\rho}_v}\right)}\right]$$

$$\bar{\lambda}_a = \frac{1}{\lambda_{ao}}(1.814\times10^{-4}T_v^{0.870}) \; ; \qquad (B.91)$$

$$\bar{\lambda}_v = \frac{1}{\lambda_{vo}}(1.177\times10^{-5}T_v^{1.281}) \; ; \qquad (B.92)$$

$$\bar{\lambda}_g = \frac{1}{\lambda_{go}}\left[\frac{\lambda_{ao}\bar{\lambda}_a}{1 + G_{av}\left(1.6015\,\frac{\rho_{vo}}{\rho_{ao}}\,\frac{\bar{\rho}_v}{\bar{\rho}_a}\right)}\right] ; \qquad (B.93)$$

$$+ \frac{1}{\lambda_{go}}\left[\frac{\lambda_{vo}\bar{\lambda}_v}{1 + G_{va}\left(0.6244\,\frac{\rho_{ao}}{\rho_{vo}}\,\frac{\bar{\rho}_a}{\bar{\rho}_v}\right)}\right]$$

$$\bar{\lambda}_{eff} = \frac{1}{\lambda_{eff,o}}[\epsilon_s\lambda_s + \epsilon_o\lambda_l\bar{\epsilon}_l(t) + \epsilon_o\lambda_{go}\bar{\epsilon}_g(t)\bar{\lambda}_g] \; ; \qquad (B.94)$$

$$\bar{\alpha}_{eff} = \frac{\bar{\lambda}_{eff}}{\bar{\rho}_g\bar{C}_{pg}} \; ; \qquad (B.95)$$

(b) Non-dimensional Boundary Values

$$\bar{T}_{in} = 1 \; ; \; \bar{T}_{out} = 0 \qquad (B.96)$$

$$\bar{C}_{in} = 1 \; ; \; \bar{C}_{out} = 0 \qquad (B.97)$$

$$\bar{C}_{pg,in} = \frac{C_{pg,in}}{C_{pgo}} \; ; \; \bar{C}_{pg,out} = \frac{C_{pg,out}}{C_{pgo}} \qquad (B.98)$$

$$\bar{P}_{in} = 1 \; ; \; \bar{P}_{out} = 0 \tag{B.99}$$

$$\bar{P}_{sv,in} = \frac{(P_{sv,in} - P_{v,out})}{\Delta P} \; ; \; \bar{P}_{sv,out} = \frac{(P_{sv,out} - P_{v,out})}{\Delta P} \tag{B.100}$$

$$\bar{P}_{v,in} = \frac{(P_{v,in} - P_{v,out})}{\Delta P} \; ; \; \bar{P}_{v,out} = 0 \tag{B.101}$$

$$\bar{P}_{a,in} = \frac{(P_{a,in} - P_{a,out})}{\Delta P} \; ; \; \bar{P}_{a,out} = 0 \tag{B.102}$$

$$\bar{\rho}_{g,in} = \frac{\rho_{g,in}}{\rho_{go}} \; ; \; \bar{\rho}_{g,out} = \frac{\rho_{g,out}}{\rho_{go}} \tag{B.103}$$

$$\bar{\rho}_{v,in} = \frac{\rho_{v,in}}{\rho_{vo}} \; ; \; \bar{\rho}_{v,out} = \frac{\rho_{v,out}}{\rho_{vo}} \tag{B.104}$$

$$\bar{\rho}_{a,in} = \frac{\rho_{a,in}}{\rho_{ao}} \; ; \; \bar{\rho}_{a,out} = \frac{\rho_{a,out}}{\rho_{ao}} \tag{B.105}$$

$$\bar{\rho}_{sv,in} = \frac{\rho_{sv,in}}{\rho_{vo}} \; ; \; \bar{\rho}_{sv,out} = \frac{\rho_{sv,out}}{\rho_{vo}} \tag{B.106}$$

$$\bar{D}_{v,in} = \frac{D_{v,in}}{D_{vo}} \; ; \; \bar{D}_{v,out} = \frac{D_{v,out}}{D_{vo}} \tag{B.107}$$

$$\bar{\mu}_{v,in} = \frac{\mu_{v,in}}{\mu_{vo}} \; ; \; \bar{\mu}_{v,out} = \frac{\mu_{v,out}}{\mu_{vo}} \tag{B.108}$$

$$\bar{\mu}_{a,in} = \frac{\mu_{a,in}}{\mu_{ao}} \; ; \; \bar{\mu}_{a,out} = \frac{\mu_{a,out}}{\mu_{ao}} \tag{B.109}$$

$$\bar{\mu}_{g,in} = \frac{\mu_{g,in}}{\mu_{o}} \; ; \; \bar{\mu}_{g,out} = \frac{\mu_{g,out}}{\mu_{o}} \tag{B.110}$$

# APPENDIX C

## FINITE DIFFERENCE APPROXIMATIONS (FDAs) FOR BOUNDARIES

Details of the finite difference approximations for all the boundary types encountered in this project are presented in this section. When applied at a cell boundary, the QUICK scheme uses two grid cells upstream of the boundary and one grid cell downstream of it. These conditions are not met for the first two grid cells from the domain boundaries. Other approximate methods have to be used.

In the approximations, f will be used to represent a general variable. However, specific details will be provided wherever generalizations cannot be applied. An example of this is when the boundary FDAs for bulk air flow, vapour convection and energy convection have different structures at a particular boundary.

The non-dimensional lengths are represented by l (horizontal distance) and d (vertical distance) as detailed below. The grid cells are shown in Figure 4.1.

$$l_1 = \bar{x}_{iv} - \bar{x}_{iv-1} \; ; \; l_2 = \bar{x}_{i-1} - \bar{x}_i \; ; \; l_3 = \bar{x}_{iv-1} - \bar{x}_{iv} \; ;$$

$$l_4 = \bar{x}_i - \bar{x}_{i-1} \; ; \; l_5 = \bar{x}_{iv-1} - \bar{x}_{iv-2} \; ; \; l_6 = \bar{x}_{i-2} - \bar{x}_{i-1} \; ;$$

and

$$d_1 = \bar{y}_{jv} - \bar{y}_{jv-1} \; ; \; d_2 = \bar{y}_{j-1} - \bar{y}_j \; ; \; d_3 = \bar{y}_{jv-1} - \bar{y}_{jv} \; ;$$

$$d_4 = \bar{y}_j - \bar{y}_{j-1} \; ; \; d_5 = \bar{y}_{jv-1} - \bar{y}_{jv-2} \; ; \; d_6 = \bar{y}_{j-2} - \bar{y}_{j-1} \; .$$

Figures C.1(a) to C.1(f) are sketches of the different boundaries encountered. Figure 4.1 gives the coordinate references. In each case the coordinates iv and jv refer to the center of the cell under consideration, while i and j refer to the cell-boundary locations.

## C.1 Forced Convective Inlet (Vertical Flow)

See Figure C.1(a).

cell #1 (jv = 1, j = 1)

The QUICK scheme cannot be applied to any of the two horizontal boundaries of cell #1. The following approximations are obtained.

$$\bar{f}_j = \left(2 - \frac{d_6}{2d_3}\right)\bar{f}_{jv} - \frac{d_2}{2d_3}\bar{f}_{jv-1}$$

$$\bar{f}_{j-1} = \frac{d_6}{2d_3}\bar{f}_{jv} + \frac{d_2}{2d_3}\bar{f}_{jv-1}$$

$$\left.\frac{\partial \bar{f}}{\partial \bar{y}}\right|_{jv} = \frac{(\bar{f}_{j-1} - \bar{f}_j)}{d_2}$$

$$\left.\frac{\partial \bar{f}}{\partial \bar{y}}\right|_{j-1} = \frac{(\bar{f}_{jv-1} - \bar{f}_{jv})}{d_3}$$

$$\left.\frac{\partial \bar{P}}{\partial \bar{y}}\right|_{j} \approx \frac{(\bar{P}_{jv} - \bar{P}_{in})}{d_2}$$

$$\left.\frac{\partial \bar{C}}{\partial \bar{y}}\right|_{j} = -\frac{h_f D}{\lambda_{effo}} \frac{\alpha_{effo}}{D_{vo}} \frac{1}{\bar{D}_{vj}\bar{\rho}_{gj}\bar{C}_{pgj}} \times \left[\frac{(\bar{C}_{in} - \bar{C}_j)}{\left(\frac{\alpha_{effo}}{D_{vo}} \frac{\bar{\lambda}_{effj}}{\bar{D}_{vj}\bar{\rho}_{gj}\bar{C}_{pgj}}\right)^{\frac{2}{3}}}\right]$$

$$\left.\frac{\partial \bar{T}}{\partial \bar{y}}\right|_{j} \approx -Bi\,\frac{(\bar{T}_{in} - \bar{T}_j)}{\bar{\lambda}_{effj}} \; ; \; Bi = \frac{h_f D}{\lambda_{effo}}$$

(where $\bar{P}_{in}$, $\bar{C}_{in}$, $\bar{T}_{in}$, are the non-dimensional interior pressure, concentration, and temperature, respectively.)

cell #2 (jv = 2, j = 2)

The QUICK scheme can be applied to the upper horizontal boundary of the cell only. The following approximations are used.

$$\bar{f}_j = \frac{d_4}{2d_1}\bar{f}_{jv} + \frac{d_2}{2d_1}\bar{f}_{jv-1}$$

$$\bar{f}_{j-1} = \left(\frac{1}{2} - \frac{qd_3}{3d_2}\right)\bar{f}_{jv-1} + \left(\frac{1}{2} + \frac{qd_3}{3d_2} + \frac{qd_3^2}{3d_1d_2}\right)\bar{f}_{jv} - \frac{qd_3^2}{3d_1d_2}\bar{f}_{jv-1}$$

$$\left.\frac{\partial \bar{f}}{\partial \bar{y}}\right|_{jv} = \frac{(\bar{f}_{j-1} - \bar{f}_j)}{d_2}$$

$$\left.\frac{\partial \bar{f}}{\partial \bar{y}}\right|_{j} = \frac{(\bar{f}_{jv} - \bar{f}_{jv-1})}{d_1}$$

$$\left.\frac{\partial \bar{f}}{\partial \bar{y}}\right|_{j-1} = \frac{(\bar{f}_{jv-1} - \bar{f}_{jv})}{d_3}$$

cell #3 (jv = 3, j = 3)

The QUICK scheme is applied to both the upper and lower horizontal cell boundaries.

$$\bar{f}_j = \left(\frac{1}{2} - \frac{qd_1}{3d_4}\right)\bar{f}_{jv} + \left(\frac{1}{2} + \frac{qd_1}{3d_4} + \frac{qd_1^2}{3d_4d_5}\right)\bar{f}_{jv-1} - \frac{qd_1^2}{3d_4d_5}\bar{f}_{jv-2}$$

$$\bar{f}_{j-1} = \left(\frac{1}{2} - \frac{qd_3}{3d_2}\right)\bar{f}_{jv+1} + \left(\frac{1}{2} + \frac{qd_3}{3d_2} + \frac{qd_3^2}{3d_1d_2}\right)\bar{f}_{jv} - \frac{qd_3^2}{3d_1d_2}\bar{f}_{jv-1}$$

$$\left.\frac{\partial \bar{f}}{\partial \bar{y}}\right|_{jv} = \frac{(\bar{f}_{j+1} - \bar{f}_j)}{d_2}$$

$$\left.\frac{\partial \bar{f}}{\partial \bar{y}}\right|_{j} = \frac{(\bar{f}_{jv} - \bar{f}_{jv-1})}{d_1}$$

$$\left.\frac{\partial \bar{f}}{\partial \bar{y}}\right|_{j+1} = \frac{(\bar{f}_{jv-1} - \bar{f}_{jv})}{d_3}$$

C.2 Dirichlet Inlet for Vertical Flow

See Figure C.1(b).

cell #1 (jv = 1, j = 1)

The following approximations are applied to the boundaries and gradients for the first grid cell.

$$\bar{f}_j = \bar{f}_{in} \text{ ; where } \bar{f}_{in} = \frac{f_{in} - f_{out}}{f_{in} - f_{out}} \ (= 1)$$

$$\bar{f}_{j-1} = \frac{d_2}{2d_3}\bar{f}_{jv-1} + \frac{d_6}{2d_3}\bar{f}_{jv}$$

$$\left.\frac{\partial \bar{f}}{\partial \bar{y}}\right|_{jv} = \frac{(\bar{f}_{j+1} - \bar{f}_j)}{d_2}$$

$$\left.\frac{\partial \bar{f}}{\partial \bar{y}}\right|_{j} \approx \frac{2(\bar{f}_{jv} - \bar{f}_{in})}{d_2}$$

$$\left.\frac{\partial \bar{f}}{\partial \bar{y}}\right|_{j+1} = \frac{(\bar{f}_{jv-1} - \bar{f}_{jv})}{d_3}$$

cell #2 (jv = 2, j = 2)

The expressions used for this case are similar to the ones

derived for cell #2 in Section C.1.

cell #3 (jv = 3, j = 3)

The expressions used for this case are similar to the ones derived for cell #3 in Section C.1.

## C.3 Conductive Entry of Heat

This boundary is impermeable to matter while heat energy transfer is by conduction only. See Figure C.1(c).

cell #1 (jv = 1, j = 1)

The QUICK scheme does not apply to any of the horizontal boundaries. The following approximations are used.

$$\bar{f}_{j-1} = \frac{d_2}{2d_3}\bar{f}_{jv-1} + \frac{d_6}{2d_3}\bar{f}_{jv}$$

$$\bar{f}_j = 2\bar{f}_{jv} - \bar{f}_{j-1}$$

$$\left.\frac{\partial \bar{f}}{\partial \bar{y}}\right|_{jv} = \frac{(\bar{f}_{j-1} - \bar{f}_j)}{d_2}$$

$$\left.\frac{\partial \bar{f}}{\partial \bar{y}}\right|_{j-1} = \frac{(\bar{f}_{jv-1} - \bar{f}_{jv})}{d_3}$$

$$\bar{v}_j = 0$$

$$\left.\frac{\partial \bar{C}}{\partial \bar{y}}\right|_j = 0$$

$$\left.\frac{\partial \bar{T}}{\partial \bar{y}}\right|_j = -\frac{D}{\lambda_{effo}}\frac{1}{\bar{\lambda}_{effj}}\left[\frac{(\bar{T}_{in} - \bar{T}_j)}{\left(\frac{1}{h_n} + \frac{y_p}{\lambda_p}\right)}\right]$$

where $y_p$ is the thickness of the plasterboard and $\lambda_p$ is its thermal conductivity.

cell #2 (iv = 2, i = 2)

The expressions used in this case are similar to the ones derived for cell #2 in Section C.1. The QUICK scheme applies to the upper horizontal cell boundary only.

cell #3 (iv = 3, i = 3)

The expressions used for this case are similar to the ones derived for cell #3 in Section C.1. The QUICK scheme applies to both horizontal boundaries.

## C.4 The Far-field

The far-field is the region where the influence of the leakage path is negligible: that is, there is insignificant transfer of energy and matter (due to the opening or leakage site) in this region. See Figure C.1(d). N is the number of interior grid cell boundaries in the x or horizontal direction.

cell #1 (iv = N-1, i = N-1)

The expressions used in this case are similar to the ones derived for cell #3 in Section C.1. The QUICK scheme applies to both vertical boundaries.

cell #2 (iv = N, i = N)

The expressions used in this case are similar to the ones derived for cell #3 in Section C.1. The QUICK scheme applies to both vertical boundaries.

cell #3 (iv = N+1, i = N+1)

Here the QUICK scheme applies to the left-hand boundary only, so that:

$$\bar{f}_i = \left(\frac{1}{2} - \frac{ql_1}{3l_4}\right)\bar{f}_{iv} + \left(\frac{1}{2} + \frac{ql_1}{3l_4} + \frac{ql_1^2}{3l_4l_5}\right)\bar{f}_{iv-1} - \frac{ql_1^2}{3l_4l_5}\bar{f}_{iv-2}$$

$$\bar{f}_{i-1} = 2\bar{f}_{iv} - \bar{f}_i$$

$$\left.\frac{\partial \bar{f}}{\partial \bar{x}}\right|_{iv} = \frac{(\bar{f}_{i-1} - \bar{f}_i)}{l_2}$$

$$\left.\frac{\partial \bar{f}}{\partial \bar{x}}\right|_{i} = \frac{(\bar{f}_{iv} - \bar{f}_{iv-1})}{l_1}$$

$$\left.\frac{\partial \bar{f}}{\partial \bar{x}}\right|_{i-1} = 0$$

$$\bar{u}_{i-1} = 0$$

C.5 Forced Convective Exit

The flow is in the vertical direction (Figure C.1(e)), and M is the number of interior grid cell boundaries in the y or vertical direction.

cell #1 (jv = M-1, j = M-1)

The expressions used for this case are similar to the ones derived for cell #3 in Section C.1. The QUICK scheme applies to both horizontal boundaries.

cell #2 (jv = M, j = M)

The expressions used for this case are similar to the ones derived for cell #3 in Section C.1. The QUICK scheme applies to both horizontal boundaries.

cell #3 (jv = M+1, j = M+1)

The QUICK scheme applies to the lower horizontal boundary only, while the upper boundary is forced convective for both heat and mass transfer.

$$\bar{f}_j = \left(\frac{1}{2} - \frac{qd_1}{3d_4}\right)\bar{f}_{jv} + \left(\frac{1}{2} + \frac{qd_1}{3d_4} + \frac{qd_1^2}{3d_4d_5}\right)\bar{f}_{jv-1} - \frac{qd_1^2}{3d_4d_5}\bar{f}_{jv-2}$$

$$\bar{f}_{j-1} = 2\bar{f}_{jv} - \bar{f}_j$$

$$\left.\frac{\partial \bar{f}}{\partial \bar{y}}\right|_{jv} = \frac{(\bar{f}_{j+1} - \bar{f}_j)}{d_2}$$

$$\left.\frac{\partial \bar{f}}{\partial \bar{y}}\right|_{j} = \frac{(\bar{f}_{jv} - \bar{f}_{jv-1})}{d_1}$$

$$\left.\frac{\partial \bar{P}}{\partial \bar{y}}\right|_{j-1} = \frac{(\bar{P}_{out} - \bar{P}_{jv})}{d_2}$$

$$\left.\frac{\partial \bar{C}}{\partial \bar{y}}\right|_{j-1} = - \frac{h_f D}{\lambda_{effo}} \frac{\alpha_{effo}}{D_{vo}} \frac{1}{\bar{\rho}_{g,j-1} \bar{C}_{pg,j-1} \bar{D}_{v,j-1}} \times \left[ \frac{(\bar{C}_{j-1} - \bar{C}_{out})}{\left( \frac{\alpha_{effo}}{D_{vo}} \frac{\bar{\lambda}_{eff,j-1}}{\bar{\rho}_{g,j-1} \bar{C}_{pg,j-1} \bar{D}_{v,j-1}} \right)^{\frac{2}{3}}} \right]$$

$$\left.\frac{\partial \bar{T}}{\partial \bar{y}}\right|_{j-1} = -Bi \frac{(\bar{T}_{j-1} - \bar{T}_{out})}{\bar{\lambda}_{eff,j-1}} \; ; \; Bi = \frac{h_f D}{\lambda_{effo}}$$

(where $\bar{P}_{out}$, $\bar{C}_{out}$, $\bar{T}_{out}$, are the non-dimensional exterior or attic pressure, concentration, and temperature, respectively.)

C.6 Symmetric Vertical "Boundary"

This boundary divides the flow domain into mirror images. There are no fluxes across the line of symmetry. See Figure C.1(f).

cell #1 (iv = 1, i = 1)

The QUICK scheme applies to neither vertical boundary.

$$\bar{f}_{i-1} = \frac{l_2}{2l_3} \bar{f}_{iv-1} + \frac{l_6}{2l_3} \bar{f}_{iv}$$

$$\bar{f}_i = 2\bar{f}_{iv} - \bar{f}_{i+1}$$

$$\left.\frac{\partial \bar{f}}{\partial \bar{x}}\right|_{iv} = \frac{(\bar{f}_{i+1} - \bar{f}_i)}{l_2}$$

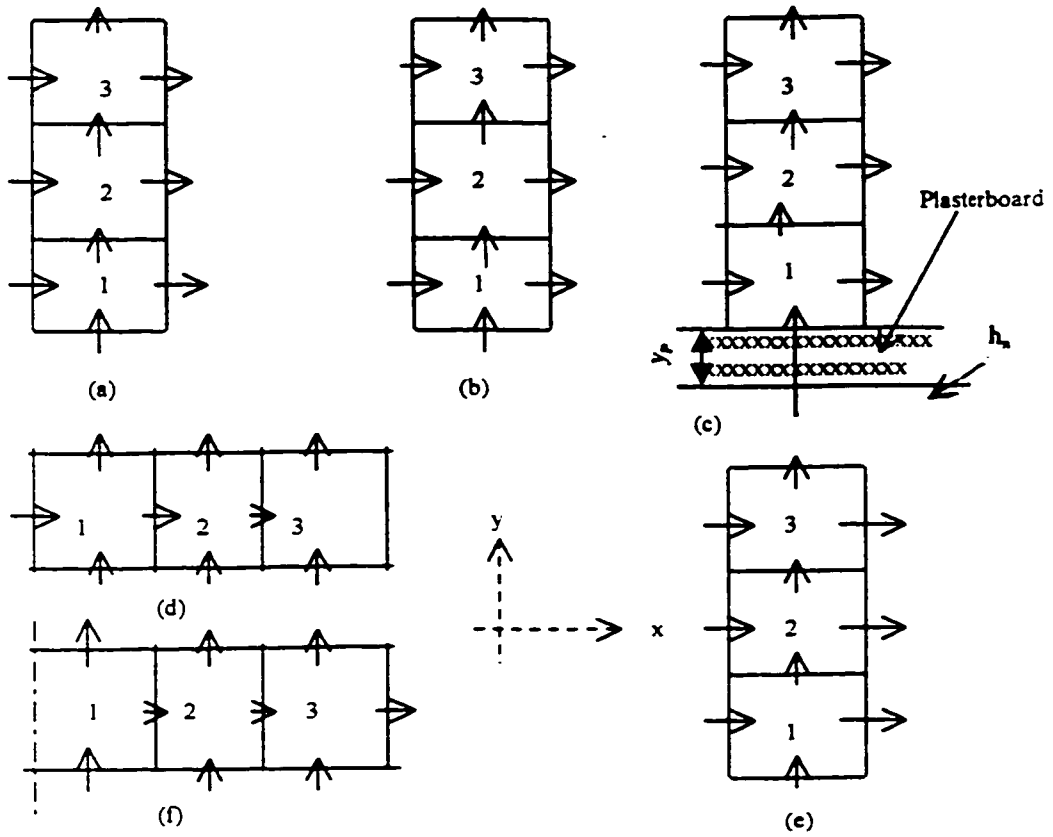


Figure c.1 : Boundary Grid Cells; (a) Forced-convective Inlet, (b) Dirichlet Inlet, (c) Conductive Inlet, (d) Far-field, (e) Forced-convective Exit, (f) Symmetric Boundary.

$$\left.\frac{\partial \bar{f}}{\partial \bar{x}}\right|_{i} = 0$$

$$\left.\frac{\partial \bar{f}}{\partial \bar{x}}\right|_{i+1} = \frac{(\bar{f}_{iv+1} - \bar{f}_{iv})}{l_3}$$

cell #2 (iv = 2, i = 2)

The expressions used in this case are similar to the ones derived for cell #2 in Section C.1. However, y must be replaced by x, d by 1, j by i, jv by iv, e.t.c., since the direction of flow now being considered is horizontal.

cell #3 (iv = 3, i = 3)

The expressions used in this case are similar to the ones derived for cell #3 in Section C.1. The QUICK scheme now applies to both vertical boundaries.

# APPENDIX D

# HEAT AND MASS TRANSFER FOR AXISYMMETRIC FLOW

## D.1 Introduction

When the geometry of the leakage path in the attic insulation is circular, the flow is axisymmetric and the governing equations are in cylindrical coordinates. The thermodynamic relations, the volumetric constraint and the variable thermophysical coefficients are independent of the coordinate system and therefore retain the forms shown in Section 3.5.

The horizontal coordinate, r, gives the radius from the axis of symmetry, while the vertical coordinate, z, gives the height from the insulation-plasterboard boundary. The situation is equivalent to a two-dimensional system since all flow quantities are independent of the angular coordinate. The flow domain is similar to Figure 3.3.

For an insulation slab D meters thick, the non-dimensional lengths are $\bar{r} = \frac{r}{D}$ and $\bar{z} = \frac{z}{D}$. All other non-dimensional variables remain as shown in Section 4.2.

## D.2 Model Equations and Other Relations

The governing equations for axisymmetric flow are given below in both the dimensional and non-dimensional forms.

The dimensional form of the mass continuity equation is

$$\frac{1}{r}\frac{\partial}{\partial r}(\rho_g r u) + \frac{\partial}{\partial z}(\rho_g v) + \dot{m} = 0 \qquad \text{(D.1)}$$

and its non-dimensional form is

$$\frac{1}{\bar{r}}\frac{\partial}{\partial \bar{r}}(\bar{\rho}_g \bar{r} \bar{u}) + \frac{\partial}{\partial \bar{z}}(\bar{\rho}_g \bar{v}) + \frac{D_{vo}\Delta C}{V_o D}\bar{\dot{m}} = 0 \qquad \text{(D.2)}$$

The vapour conservation equation in dimensional form is

$$\frac{1}{r}\frac{\partial}{\partial r}(\rho_g r u C) + \frac{\partial}{\partial z}(\rho_g v C) + \dot{m}$$

$$= \qquad (D.3)$$

$$\frac{1}{r}\frac{\partial}{\partial r}\left(D_v r \rho_g \frac{\partial C}{\partial r}\right) + \frac{\partial}{\partial z}\left(D_v \rho_g \frac{\partial C}{\partial z}\right)$$

Substituting the mass conservation equation (D.1) into the vapour conservation equation (D.3), then rearranging, gives

$$\rho_g u \frac{\partial C}{\partial r} + \rho_g v \frac{\partial C}{\partial z} - \frac{1}{r}\frac{\partial}{\partial r}\left(D_v r \rho_g \frac{\partial C}{\partial r}\right) - \frac{\partial}{\partial z}\left(D_v \rho_g \frac{\partial C}{\partial z}\right) + (1-C)\dot{m} = 0 \qquad (D.4)$$

where, $C = \frac{\rho_v}{\rho_g}$ .

The non-dimensional form of Equation D.4 is

$$\frac{V_o D}{D_{vo}}\bar{\rho}_g \bar{u}\frac{\partial \bar{C}}{\partial \bar{r}} + \frac{V_o D}{D_{vo}}\bar{\rho}_g \bar{v}\frac{\partial \bar{C}}{\partial \bar{z}}$$

$$- \frac{1}{\bar{r}}\frac{\partial}{\partial \bar{r}}\left(\bar{D}_v \bar{\rho}_g \bar{r}\frac{\partial \bar{C}}{\partial \bar{r}}\right) - \frac{\partial}{\partial \bar{z}}\left(\bar{D}_v \bar{\rho}_g \frac{\partial \bar{C}}{\partial \bar{z}}\right) \qquad (D.5)$$

$$- \Delta C \bar{C}\bar{m} + (1-C_{out})\bar{m} = 0$$

The energy conservation equation in dimensional form is

$$\rho_g C_{pg} u \frac{\partial T}{\partial r} + \rho_g C_{pg} v \frac{\partial T}{\partial z} - \frac{1}{r}\frac{\partial}{\partial r}\left(\lambda_{eff} r \frac{\partial T}{\partial r}\right) - \frac{\partial}{\partial z}\left(\lambda_{eff}\frac{\partial T}{\partial z}\right) - h_{vap}\dot{m} = 0 \qquad (D.6)$$

In non-dimensional form, Equation D.6 becomes

$$\frac{V_o D}{\alpha_{effo}} \bar{\rho}_g \bar{C}_{pg} \bar{u} \frac{\partial \bar{T}}{\partial \bar{r}} + \frac{V_o D}{\alpha_{effo}} \bar{\rho}_g \bar{C}_{pg} \bar{v} \frac{\partial \bar{T}}{\partial \bar{z}}$$

$$- \frac{1}{\bar{r}} \frac{\partial}{\partial \bar{r}} \left( \bar{\lambda}_{eff} \bar{r} \frac{\partial \bar{T}}{\partial \bar{r}} \right) - \frac{\partial}{\partial \bar{z}} \left( \bar{\lambda}_{eff} \frac{\partial \bar{T}}{\partial \bar{z}} \right) \qquad (D.7)$$

$$- h_{vap} \frac{D_{vo}}{\alpha_{effo} C_{pgo}} \frac{\Delta C}{\Delta T} \bar{m} = 0$$

Darcy's law gives the velocities for the two-dimensional system as

$$u = - \frac{K}{\mu_g} \frac{\partial p}{\partial r} \qquad (D.8)$$

and

$$v = - \frac{K}{\mu_g} \frac{\partial p}{\partial z} \qquad (D.9)$$

in dimensional variables. In non-dimensional variables these become

$$\bar{u} = - \frac{K \Delta P}{\mu_o V_o D} \frac{1}{\bar{\mu}_g} \frac{\partial \bar{p}}{\partial \bar{r}} \qquad (D.10)$$

and

$$\bar{v} = - \frac{K \Delta P}{\mu_o V_o D} \frac{1}{\bar{\mu}_g} \frac{\partial \bar{p}}{\partial \bar{z}}, \qquad (D.11)$$

respectively.

The control volume approach, with a staggered grid system, is used in deriving the finite difference approximations of the governing equations and other relations. Discretization is by the QUICK scheme (Section 4.3). The differences between these FDAs and the ones used for a slit in Section 4.3 arise from the different cross-sectional geometries of the control volumes; i.e., 1 m long and rectangular for the slit, but circular with a radius for axisymmetric flow. The control volume for axisymmetric flow is a disc of thickness $\Delta r$ and depth $\Delta z$, shown in Figure D.1.

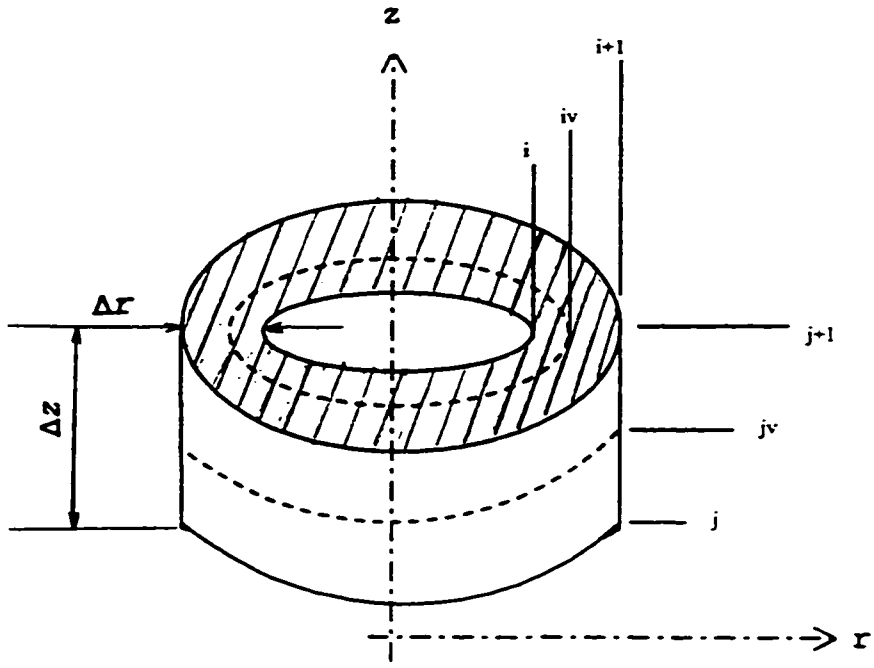


Figure D.1 : Control Volume for Axisymmetric Flow.

The main flow variables (i.e., temperature, pressure, concentration, and condensation rate) are computed at the grid cell centres while all fluxes are computed at the grid cell boundaries.

In Figure D.1 "jv" and "iv" denote the cell centers while "j" and "i" are used at the cell boundaries. The result is a two-grid system, one displaced relative to the other, in co-existence.

The finite difference approximations (FDAs) for a grid cell whose center is located at (iv,jv) can now be summarized as shown below.

The FDA for the mass conservation equation is

$$\frac{1}{(\bar{r}_{i-1}-\bar{r}_i)}\left[\frac{\bar{r}_{i-1}}{\bar{r}_{iv}}\bar{\rho}_{g,i-1}\bar{u}_{i-1} - \frac{\bar{r}_i}{\bar{r}_{iv}}\bar{\rho}_{g,i}\bar{u}_i\right] + \frac{1}{(\bar{z}_{j-1}-\bar{z}_j)}\left[\bar{\rho}_{g,j-1}\bar{v}_{j-1} - \bar{\rho}_{g,j}\bar{v}_j\right] + \frac{D_{vo}\Delta C}{V_o D}\bar{m}_{(iv,jv)} = 0 \qquad \text{(D.12)}$$

At the cell boundaries, the velocities are given by

$$\bar{u}_i = -\frac{K\Delta P}{\mu_o V_o D}\frac{1}{\bar{\mu}_{g,i}}\left.\frac{\partial \bar{p}}{\partial \bar{r}}\right|_i \qquad \text{(D.13)}$$

$$\bar{u}_{i-1} = -\frac{K\Delta P}{\mu_o V_o D}\frac{1}{\bar{\mu}_{g,i-1}}\left.\frac{\partial \bar{p}}{\partial \bar{r}}\right|_{i-1} \qquad \text{(D.14)}$$

$$\bar{v}_j = -\frac{K\Delta P}{\mu_o V_o D}\frac{1}{\bar{\mu}_{g,j}}\left.\frac{\partial \bar{p}}{\partial \bar{z}}\right|_j \qquad \text{(D.15)}$$

and

$$\bar{v}_{j-1} = -\frac{K\Delta P}{\mu_o V_o D}\frac{1}{\bar{\mu}_{g,j-1}}\left.\frac{\partial \bar{p}}{\partial \bar{z}}\right|_{j-1} \tag{D.16}$$

The flow is driven mainly by the pressure difference, and the pressure equation for the flow-field is obtained by substituting for velocities (Equations D.13 to D.16) in the mass conservation equation (D.12). This gives

$$\begin{aligned}
&\frac{\bar{\rho}_{g,i-1}}{(\bar{r}_{i-1}-\bar{r}_i)}\frac{\bar{r}_{i-1}}{\bar{r}_{iv}}\left(-\frac{K\Delta P}{\mu_o V_o D}\right)\frac{1}{\bar{\mu}_{g,i-1}}\left.\frac{\partial \bar{p}}{\partial \bar{r}}\right|_{i-1} \\
&-\frac{\bar{\rho}_{g,i}}{(\bar{r}_{i-1}-\bar{r}_i)}\frac{\bar{r}_i}{\bar{r}_{iv}}\left(-\frac{K\Delta P}{\mu_o V_o D}\right)\frac{1}{\bar{\mu}_{g,i}}\left.\frac{\partial \bar{p}}{\partial \bar{r}}\right|_{i} \\
&+\frac{\bar{\rho}_{g,j-1}}{(\bar{z}_{j-1}-\bar{z}_j)}\left(-\frac{K\Delta P}{\mu_o V_o D}\right)\frac{1}{\bar{\mu}_{g,j-1}}\left.\frac{\partial \bar{p}}{\partial \bar{z}}\right|_{j-1} \\
&-\frac{\bar{\rho}_{g,j}}{(\bar{z}_{j-1}-\bar{z}_j)}\left(-\frac{K\Delta P}{\mu_o V_o D}\right)\frac{1}{\bar{\mu}_{g,j}}\left.\frac{\partial \bar{p}}{\partial \bar{z}}\right|_{j} \\
&+\frac{D_{vo}\Delta C}{V_o D}\bar{\dot{m}}_{(iv,jv)} = 0
\end{aligned} \tag{D.17}$$

The FDA for the vapour conservation equation (D.5) is written as

$$\begin{aligned}
&\frac{V_o D}{D_{vo}}\bar{\rho}_{g,i}\bar{u}_i\left.\frac{\partial \bar{C}}{\partial \bar{r}}\right|_{iv} + \frac{V_o D}{D_{vo}}\bar{\rho}_{g,j}\bar{v}_j\left.\frac{\partial \bar{C}}{\partial \bar{z}}\right|_{jv} \\
&-\frac{1}{(\bar{r}_{i-1}-\bar{r}_i)}\left[\bar{D}_{v,i-1}\bar{\rho}_{g,i-1}\frac{\bar{r}_{i-1}}{\bar{r}_{iv}}\left.\frac{\partial \bar{C}}{\partial \bar{r}}\right|_{i-1} - \bar{D}_{v,i}\bar{\rho}_{g,i}\frac{\bar{r}_i}{\bar{r}_{iv}}\left.\frac{\partial \bar{C}}{\partial \bar{r}}\right|_{i}\right] \\
&-\frac{1}{(\bar{z}_{j-1}-\bar{z}_j)}\left[\bar{D}_{v,j-1}\bar{\rho}_{g,j-1}\left.\frac{\partial \bar{C}}{\partial \bar{z}}\right|_{j-1} - \bar{D}_{v,j}\bar{\rho}_{g,j}\left.\frac{\partial \bar{C}}{\partial \bar{z}}\right|_{j}\right] \\
&-\Delta C\bar{\dot{m}}_{(iv,jv)}\bar{C}_{(iv,jv)} + (1-C_{out})\bar{\dot{m}}_{(iv,jv)} = 0
\end{aligned} \tag{D.18}$$

The FDA of the energy conservation equation (D.7) is written

as

$$\frac{V_o D}{\alpha_{effo}} \bar{\rho}_{g,i} \bar{C}_{pg,i} \bar{u}_i \left.\frac{\partial \bar{T}}{\partial \bar{r}}\right|_{iv} + \frac{V_o D}{\alpha_{effo}} \bar{\rho}_{g,j} \bar{C}_{pg,j} \bar{v}_j \left.\frac{\partial \bar{T}}{\partial \bar{z}}\right|_{jv}$$

$$- \frac{1}{(\bar{r}_{i-1} - \bar{r}_i)} \left[ \bar{\lambda}_{eff,i-1} \frac{\bar{r}_{i-1}}{\bar{r}_{iv}} \left.\frac{\partial \bar{T}}{\partial \bar{r}}\right|_{i-1} - \bar{\lambda}_{eff,i} \frac{\bar{r}_i}{\bar{r}_{iv}} \left.\frac{\partial \bar{T}}{\partial \bar{r}}\right|_{i} \right] \qquad \text{(D.19)}$$

$$- \frac{1}{(\bar{z}_{j-1} - \bar{z}_j)} \left[ \bar{\lambda}_{eff,j-1} \left.\frac{\partial \bar{T}}{\partial \bar{z}}\right|_{j-1} - \bar{\lambda}_{eff,j} \left.\frac{\partial \bar{T}}{\partial \bar{z}}\right|_{j} \right]$$

$$- h_{vap} \frac{D_{vo}}{\alpha_{effo} C_{pgo}} \frac{\Delta C}{\Delta T} \bar{\dot{m}}_{(iv,jv)} = 0$$

Consider the volume element shown earlier in Figure D.1. The different element surface areas are given by

$$A_i = 2\pi r_i (z_{j-1} - z_j),$$

$$A_{i-1} = 2\pi r_{i-1} (z_{j-1} - z_j),$$

$$A_j = \pi r_{i-1}^2 - \pi r_i^2, \text{ and}$$

$$A_{j-1} = A_j = \pi r_{i-1}^2 - \pi r_i^2.$$

The elemental volume is given by

$$\Delta Vol. = \pi (r_{i-1}^2 - r_i^2)(z_{j-1} - z_j)$$

Suppose that vapour enters the volume element in a supersaturated state, with a vapour density $\rho_v$, and leaves in a saturated state, with a vapour density $\rho_{sv}$. This is the basic principle of SMARC.

A mass balance for the vapour flow in the element gives

$$\dot{m} \times \Delta Vol. = (\rho_{v,i} A_i u_i + \rho_{v,j} A_j v_j) - (\rho_{sv} A_{i-1} u_{i-1} + \rho_{sv} A_{j-1} v_{j-1})$$

That is,

$$\dot{m}\pi (r_{i-1}^2 - r_i^2)(z_{j-1} - z_j) =$$
$$(\rho_{v,i} 2\pi r_i (z_{j-1} - z_j) u_i + \rho_{v,j} \pi (r_{i-1}^2 - r_i^2) v_j)$$
$$- (\rho_{sv} 2\pi r_{i-1} (z_{j-1} - z_j) u_{i-1} + \rho_{sv} \pi (r_{i-1}^2 - r_i^2) v_{j-1})$$

or

$$\dot{m} = \frac{2(\rho_{v,i} r_i u_i - \rho_{sv} r_{i-1} u_{i-1})}{(r_{i-1}^2 - r_i^2)} + \frac{(\rho_{v,j} v_j - \rho_{sv} v_{j-1})}{(z_{j-1} - z_j)} \qquad \text{(D.20)}$$

Equation D.20 is the axisymmetric version of SMARC. In non-dimensional form, it is written as

$$\bar{\dot{m}}_{(iv,jv)} = \left[ \frac{D^2}{D_{vo} \rho_{go} \Delta C} \frac{\rho_{vo} V_o}{D} \right] \times \left[ 2 \frac{(\bar{\rho}_{v,i} \bar{r}_i \bar{u}_i - \bar{\rho}_{sv}|_{(iv,jv)} \bar{r}_{i-1} \bar{u}_{i-1})}{(\bar{r}_{i-1}^2 - \bar{r}_i^2)} + \frac{(\bar{\rho}_{v,j} \bar{v}_j - \bar{\rho}_{sv}|_{(iv,jv)} \bar{v}_{j-1})}{(\bar{z}_{j-1} - \bar{z}_j)} \right] \qquad \text{(D.21)}$$

where $\bar{\rho}_{v,i} = \frac{\rho_{go}}{\rho_{vo}} \bar{\rho}_{g,i} (\Delta C \bar{C}_i + C_{out})$ ,

$$\bar{\rho}_{v,j} = \frac{\rho_{go}}{\rho_{vo}} \bar{\rho}_{g,j} (\Delta C \bar{C}_j + C_{out})$$

(since $\rho_v = C \rho_g$),

and, $\bar{\rho}_{sv}|_{(iv,jv)} = \frac{P_{sv}|_{(iv,jv)}}{\rho_{vo} R_v T_{(iv,jv)}}$

(where $T_{(iv,jv)} = \Delta T \bar{T}_{(iv,jv)} + T_{out}$).

The QUICK scheme [Leonard, 1979], given in Section 4.3, is used to discretize the forced convective terms in the equations and also in the estimation of property/variable values at the cell boundaries.

The equations for the global flowrates and balances, given in Section 4.4, are modified to take into account the circular cross-sections of the axisymmetric flow-field. The modifications result in the following non-dimensional formulae.

At the inlet (j = 1), the bulk air flowrate is given by

$$Q_{g,in} = (\rho_{go} V_o \pi D^2) \sum_{i=1}^{k_3} \overline{\rho}_{g,j} \overline{v}_j (\overline{r}_{i-1}^{\,2} - \overline{r}_i^{\,2}) \qquad \text{(D.22)}$$

At the outlet (j = M+1), the flowrate is given by

$$Q_{g,out} = (\rho_{go} V_o \pi D^2) \sum_{i=1}^{N-1} \overline{\rho}_{g,j-1} \overline{v}_{j-1} (\overline{r}_{i-1}^{\,2} - \overline{r}_i^{\,2}) \qquad \text{(D.23)}$$

At the inlet (j = 1), the vapour flowrate is given by

$$\begin{aligned} Q_{v,in} = & \sum_{i=1}^{k_3} \left[ (\rho_{go} V_o \pi D^2) (\Delta C \overline{C}_j + C_{out}) \overline{\rho}_{g,j} \overline{v}_j (\overline{r}_{i-1}^{\,2} - \overline{r}_i^{\,2}) \right] \\ & - \sum_{i=1}^{k_3} \left[ (\rho_{go} D_{vo} \Delta C \pi D) \overline{\rho}_{g,j} \overline{D}_{v,j} \left. \frac{\partial \overline{C}}{\partial \overline{z}} \right|_j (\overline{r}_{i-1}^{\,2} - \overline{r}_i^{\,2}) \right] \end{aligned} \qquad \text{(D.24)}$$

At the outlet (j = M+1), the vapour flowrate equation is

$$Q_{v,out} = \sum_{i=1}^{N-1} \left[ (\rho_{go} V_o \pi D^2) (\Delta C \bar{C}_{j-1} + C_{out}) \bar{\rho}_{g,j-1} \bar{v}_{j-1} (\bar{r}_{i-1}^2 - \bar{r}_i^2) \right]$$
$$- \sum_{i=1}^{N-1} \left[ (\rho_{go} D_{vo} \Delta C \pi D) \bar{\rho}_{g,j-1} \bar{D}_{v,j-1} \left. \frac{\partial \bar{C}}{\partial \bar{z}} \right|_{j-1} (\bar{r}_{i-1}^2 - \bar{r}_i^2) \right] \quad (D.25)$$

The heat energy flowrate at the inlet (j = 1) is

$$H_{s,in} = \sum_{i=1}^{k_3} \left[ (\rho_{go} C_{pgo} V_o \pi D^2) (\Delta T \bar{T}_j + T_{out}) \bar{\rho}_{g,j} \bar{C}_{pg,j} \bar{v}_j (\bar{r}_{i-1}^2 - \bar{r}_i^2) \right]$$
$$- \sum_{i=1}^{k_3} \left[ (\lambda_{effo} \Delta T \pi D) \bar{\lambda}_{eff,j} \left. \frac{\partial \bar{T}}{\partial \bar{z}} \right|_j (\bar{r}_{i-1}^2 - \bar{r}_i^2) \right] \quad (D.26)$$
$$- \sum_{i=k_3-1}^{N-1} \left[ \frac{\pi D^2 \Delta T}{\left( \frac{1}{h_n} + \frac{y_p}{\lambda_p} \right)} (\bar{T}_j - \bar{T}_{in}) (\bar{r}_{i-1}^2 - \bar{r}_i^2) \right]$$

and at the outlet (j = M+1), it is

$$H_{s,out} = \sum_{i=1}^{N-1} \left[ (\rho_{go} C_{pgo} V_o \pi D^2) (\Delta T \bar{T}_{j-1} + T_{out}) \right.$$
$$\left. (\bar{\rho}_{g,j-1} \bar{C}_{pg,j-1} \bar{v}_{j-1}) (\bar{r}_{i-1}^2 - \bar{r}_i^2) \right] \quad (D.27)$$
$$- \sum_{i=1}^{N-1} \left[ (\lambda_{effo} \Delta T \pi D) \bar{\lambda}_{eff,j-1} \left. \frac{\partial \bar{T}}{\partial \bar{z}} \right|_{j-1} (\bar{r}_{i-1}^2 - \bar{r}_i^2) \right]$$

The total condensation rate is obtained by a summation process covering the entire flow domain

$$Q_c = \sum_{j=1}^{M-1}\sum_{i=1}^{N-1}\left[\left(\frac{D_{vo}\rho_{go}\Delta C}{D^2}\times\pi D^3\right)\right]\times \left[\bar{m}_{(iv,jv)}(\bar{z}_{j-1}-\bar{z}_j)(\bar{r}_{i-1}^{\,2}-\bar{r}_i^{\,2})\right] \tag{D.28}$$

Note that iv = i and jv = j, numerically. But (iv,jv) refers to cell center coordinates, whereas i and j refer to cell boundary locations of the same cell for the staggered grid system.

The corresponding total latent heat equation becomes

$$H_L = \sum_{j=1}^{M-1}\sum_{i=1}^{N-1}\left[\left(h_{vap}\frac{D_{vo}\rho_{go}\Delta C}{D^2}\times\pi D^3\right)\right]\times \left[\bar{m}_{(iv,jv)}(\bar{z}_{j-1}-\bar{z}_j)(\bar{r}_{i-1}^{\,2}-\bar{r}_i^{\,2})\right] \tag{D.29}$$

$h_{sub}$ replaces $h_{vap}$ in Equation D.29 wherever the temperature is below 273.15 K.

The equations and relations in this section (D.2) are solved by the same procedure detailed in Section 4.4. It was found that the same grid (91X91) used for the slit could be used for the axisymmetric system. In the investigation: the pressure differences considered are 2, 8, 14, 20, and 30 Pa; the hole diameters used are 6, 14, 22, 30, and 40 mm; the inlet relative humidities considered are 40, 50, 60, 70, and 80%; and, the exit temperatures investigated are 273, 263, 253, 243, and 233 K. The exit relative humidity is fixed at 100%.

D.3 Quasi-steady Results for Holes

The mechanics of the occurrences in this appendix are explained in detail in Chapter 6 (slits), and only the results are summarized here.

Typical velocity vectors at the inlet are shown in Figure D.2, and typical temperature contours are shown in Figure

D.3. Figure D.4 shows the relationship between the actual vapour density contours and the saturation vapour density contours in the wet and dry regions of the domain. In the former region the vapour density contours coincide. Figure D.5 shows the contours of the moisture volume fractions, which in the specific case are less than $10^{-6}$ and may, therefore, be attributed to adsorption [Langlais et al., 1982].

Table D.1 gives the results for heat and mass transfer rates for different pressure differences, $\Delta P$. The bulk air flowrate at the exit, $Q_{g,out}$, increases by about $0.335 \times 10^{-6}$ kg/s for every 1 Pa increase in the pressure difference, this being 48.6% of the flowrate at 2 Pa. The total condensation rate, $Q_c$, increases with the pressure difference in a non-linear way by an order of $10^{-9}$ kg/s for each Pascal increase in the pressure difference. The relationship between the pressure difference and the total heat transfer rate at the exit, $H_{s,out}$, is approximately linear, giving an average increase of 0.095 W in $H_{s,out}$ (or 0.5% of the value at 2 Pa) for every 1 Pa increase in $\Delta P$. The total latent heat released, $H_L$, increases in a similar way to $Q_c$. Figures D.6 and D.7 show the moisture distribution profiles for 8 Pa and 30 Pa, respectively. The figures show the condensation rates increasing with $\Delta P$, and the wet region expanding in both the vertical and radial directions as $\Delta P$ increases. Usually, a higher pressure difference shifts the wet-dry interface towards the exit, but in this case the extra vapour introduced into the domain at the higher pressure difference has overcome the effect of increased thermal penetration, causing the wet-dry interface to shift in the opposite direction. Figure D.7 contains both water and frost, unlike Figure D.6 which contains only frost.

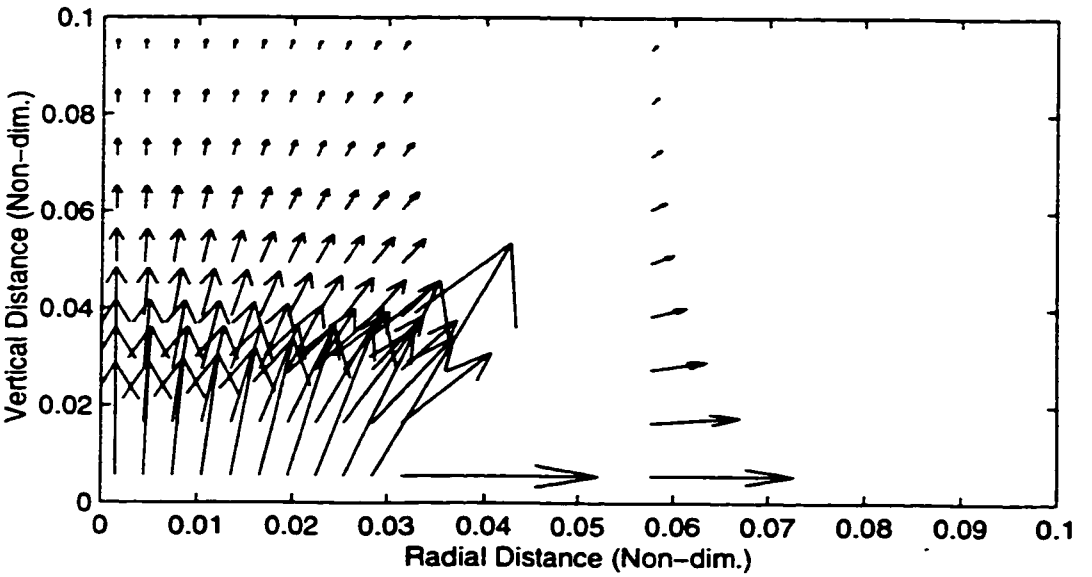


Figure D.2. Typical Inlet Velocity Vectors.
(Hole Diam.=6 mm, Press. Diff.=8 Pa)

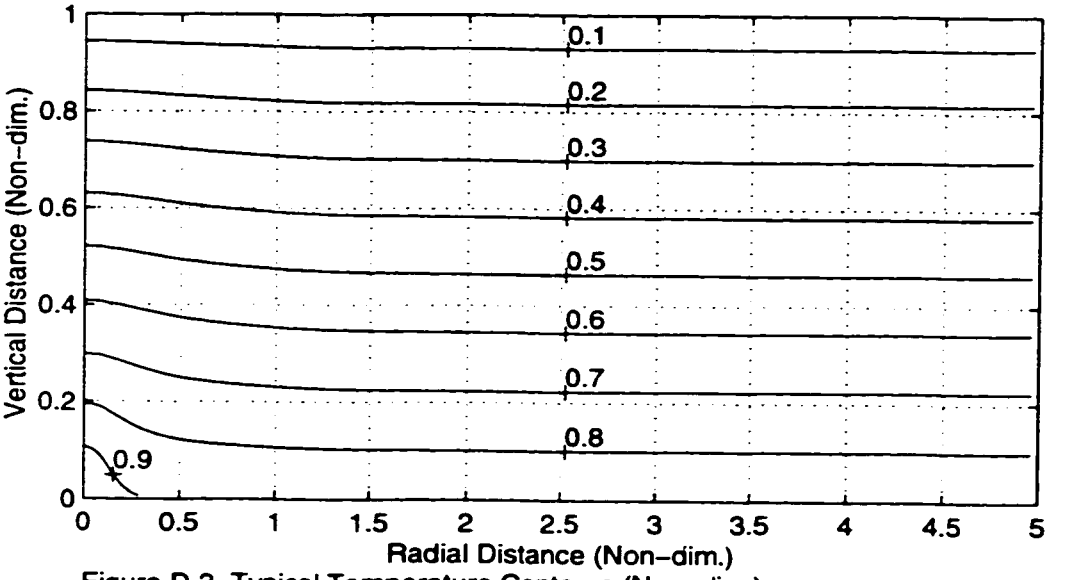


Figure D.3. Typical Temperature Contours (Non-dim.).
(Hole Diam.=6 mm, Press. Diff.=8 Pa, Exit Temp.=233 K)

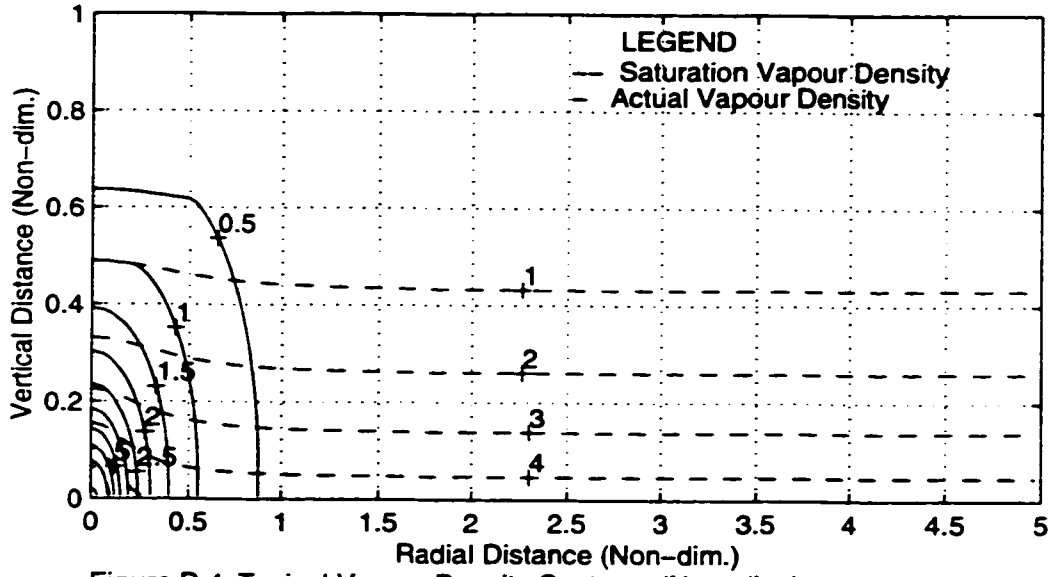


Figure D.4. Typical Vapour Density Contours (Non-dim.).
(Hole Diam.=6 mm, Press. Diff.=8 Pa, Ex. Temp.=233 K, In. RH=70%, Ex. RH=100%)

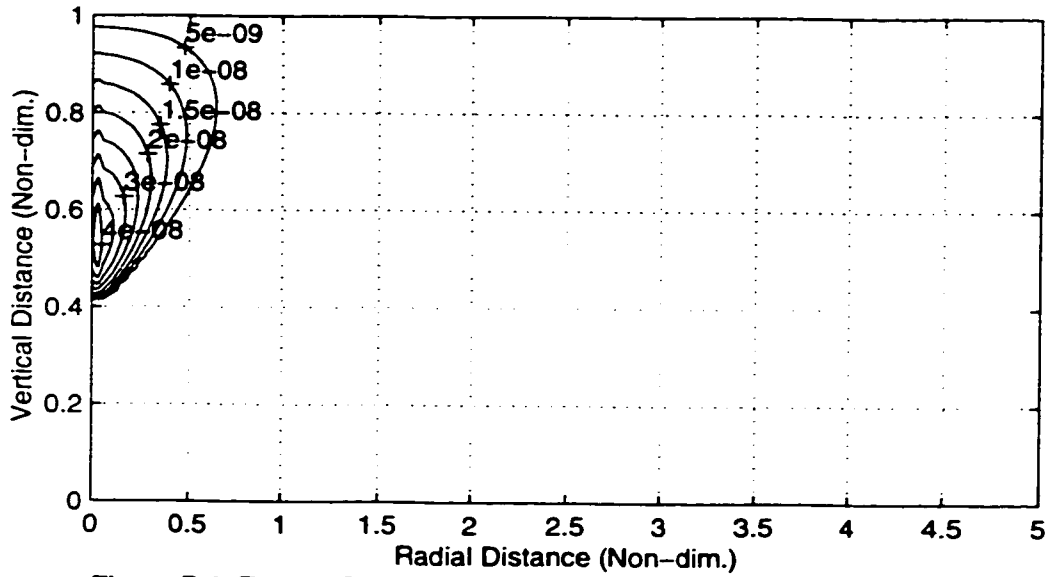


Figure D.5. Typical Condensate Volume Fraction Contours (Non-dim.).
(Hole Diam.=6 mm, Press. Diff.=8 Pa, Ex. Temp.=233 K, In. RH=70%, Ex. RH=100%)

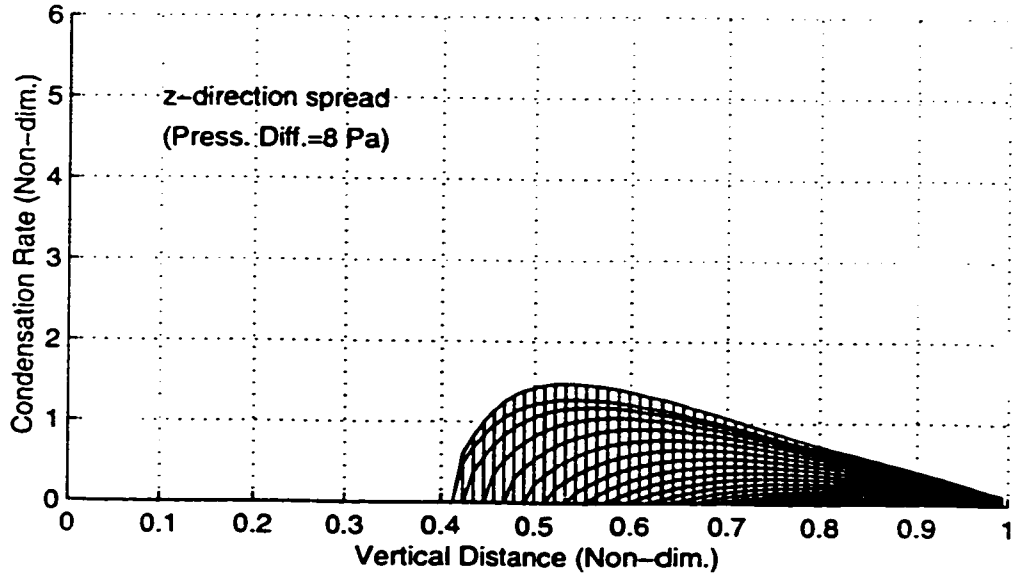


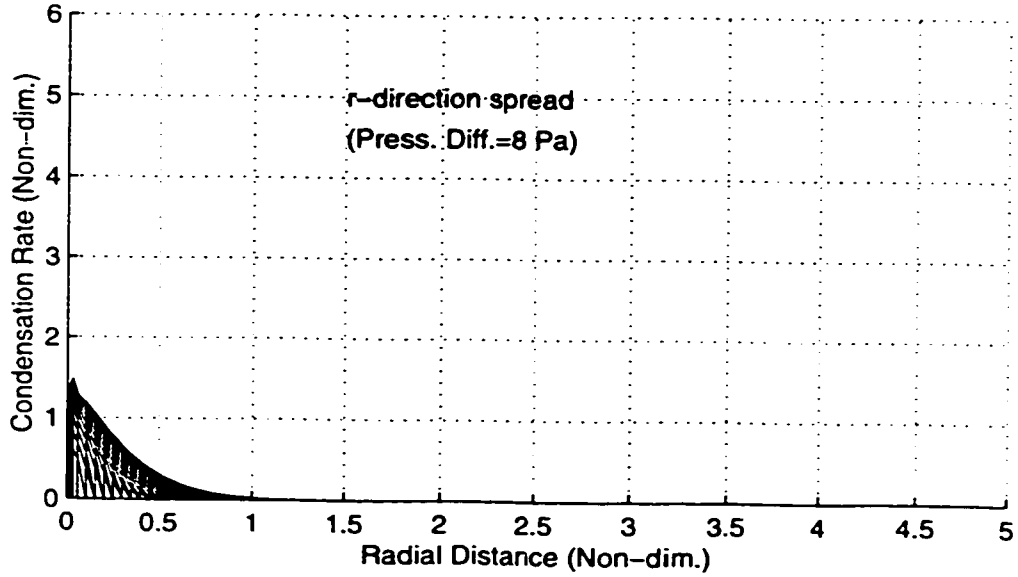


Figure D.6. Condensation Rate Profiles (r and z direction) for 8 Pa.
(Hole Diam.=6 mm, Exit Temp.=233 K, Inlet RH=70%, Exit RH=100%)

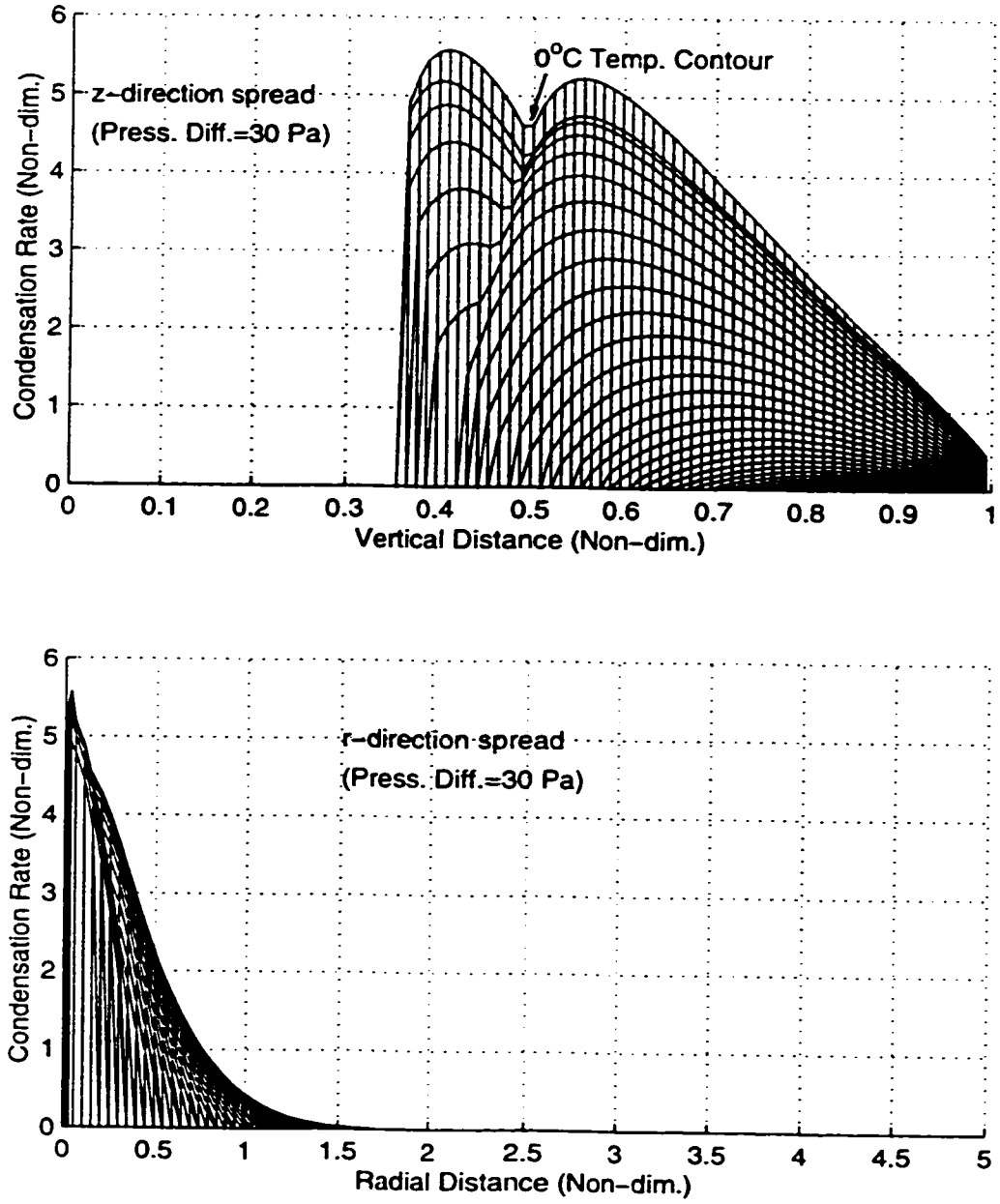


Figure D.7. Condensation Rate Profiles (r and z direction) for 30 Pa.
(Hole Diam.=6 mm, Exit Temp.=233 K, Inlet RH=70%, Exit RH=100%)

Table D.1. Effect of Pressure Difference on Quasi-steady Heat and Mass Transfer Rates: Exit Temperature is 233 K, Hole Diameter is 6 mm, Inlet Relative Humidity is 70%, and Exit Relative Humidity is 100%. ($Q_{g,out}$ is exit bulk air flowrate, $Q_c$ is total condensation rate, $H_{s,out}$ is exit total heat transfer rate, and $H_L$ is total latent heat released.)

| Press. Diff., $\Delta P$ (Pa) | Mass Flowrate | | Heat Transfer rate | |
|---|---|---|---|---|
| | $Q_{g,out}$ ($\times 10^{-6}$) kg/s | $Q_c$ ($\times 10^{-6}$) kg/s | $H_{s,out}$ (W) | $H_L$ (W) |
| 2 | 0.69 | 0.00 | 18.33 | 0.00 |
| [illegible] | 2.71 | 0.006 | 18.88 | 0.017 |
| 14 | 4.72 | 0.018 | 19.45 | 0.051 |
| 20 | 6.73 | 0.032 | 20.02 | 0.089 |
| 30 | 10.07 | 0.056 | 20.98 | 0.157 |

In Table D.2 it is seen that increasing the inlet relative humidity, $RH_{in}$, has very little effect on $Q_{g,out}$, the minute decrease with increasing $RH_{in}$ being due to the increase in the condensation rate. The total condensation rate, the total heat transfer rate at the exit, and the total latent heat released, all increase with increasing inlet relative humidity in a non-linear way. For unit increase in $RH_{in}$, the increase of $Q_c$ is of the order of $10^{-10}$ kg/s, the increase of $H_{s,out}$ is of the order of $10^{-3}$ W, and the increase of $H_L$ is of the order of $10^{-4}$ W. Figures D.8 and D.9 show that when $RH_{in}$ is increased from 40% to 70%, the local condensation rates increase and the wet zone advances towards the inlet and expands in the radial direction as well.

Table D.2. Effect of Inlet Relative Humidity on Quasi-steady Heat and Mass Transfer Rates: Exit Temperature is 233 K, Hole Diameter is 6 mm, Pressure Difference is 8 Pa, and Exit Relative Humidity is 100%. ($Q_{g,out}$ is exit bulk air flowrate, $Q_c$ is total condensation rate, $H_{s,out}$ is exit total heat transfer rate, and $H_L$ is total latent heat released.)

| Inlet RH, $RH_{in}$ (%) | Mass Flowrate | | Heat Transfer rate | |
|---|---|---|---|---|
| | $Q_{g,out}$ ($\times 10^{-6}$) kg/s | $Q_c$ ($\times 10^{-6}$) kg/s | $H_{s,out}$ | $H_L$ |
| 40 | 2.715 | 0.001 | 18.87 | 0.003 |
| 50 | 2.715 | 0.002 | 18.87 | 0.007 |
| 60 | 2.714 | 0.004 | 18.88 | 0.011 |
| 70 | 2.712 | 0.006 | 18.88 | 0.017 |
| 80 | 2.711 | 0.008 | 18.89 | 0.024 |

Table D.3 shows that for each 1 mm increase in the hole diameter: $Q_{g,out}$ increases by about $0.6 \times 10^{-6}$ kg/s or 22% of the value at a diameter of 6 mm; $H_{s,out}$ increases by about 0.175 W or 0.9% of the value at a diameter of 6 mm; and $H_L$ increases by about 0.012 W or 70.6% of the value at a diameter of 6 mm. The increase in $Q_c$ is not linear but lies between $3.6 \times 10^{-9}$ and $5.0 \times 10^{-9}$ kg/s (i.e., between 60% and 83% of the value at a diameter of 6 mm) for each 1 mm increase in the hole diameter. Figures D.10 and D.11 show that increasing the hole diameter has a similar effect on the magnitudes and distribution of the local condensation rates as increasing the pressure difference has. However, computations from the data in Tables D.1 and D.3 show that increasing the hole diameter by 1 mm and increasing the pressure difference by 1 Pa cause different percentage increases in the heat and mass transfer rates.

Table D.3. Effect of Hole Diameter on Quasi-steady Heat and Mass Transfer Rates: Exit Temperature is 233 K, Pressure Difference is 8 Pa, Inlet Relative Humidity is 70%, and Exit Relative Humidity is 100%. ($Q_{g,out}$ is exit bulk air flowrate, $Q_c$ is total condensation rate, $H_{s,out}$ is exit total heat transfer rate, and $H_L$ is total latent heat released.)

| Hole Diam., dl (mm) | Mass Flowrate | | Heat Transfer rate | |
|---|---|---|---|---|
| | $Q_{g,out}$ ($\times 10^{-6}$) kg/s | $Q_c$ ($\times 10^{-6}$) kg/s | $H_{s,out}$ | $H_L$ |
| 6 | 2.71 | 0.006 | 18.88 | 0.017 |
| 14 | 7.23 | 0.035 | 20.16 | 0.099 |
| 22 | 11.98 | 0.070 | 21.53 | 0.196 |
| 30 | 16.90 | 0.107 | 22.97 | 0.301 |
| 40 | 23.31 | 0.156 | 24.85 | 0.438 |

In Table D.4, condensation does not occur until the exit temperature has been lowered to 243 K. The effect of the exit temperature, $T_{out}$, on $Q_{g,out}$ is negligible, there being an increase of the order of $10^{-10}$ kg/s (or 0.004% of the value at 273 K) for each 1 K decrease in $T_{out}$. $H_{s,out}$ increases by about 0.3 W (or 4.3% of the value at 273 K) for each 1 K decrease in $T_{out}$ due mainly to the increase in conduction heat transfer arising from a larger temperature difference. $H_L$ increases very little in association with the increase in the total condensation rate. Figure D.12 shows the radial and vertical profiles of the condensation rate for an exit temperature of 233 K.

Table D.4. Effect of Exit Temperature on Quasi-steady Heat and Mass Transfer Rates: Pressure Difference is 8 Pa, Hole Diameter is 6 mm, Inlet Relative Humidity is 70%, and Exit Relative Humidity is 100%. ($Q_{g,out}$ is exit bulk air flowrate, $Q_c$ is total condensation rate, $H_{s,out}$ is exit total heat transfer rate, and $H_L$ is total latent heat released.)

| Exit Temp., $T_{out}$ (K) | Mass Flowrate | | Heat Transfer rate | |
|---|---|---|---|---|
| | $Q_{g,out}$ ($\times 10^{-6}$) kg/s | $Q_c$ ($\times 10^{-6}$) kg/s | $H_{s,out}$ | $H_L$ |
| 273 | 2.697 | 0.000 | 7.00 | 0.000 |
| 263 | 2.703 | 0.000 | 10.03 | 0.000 |
| 253 | 2.708 | 0.000 | 13.02 | 0.000 |
| 243 | 2.712 | 0.001 | 15.97 | 0.004 |
| 233 | 2.712 | 0.006 | 18.88 | 0.017 |

## D.4 Effect of Moisture Accumulation

Table D.5 shows that during a 30-hour period starting from the quasi-steady state:

(1) $Q_{g,out}$ remains constant;

(2) the percentage of vapour condensed increases from 58.8% to 61.8%;

(3) the total condensation rate increases from $0.107 \times 10^{-6}$ kg/s to $0.112 \times 10^{-6}$ kg/s;

(4) $H_{s,out}$ increases very little, from 22.97 to 23.06 W; and,

(5) $H_L$ increases from 0.301 to 0.312 W, these being 1.31% and 1.35% of the respective values of $H_{s,out}$.

Figures D.13 and D.14 show the wet zone advancing gradually with time towards the inlet, and the peak of the condensation rate profile also increasing with time. However, the magnitudes of the local condensation rates in regions closer

to the exit decrease with time.

Figure D.15 shows the moisture volume fraction contours of the condensate for 6 and 18 hours after the quasi-steady stage. The volume fractions increase with time as the condensate accumulates and the wet region expands in both the vertical and radial directions. Figure D.16 shows that the increase in the total moisture content with time is approximately linear.

Table D.5. Effect of Moisture Accumulation with Time on Heat and Mass Transfer Rates: Hole Diameter is 30 mm, Pressure Difference is 8 Pa, Exit Temperature is 233 K, Inlet RH is 70%, and Exit RH 100%. ($Q_{g,out}$ is bulk air flowrate at exit, VC is percentage of inlet vapour which condenses, $Q_c$ is total condensation rate, MC is total liquid/frost content, $H_{s,out}$ is total heat transfer rate at exit, and $H_L$ is total latent heat released.)

| Time (hrs) | $Q_{g,out}$ ($\times 10^{-6}$) kg/s | VC (%) | $Q_C$ ($\times 10^{-6}$) kg/s | MC (kg) | $H_{s,out}$ (W) | $H_L$ (W) |
|---|---|---|---|---|---|---|
| 0 | 16.9 | 58.8 | 0.107 | 1.1e-7 | 22.97 | 0.301 |
| 6 | 16.9 | 59.4 | 0.108 | 0.002 | 22.99 | 0.303 |
| 12 | 16.9 | 60.0 | 0.110 | 0.005 | 23.01 | 0.306 |
| 18 | 16.9 | 60.6 | 0.111 | 0.007 | 23.03 | 0.308 |
| 24 | 16.9 | 61.2 | 0.111 | 0.010 | 23.05 | 0.310 |
| 30 | 16.9 | 61.8 | 0.112 | 0.012 | 23.06 | 0.312 |

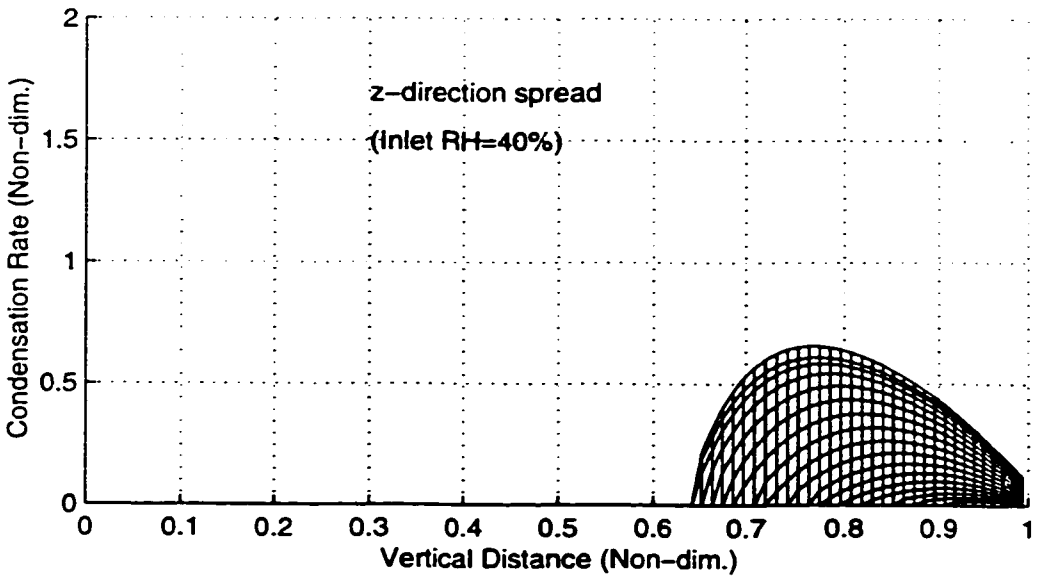


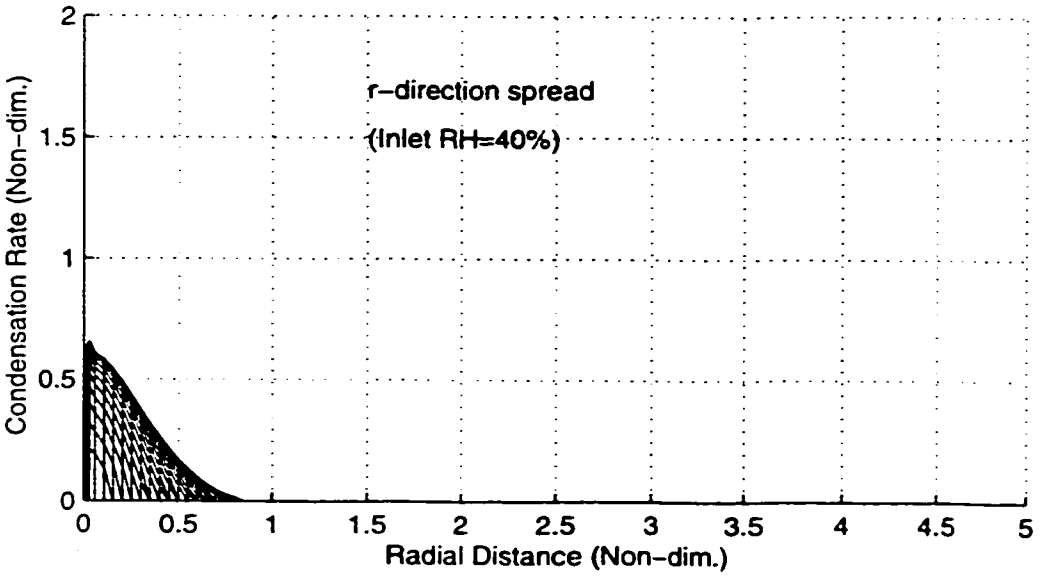


Figure D.8. Condensation Rate Profiles (r and z direction) for 40% Inlet RH. (Hole Diam.=6 mm, Press. Diff.=8 Pa, Exit Temp.=233 K, Exit RH=100%)

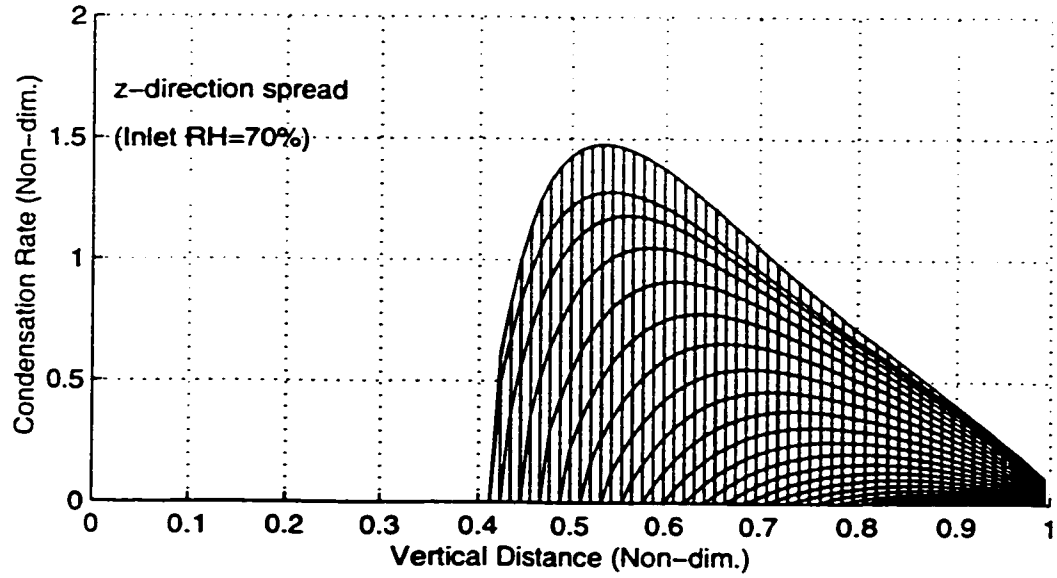


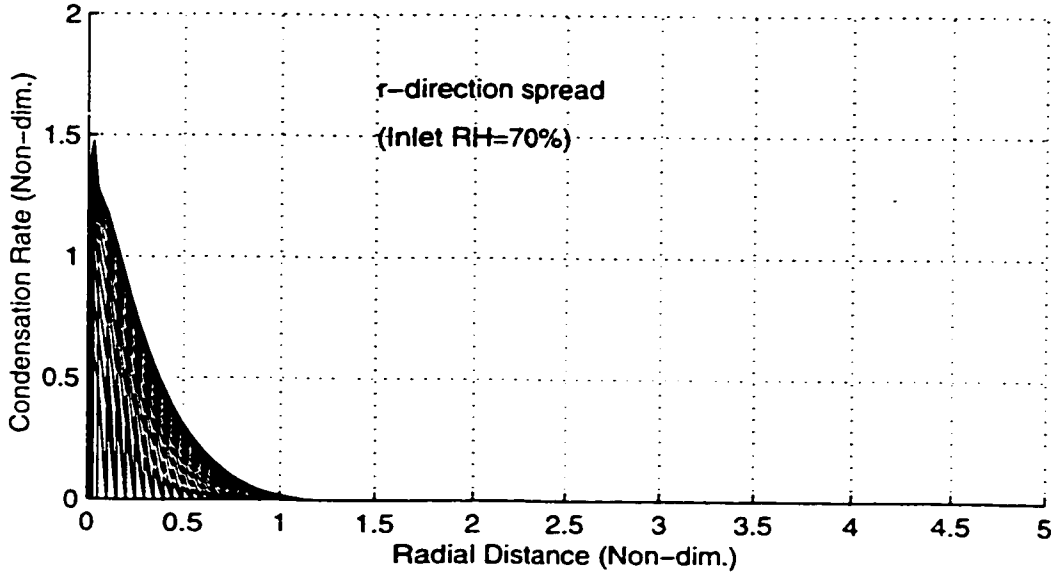


Figure D.9. Condensation Rate Profiles (r and z direction) for 70% Inlet RH. (Hole Diam.=6 mm, Press. Diff.=8 Pa, Exit Temp.=233 K, Exit RH=100%)

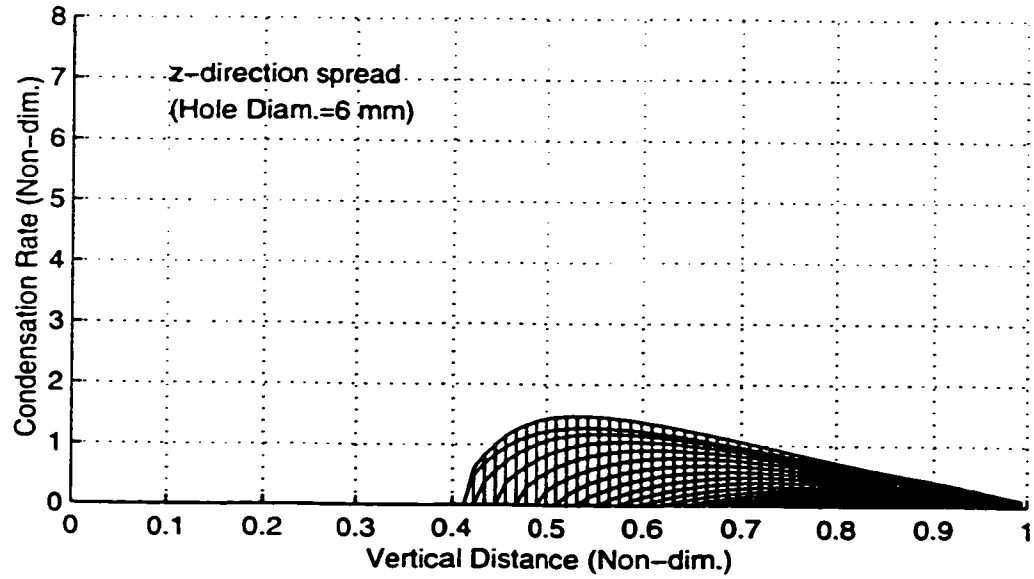


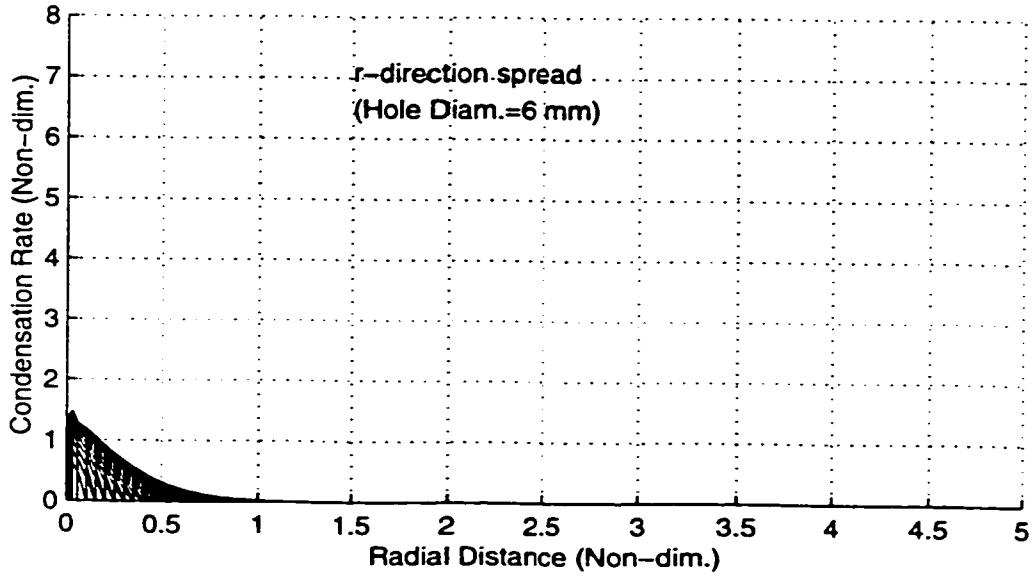


Figure D.10. Condensation Rate Profiles (r and z direction) for 6 mm Hole Diameter (Press. Diff.=8 Pa, Exit Temp.=233 K, Inlet RH=70%, Exit RH=100%)

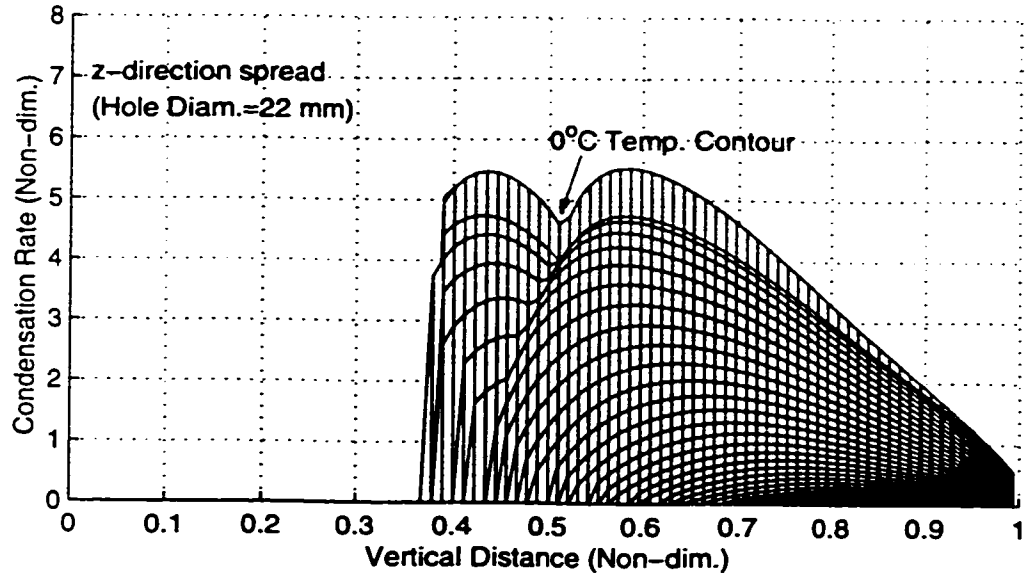


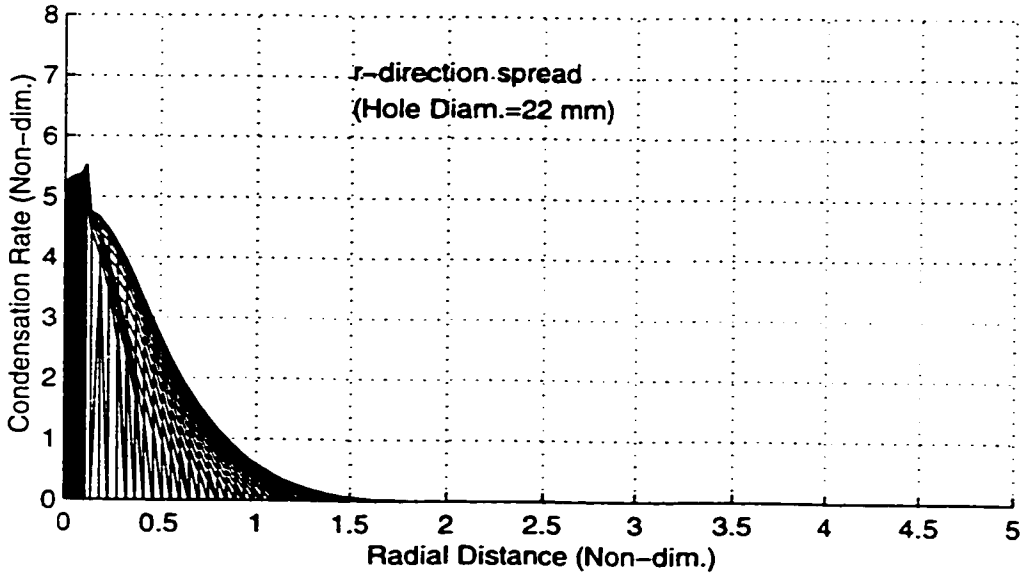


Figure D.11. Condensation Rate Profiles (r and z direction) for 22 mm Hole Diameter (Press. Diff.=8 Pa, Exit Temp.=233 K, Inlet RH=70%, Exit RH=100%)

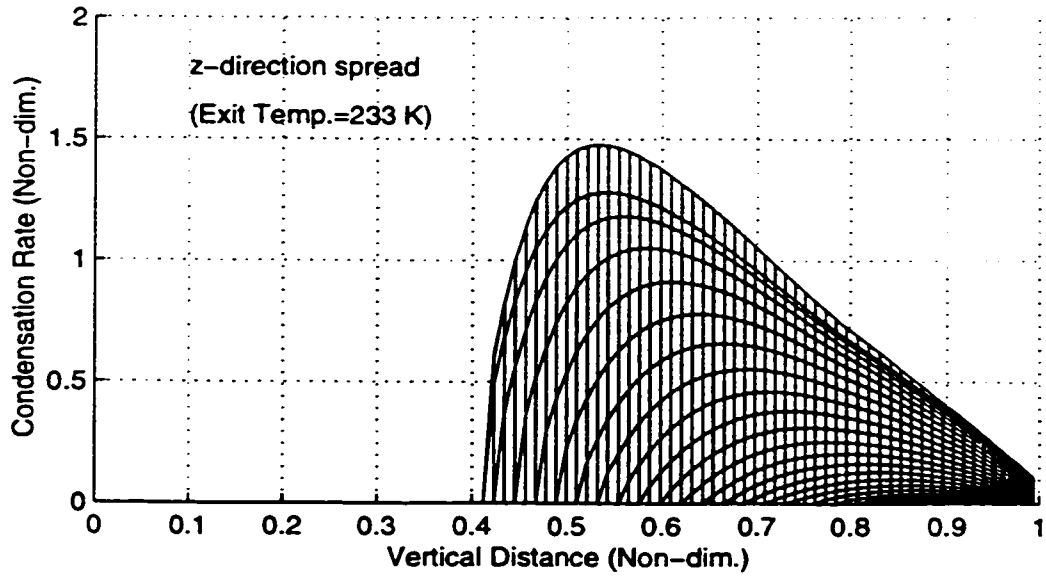


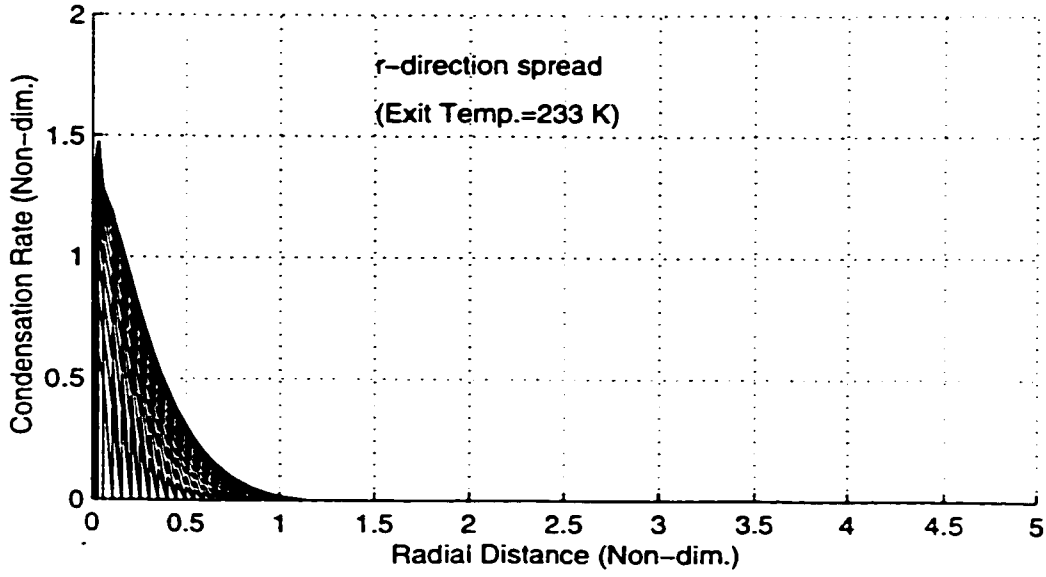


Figure D.12. Condensation Rate Profiles (r and z direction) for 233 K Exit Temp. (Hole Diam.=6 mm, Press. Diff.=8 Pa, Inlet RH=70%, Exit RH=100%)

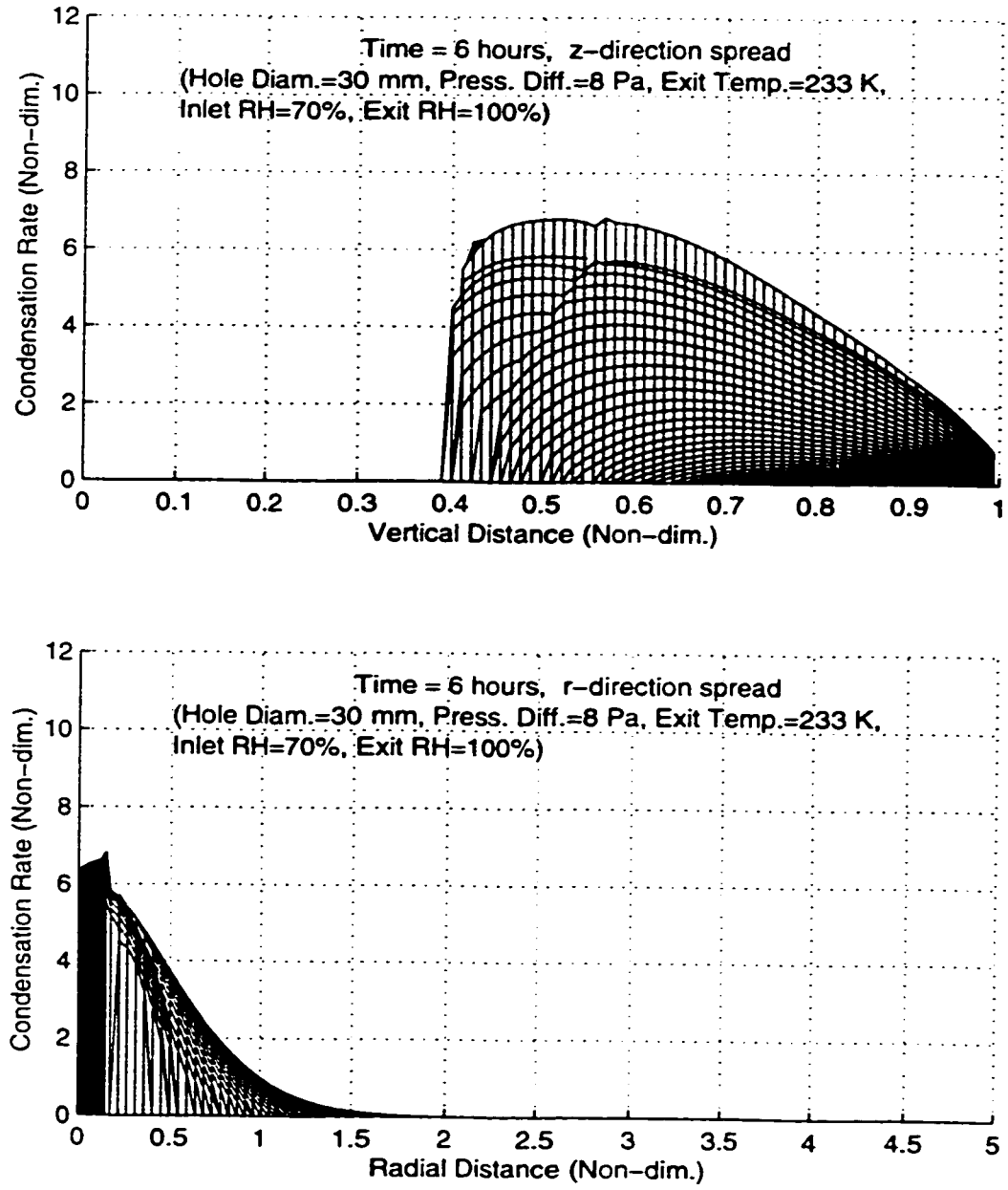


Figure D.13. Condensation Rate Profiles (r and z direction) after 6 Hours.

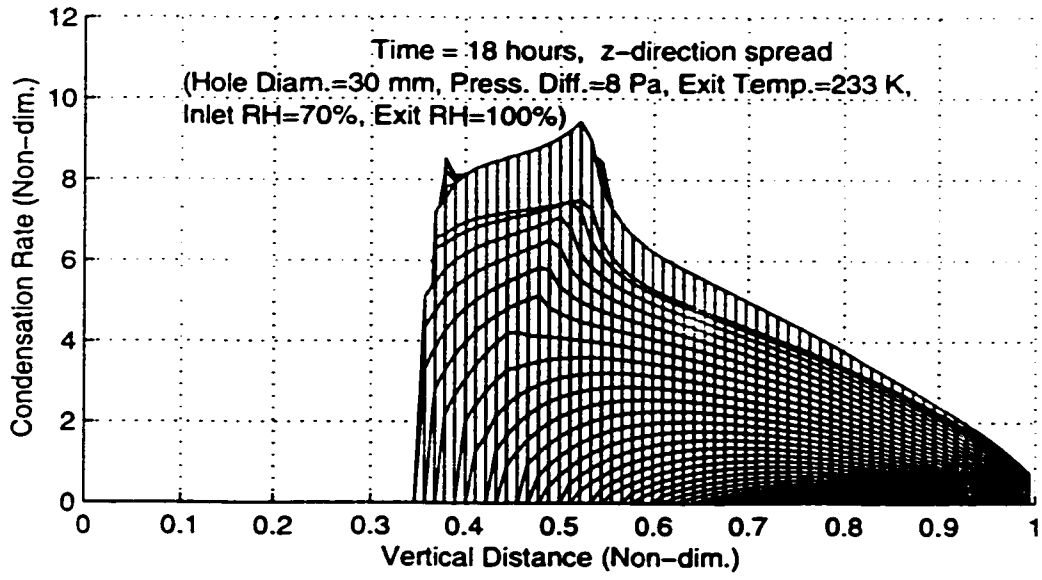


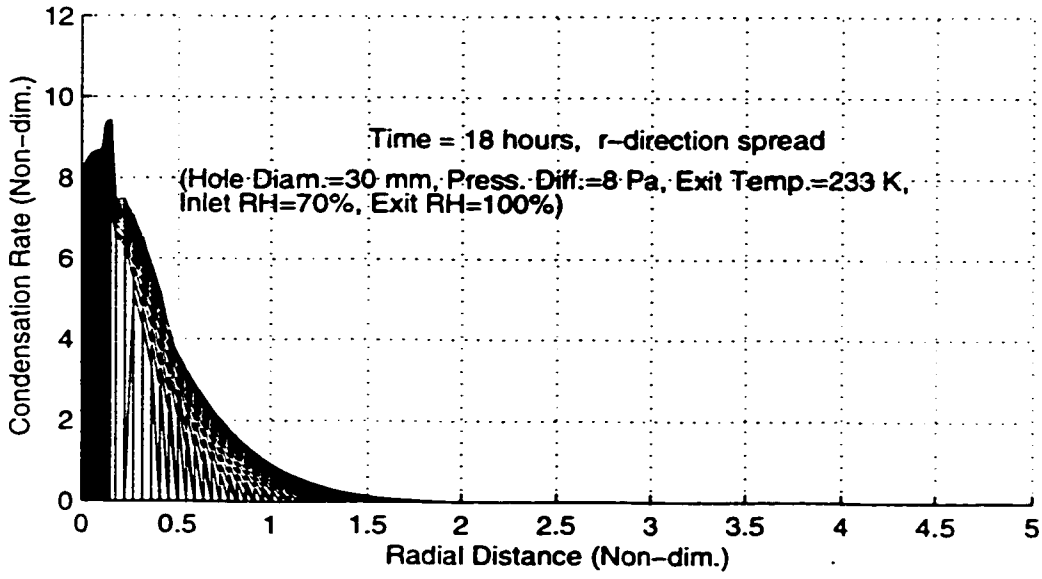


Figure D.14. Condensation Rate Profiles (r and z direction) after 18 Hours.

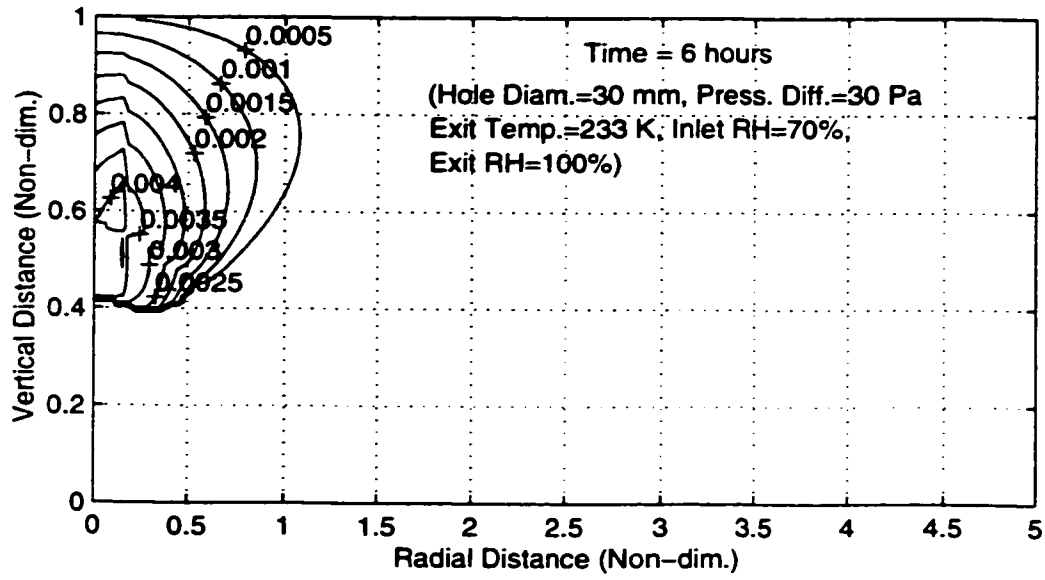


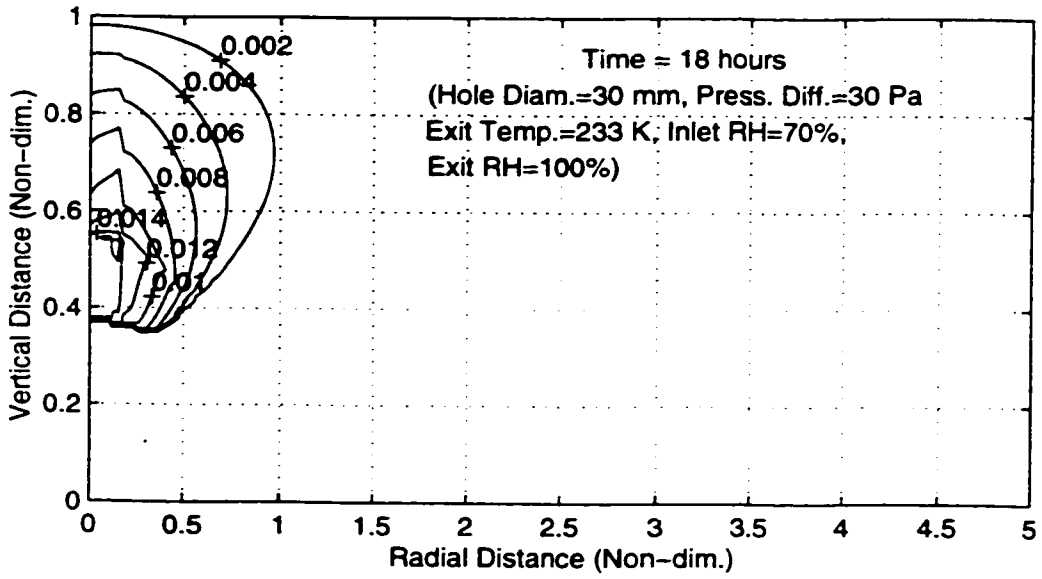


Figure D.15. Condensate/Ablimate Volume Fraction Contours for 6 and 18 Hours.

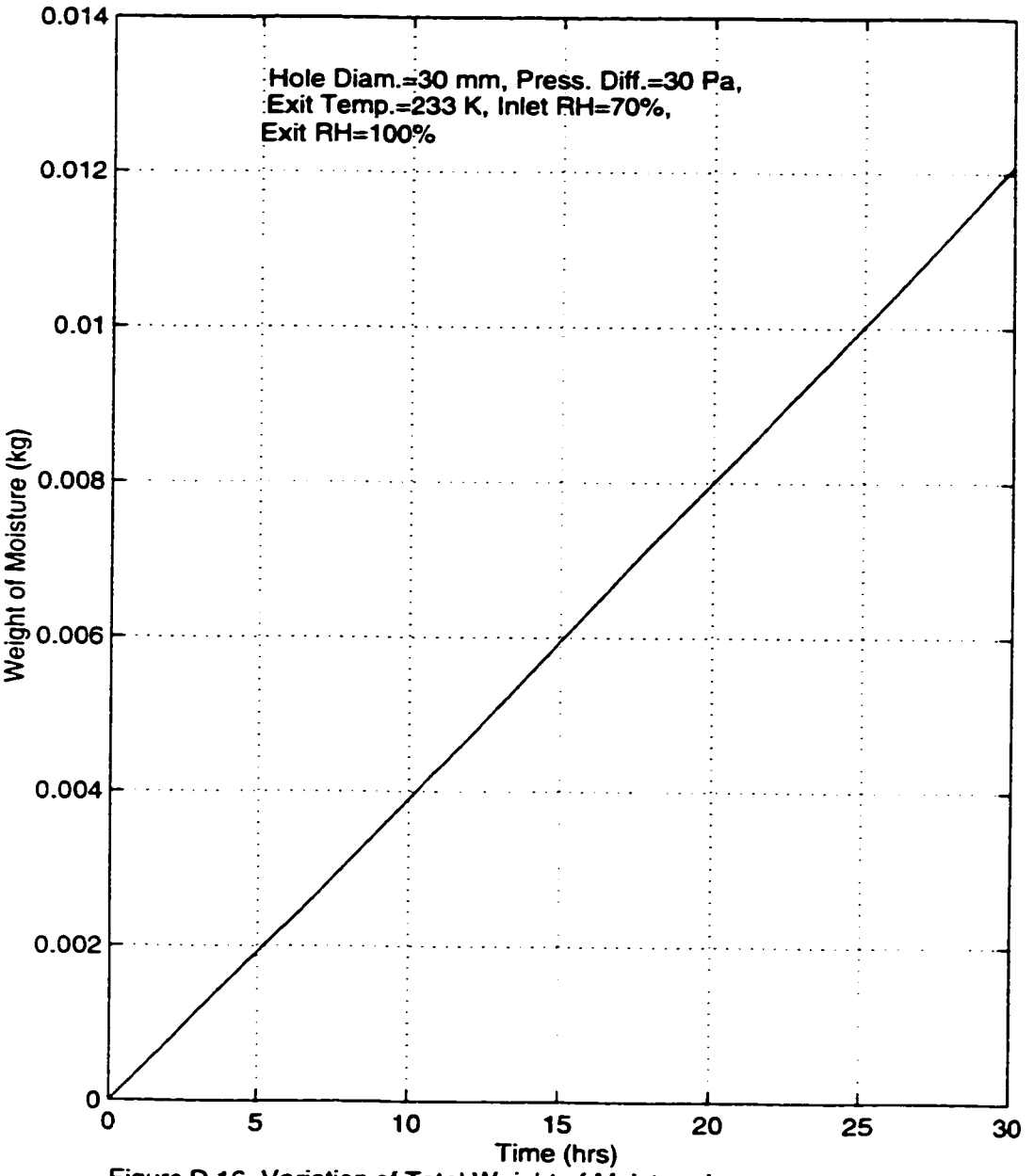


Figure D.16. Variation of Total Weight of Moisture in the Insulation with Time for a Round Hole.

# APPENDIX E

# NATURAL CONVECTION

## E.1 Darcy-modified Rayleigh Number

In the regions of the flow-field (Figure 3.3), far from the leakage path and where the effect of the opening is negligible, the dominant transfer mechanism is heat conduction. This is evident from the horizontal isothermals in these regions shown in Figure 6.2.

Far from the leakage site, the flow domain shown in Figure 3.3 resembles an insulation slab heated from below. The theory of natural convection in a horizontal fluid-saturated porous medium predicts that convective motion will commence only when the Darcy-modified Rayleigh number ($Ra_K$) is greater than a certain critical value. For a homogeneous, isotrcpic porous medium, this Rayleigh number can be expressed as [Bejan, 1984]:

$$Ra_K = \frac{gK\beta\Delta TD}{\nu_{av.}\alpha_{av.}} \qquad (E.1)$$

where g is the acceleration due to gravity, K is the permeability of the porous medium, $\beta$ is the volumetric thermal expansion coefficient, $\Delta T$ is the temperature difference across the insulation slab, D is the insulation thickness, $\nu_{av.}$ is the kinematic viscosity calculated at the average temperature of the slab, and $\alpha_{av.}$ is the thermal diffusivity calculated at the average temperature of the slab.

Now, the temperature difference, $\Delta T = T_{in} - T_{out}$,

the average temperature, $T_{av.} = T_{in} - \frac{\Delta T}{2}$,

the average density, $\rho_{av.} = \frac{P_{out}}{R_a T_{av.}}$,

the volumetric thermal expansion coefficient, $\beta = \frac{1}{T_{av.}}$,

the average kinematic viscosity, $\nu_{av.} = \frac{\mu_{av.}}{\rho_{av.}}$, and

the average thermal diffusivity, $\alpha_{av.} = \frac{\lambda_{av.}}{\rho_{av.} C_{pa,av.}}$.

(All average property values are computed at the average temperature, $T_{av.}$)

Hence Equation E.1 can be re-written as

$$Ra_K = \frac{gKC_{pa,av.}\rho_{av.}^2 \Delta TD}{\mu_{av.}\lambda_{av.}T_{av.}} \qquad (E.2)$$

Heat conduction remains stable if $Ra_K$ is below the critical value. Above this value, the Nusselt number becomes a strong function of the Rayleigh number [Bejan, 1984] and engineers have to rely on experimental and numerical measurements. Theories predict that the critical Rayleigh number depends upon the thermal and mechanical boundary conditions imposed at the top and bottom of the insulation [Wilkes and Childs, 1992].

Bejan (1984) and Nield and Bejan (1992) showed that when the medium is homogeneous, isotropic, finite, and is bounded by two impermeable isothermal plates, the theoretical value of the critical Rayleigh number is $4\pi^2$ (39.5). In most practical cases, which are neither homogeneous nor isotropic, the critical Rayleigh number for these boundary conditions lies between 30 and 40 [Langlais et al, 1990].

Lapwood (1948) showed that for an open configuration (i.e.,

an impermeable isothermal hot bottom face and a permeable isothermal cold top face) with an "infinite" air layer above the slab, the theoretical critical Rayleigh number is 27.1 if still conditions are assumed at the top. However, such ideal conditions are difficult to achieve. Other boundary conditions such as uniform heat flux (instead of uniform temperature) yield even lower critical Rayleigh numbers [Nield, 1968]. Wilkes et al. (1991) report that the critical Rayleigh number for uniform heat flux at the top boundary is $\pi^2$ (9.9).

Attic configurations are usually of the open type with an "infinite" air layer above the insulation. Numerous experiments have been performed by different researchers to determine critical Rayleigh numbers for open loose-fill insulation. Langlais et al. (1990) found that the Nusselt number exceeded 1.0 only when the Rayleigh number became greater than 30. Wilkes et al. (1991) found critical Rayleigh numbers between 13 and 20 when they investigated vented attics. Silberstein et al. (1990) observed an experimental critical Rayleigh number of about 30 for open loose-fill fibrous insulation with a uniform temperature boundary at the top. They reported that as soon as there was a departure from the ideal temperature condition, convection set in almost as soon as a thermal gradient was observed. However, the convection did not become significant until a Rayleigh number of about 15 was exceeded. Their critical Rayleigh number for an unvented air space above the insulation was 12. Wilkes and Rucker (1983) experimented with open loose-fill insulation and found that the experimental data agreed qualitatively, but not quantitatively, with theory. The critical Rayleigh numbers from their experiments (i.e., in the range 10 to 30) were generally lower than the theoretical values and did not fall on a universal curve. Wilkes and Childs (1992) found critical Rayleigh numbers between 11 and 17 for loose-fill fiberglass insulation.

In this project, the boundary conditions at the top face of the open fiberglass insulation slab are neither isothermal nor of the uniform heat flux type. The general condition of the attic, i.e. whether it is vented or not, does not even enter the equations. However, the research findings by others, discussed above, serve as a useful and reliable guide to assessing whether the effects of natural convection should be considered in the data analysis. In general, the findings indicate that it is safe to neglect the effects of natural convection if the Darcy-modified Rayleigh numbers are less than 10.

This research project's most severe boundary conditions (i.e., a temperature of 233 K in the attic and 293 K in the room) are now examined for the occurrence of natural convection. For these temperature boundary conditions, $T_{av}$ = 263 K, from which

$C_{pa,av.}$ = 1015 J/kg-K,

$\rho_{av.}$ = 1.342 kg/m$^3$,

$\mu_{av.}$ = 1.661 x $10^{-5}$ kg/m-s, and

$\lambda_{av.}$ = 0.0459 W/m-K, this average being obtained from $\lambda_a$ = **0.0231**, $\lambda_s$ = **0.78** ***and*** $\epsilon$ = **0.97**.

Other values are g = 9.81 m/s$^2$ and D = 0.1 m . (The fluid is assumed to be pure dry air.)

The formulae used in the computation of the above thermophysical properties are discussed in Sections A.1 and A.2. Substituting the values into Equation E.2 gives $Ra_K$ = 0.269, which is far less than the target critical Rayleigh number of 10. It can now be concluded that the effect of natural convection, in all the situations considered in this research project, is negligible.

To arrive at a Rayleigh number of 0.269 the temperature at the bottom of the insulation slab was assumed to be the same as

the room temperature (i.e., 293 K). This in effect assumes that the thermal resistance of the plasterboard is zero. Due to the thermal resistance of the plasterboard, the bottom surface of the insulation is actually at a lower temperature than the room temperature, making the actual Rayleigh number less than 0.269.

The permeability of loose-fill fiberglass insulation usually falls within the range of values $10^{-8}$ to $10^{-11}$ $m^2$, depending on such factors as fiber density, dimensions, and orientation. It is noted here that if all parameters in Equation E.2, except the permeability, retained their values, it would take a permeability value of $1.862 \times 10^{-8}$ $m^2$ to raise the Rayleigh number to the target critical value of 10.

## E.2 Conclusion

It has been established that the maximum possible Darcy-modified Rayleigh number in this project is so much less than the critical value for the onset of convective instabilities that it is absolutely justified to disregard natural convection in the model.

# APPENDIX F

## TABLES OF SIMULATION DATA

Table F.1. Effect of Pressure Difference and Inlet Relative Humidity on Quasi-steady Heat and Mass Transfer Rates in a Slit: Exit Temp. is 233 K, Slit Width is 6 mm, and Exit RH is 100%. ($Q_{g,out}$ is exit bulk air-flowrate, $Q_{v,in}$ is inlet vapour-flowrate, $Q_c$ is total condensation rate, $H_{s,out}$ is exit total heat transfer rate, and $H_L$ is total latent heat released.)

| $\Delta P$ (Pa) | $RH_{in}$ (%) | $Q_{g,out}$ ($\times 10^{-6}$) kg/s | $Q_{v,in}$ ($\times 10^{-6}$) kg/s | $Q_c$ ($\times 10^{-6}$) kg/s | $H_{s,out}$ (W) | $H_L$ (W) |
|---|---|---|---|---|---|---|
| 2 | 40 | 48.3 | 0.30 | 0.15 | 36.5 | 0.43 |
| 8 | 40 | 187.3 | 1.07 | 0.73 | 76.7 | 2.07 |
| 14 | 40 | 323.8 | 1.85 | 1.26 | 117.2 | 3.57 |
| 20 | 40 | 459.9 | 2.63 | 1.73 | 157.9 | 4.90 |
| 30 | 40 | 686.5 | 3.92 | 2.37 | 225.9 | 6.74 |
| 2 | 50 | 48.2 | 0.38 | 0.22 | 36.6 | 0.62 |
| 8 | 50 | 186.9 | 1.34 | 0.97 | 77.2 | 2.75 |
| 14 | 50 | 323.3 | 2.31 | 1.67 | 118.1 | 4.73 |
| 20 | 50 | 459.2 | 3.29 | 2.29 | 159.2 | 6.48 |
| 30 | 50 | 685.5 | 4.91 | 3.19 | 227.9 | 9.02 |
| 2 | 60 | 48.1 | 0.45 | 0.28 | 36.7 | 0.81 |
| 8 | 60 | 186.5 | 1.61 | 1.21 | 77.6 | 3.42 |
| 14 | 60 | 322.7 | 2.78 | 2.08 | 118.9 | 5.84 |
| 20 | 60 | 458.4 | 3.95 | 2.87 | 160.4 | 8.01 |
| 30 | 60 | 684.6 | 5.89 | 4.01 | 229.7 | 11.17 |
| 2 | 70 | 48.0 | 0.53 | 0.35 | 36.8 | 1.00 |
| 8 | 70 | 186.1 | 1.87 | 1.46 | 78.0 | 4.07 |
| 14 | 70 | 322.1 | 3.24 | 2.49 | 119.7 | 6.90 |
| 20 | 70 | 457.7 | 4.61 | 3.44 | 161.6 | 9.49 |
| 30 | 70 | 683.6 | 6.88 | 4.82 | 231.4 | 13.23 |
| 2 | 80 | 47.9 | 0.61 | 0.42 | 36.9 | 1.20 |
| 8 | 80 | 185.7 | 2.14 | 1.71 | 78.4 | 4.71 |
| 14 | 80 | 321.4 | 3.71 | 2.89 | 120.5 | 7.94 |
| 20 | 80 | 456.9 | 5.27 | 4.03 | 162.7 | 11.00 |
| 30 | 80 | 682.6 | 7.86 | 5.63 | 233.1 | 15.31 |

Table F.2. Effect of Pressure Difference and Inlet Relative Humidity on Quasi-steady Heat and Mass Transfer Rates in a Hole: Exit Temp. is 233 K, Hole diam. is 6 mm, and Exit RH is 100%. ($Q_{g,out}$ is exit bulk air-flowrate, $Q_{v,in}$ is inlet vapour-flowrate, $Q_c$ is total condensation rate, $H_{s,out}$ is exit total heat transfer rate, and $H_L$ is total latent heat released.)

| $\Delta P$ (Pa) | $RH_{in}$ (%) | $Q_{g,out}$ ($x10^{-6}$) kg/s | $Q_{v,in}$ ($x10^{-6}$) kg/s | $Q_c$ ($x10^{-6}$) kg/s | $H_{s,out}$ (W) | $H_L$ (W) |
|---|---|---|---|---|---|---|
| 2 | 40 | 0.69 | 0.004 | 0.00 | 18.33 | 0.00 |
| 8 | 40 | 2.72 | 0.016 | 0.001 | 18.87 | 0.003 |
| 14 | 40 | 4.73 | 0.027 | 0.005 | 19.43 | 0.015 |
| 20 | 40 | 6.75 | 0.038 | 0.011 | 19.98 | 0.031 |
| 30 | 40 | 10.10 | 0.058 | 0.022 | 20.92 | 0.062 |
| 2 | 50 | 0.69 | 0.005 | 0.00 | 18.33 | 0.00 |
| 8 | 50 | 2.72 | 0.019 | 0.002 | 18.88 | 0.007 |
| 14 | 50 | 4.73 | 0.034 | 0.009 | 19.43 | 0.025 |
| 20 | 50 | 6.74 | 0.048 | 0.017 | 20.00 | 0.049 |
| 30 | 50 | 10.09 | 0.072 | 0.033 | 20.94 | 0.092 |
| 2 | 60 | 0.69 | 0.006 | 0.00 | 18.33 | 0.00 |
| 8 | 60 | 2.71 | 0.023 | 0.004 | 18.88 | 0.011 |
| 14 | 60 | 4.73 | 0.041 | 0.013 | 19.44 | 0.037 |
| 20 | 60 | 6.74 | 0.058 | 0.024 | 20.01 | 0.068 |
| 30 | 60 | 10.09 | 0.087 | 0.044 | 20.96 | 0.124 |
| 2 | 70 | 0.69 | 0.007 | 0.00 | 18.33 | 0.00 |
| 8 | 70 | 2.71 | 0.027 | 0.006 | 18.88 | 0.017 |
| 14 | 70 | 4.72 | 0.047 | 0.018 | 19.45 | 0.051 |
| 20 | 70 | 6.73 | 0.068 | 0.032 | 20.02 | 0.089 |
| 30 | 70 | 10.07 | 0.101 | 0.056 | 20.89 | 0.157 |
| 2 | 80 | 0.69 | 0.008 | 0.00 | 18.33 | 0.00 |
| 8 | 80 | 2.71 | 0.031 | 0.008 | 18.89 | 0.024 |
| 14 | 80 | 4.72 | 0.054 | 0.023 | 19.46 | 0.065 |
| 20 | 80 | 6.72 | 0.077 | 0.040 | 20.03 | 0.111 |
| 30 | 80 | 10.06 | 0.116 | 0.068 | 21.00 | 0.191 |

Table F.3. Dry-air Flowrates for Slits ($x10^{-6}$ kg/s)

| $T_{out}$ (K) | $\Delta P$ (Pa) | 6 (mm) | 14 (mm) | 22 (mm) | 30 (mm) | 40 (mm) |
|---|---|---|---|---|---|---|
| 293 | 2 | 43.69 | 55.76 | 64.47 | 71.76 | 79.99 |
| 293 | 8 | 174.8 | 223.0 | 257.9 | 287.0 | 320.0 |
| 293 | 14 | 305.9 | 390.3 | 451.3 | 502.3 | 560.0 |
| 293 | 20 | 437.0 | 557.6 | 644.7 | 717.6 | 800.0 |
| 293 | 30 | 655.5 | 836.4 | 967.1 | 1077 | 1200 |
| 273 | 2 | 44.67 | 57.18 | 66.24 | 73.83 | 82.41 |
| 273 | 8 | 177.0 | 226.2 | 261.6 | 291.3 | 324.9 |
| 273 | 14 | 308.5 | 393.9 | 455.5 | 507.0 | 565.3 |
| 273 | 20 | 439.8 | 561.3 | 649.0 | 722.5 | 805.4 |
| 273 | 30 | 658.4 | 840.2 | 971.5 | 1081 | 1206 |
| 263 | 2 | 45.15 | 57.90 | 67.13 | 74.87 | 83.63 |
| 263 | 8 | 178.1 | 227.7 | 263.5 | 293.4 | 327.2 |
| 263 | 14 | 309.8 | 395.6 | 457.5 | 509.3 | 567.9 |
| 263 | 20 | 441.1 | 563.1 | 651.1 | 724.8 | 808.0 |
| 263 | 30 | 659.8 | 842.1 | 973.6 | 1084 | 1208 |
| 253 | 2 | 45.64 | 58.61 | 68.02 | 75.91 | 84.85 |
| 253 | 8 | 179.2 | 229.2 | 265.2 | 295.4 | 329.6 |
| 253 | 14 | 311.1 | 397.3 | 459.5 | 511.6 | 570.4 |
| 253 | 20 | 442.5 | 564.8 | 653.2 | 727.1 | 810.6 |
| 253 | 30 | 661.2 | 843.9 | 975.7 | 1086 | 1210 |
| 243 | 2 | 46.12 | 59.32 | 68.90 | 76.95 | 86.06 |
| 243 | 8 | 180.3 | 230.6 | 267.0 | 297.4 | 331.8 |
| 243 | 14 | 312.3 | 398.9 | 461.4 | 513.7 | 572.8 |
| 243 | 20 | 443.8 | 566.6 | 655.2 | 729.4 | 813.1 |
| 243 | 30 | 662.6 | 845.6 | 977.8 | 1088 | 1213 |
| 233 | 2 | 46.60 | 60.03 | 69.79 | 77.99 | 87.27 |
| 233 | 8 | 181.3 | 232.0 | 268.7 | 299.4 | 331.1 |
| 233 | 14 | 313.5 | 400.5 | 463.3 | 515.9 | 575.2 |
| 233 | 20 | 445.1 | 568.2 | 657.1 | 731.6 | 815.6 |
| 233 | 30 | 663.9 | 847.3 | 979.8 | 1091 | 1216 |

Table F.4. Dry-air Heat Transfer Rates for Slits (W)

| $T_{out}$ (K) | $\Delta P$ (Pa) | 6 (mm) | 14 (mm) | 22 (mm) | 30 (mm) | 40 (mm) |
|---|---|---|---|---|---|---|
| 273 | 0 | 7.93 | 7.94 | 7.96 | 7.97 | 7.98 |
| 273 | 2 | 20.88 | 24.53 | 27.18 | 29.40 | 31.91 |
| 273 | 8 | 59.61 | 74.08 | 84.55 | 93.32 | 103.2 |
| 273 | 14 | 98.42 | 123.7 | 142.0 | 157.3 | 174.6 |
| 273 | 20 | 137.3 | 173.4 | 199.5 | 221.4 | 246.0 |
| 273 | 30 | 202.3 | 256.4 | 295.5 | 328.3 | 365.3 |
| 263 | 0 | 11.82 | 11.82 | 11.85 | 11.87 | 11.89 |
| 263 | 2 | 24.70 | 28.37 | 31.04 | 33.27 | 35.81 |
| 263 | 8 | 63.19 | 77.67 | 88.16 | 96.96 | 106.9 |
| 263 | 14 | 101.8 | 127.1 | 145.4 | 160.7 | 178.0 |
| 263 | 20 | 140.6 | 176.7 | 202.8 | 224.6 | 249.3 |
| 263 | 30 | 205.4 | 259.5 | 298.6 | 331.4 | 368.4 |
| 253 | 0 | 15.64 | 15.65 | 15.69 | 15.71 | 15.74 |
| 253 | 2 | 28.46 | 32.15 | 34.83 | 37.09 | 39.65 |
| 253 | 8 | 66.71 | 81.21 | 91.72 | 100.5 | 110.5 |
| 253 | 14 | 105.1 | 130.4 | 148.7 | 164.1 | 181.4 |
| 253 | 20 | 143.8 | 179.9 | 206.0 | 227.9 | 252.6 |
| 253 | 30 | 208.4 | 262.5 | 301.6 | 334.4 | 371.5 |
| 243 | 0 | 19.41 | 19.42 | 19.47 | 19.5 | 19.54 |
| 243 | 2 | 32.16 | 35.87 | 38.57 | 40.84 | 43.42 |
| 243 | 8 | 70.17 | 84.68 | 95.21 | 104.0 | 114.0 |
| 243 | 14 | 108.4 | 133.7 | 152.0 | 167.4 | 184.8 |
| 243 | 20 | 146.9 | 183.0 | 209.1 | 231.0 | 255.8 |
| 243 | 30 | 211.31 | 265.4 | 304.6 | 337.4 | 374.5 |
| 233 | 0 | 23.12 | 23.14 | 23.20 | 23.23 | 23.27 |
| 233 | 2 | 35.80 | 39.52 | 42.24 | 44.53 | 47.13 |
| 233 | 8 | 73.56 | 88.09 | 98.64 | 107.5 | 117.5 |
| 233 | 14 | 111.6 | 136.92 | 155.3 | 170.7 | 188.0 |
| 233 | 20 | 150.0 | 186.1 | 212.2 | 234.1 | 258.9 |
| 233 | 30 | 214.2 | 268.4 | 307.5 | 340.3 | 377.4 |

Table F.5. Dry-air Flowrates for Holes ($x10^{-6}$ kg/s)

| $T_{out}$ (K) | $\Delta P$ (Pa) | 6 (mm) | 14 (mm) | 22 (mm) | 30 (mm) | 40 (mm) |
|---|---|---|---|---|---|---|
| 293 | 2 | 0.580 | 1.633 | 2.775 | 3.948 | 5.486 |
| 293 | 8 | 2.322 | 6.533 | 11.10 | 15.79 | 21.95 |
| 293 | 14 | 4.063 | 11.43 | 19.43 | 27.64 | 38.40 |
| 293 | 20 | 5.805 | 16.33 | 27.76 | 39.49 | 54.86 |
| 293 | 30 | 8.707 | 24.50 | 41.64 | 59.23 | 82.30 |
| 273 | 2 | 0.585 | 1.652 | 2.814 | 4.011 | 5.585 |
| 273 | 8 | 2.330 | 6.573 | 11.19 | 15.93 | 22.16 |
| 273 | 14 | 4.074 | 11.48 | 19.53 | 27.81 | 38.66 |
| 273 | 20 | 5.817 | 16.39 | 27.87 | 39.67 | 55.15 |
| 273 | 30 | 8.723 | 24.57 | 41.77 | 59.44 | 82.61 |
| 263 | 2 | 0.587 | 1.661 | 2.833 | 4.042 | 5.634 |
| 263 | 8 | 2.335 | 6.593 | 11.23 | 16.00 | 22.27 |
| 263 | 14 | 4.079 | 11.51 | 19.58 | 27.89 | 38.79 |
| 263 | 20 | 5.824 | 16.42 | 27.93 | 39.76 | 55.28 |
| 263 | 30 | 8.730 | 24.60 | 41.83 | 59.54 | 82.75 |
| 253 | 2 | 0.589 | 1.670 | 2.852 | 4.073 | 5.683 |
| 253 | 8 | 2.339 | 6.612 | 11.27 | 16.07 | 22.37 |
| 253 | 14 | 4.085 | 11.53 | 19.63 | 27.97 | 38.91 |
| 253 | 20 | 5.830 | 16.45 | 27.99 | 39.85 | 55.41 |
| 253 | 30 | 8.738 | 24.63 | 41.90 | 59.63 | 82.90 |
| 243 | 2 | 0.591 | 1.679 | 2.871 | 4.104 | 5.732 |
| 243 | 8 | 2.343 | 6.631 | 11.31 | 16.13 | 22.47 |
| 243 | 14 | 4.090 | 11.56 | 19.68 | 28.05 | 39.03 |
| 243 | 20 | 5.836 | 16.47 | 28.04 | 39.94 | 55.54 |
| 243 | 30 | 8.745 | 24.66 | 41.96 | 59.73 | 83.04 |
| 233 | 2 | 0.593 | 1.687 | 2.889 | 4.135 | 5.780 |
| 233 | 8 | 2.347 | 6.649 | 11.35 | 16.19 | 22.57 |
| 233 | 14 | 4.095 | 11.58 | 19.73 | 28.12 | 39.14 |
| 233 | 20 | 5.842 | 16.50 | 28.10 | 40.02 | 55.67 |
| 233 | 30 | 8.752 | 24.70 | 42.02 | 59.82 | 83.17 |

Table F.6. Dry-air Heat Transfer Rates for Holes (W)

| $T_{out}$ (K) | $\Delta P$ (Pa) | 6 (mm) | 14 (mm) | 22 (mm) | 30 (mm) | 40 (mm) |
|---|---|---|---|---|---|---|
| 273 | 0 | 6.225 | 6.225 | 6.226 | 6.227 | 6.228 |
| 273 | 2 | 6.393 | 6.702 | 7.039 | 7.386 | 7.843 |
| 273 | 8 | 6.896 | 8.126 | 9.467 | 10.85 | 12.67 |
| 273 | 14 | 7.401 | 9.553 | 11.90 | 14.32 | 14.50 |
| 273 | 20 | 7.906 | 10.98 | 14.34 | 17.80 | 22.34 |
| 273 | 30 | 8.751 | 13.37 | 18.41 | 23.61 | 30.43 |
| 263 | 0 | 9.272 | 9.272 | 9.273 | 9.274 | 9.275 |
| 263 | 2 | 9.437 | 9.742 | 10.08 | 10.42 | 10.88 |
| 263 | 8 | 9.931 | 11.15 | 12.47 | 13.85 | 15.65 |
| 263 | 14 | 10.43 | 12.55 | 14.88 | 17.28 | 20.44 |
| 263 | 20 | 10.93 | 13.97 | 17.29 | 20.72 | 25.24 |
| 263 | 30 | 11.76 | 16.33 | 21.33 | 26.49 | 33.28 |
| 253 | 0 | 12.27 | 12.27 | 12.28 | 12.28 | 12.28 |
| 253 | 2 | 12.44 | 12.74 | 13.07 | 13.41 | 13.87 |
| 253 | 8 | 12.92 | 14.12 | 15.44 | 16.80 | 18.59 |
| 253 | 14 | 13.41 | 15.51 | 17.81 | 20.19 | 23.33 |
| 253 | 20 | 13.90 | 16.91 | 20.20 | 23.61 | 28.10 |
| 253 | 30 | 14.72 | 19.24 | 24.20 | 29.33 | 36.08 |
| 243 | 0 | 15.23 | 15.23 | 15.23 | 15.23 | 15.24 |
| 243 | 2 | 15.39 | 15.69 | 16.02 | 16.36 | 16.81 |
| 243 | 8 | 15.87 | 17.05 | 18.36 | 19.70 | 21.49 |
| 243 | 14 | 16.35 | 18.42 | 20.70 | 23.07 | 26.18 |
| 243 | 20 | 16.83 | 19.80 | 23.07 | 26.45 | 30.91 |
| 243 | 30 | 17.64 | 22.11 | 27.03 | 32.12 | 38.84 |
| 233 | 0 | 18.14 | 18.14 | 18.15 | 18.15 | 18.15 |
| 233 | 2 | 18.30 | 18.60 | 18.92 | 19.26 | 19.71 |
| 233 | 8 | 18.77 | 19.94 | 21.23 | 22.57 | 24.34 |
| 233 | 14 | 19.24 | 21.29 | 23.55 | 25.89 | 28.99 |
| 233 | 20 | 19.72 | 22.65 | 25.89 | 29.25 | 33.68 |
| 233 | 30 | 20.51 | 24.94 | 29.81 | 34.87 | 41.56 |